In gas jet laser spectroscopy optimization for high resolution measurement of actinides

Anjali Ajayakumar

Normandie Université

UNIVERSITÉ CAEN NORMANDIE

THÈSE

Pour obtenir le diplôme de doctorat

Spécialité **PHYSIQUE**

Préparée au sein de l'**Université de Caen Normandie**

IN GAS JET LASER SPECTROSCOPY OPTIMIZATION FOR HIGH RESOLUTION MEASUREMENT OF ACTINIDES

Présentée et soutenue par

ANJALI AJAYAKUMAR

Thèse soutenue le 21/12/2023

devant le jury composé de :

MME JULIA EVEN	Professeur - GRONINGEN - UNIVERSITY OF GRONINGEN	Rapporteur du jury
M. BRUCE MARSH	Chercheur HDR - CERN	Rapporteur du jury
M. BERTRAM BLANK	Directeur de recherche au CNRS - UNIVERSITE BORDEAUX 1 SCIENCES ET TECHNOLOGIE	Membre du jury
MME NATHALIE LECESNE	Ingénieur de recherche au CNRS - 14 GANIL de CAEN	Membre du jury Co-encadrante
M. ETIENNE LIENARD	Professeur des universités - Université de Caen Normandie	Président du jury
M. HERVÉ SAVAJOLS	Directeur de recherche au CNRS - 14 GANIL de CAEN	Directeur de thèse

Thèse dirigée par **HERVÉ SAVAJOLS** (Grand Accélérateur National d'Ions Lourds)

ED 591 PSIME

GANIL laboratoire commun CEA/DRF Spiral2 CNRS/IN2P3

Acknowledgments

This thesis would not have been possible without the support of my team.

I am grateful to Dr. Nathalie Lecesne, my supervisor, and Dr. Hervé Savajols, my thesis director, for allowing me to be part of the S^3-LEB group. Thank you for being patient with me and for correcting and guiding me with your valuable feedback throughout this journey.

Jekabs, Alex, and Wenling, I am grateful for your time and guidance professionally and personally. Thank you for the wonderful memories from our lab, workshops, and conferences to hiking trips and beaches. I would also like to thank Alexandre, Antoine, and Lucia for the valuable discussions.

I would like to express my indebt gratitude to Vladimir, Serge, and Sarina, for mentoring me. You have been constantly guiding me in my Ph.D. endeavours from clearing my doubts to participating in hands-on measurements in the lab and correcting my reports. I am also sincerely grateful to Volker for your suggestions regarding the laser work.

I would like to thank the LISA ITN collaboration for creating such a dynamic environment for all of the Ph.D. students in the network. Interaction with the LISA community on several occasions has helped us improve and widen our skills and knowledge. LISA ESRs, it has been a pleasure to be one among you and learn with/from you.

I would also like to thank my jury members for their valuable suggestions for the completion of my thesis.

Finally, I would like to express my deep gratitude to my family and friends for believing in me even when I had my doubts. Thank you for being there for me in my ups and downs, for motivating me, and for inspiring me to work harder and learn new things. To my friends from campus 2, thank you for making these three years fun-filled.

Anjali Ajayakumar

Abstract

The Super Separator Spectrometer-Low Energy Branch (S3-LEB) is a low-energy radioactive ion beam experimental setup under commissioning as part of the GANIL-SPIRAL2 facility [1]. It will be used for the production and study of exotic nuclei by in-gas laser ionization and spectroscopy (IGLIS), decay spectroscopy, and mass spectrometry. The GANIL SPIRAL 2 facility, of which the S^3-LEB is a part, will allow for increased production capabilities and a combination of several low-energy techniques of study for the produced nuclei can contribute to many physics opportunities and new discoveries.

In this thesis work, the off-line commissioning of the S^3-LEB setup at LPC Caen, including first laser spectroscopy measurements in both the gas cell and the supersonic gas jet, the determination of the transport efficiency of laser ions from the gas cell through the RFQ chain, and time-of-flight measurements with the multi-reflection time-of-flight mass spectrometer PILGRIM are discussed. The measurements were performed using erbium, introduced by evaporation from a heated filament in the gas environment. The reported laser spectroscopy results include a characterization of the pressure broadening in the gas cell, proof-of-principle isotope shift measurements, and hyperfine-structure measurements. This work proves the potential of the setup to conduct the future online test, where erbium is chosen as the first case for online commissioning. Also, offline laser ionization and spectroscopy of uranium and americium from the actinide series have been discussed. The tests have been performed at IGISOL, Jyvaskyla and RISIKO, MAINZ as a part of the LISA ITN MSCA collaboration. Uranium tests discuss laser scheme tests and preliminary gas cell tests performed as part of the study of collisional effects in gas cells hindering the laser ionization efficiency.

This thesis work also includes technical developments such as the implementation of the titanium sapphire laser systems and a dedicated entrance window testbench for the S^3-LEB. A continuous wave diode-pumped laser system is built from scratch for high-resolution laser spectroscopy application. These developments will be crucial for the offline resonance ionization laser scheme developments and tests to find the optimum schemes that can extract atomic and nuclear information. Americium laser spectroscopy measurements at RISIKO present the potential of such a laser system in performing high-resolution measurements in actinides. The laser characterization work is performed in the

GISELE lab, an offline lab to study stable isotopes, and will be utilized for tests on the future S^3-LEB experiments on radioactive elements. The entrance window test bench will be used for testing and careful mounting of the window foil before its installation in the gas cell for online experiments. This thesis work also includes the estimation of the best entrance window and gas cell pressure combinations for S^3-LEB.

Contents

List of Figures

List of Tables

Introduction

The quest to know the fundamental nature of matter began in the early history of Democritus' speculation of atoms. Much later, the field of nuclear physics emerged at the time of the discovery of radioactivity in 1896. In the following year, electrons were discovered by J.J Thompson. Fourteen years later, the nucleus was discovered by Rutherford. From then to now, tremendous understanding has been achieved in the field, and yet more to explore. The reason for the progress in the field is often linked with the development of new technologies and applications, its scope extending to the understanding of fundamental constituents of matter, the interaction between neutrons and protons, and the nuclear structure and reactions.

Laser ionization and spectroscopy have significant contributions to the field of atomic and nuclear physics [2]. With the availability of tunable narrow-linewidth lasers, new opportunities opened up for the study of atomic and nuclear structures with high sensitivity and resolution. Radioactive ion beam (RIB) facilities along with laser ionization and spectroscopy allow the study of unstable nuclides, thereby shedding light on the new patterns. In RIB facilities, laser spectroscopy techniques such as collinear laser spectroscopy (CLS) and resonance ionization laser spectroscopy (RIS) are commonly used. Figure 1 shows a nuclide chart with nuclei investigated using laser spectroscopy by RIB facilities [3]. The black squares in the figure show the stable nuclei existing in nature. The blue and red squares show the nuclei studied with RIS and CLS respectively. It can be seen from the chart that a lot of nuclei have to be still investigated using the laser spectroscopy technique. The challenges in studying these nuclei include difficulties in their production due to low production cross-sections, short lifetimes, or their refractory nature.

Some of the leading RIB facilities in the world with dedicated laser spectroscopy lines to study RIBs are ISOLDE (CERN, Switzerland), FRIB (MSU, USA), ISAC (TRIUMF, Canada), IGISOL (Jyvaskyla, Finland) and, KISS (RIBF, Japan). Other emerging RIB facilities to use laser spectroscopy for nuclear physics are CARIBU (ANL, USA), SPIRAL2 (GANIL, France), FAIR (GSI, Germany), and BRIF (China). There are several approaches for laser ion sources implemented in these facilities. The most often used method in Isotope Separator Online (ISOL)-type facilities is the hot cavity approach using thick targets. The hot cavity approach requires the target to be heated to very high

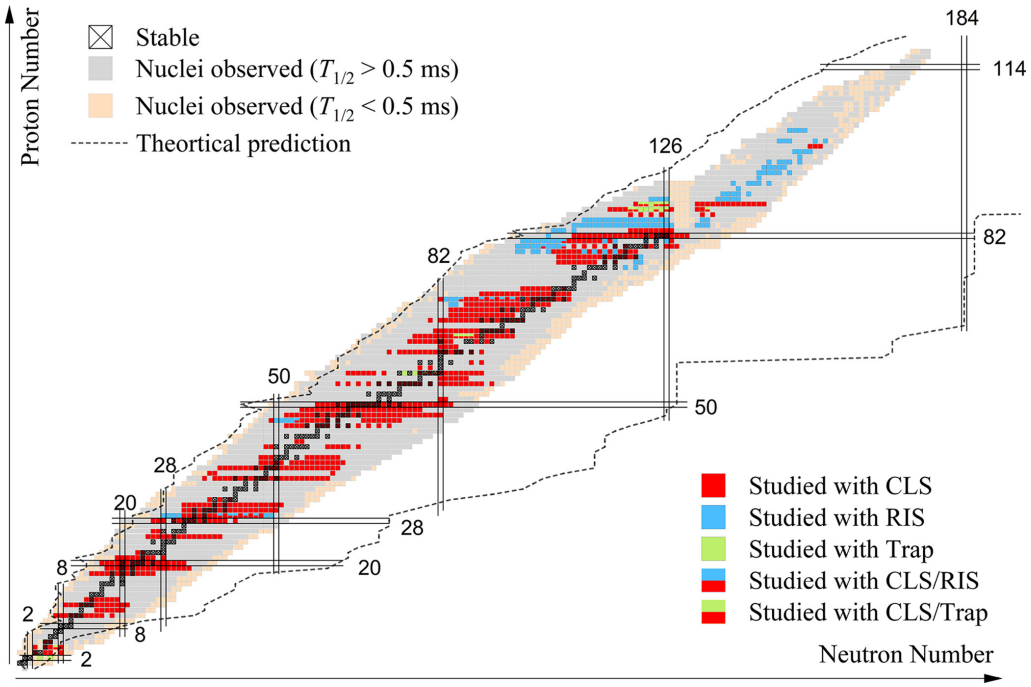

Figure 1: Nuclide chart showing the species investigated using laser spectroscopy (taken from [3]).

temperatures to enable diffusion and release of the ions from the target to the ion source region. It produces exotic species at a high production rate but is restricted in performance when it comes to the study of refractory and short-lived elements due to the limitations in release from the thick target and chemical sensitivity. An alternative approach is the thermalization of the reaction products in a buffer gas and the use of RF structures for guiding them to detection. This method, called the in-gas laser ionization and spectroscopy (IGLIS) technique, was first developed by the Leuven Isotope Separation On-line facility (LISOL) Belgium [4] and later implemented in the IGISOL facility where the recoil products were stopped in a gaseous chamber and transported for further analysis. Both approaches can be used for in-source laser spectroscopy to measure isotope shift and hyperfine structures but are limited in resolution due to the high temperature or pressure environments. An improved spectral resolution can be achieved in the hot cavity by the laser ion source and trap (LIST) method. Here, the laser ionization occurs in a subsequent radiofrequency ion guide structure separated from the high-temperature environment for the hot cavity method [5].

In the buffer-gas cell laser ion source, the gas cell designs were improved over the years and a dual gas cell chamber design was later implemented to separate the stopping and laser ionization regions to decouple the accelerated beam path from the laser-produced ions, thus reducing the isobaric backgrounds and recombination of laser ions [6]. Laser ionization efficiency could be improved by this design. However, for in-gas cell laser ionization, the resolution for laser spectroscopic studies is limited by the high-pressure environment. A supersonic gas jet created by the addition of a De-Laval nozzle to the gas cell exit was then developed to allow laser interaction in a reduced temperature and pressure environment thereby enabling improved spectral resolution [7].

In this work, the importance of the RIS technique in RIBs to extract the nuclear structure and its challenges are illustrated in several ways. Resonance laser ionization with multiple excitation steps, is an efficient means of producing ions, with elemental selectivity, as well as a spectroscopic technique. This thesis work is mainly focused on the commissioning and related developments of a dedicated resonance laser ionization and spectroscopy setup, Super Separator Spectrometer-Low Energy Branch (S^3-LEB) for the SPIRAL2 facility in GANIL, France, that will come online in the coming years [1]. It combines the advantages of inflight and ISOL techniques, providing selectivity and high production cross-section. The setup will allow the study of neutron-deficient and heavy nuclei using a combination of low-energy techniques after stopping them in a thermalization and neutralization gas cell. The S^3-LEB setup uses the IGLIS technique for laser ionization and spectroscopy of exotic RIBs either in the gas cell or outside the gas cell in a supersonic gas jet environment. S^3-LEB, with in-gas jet spectroscopy technique, can provide enhanced spectral resolution giving access to ground-state and isomeric-state isotope shifts and hyperfine structure measurements. Coupling to a multi-reflection time of flight mass spectrometer (MR-TOF-MS) called "Piège à Ions Linéaire du GANIL pour la Résolution des Isobares et la mesure de Masse" (PILGRIM) [8] or a decay station called Spectroscopy Electron Alpha in Silicon bOx couNter (SEASON) [9] extends its possibilities for mass measurements and decay studies with suppressed isobaric contamination. S^3-LEB is currently installed at LPC Caen and the entire setup including the gas cell, radiofrequency quadrupole (RFQ) ion guides, ion cooler and buncher, and MR-TOF MS was completed. Its offline commissioning with in-gas cell and in-gas jet laser spectroscopy has been reported in this work.

The following will be discussed in this thesis. Chapter 1 will summarize the theoretical background necessary for the conduction of this research work. It will outline the basics of nuclear ground state properties, concepts of laser physics, and their application in ionization and spectroscopy for deducing atomic and nuclear observables.

Chapter 2 gives a summary of resonant laser ionization-based spectroscopy techniques for conducting atomic and nuclear structural studies in radioactive ion beam facilities. The chapter mainly focuses on the description of gas-cell-based laser ion source and their implementation in a low-energy ion beam facility, S^3-LEB. The current status of this setup is presented as the thesis work mainly focuses on its commissioning work.

Chapter 3 presents the technical developments performed for the laser spectroscopy in S^3-LEB. The Ti: sapphire laser systems installed for S^3-LEB are discussed. It also details the development work of a continuous wave (CW) Ti: sapphire-based laser system and its characterization performed in regard to its application in high-resolution laser spectroscopy.

Chapter 4 details the work performed related to the offline commissioning of the S^3-LEB setup. The setup uses resonance laser ionization combined with ion guides and mass separators, providing capabilities in the study of individual isotopes. Resonance ionization laser spectroscopy was performed on the stable isotopes of erbium. Optimization of the relative transport efficiency of laser ions through the entire setup and time-of-flight measurements with the multi-reflection time-of-flight mass spectrometer PILGRIM is presented. The

laser spectroscopy results include a characterization of the pressure broadening in the gas cell, proof-of-principle isotope shift measurements, and hyperfine-structure measurements. Part of this work has been reviewed and published in the special issue VSI: EMIS at Raon, Nuclear Instruments and Methods in Physics Research B (2023).

Chapter 5 discusses the offline laser spectroscopy tests performed at RISIKO, JGU Mainz, and at IGISOL, University of Jyvaskyla, Finland. The experiments were performed on actinide elements which are located in the heavier mass regions of the nuclide chart. The americium laser spectroscopy performed at RISIKO gives an evaluation of the performance of a newly designed continuous wave laser system in high-resolution laser spectroscopy of actinides. The offline atomic beam unit (ABU) experiments on uranium in IGISOL discuss the RIS laser scheme tests as a part of the preparation for the in-gas cell laser ionization spectroscopy experiment in IGISOL and later at S^3. This section summarizes the challenges in performing laser spectroscopy on actinides in high-pressure gas cells due to the collisional effects.

Chapter 6 concludes this thesis work with a general summary of the work and future outlook.

CHAPTER 1

Theoretical concepts

Nuclear structure research is a quest to understand the constituents of matter. That quest is often linked with the development of new technologies and applications. Atomic physics techniques can provide fundamental and nuclear model-independent data that can give insight into the structure of nuclear ground states and isomeric states. Knowledge of nuclear properties such as shape, spin, and moments can be gained by probing the perturbed atomic energy level due to its coupling with the nucleus. Owing to the nucleus not being a point charge and of finite mass, the atomic levels for isotopes show a shift in the probed energy levels. Apart from the shift in the energy level, the interaction between the electrons and electrons with the nucleus causes the splitting of the atomic energy levels to fine and hyperfine structures. There are different techniques both optical and non-optical to probe the isotope shifts and hyperfine structure. In this work, we focus on the resonant laser ionization spectroscopy technique to probe these atomic observables. In the following section, the basic theory of the nuclear properties that can be deduced from the isotope shift and hyperfine structure measurements are summarised. Since this research work is concerned with laser spectroscopy and the developments involved with it, the basic theory of laser physics is mentioned as well.

1.1 Nuclear ground state properties

The atomic nucleus is composed of nucleons that are bound by their mutual interactions. However, the absence of a comprehensive nuclear theory that can account for all nuclei and nuclear phenomena is due to the restricted understanding of inter-nucleon forces and the complexities associated with resolving the quantum many-body problem. Various nuclear models are employed for comprehending nuclear structure such as the ab initio techniques (that solve the Schrödinger equation for all nucleons), liquid-drop and droplet models, shell model, and collective model. Diverse levels of detail and approximation are provided by these models to address different aspects of nuclear behavior. The liquid drop model regards the nucleus as a charged liquid that is incompressible giving an understanding of the nuclear properties like nuclear masses and

binding energies. The collective model integrates aspects of the liquid-drop framework and shell-model phenomena. It takes into account the collective motion of nucleons like nuclear vibrations and rotations. Shell model theory explores the concept of a nuclear shell similar to atomic shells. Shell model calculates the wavefunctions of the nuclear states as mixtures of configurations in which nucleons occupy discrete energy levels, called single-particle orbitals. The nucleons can occupy only certain energy-level shells separated by a gap. Following the quantum mechanical rule, protons and neutrons are organized in the shells to define specific nuclei. A certain number of protons and neutrons form a completely filled shell or closed shell giving rise to magic numbers in the order 2, 8, 20, 28, 50, 82, and 126 (for neutrons). Different theoretical predictions give the proton shell closures at higher Z to be 114, 120 or 126. The shell model was developed to explain the interesting properties that came with nuclei exhibiting this magic number of nucleons such as enhanced stability, an abundance in the number of stable nuclei with a magic number of protons/neutrons, and an increase in the first excitation energy and so on. To understand better, the nucleus can be considered as a many-body system of interacting nucleons with a mean-field potential. The many-body problem can be expressed as [10]:

$$H\big|\psi\big\rangle = E\big|\psi\big\rangle = (T+V)\big|\psi\big\rangle \tag{1.1}$$

where E is the total energy, T and V are the kinetic energy operator and potential energy of the interacting nucleons respectively. The potential energy calculation can be restricted to two-body interactions (e.g.: H nuclei) for simplicity and can be expressed as [10]:

$$V = \sum_{i<j}^{N} v_{ij} + \sum_{i<j<k}^{N} v_{i,j,k} + ... \approx \sum_{i<j}^{N} v_{ij} \tag{1.2}$$

where i represent one of the nucleons, j a second one (two-body), and k, a third nucleon (three-body). Introducing the mean-field potential U, the Hamiltonian in equation 1.1 can be expressed as [10]:

$$H = T + \sum_{i} U_i + V - \sum_{i} U_i = H_0 + H_{res} \tag{1.3}$$

where H_0 is Hamiltonian describing the independent particle shell model calculations. H_{res} is the Hamiltonian describing residual interactions that are added as perturbations to the single particle shell model calculations. The independent particle shell model works well when these residual interactions are small. The independent particle shell model takes into account a harmonic oscillator potential, spin-orbit coupling, and an additional term proportional to the square of the total angular momentum for the mean-field potential. It can be expressed as [10]:

$$U(r) = \frac{1}{2} m\omega^2 r^2 + C\ l.s + D\ l.l \tag{1.4}$$

where m is the particle mass, ω is the angular frequency of the oscillator, r is the orbital radius, l is the orbital angular momentum, s is the spin angular momentum, and C and D are constants defining the strength of coupling. The experimental results from laser spectroscopy can be used to benchmark these

nuclear models and these theoretical models provide interpretation to the experimental observations, both playing a crucial role. Some of the nuclear ground state properties that can be probed by laser spectroscopy are explained below based on these models.

1.1.1 Nuclear spin

In the independent-particle shell model, each nucleon occupies an orbital designated by an orbital angular momentum (l) and a spin angular momentum (s). In a nucleus, the orbital angular momentum of the nucleons (l_i) and spin angular momentum (s_i) couple to generate a total angular momentum (j_i). The parity of the orbital is given by $\pi_i = (-1)^l$. The summation of the angular momenta of all nucleons results in the nuclear spin (I), which is a vector quantity. It represents the total angular momentum of all nucleons in the nucleus, given by [10]:

$$I = \sum_{i=1}^{A}(l_i + s_i) = L + S \tag{1.5}$$

Here L and S represent the orbital and intrinsic contributions to angular momentum.

For even-even nuclei, the total ground state spin is zero with positive parity because of the pairing of nucleons to form a couple. The ground−state spin and parity in odd-even nuclei are established by the final odd particle present in the orbital that possesses angular momentum j. This is not always true mostly close to magic numbers when pairing coupling dominates over other interactions (see section 1.2.1). For odd-odd nuclei, the ground state spin is calculated according to the angular momentum coupling rule for the unpaired neutron and unpaired proton [10].

In the case of deformed nuclei, the particle-rotor model comes into the picture. Here, the unpaired valence nucleons are used to determine the ground state spin where the projection of angular momentum on the nuclear symmetry axis (Ω) is considered such that $\Omega = \sum_{i=1}^{A} \Omega_i$. In odd-even nuclei, Ω is the same as the $|\Omega_i|$ of the last unpaired nucleon. For odd-odd nuclei, Ω is equal to $|\Omega_\pi + \Omega_\nu|$, angular momentum components of unpaired proton (π) and neutron (ν).

1.1.2 Nuclear moments

Nuclear charge radii

Nuclear size is defined by the density distribution of neutrons and protons. According to the liquid drop model, the radius of proton distribution in the nucleus can be assumed as:

$$R = R_0 A^{1/3} \tag{1.6}$$

where R_0= 1.2 fm and A is the atomic mass number or the number of nucleons in the nucleus. Laser spectroscopy cannot access the density distribution but can give information on charge radius which is related to the proton and neutron density distribution. Absolute charge radii can be measured by muonic and x-ray scattering experiments. Laser spectroscopy cannot extract absolute charge radii but the changes in the charge radii between isotopes can be determined

from the isotope shift measurements. Nuclear mean-square charge radii is the second radial moment of the nuclear charge distribution given by [11]:

$$\langle r^2 \rangle = \frac{\int_0^R \rho(r) r^2 dr}{\int_0^R \rho(r) dr} \tag{1.7}$$

Here $\int_0^R \rho(r)dr$ is the nuclear charge Ze. Generally, the mean square charge radius is used to characterize the finite nuclear size. The contribution of radial moments higher than the second order is much smaller and can only be deduced with high-precision experimental techniques. The change in mean square charge radii as a result of the neutron number is revealed by isotope shifts. The mean square charge radius of a deformed nucleus is given by [11]:

$$\langle r^2 \rangle = \langle r^2 \rangle_{sph} \big(1 + \frac{5}{4\pi} \langle \beta^2 \rangle\big) \tag{1.8}$$

where $\langle r^2 \rangle_{sph}$ is the radius of a spherical nucleus with the same volume and β is the quadrupole deformation factor. Mean square charge radii are thus sensitive to nuclear deformation. Liquid drop model mean square charge radii is often considered for the radius of the spherical nucleus and is expressed as [10]:

$$\langle r_{LD}^2 \rangle = \frac{3}{5} R_0^2 A^{2/3} \tag{1.9}$$

and its differential gives:

$$\delta \langle r_{LD}^2 \rangle = \frac{2}{5} R_0^2 A^{-1/3} \delta A \tag{1.10}$$

Nuclear magnetic dipole moment

The nucleus consists of charged particles (protons) and the motion of these charged particles in classical treatment causes a magnetic effect on other nearby charged particles. The nuclear magnetic dipole moment is the lowest order term in a multipole expansion of current distribution due to the motion of charges over a nuclear volume v with an orbital (l) and intrinsic angular momentum (s). Excluding the intrinsic spin, from the truncated multipole expansion, the magnetic dipole moment corresponding to a wavefunction for a specific state $l_z = m_l \hbar$ is given by [10]:

$$\mu_z = \frac{e}{2m} \int \psi^*(r') l_z \psi(r')\, dv' = \frac{e\hbar}{2m} m_l \tag{1.11}$$

where e is the charge of the particle, $\hbar$ is reduced Planck's constant, m is the mass of the particle, m_l is the orbital angular momentum quantum number ranging from $-l$ to $+l$, and $e\hbar/2m$ is called a magneton, a quantity having dimensions of the magnetic moment. When the proton is the particle considered, it is referred to as a nuclear magneton μ_N. Magnetic moment due to orbiting proton thus becomes $\mu = g_l l \mu_N$. Proton also has an intrinsic spin contributing to the magnetic moment as $\mu = g_s s \mu_N$. Here g_l and g_s are dimensionless quantities known as g-factors. Thus magnetic moment of the nucleus is due to orbiting protons as well as the intrinsic spin of the nucleons (protons and

neutrons). The magnetic dipole moment of the nucleus is then given by a dipole operator $\hat{\mu}$ [11]:

$$\hat{\mu} = \sum_{i=0}^{Z} g_L^{\pi} \hat{L}_i + \sum_{i=0}^{Z} g_S^{\pi} \hat{S}_i + \sum_{j=0}^{N} g_L^{\nu} \hat{L}_i + \sum_{j=0}^{N} g_S^{\nu} \hat{S}_j \tag{1.12}$$

where Z is the number of protons (π) and N is the number of neutrons (ν) in the nucleus. The factors g_L and g_S are gyromagnetic factors characterizing the orbital magnetic field and the intrinsic magnetic field (due to its spin) for protons (π) and neutrons (ν) respectively. The magnetic moment is the expectation value of the z-components of the dipole operator with maximal spin projection $m = I$ expressed as [10]:

$$\mu(I) = \langle I, m = I | \hat{\mu_z} | I, m = I \rangle = \left(\frac{I}{I+1} \right)^{1/2} \langle I || \hat{\mu} || I \rangle \tag{1.13}$$

It is related to nuclear spin I as $\mu = g_I I \mu_N$, where $\mu_N = e\hbar/2m_\pi$ is the nuclear magneton and g_I is the g-factor considering the influence of other nucleons. From the above equation, it can be understood that when the nuclear spin is zero as in the case of even-A nuclei, observable magnetic dipole moment is not present. Also, paired nucleons do not contribute to magnetic dipole moment. Only the unpaired valence nucleons contribute to the magnetic dipole moment of the nucleus. For odd-A nuclei, the magnetic moment is due to the last odd nucleon (proton or neutron).

The dipole moment operator is a one-body operator or a tensor with rank 1. The g-factors for a single particle in an orbital j is given by:

$$g = \frac{\mu(j)}{j} \tag{1.14}$$

For a nuclear state with spin I, the expectation value for the z-component of the dipole operator is given by :

$$\mu(I) = \langle I(j_1, j_2, ..., j_n), m = I | \hat{\mu_z(i)} | I(j_1, j_2, ..., j_n), m = I \rangle \tag{1.15}$$

For a nuclear state with orbits j_i (containing valence nucleons) coupled to I, the magnetic moment can be deduced as a function of its single particle components by applying additivity rules to the equation 1.15. If nuclear spin is not known, the g-factors known as Schmidt values can be deduced as a function of free nucleon g-factors by the additivity rules [3]. Experimental deduction of these g-factors and their comparison with calculations and effective $g_{l,s}$ (real nuclei have additional contributions to magnetic moments from the presence of other nucleons leading to effective moments) gives information on how configuration mixing and valence particle occupation influence the properties of the atomic nucleus [3]. Figure 1.1 shows an example of the experimental nuclear magnetic moments for an isotopic chain of Cu where the experimentally extracted moments are compared with estimated effective Schmidt moments. The Schmidt moments are estimated using effective spin g-factor, $g_s^{eff} = 0.7 g_s^{free}$ for a single proton. These measurements from laser spectroscopy experiments validated the theoretical prediction of inversion of proton $\pi 0f_{5/2}$ and $\pi 1p_{3/2}$ single particle orbital occurring when neutrons occupy $\nu 1g_{9/2}$ orbital [3].

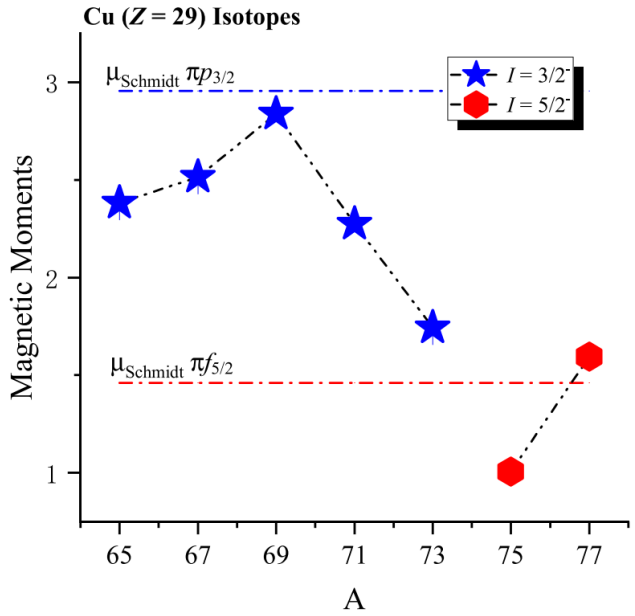

Figure 1.1: An example showing the experimental $3/2^-$ and $5/2^-$ magnetic moments of Cu isotopes compared with the estimated effective Schmidt moments (plot taken from [3]).

1.1.3 Nuclear electric quadrupole moment

The nuclear electric quadrupole moment is another ground state property, indicative of the non-spherical charge distribution in a given nucleus. The electric potential from a reference point r due to a charge distribution over a volume v is given by [10]:

$$V(r) = \frac{1}{4\pi\epsilon_0}\int \frac{\rho(r')\,dv'}{|r-r'|} \tag{1.16}$$

where $\rho(r')$ is the charge distribution. The multipole expansion of the electric field by expanding $|r-r'|$ gives a constant term corresponding to the total charge Ze, a second term which is a dipole term, followed by a quadrupole term, and higher order terms. Here θ is the angle between r and r' with the assumption that observation point $r' >> r$, where r is the reference point for the nucleus [10].

$$\begin{aligned} V(r) = \frac{1}{4\pi\epsilon_0}\Bigg[\frac{1}{r}\int \rho(r')\,dv' + \frac{1}{r^2}\int \rho(r')\,r'\cos\theta dv' \\ + \frac{1}{r^3}\int \rho(r')\,r'^2(3\cos^2\theta' - 1)dv' + ...\Bigg] \end{aligned} \tag{1.17}$$

The quadrupole term in the electric field expansion varies as r^{-4} and defines the nuclear electric quadrupole moment. In a spherical coordinate system, it can be expressed as [10] :

$$eQ = \int \rho(r')r'^2(3\cos^2\theta' - 1) \tag{1.18}$$

where θ' is the angle measured from an axis corresponding to the maximum projection of nuclear spin. In cartesian coordinate, r becomes z and $r'\cos\theta$ becomes z'. The nuclear quadrupole moment tells whether the nuclei are spherical

or nonspherical. If the quantity $3\cos^2\theta' - 1 = 3z'^2 - 1$ is on the average positive, $Q > 0$ and are prolate shaped. It means that the nuclear charge density is more concentrated along the z' axis than the average radius. If $3z'^2 - 1$ is negative, $Q < 0$ and is oblate shaped. For a nucleus of mass number A, then the charge quadrupole moment becomes [11]:

$$Q_z = \sum_{i=1}^{A} Q_z(i) = \sum_{i=1}^{A} e_i(3z_i^2 - r_i^2) \tag{1.19}$$

where e_i is the charge of the nucleons. The z^{th} component of the quadrupole moment operator in spherical coordinate is a zero-order tensor component of rank 2 and can be expressed as:

$$\hat{Q_z} = \hat{Q_2^0} = \sqrt{\frac{16\pi}{5}} \sum_{i=1}^{A} e_i r_i^2 Y_2^0(\theta_i, \phi_i) \tag{1.20}$$

The quadrupole moment which can be determined from the experiment is an expectation of the quadrupole moment operator in a nuclear state $m = I$ [11] given by [11]:

$$Q_s = \langle I, m = I|\hat{Q_z}|I, m = I\rangle = \sqrt{\frac{I(2I-1)}{(2I+1)(2I+3)(I+1)}}\langle I||\hat{Q}||I\rangle \tag{1.21}$$

where $\langle I||Q||I\rangle$ is the reduced matrix element from Wigner-Eckart theorem [12]. Experiments measure the maximum projection of the intrinsic electric quadrupole moment along the quantization axis, which is different from the intrinsic quadrupole moment.

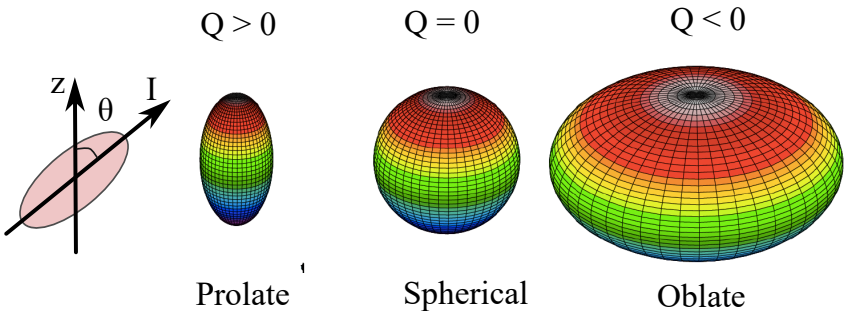

Figure 1.2: A pictorial representation of nuclear shape for different quadrupole moment values.

For $I < 1$, $Q_s = 0$ according to expression 1.21 though $I = 0$ or $1/2$ can have an intrinsic deformation. $Q_s < 0$ indicates to oblate deformation and $Q_s > 0$ to prolate deformation. Assuming the deformation of the nucleus to be axially symmetric with nuclear spin, the Q_s is related to the intrinsic quadrupole moment Q_0 as [11]:

$$Q_s = \frac{3K^2 - I(I+1)}{(I+1)(2I+3)}Q_0 \tag{1.22}$$

where K is the projection along the symmetry axis of the nuclear spin I. It should be noted here that the rotor model is considered for the above expression

and is applicable only for well-deformed nuclei. The Q_0 is then related to the nuclear quadrupole deformation parameter β as [11]:

$$Q_0 = \frac{3}{\sqrt{5\pi}} zR^2\beta(1 + 0.36\beta) \tag{1.23}$$

where $R = R_0A^{1/3}$ is the radius of the proton distribution considering the liquid drop model. Similar to the magnetic dipole operator, the electric quadrupole moment operator is also a one-body operator. The single particle quadrupole moment for an unpaired nucleon with angular momentum j and effective charge e_j can be calculated from equation 1.21 as [11]:

$$Q_{s.p.} = -e_j \frac{2j-1}{2j+2} \langle r_j^2 \rangle \tag{1.24}$$

The effective charge comes into the picture when the interaction of nucleons with the nuclear mean field (core) is considered. For neutrons, the charge is zero and hence induces zero single-particle quadrupole moment. But neutrons in a nucleus can interact with the core. According to the shell field, the nucleus can be described as a core with a mean field and valence nucleons moving and interacting with each other and polarizing it thus giving an effective charge for neutrons. Thus the valence particle with negative spectroscopic quadrupole moment can polarize the core toward oblate deformation and a hole in the j orbital can polarize the core to prolate deformation.

1.2 Laser spectroscopy as an atomic probe

Laser spectroscopy can probe perturbations in the atomic energy level caused by the interaction of the electrons between them as well as with the nucleus. Resonance ionization laser spectroscopy is one of the laser spectroscopic techniques used for probing atomic transition and exploring the nuclear structure of elements. It uses two or more lasers to resonantly excite the atoms until it is ionized. This technique is advantageous because of its higher cross-section due to its resonant nature giving higher ionization efficiency. The use of high-resolution, tunable lasers for resonance ionization spectroscopy provides high spectral power density and spectral resolution. It allows extraction of atomic observables like isotope/isomer shift and hyperfine structure. These atomic observables can then be used to deduce nuclear information such as the nuclear spin, and the electromagnetic moments of the nucleus which was discussed in detail in section 1.1. In this section, the basic concepts of atomic-energy level transitions related to electron-nucleus interaction will be discussed.

1.2.1 Atomic transition

An atomic state can be defined by a wavefunction ψ given by the Hamiltonian:

$$H\psi = E\psi \tag{1.25}$$

An atom can go to an excited state or decay from the excited state by absorbing or emitting photons. Spectral analysis of these radiative transitions gives knowledge of the atomic structure and also to some extent nuclear structure.

Atomic energy states are affected by the finite nuclear size and mass which are treated as perturbations and some of these effects such as the isotope shift and the hyperfine splitting are described in the following subsections.

The interaction of the nucleus with the electromagnetic fields of the atomic electrons can be expressed using a Hamiltonian of multipole series expansion [13]:

$$H_{eN} = \sum_k T^k(N) \cdot T^k(e) \tag{1.26}$$

where $T^k(N)$ and $T^k(e)$ are tensor operators of rank k operating in the nuclear space and space of the electrons. Only even electric multipoles and odd magnetic multipoles contribute to the series. The term $k = 0$ contributes to the structure and fine structure of the atomic levels. Fine structure splitting is a characteristic of the spin-orbit interaction of the electrons in the atoms. This is because an electron in an atomic system with charge e^- moving with orbital angular momentum l around the nucleus produces a magnetic moment μ_l given by:

$$\mu_l = \frac{-e}{2m_e} l = -g_l(\mu_B/\hbar)l \tag{1.27}$$

Apart from the electron's orbital angular momentum, the spin of the electron causes additional magnetic moment given by:

$$\mu_s = -g_s \frac{e}{2m_e} s = -g_s(\mu_B/\hbar)s \tag{1.28}$$

where μ_B is the Bohr magneton and $g_s \approx 2$ and $g_l \approx 1$ are the Lande g-factors. The interaction of the spin magnetic moment with the internal magnetic field produced by the orbital motion of the electrons causes a perturbation in the electronic energy level. In other words, in the reference frame of electrons, the nucleus spins around it and produces a magnetic field that interacts with the intrinsic spin of the electron. This introduces the quantum number $j = l + s$ which is the total angular momentum where $j \neq 0$ if $l \geq 1$. The perturbed energy level is given by:

$$E_{n,l,j} = E_n + \frac{a}{2}[j(j+1) - l(l+1) - s(s+1)] \tag{1.29}$$

where

$$a = \frac{\mu_0 Z e^2 \hbar^2}{8\pi m_e^2 r^3} \tag{1.30}$$

where E_n is the unperturbed energy levels and a is the spin-orbit coupling constant for a hydrogen-like atom with a single electron. For atomic systems with multiple electrons, the spin-orbit coupling is mainly described with LS coupling and jj coupling mechanisms. The LS coupling mechanism describes the interaction in the light atoms where spin-orbit coupling is weaker than the electron-electron interaction. So, the total angular momentum J is approximated as the sum of the orbital angular momenta of the individual electrons coupled with the sum of the spin angular momenta. Thus total angular momentum for the atomic system is given by:

$$\vec{J} = \vec{L} + \vec{S} \tag{1.31}$$

with $\vec{L} = \sum_{i=1}^{N} \vec{l_i}$ and $\vec{S} = \sum_{i=1}^{N} \vec{s_i}$. Here the momenta of the N individual electrons are added up to obtain the total orbital and spin angular momenta.

Then, the possible J values are $|L-S| < J < |L+S|$. An atomic energy level described by the LS coupling is defined as ${}^{2S+1}L_J$ where each state can have $L =$ 0, 1, 2,.. denoted by S, P, D, ..The $2S+1$ term represents the spin multiplicity describing the number of possible orientations of the spin angular momentum corresponding to a total spin quantum number S. The transition between two states can occur only according to the selection rule where $\Delta L = \pm 1$ for the conservation of angular momentum.

In the jj coupling mechanism, the total angular momenta of each electron results from the coupling of individual momenta l_i and s_i related to it. Thus total angular momentum for an N-electron system is represented by:

$$\vec{J} = \sum_{i=1}^{N} \vec{j_i} = \sum_{i=1}^{N} (\vec{l_i} + \vec{s_i}) \tag{1.32}$$

where total angular momenta of individual electrons $\vec{j_i} = \vec{l_i} + \vec{s_i}$.This mechanism describes heavy atoms with large Z values as spin-orbit interaction dominates the electron-electron interaction. Here total orbital angular momentum L and total spin S are not defined. The resulting multiplet formation is from the individual spin-orbit couplings of a $\vec{j_i}$ which makes the spectra crowded and complicated to assign.

The resulting energy levels in an N-electron system due to spin-orbit coupling in the LS mechanism can be expressed as:

$$E = E_0 + E_{FS} = E_0 + \beta_{LS}\langle \vec{L}\vec{S} \rangle = E_0 + \frac{\beta_{LS}}{2}[J(J+1) - L(L+1) - S(S+1)] \tag{1.33}$$

where E_0 is the unperturbed energy level, E_{FS} is the fine structure energy levels and β_{LS} is the spin-orbit coupling constant. The energy difference between two neighboring fine structure levels is then given by:

$$\Delta E_{FS} = E_J - E_{J+1} = \beta_{LS} J \tag{1.34}$$

Apart from the spin-orbit coupling, the Hamiltonian involves additional corrections in the energy level calculation including a relativistic term as well as Darwin's term that are not discussed in the scope of this work.

1.2.2 Hyperfine structure

Atomic energy levels are also perturbed by the effect of higher multipole electromagnetic moments of the nuclei with a non-zero spin. The interaction of the nucleus with the electromagnetic fields of the shell electrons, in addition to the spin-orbit coupling of electrons, causes a shift and splitting of fine structure energy levels into hyperfine structures. Hyperfine Hamiltonian is defined by [13]:

$$H_{HFS} = \sum_{i} T^0(N)T^0(i) - (-Ze^2/r_i) + \sum_{k=1} T^k(N)T^k(e) \tag{1.35}$$

Here the difference in the monopole term and Ze^2/r contribute to a finite nuclear size effect/field effect in the isotope shift (discussed in section 1.2.3) and the remaining terms contribute to the multipoles (dipole with $k = 1$ and quadrupole

with $k = 2$ and so on) in the hyperfine structure. Multipole expansion of the nucleus-electron interaction with a non-zero contribution to the hyperfine levels can be expressed as :

$$H = H_0 + H_{M1} + H_{E2} + H_{M3} + \cdots \tag{1.36}$$

Only moments with even parity contribute to hyperfine energies. Magnetic dipole and electric quadrupole interaction of the nucleus with the electrons are considered here. The magnetic dipole interaction is between the magnetic dipole moment of the nucleus and the magnetic field generated by the electrons. Electric quadrupole interaction is between the electric quadrupole moment of the nucleus and the electric field gradient generated by the electrons. Higher-order electromagnetic moments also contribute to the hyperfine structure but the effect is decreasing and hence the Hamiltonian expansion is often truncated to the electric quadrupole term. High-precision spectroscopy can probe these higher-order effects as reported in [14].

The Hamiltonian for magnetic dipole interaction can be expressed as [13]:

$$H_{M1} = -\hat{\mu}.\hat{B_0} = -\frac{\mu B_0}{\hbar^2 IJ}\vec{I}.\vec{J} \tag{1.37}$$

where $\hat{\mu}$ is the nuclear magnetic dipole moment considering a constant magnetic field B_0 over the nuclear volume. For an atomic level of electronic angular momentum J and nuclear spin I, coupling causes the new angular momentum to be defined by the vector operators [2]:

$$\vec{F} = \vec{I} + \vec{J} \tag{1.38}$$

such that range of F values can be $|I - J|\,| \leq F \leq |I + J|$. The perturbation in atomic energy due to magnetic dipole moment can be expressed as [2]:

$$\Delta E_{M1} = \frac{1}{2}\frac{\mu B_0}{IJ}[F(F+1) - I(I+1) - J(J+1))] = \frac{1}{2}AC \tag{1.39}$$

where $C = \vec{I}.\vec{J}$ is known as the Casimir Factor.

The atomic energy perturbation due to the electric quadrupole moment is given by [2]:

$$\Delta E_{E2} = eQ_s\langle\frac{\delta^2 V}{\delta z^2}\rangle\frac{3C(C+1) - 4I(I+1)J(J+1)}{8I(2I-1)J(2J-1)} \tag{1.40}$$

Using quantum mechanical vector coupling rules one obtains an expression for the hyperfine structure energies of all F levels of a hyperfine structure multiplet with respect to the atomic fine structure level J [2]:

$$W_F = \frac{1}{2}AC + B\frac{\frac{3}{4}C(C+1) - I(I+1)J(J+1)}{2I(2I-1)J(2J-1)} \tag{1.41}$$

$$C = F(F+1) - I(I+1) - J(J+1) \tag{1.42}$$

Here A is the magnetic dipole hyperfine constant and B is the electric quadrupole splitting constant. As an example, figure 1.3 shows the hyperfine splitting of the ground state and an excited state for copper isotopes with nuclear spin $I = 3/2$

for a transition from $^2S_{1/2}$ to $^4P^0_{1/2}$. The hyperfine structure measurement can directly assign nuclear spin value isotopes of unknown spin, the ones that are far from stability. For those with known I and J values, the hyperfine A and B constants can be deduced which gives information on the nuclear moments from the formula [2]:

$$A = \mu_I B_0/(IJ) \tag{1.43}$$

$$B = eQ_s \frac{\delta^2 V}{\delta z^2} \tag{1.44}$$

where B_0 is the magnetic field caused by the electrons and $\frac{\delta^2 V}{\delta z^2}$ is the electric field gradient of the shell electrons at the site of the nucleus. μ_I is the nuclear magnetic dipole moment and Q_s is the spectroscopic quadrupole moment. $\frac{\delta^2 V}{\delta z^2}$ can be predicted using ab-initio calculations. The size of a hyperfine structure depends on the coupling of spins and orbital angular momenta of the shell electrons in a particular atomic state. The energy difference between two neighboring hyperfine structure levels F and $F-1$ is proportional to F. The absolute transition intensities $S_{FF'}$ between F and F' state between different fine structure levels can be expressed using the Wigner 6-j symbol as in equation 1.45 [2]. The curly matrix in equation 1.45 is a Wigner 6-j symbol [12]. It depends on the angular momenta of the participating hyperfine levels along with the unperturbed fine structure transition strength $S_{JJ'}$. The relative intensities (I_{rel}) observed in a hyperfine structure pattern, known as Racah intensities given by equation 1.46, thus can be used for spin assignments due to their I dependence.

$$S_{FF'} = (2F+1)(2F'+1) \begin{Bmatrix} F' & F' & 1 \\ J' & J & I \end{Bmatrix}^2 S_{JJ'} \tag{1.45}$$

$$I_{rel} = \frac{S_{FF'}}{S_{JJ'}} \tag{1.46}$$

With modern calculations, absolute values of magnetic dipole moment and spectroscopic quadrupole moment can be extracted [2]. If the moments of a reference isotope are known from other experiments such as NMR spectroscopy, the unknown moments can be extracted by scaling and by taking the ratio of nuclear moments of a pair of different isotopes using the expression [2]:

$$\frac{A}{A'} = \frac{\mu}{\mu'} \frac{I'}{I} \tag{1.47}$$

$$\frac{B}{B'} = \frac{Q_s}{Q'_s} \tag{1.48}$$

This is valid under the assumption of uniform nuclear magnetization and that the atomic field does not vary. The magnitude of magnetic splitting generated by an individual electron exhibits a range from about 100 MHz for lighter elements to around 50 GHz for the heaviest elements. In order to determine the quadrupole term, it is necessary to consider states with $J \geq 1$, where J represents the total angular momentum, and at least one electron in an open shell must possess a non-zero orbital angular momentum. This effect cannot be resolved for lighter nuclei($Z < 20$), where both the electric field gradients and the quadrupole moments are minimal [11]. Transitions between hyperfine

structure multiplets can happen according to the selection rules, i.e. $\Delta J = 0, \pm 1$ and $\Delta F = 0, \pm 1$. This is because the Wigner 6-j symbol (see equation 1.46) will be equal to zero if $|F - F'| > 1$. Figure 1.3 shows an example of the hyperfine splitting in copper isotope with a nuclear spin $I = 3/2$ for the ground state and an excited state at 40956 cm^{-1} both with $J = 1/2$. Here the F quantum number can have values 1 and 2.

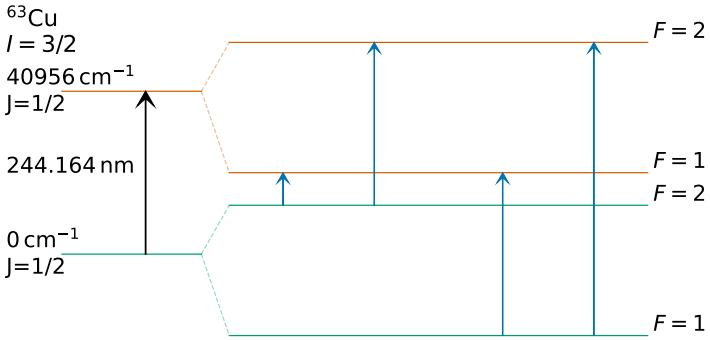

Figure 1.3: Hyperfine splitting of the ground state $^2S_{1/2}$ and an excited state $^4P^0_{1/2}$ of copper with nuclear spin $I = 3/2$.

1.2.3 Isotope shift of an atomic transition

Atomic transition frequencies of different isotopes experience a 'mass shift' due to the finite nuclear mass as well as a 'volume shift' due to the charge distribution in the nucleus, unlike a layman's point of view of the nucleus as a point charge and with infinite mass. Isotope shift is a combination of the mass shift and field shift effects. Laser spectroscopic techniques are sensitive to these effects. By the measurement of isotope shift, the differences in mean square charge radii between different isotopes can be deduced. Nuclear charge radii are sensitive to shell effects and deformation and thus studies on them are important for exploring the nuclear system.

Isotope shift between two isotopes of atomic mass A and A' with transition frequencies ν and ν' can be expressed as [2]:

$$\delta\nu^{AA'} = \nu^{A'} - \nu^{A} = \delta\nu^{AA'}_{MS} + \delta\nu^{AA'}_{FS} \tag{1.49}$$

where $\delta\nu^{AA'}_{MS}$ and $\delta\nu^{AA'}_{FS}$ are the mass shift and volume/field shift components. The mass shift occurs due to the change in the number of neutrons between the isotopes causing a difference in the reduced mass and thus a shift in the fine structure energy levels. It has a specific mass shift and a normal mass shift contribution defined as [2]:

$$\delta\nu^{AA'}_{MS} = (K_{NMS} + K_{SMS})\frac{m_{A'} - m_A}{m_{A'}m_A} = M\frac{m_{A'} - m_A}{m_{A'}m_A} \tag{1.50}$$

where M is the mass shift factor which is the sum of K_{NMS}, the normal mass shift constant, and K_{SMS}, the specific mass shift constant. The normal mass shift contribution arises from a change in the reduced mass due to an individual

electron in the atom and the specific mass shift from the electron interactions in a multi-electron system.

The field shift contribution to the isotope shift arises from the difference in the nuclear charge distribution between the isotopes. It can be considered as a monopole part of the electron-nucleus interaction (see equation 1.30). It causes a perturbation in the electronic energy levels due to the electron's wavefunction overlap ($\psi_e(r)$) with the nuclear volume. The change in transition frequency due to field shift under the assumption of constant electronic wavefunction over the nuclear volume is given by [2]:

$$\delta\nu_{FS}^{AA'} = \frac{Ze^2}{6h\epsilon_0}\Delta|\psi_e(0)|^2\delta\langle r^2\rangle^{A,A'} \tag{1.51}$$

Here, ϵ_0 is the dielectric constant, h is the Planck's constant, $\delta\langle r^2\rangle$ is the change in mean square charge radii of two isotopes and the $\Delta|\psi_e(0)|^2$ term describes the differences in the electron density for the two atomic levels of the concerned transition. This approximation is valid only for low Z-nuclei. Commonly, the field shift for a transition can be expressed as [13] :

$$\delta\nu_{FS}^{AA'} = F\lambda^{AA'} \tag{1.52}$$

where

$$\lambda^{AA'} = \delta\langle r^2\rangle^{AA'} + (C_2/C_1)\delta\langle r^4\rangle^{AA'} + ... \tag{1.53}$$

Here $\lambda^{A,A'}$ is the nuclear parameter with the charge radii moments. The F factor is an electronic factor describing the change in the electron density between the atomic transition states. The ratios C_2/C_1,.. etc. are the weights for the higher order even moments, known as the Seltzer coefficients [13]. Neglecting the higher order moments in the λ, isotope shift for a transition is given by [2]:

$$\delta\nu_i^{AA'} = M_i\frac{m_{A'} - m_A}{m_{A'}m_A} + F_i\delta\langle r^2\rangle^{A,A'} \tag{1.54}$$

where the F factor (from the field shift) and the M factor (from the mass shift) have to be known to obtain the difference in the nuclear mean-square charge radii. These factors are transition-dependent. For light nuclei, mass shift is the dominant contributing factor, and in heavier nuclides, field shift effects will be larger. By multiplying the equation 1.54 with reduced mass $\mu_{A,A'} = \frac{m_{A'}m_A}{m_{A'}-m_A}$, it becomes [2]:

$$\mu^{A,A'}\delta\nu_i^{AA'} = M_i + F_i\mu^{A,A'}\delta\langle r^2\rangle^{A,A'} \tag{1.55}$$

Equation 1.55 is a linear relation allowing King plot analysis, a commonly used method to extract these factors. A reference isotope shift measurement with known atomic factors or more commonly mean square charge radii data from other experiments, such as muonic atom spectroscopy or electron scattering [15] are required for this method. By performing a linear fit using equation 1.55, the mass and field shift factors for the required transition can be extracted from the deduced intercept and slope. Figure 1.4 shows an example of a 2-D King's plot of modified isotope shifts of 415 nm with respect to 583 nm transitions (left inset) as well as $\lambda^{A',170}$ from muonic x-ray data (right inset) for Er^+ ions reported in [16].

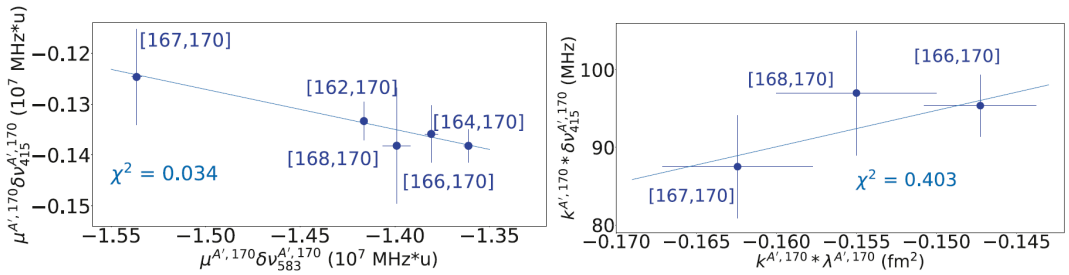

Figure 1.4: 2D King's plot for modified isotope shift in Er taken from [16].

1.2.4 Spectral line broadening

Probing atomic energy transitions between two levels i and j using laser spectroscopy involves the absorption or emission of photons. The excitation, spontaneous, and stimulated decay of an atomic state by its interaction with external electromagnetic radiation is governed by the spectral energy density of the radiation fields and the transition probabilities referred to as Einsteins' coefficients [17]. To excite electrons from an energy state 1 to 2 in a two-level atomic system, the energy of the photons should be:

$$E_{photon} = h\nu = \frac{hc}{\lambda} = E_2 - E_1 \tag{1.56}$$

The change in population in an absorption process is given by:

$$\frac{dN_1}{dt} = -B_{12}N_1\rho(\nu) \tag{1.57}$$

where N_1 is the number of atoms in the excited energy state 1, N_2 is the number of atoms in the energy state 2, B_{ij} is the Einsteins coefficient for absorption, and $\rho(\nu)$ is the spectral energy density of the electromagnetic radiation. Similarly, the external radiation field can stimulate the emission of photons by the decay of an excited atomic state whose probability is described by the Einstein coefficient B_{21}. The Einsteins coefficient for spontaneous emission is expressed as A_{21}. The change in population in spontaneous is given by:

$$\frac{dN_2}{dt} = -A_{21}N_2\rho(\nu) \tag{1.58}$$

and in stimulated decay by:

$$\frac{dN_2}{dt} = -B_{21}N_2\rho(\nu) \tag{1.59}$$

Spectral lines corresponding to an atomic transition of energy difference $\delta E = E_j - E_i$ are not monochromatic. By considering an excited atom electron to be a damped harmonic oscillator with frequency ω, the amplitude of oscillation can be approximated according to the equation [17]:

$$x(t) = x_0 \exp\left[-(\gamma/2)t\cos\omega_0 t\right] \tag{1.60}$$

where γ is the damping constant, $\omega_0 = 2\pi\nu_0$ is the frequency of the oscillator corresponding to center frequency $\omega_{ij} = (E_j - E_i)/\hbar$ of the atomic transition

from E_i to E_j. The amplitude decreases gradually and hence the frequency is no longer monochromatic giving a Lorentzian distribution for the emitted radiation. The normalized Lorentzian profile is then given by [17]:

$$L(\omega - \omega_0) = \frac{1}{2\pi} \frac{\gamma}{(\omega - \omega_0)^2 + (\gamma/2)^2} \tag{1.61}$$

The FWHM of this Lorentzian distribution is known as the natural line width. It is also called lifetime broadening as is related to the uncertainty in the energy of the atomic levels due to the finite lifetime τ of an excited state. The natural line width Γ_{nat} for a transition involving energy difference ΔE can thus be defined by:

$$\Gamma_{nat} = \frac{\Delta E}{h} = \frac{1}{2\pi\Gamma} = \frac{A_{12}}{2\pi} \tag{1.62}$$

where A_{12} is the decay constant in s^{-1} or the Einsteins coefficient describing the transition probability for the spontaneous transition from an excited level to a lower level.

The Lorentzian line profile of the natural linewidth is completely concealed by other broadening effects as well. The source of the finite linewidth due to the several broadening effects should be taken into account for high-resolution spectroscopy. Spectral line broadening can be homogenous and inhomogenous. Power broadening, pressure broadening, and Doppler broadening are the main contributions to spectral linewidth and will be discussed here.

Power broadening

At low laser intensities, the population difference between the two states in a transition is not affected by laser intensities. Power broadening is a Lorentzian line broadening phenomenon occurring due to intense laser power causing a reduction of the population in the absorbing levels. This saturation of the population densities occurs when the pumping rate becomes much larger than the relaxation rate. Considering two-level atoms for simplicity with a monochromatic laser source of intensity $I(\omega)$ used to excite an atom from its state 1 to 2, the saturation parameter describes the ratio of the pumping rate to the relaxation rate and is defined by [18]:

$$S = \frac{2\sigma_{12} I(\omega)}{\hbar\omega A_{12}} \tag{1.63}$$

where σ_{12} is the absorption cross-section and A_{12} is the Einstein coefficient for spontaneous decay from state 2. The mean population probability for the excited state 2 with decay constant γ is given by [18]:

$$P_2(\omega) = \frac{1}{2} \frac{S}{(\omega - \omega_0)^2/\gamma^2 + (1 + S)} \tag{1.64}$$

The saturation of the excited level is related to the population of the excited state which according to equation 1.64 gives a Lorentzian line profile. The line width can be then expressed as [18]:

$$\gamma_s = \gamma\sqrt{1 + S_0} \tag{1.65}$$

where S_0 is the saturation parameter at the line center ω_0. The saturation parameter is frequency-dependent meaning that the factor $(1+S_0)$ is maximum at the line center and approaches zero for $\omega - \omega_0 \to \infty$ [18]. To avoid power broadening, laser spectroscopy measurements should be performed at sufficiently low power. For this purpose saturation tests are performed to plot a saturation curve with ion intensity versus laser intensity and the laser powers are kept at the linear region of the curve. Additional power broadening can also be caused by the ionization laser when the laser pulses are completely temporally overlapped. This is because of the additional uncertainty in energy introduced by the ionization laser pulse at the time of excitation when temporally overlapped due to the reduction of the excited state lifetime. This can be solved by delaying the ionization laser pulses temporally compared to the excitation laser pulses [19].

Pressure broadening

Another Lorentzian contribution to the linewidth broadening is the pressure broadening mechanism especially crucial in gas cell-based laser spectroscopy. This occurs due to the collision of the atoms with the buffer gas. These collisions are elastic if no internal energy of the collision partners is transferred by non-radiative transitions. This kind of collision causes a shift in the energy levels of the atoms. The energy shifts depend on the electronic configuration of the collision partners as well as the distance between them. This shift can be positive or negative depending on whether the interaction between the collision partners is repulsive or attractive. The shift in the frequency changes the phase of the damped oscillator (see equation 1.60) and is called phase-perturbing collisions. Inelastic collision can also occur where the excitation energy of the atom might partially or completely be transferred to the internal energy of the collision partner which in turn decreases the number of excited atoms at the excited level. This quenches the emission intensity and is hence called quenching collisions. The total transition probability of the depopulation of the excited level is a sum of the radiative and collision-induced probability. Thus the pressure-dependent transition probability causes a pressure-dependent line width given by [18]:

$$\Gamma = \Gamma_{nat} + \Gamma_{coll} = \Gamma_{nat} + ap_B \tag{1.66}$$

where ap_B is the additional line broadening called pressure broadening with $p_B = N_B kT$ (T - gas temperature, N_B - number density of the gas particles) being the responsible pressure of the collision partner/buffer gas and $a = 2\sigma_{ik}\sqrt{\frac{2}{\pi\mu kT}}$ (σ_{ik}- collision cross-section, μ-reduced mass). Here Γ is the FWHM to a Lorentzian profile. Considering the line shift due to elastic collision and the additional broadening, the line profile can be described by the Lorentzian function defined by [18]:

$$I(\omega) = \frac{(\frac{I_0}{2\pi})\Gamma}{(\omega - \omega_0 - \Delta\omega)^2 + (\Gamma/2)^2} \tag{1.67}$$

where $\Delta\omega = N_B.\overline{\nu}.\sigma_s$ is the line shift and $\Gamma = \Gamma_{nat} + N_B.\overline{\nu}.\sigma_b$ is the line broadening. σ_s and σ_b are the cross-sections for the collision-induced shift and broadening. The line shift and broadening are affected by these collision cross

sections and the number density N_B of the collision partner/buffer gas as well as the $\bar{\nu}$-mean relative velocity of the gas particle. However, in reality, it is also affected by the interaction potentials between the colliding partners and may no longer remain a symmetric Lorentzian profile.

The pressure broadening and the pressure-induced shift is linearly related to the gas density ρ by the following equations [20]:

$$\Gamma_{coll} = \gamma_{coll}\rho \tag{1.68}$$

$$\Gamma_{sh} = \gamma_{sh}\rho \tag{1.69}$$

where γ_{coll} and γ_{sh} are the collision and shift broadening rate coefficients respectively. These rate coefficients can be determined using laser spectroscopy measurements which have been performed as part of this thesis work. Typical values for these coefficients are a few MHz/mbar [20, 21].

Doppler broadening

Apart from the Loretzian broadening, Gaussian contributions also affect the lineshape. Doppler broadening is Gaussian in nature. Doppler width of the spectrum is due to the thermal motion of the atoms producing a velocity distribution according to the Maxwell-Boltzmann distribution of atoms. The movement of the atom causes a shift in the atomic transition frequency given by the equation [18]:

$$\nu' = \nu_0(1 + \frac{\upsilon}{c}) \tag{1.70}$$

where ν_0 is the atomic transition frequency, υ is the velocity component of the atom in the direction of the incoming laser beam and c is the speed of light. The velocity distribution function due to the thermal motion of the atoms is given by [18]:

$$n(v) = \sqrt{\frac{m}{2\pi k_b T}} \exp\left[-\frac{mv^2}{2k_b T}\right] \tag{1.71}$$

where v is the velocity, m is the atomic mass, T is the temperature and k_b is the Boltzmann constant. The contribution to the line shape due to this Doppler effect is given by the Gaussian function [20]:

$$G(\nu) = G_0.exp\left[-\frac{c^2(\nu-\nu_0)^2}{\nu_0^2\frac{2k_bT}{m}}\right] \tag{1.72}$$

The FWHM linewidth due to the above Gaussian distribution is given by [20]:

$$\Delta\nu_{Dopp} = \nu_0\sqrt{\frac{8k_bTln2}{mc^2}} \tag{1.73}$$

with FWHM in cm^{-1} given by:

$$\Delta\nu_{Dopp} = 7.16 \times 10^{-7}\nu_0\sqrt{\frac{T}{A}} \tag{1.74}$$

where T in K is the temperature, k_B is the Boltzmann constant, m in kg is the mass, c is the speed of light, A is the atomic mass number, and ν_0 in cm^{-1}

is the atomic transition frequency. Doppler broadening thus increases with increased temperature. In order to reduce Doppler broadening, laser spectroscopy measurements could be performed in reduced temperature environments and in crossed-beam geometries as it will be discussed in the following chapters.

The laser linewidth also affects the spectral line width and hence for high-resolution laser spectroscopy measurements, the laser line width should be in the range of a few MHz which can be achieved by seeding narrow linewidth continuous wave tunable laser beam to pulsed dye or pulsed Ti: sapphire laser cavities. In most cases, the approximate formula for linewidth is obtained from a Voigt profile taking into account the Doppler broadening and collisional broadening. The Voigt distribution is obtained by convolution of the Gaussian and Lorentzian distributions describing the different broadening effects. Figure 1.5 shows the comparison of Gaussian, Lorentzian, and Voigt line profiles all normalized to unity. The line width of the Voigt profile is given by [20]:

$$\Delta_{Voigt} \approx 0.5346 \times \Gamma + \sqrt{0.2166\Gamma^2 + \Delta^2_{Gaussian}} \tag{1.75}$$

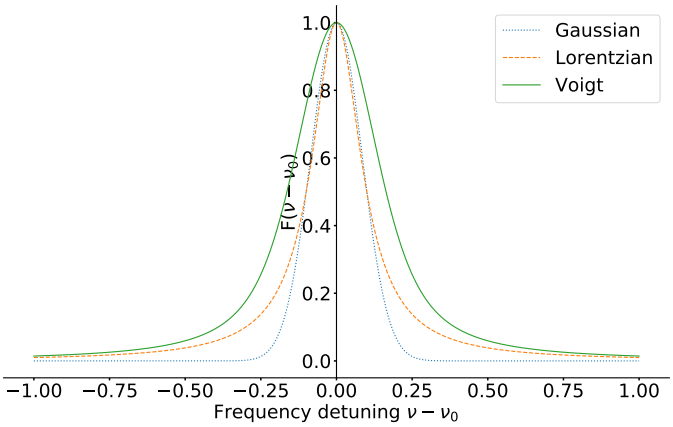

Figure 1.5: Line profiles of Gaussian, Lorentzian, and Voigt distributions as a function of frequency $F(\nu - \nu_0)$ with center frequency as ν_0.

1.3 Laser physics

Light amplification by stimulated emission of radiation are electromagnetic waves, defined by their high level of coherence, monochromaticity, and directionality. Tunable lasers, with nonlinear optics, have been of interest for spectroscopic applications providing a wide range of frequencies to probe atoms and molecules. The basic components of a laser system are a gain medium that can amplify the electromagnetic wave, a resonator composed of a minimum of two mirrors for optical feedback, and a pumping mechanism to achieve population inversion (see figure 1.6). Laser operate on the principle of stimulated emission dominating over spontaneous emission. This section describes in particular the operating principle of the Ti: sapphire laser systems which have been utilized in this thesis work with topics covering the gain medium, pulsed and continuous wave output, and frequency selection.

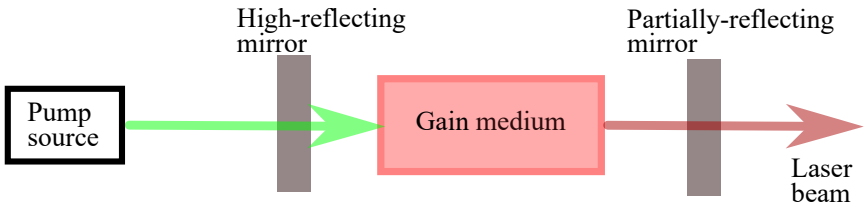

Figure 1.6: Schematic of a simple laser oscillator

1.3.1 Gain medium

The gain medium of a Ti: sapphire laser is an Al_2O_3 solid-state crystal doped with Ti^{3+}. It is one of the vibronic solid-state materials where the interaction between the Ti^{3+} ions and the Al_2O_3 crystal lattice give rise to a distribution of electronic ground state levels and excited state levels known as vibronic energy levels [22]. The crystal field splitting of the 3d electronic state of Ti^{3+} and the coupling of the electronic states with lattice vibrations form the basis for the Ti: sapphire laser. The absorption and emission properties of the Ti: sapphire crystal are associated with the energy level transitions of 3d electrons in the outer shell of Ti^{3+} ions and the strong electron-vibration coupling. The four-level structure of the Ti: sapphire system is shown in figure 1.7. The Ti^{3+} ion

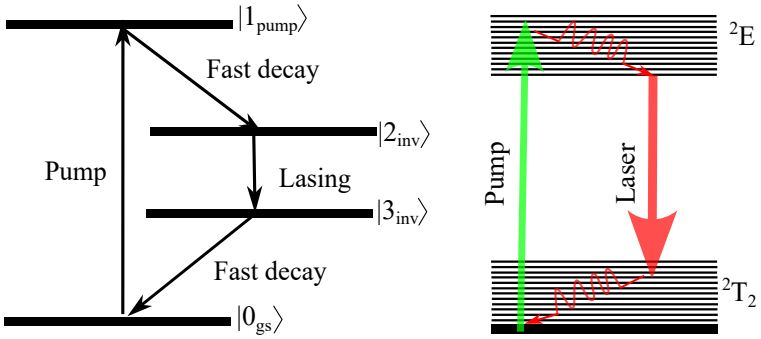

Figure 1.7: Four level scheme of Ti: sapphire laser system.

can absorb pump laser photon to get excited to the higher vibrational states of the ^2E electronic level. The excited state can undergo non-radiative fast decay or phonon relaxation to the vibrational ground state of ^2E, shown by the $|2_{inv}\rangle$ state. Radiative decay then occurs to the $|3_{inv}\rangle$ with a fluorescence lifetime of 3.2 μs. From the $|3_{inv}\rangle$, fast non-radiative decay happens to the vibrational ground state of $^2T_2$ shown by $|0_{gs}\rangle$. Here the population inversion for lasing can be easily achieved between $|2_{inv}\rangle$ and $|3_{inv}\rangle$. Figure 1.8 shows the absorption and emission spectra of the Ti: sapphire at room temperature [23].

1.3.2 Frequency selection

The spectral bandwidth of Ti: sapphire covers a wavelength range of 660-1100 nm. With the cavity mirrors, the system forms an optical resonator that acts as feedback for the amplification of the electromagnetic wave passing through the gain medium in each round trip until the threshold condition for lasing is achieved. These resonators basically act like a Fabry Perot cavity and have discrete resonances called eigenmodes [18]. These eigenmodes have well-defined frequencies separated by $\Delta\nu = c/2d$ known as the free spectral

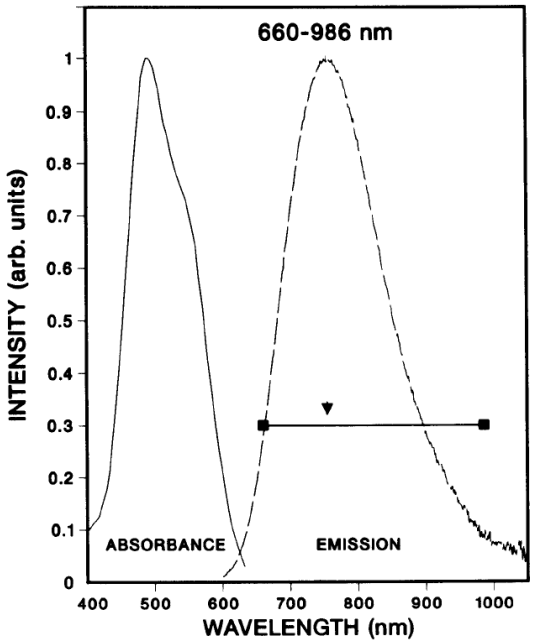

Figure 1.8: Absorption and emission spectra of the Ti:sa at room temperature. The black line shows the tuning range of the gain medium [23].

range (FSR) where d is the distance between the end mirrors. The spectral width of the individual eigenmodes is the ratio of Finesse (depends further on the reflectivity of the cavity mirrors) and FSR. For Ti: sapphire crystal, the gain bandwidth is very large compared to the FSR of the resonator and hence allows a vast number of modes to oscillate within the resonator. Figure 1.9 shows the resonator modes within the gain profile of an active medium for a simple two-mirror resonator cavity with active medium length L and resonator length d. The transmission function for the resonator as a Fabry-Perot cavity

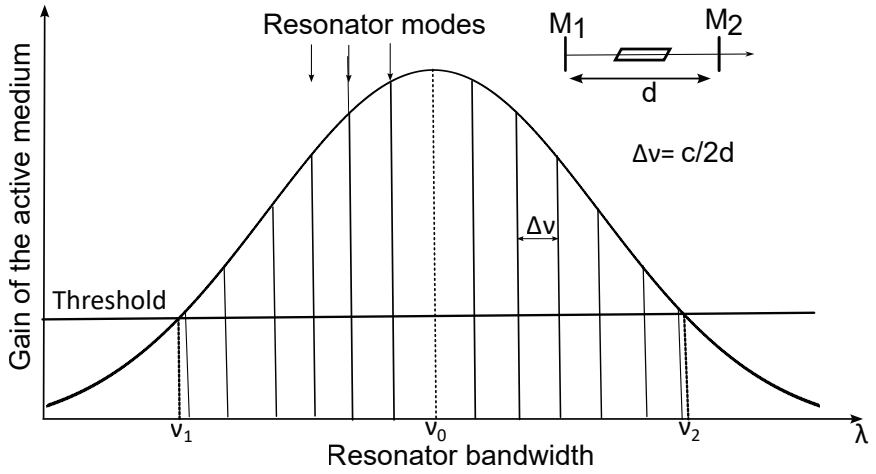

Figure 1.9: Gain profile of a laser transition with eigen frequencies of longitudinal resonator modes [18].

is given by [24]:

$$\tau(\nu) = \frac{\tau_{max}}{1 + (2\mathcal{F}/\pi)^2 \sin^2[\frac{\pi\nu}{\Delta\nu_{FSR}}]} \tag{1.76}$$

where $\mathcal{F}$ is the Finnese of the resonator given by [24]:

$$\mathcal{F} = \frac{\pi\sqrt{r_1 r_2}}{1 - r_1 r_2} \tag{1.77}$$

where τ_{max} is the maximum transmittance occuring at resonant frequencies and r_1 and r_2 are the amplitude reflectances of the cavity mirrors. Here the cavity mirrors can be coated such that it allows high reflectivity ($R_i = r_i^2$) and thus gains maximum and high transmission for a certain wavelength range. High-resolution laser spectroscopic applications require lasers to operate in a single mode for optimum spectral resolution. To achieve single-mode operation, additional frequency-selective optical elements have to be added. These elements basically introduce losses for the unwanted frequencies in the cavity. Frequency selection of the laser cavity is performed by the use of optical components such as the birefringent filter and the etalon.

Birefringent filter

A birefringent filter is made of optically anisotropic crystalline plates showing the property of birefringence, i.e., having two refractive indices, n_e and n_o depending on the plane of propagation of the light. It will cause polarization-dependent transmission losses in the cavity. It can be a single birefringent plate or multiple plates stacked together with air as the medium in between. The main principle is that the light superimposes with itself during its propagation through the filter due to the relative delay arising between the two orthogonal components of the polarised beam. The phase shift between these orthogonal components, $\delta = (2\pi/\lambda)(n_e - n_o)L$, causes wavelength dependence of the transmission. It is usually kept at Brewster angle to minimize the reflection losses for p-polarized beams. The transmission through a single birefringent plate is given by [18]:

$$T(\lambda) = T_0 \cos^2\left[\frac{\pi \Delta n L}{\lambda}\right] \tag{1.78}$$

where $\Delta n = n_e - n_o$, L is the optical path length through the crystal. For N-birefringent plates, the total transmission function is given by [25]:

$$T(\lambda) = \frac{\sin^2\left(\frac{2^N \pi (n_e - n_o) l}{\lambda}\right)}{2^{2N} \sin^2\left(\frac{\pi (n_e - n_o) l}{\lambda}\right)} \tag{1.79}$$

where l is the thickness of the thinnest plate, $\Delta n = n_e - n_o$ is the difference in the refractive indices for ordinary and extraordinary rays. At a fixed wavelength λ, the birefringent filter will maintain p-polarization for the wavelength in the transmission peak while others develop a s-polarization and cannot survive in the cavity due to reflection losses. To tune the wavelength, the birefringent plate is rotated around an axis perpendicular to the plate surface such that n_e is changed. This allows shifting the transmission curves and thus tuning the wavelength. The free spectral range of the filter is determined by the thickness of the thinnest plate. The thickest plate determines the spectral width given as $\Delta\nu = c/2^{N-1}\Delta n L$. The increasing thickness gives a sharper filtering response or spectral width but gives a reduced free spectral range. Using multiple plates

of different thicknesses stacked parallel allows for increased FSR and good transmission contrast. These birefringent filters can reduce the laser linewidth to less than 5 GHz [26].

Etalon

Finer wavelength selection is performed by the use of an etalon reducing the linewidth to less than 2 GHz [26]. Etalons are basically two partially reflecting parallel surfaces causing multiple reflections and transmissions of the incident beam. The transmitted beams interfere constructively or destructively, following the phase conditions due to the path differences during propagation. Consider a light beam with a frequency ν entering the etalon surface at an angle of incidence θ_i and with wave vector $k_2 = 2\pi n\nu/c$. Here n is the refractive index of the etalon. If the reflectivities of the surfaces with spacing d are considered to be $R_A = R_B = R$ and assuming no absorption losses such that $R + T = 1$, the m^{th} order transmitted amplitude is given by [24]:

$$A_m = \sqrt{T_A T_B}(R_A R_B)^{m/2} e^{im\delta} \tag{1.80}$$

where $\delta = 2k_2 d\cos\theta_r$ is the phase difference between subsequent orders with θ_r being the refracted angle at surface A. Then the sum of the transmitted amplitudes will be [24]:

$$t = \sqrt{T_A T_B}\sum_{m=0}^{\infty}(R_A R_B)^{m/2} e^{im\delta} \tag{1.81}$$

The transmission is then given by [24]:

$$T = tt^* = \frac{T_A T_B}{1 + R_A R_B - 2\sqrt{R_A R_B}\cos\delta} \tag{1.82}$$

With the assumption of equal reflectivities for the surfaces $R_A = R_B = R$ and R + T = 1, by replacing $\cos\delta$ by 1-$\sin^2\delta$, the transmission can be expressed as [24]:

$$T = \frac{(1-R)^2}{(1-R)^2 + 4R\sin^2\delta/2} = \frac{1}{1 + F\sin^2\delta/2} \tag{1.83}$$

where

$$F = \frac{4R}{(1-R)^2} \tag{1.84}$$

The transmission function is maximum when:

$$\Delta\nu_{FSR} = \frac{c}{2nd} \tag{1.85}$$

where n is the refractive index of the etalon medium, and d is the thickness of the etalon. FSR is the free spectral range of the etalon with nd being the optical path length. The spectral FWHM of the transmission peak $\delta\nu$ and the FSR gives the Finesse of the etalon given by [24]:

$$\mathcal{F} = \frac{\delta\nu_{FSR}}{\delta\nu} = \frac{\pi}{2\sin^{-1}\sqrt{(1/F)}} \approx \frac{\pi\sqrt{R}}{1-R} \tag{1.86}$$

Note that $\mathcal{F}$ is the finesse or figure of merit whereas F is the coefficient of finesse related to each other as $\mathcal{F}=\pi\sqrt{F}/2$. The transmission function then can be expressed similarly to equation 1.77 representing a Fabry-Perot resonator as [24]:

$$\tau(\nu) = \frac{\tau_{max}}{1 + (2\mathcal{F}/\pi)^2 \sin^2[\frac{\pi\nu}{\Delta\nu_{FSR}} \cos\theta]} \tag{1.87}$$

The desired FSR and spectral width can be achieved by choosing the correct reflectivities and thickness of the etalon. A thin etalon of $\approx$ 0.2 - 0.3 mm thickness and reflectivity of 40% can ideally give a Finesse of 3.3, FSR of 330 GHz, and a spectral width of 100 GHz. For tuning the etalon installed in a laser cavity, the etalon angle (θ) with respect to the beam propagation is changed thereby changing the δ term in the transmission function (See equation 1.82). In some cases when one needs to perform laser spectroscopy with improved resolution say several GHz, a thick etalon of $\approx$ 6 mm is used in combination with a thin etalon but with increased reflection losses in the laser cavity.

1.3.3 Ring cavity

Lasers are optical resonators that can have either a standing wave configuration or a traveling wave ring configuration according to the feedback mechanisms. If the cavity mirrors in the resonator system are arranged such that the waves travel in opposite directions and interfere, standing wave patterns are formed. In these types of laser resonators, there would be regions of unsaturated population inversion at the nodes of the standing waves. This spatial modulation of inversion known as spatial hole burning along with acoustic vibrations in the laser cavity alters the gain competition. This results in fluctuations in the intensities of the simultaneously existing modes. These standing wave configurations do not allow a single-mode operation and are hence used for laser spectroscopy requiring broad-band resolution in the order of GHz. For high-resolution laser spectroscopy requiring several MHz resolution, ring-resonator configurations are used. In a ring configuration, the waves circulate within the resonator without traveling back and thus no standing wave exists in them. The cavity mirrors are arranged such that there is no normal incidence of light. Ring lasers in unidirectional operation are preferred for single-mode operation because they prevent spatial hole burning effect otherwise present in standing wave configuration resonators. Wave propagating in one direction can saturate the spatially distributed inversion [18].

If the laser cavity is in the shape of a ring and oscillation is restricted to being unidirectional, a single-longitudinal mode operation can automatically be achieved. In reality, additional bandwidth-selecting components like birefringent filters and/or Fabry-Perot etalons may also be required if the transition is only partially homogeneously broadened especially when the gain profile is quite broad [18]. The unidirectional operation is usually obtained using a Faraday isolator and birefringent plate. A Faraday rotator works on the principle of rotation of polarization by a material in the presence of a static magnetic field known as the Faraday effect. The angle of rotation is determined by the thickness of the material and the magnetic flux density in the direction of propagation. The angle of rotation per unit length can be expressed as [24]:

$$\rho = VB \tag{1.88}$$

where V is called the Verdet constant that governs the sense of rotation and B is the strength of magnetic flux density. It is invariant to the direction of propagation. Figure 1.10 shows the polarization rotation in forward and backward direction through a medium exhibiting the Faraday effect. In the ring

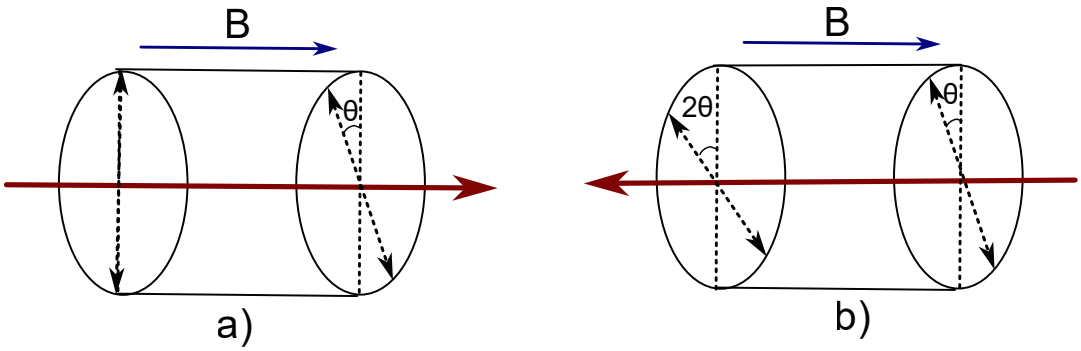

Figure 1.10: Polarization rotation in a medium possessing Faraday effect. a) shows a forward wave and b) a backward wave with a sense of rotation invariant to the direction of propagation showing the non-reciprocal nature

laser cavities, the beam passes through an input polarizer, a Faraday rotator (a transparent magneto-optic crystal with an applied magnetic field), and an output polarizer together known as a Faraday isolator. The plane of polarization of a linearly polarized wave passing through a Faraday rotator is rotated about its propagation axis depending on the direction of the magnetic field and beam propagation. This in combination with the polarizer in the laser cavity will generate beams in p-polarization in one direction and s-polarization in the other direction. The beam rotated to p-polarization survives the reflection losses in combination with the birefringent filter whereas the other does not. The unidirectional operation can also be achieved by using a non-planar/off-axis cavity instead of a polarizer where the rotation of the planes of incidence causes an image rotation and a net polarization rotation. Here the polarization selective element becomes the off-axis mirror reflectivity which depends on the beam polarization [27].

For high-resolution laser spectroscopy performed in this work, an injection-locked cavity with a bow-tie ring configuration is used. Here the narrow laser linewidth is obtained by injecting a single-mode continuous wave laser beam into the ring cavity and seeding the cavity thereby enhancing the probability for the seeded modes to win over the naturally occurring modes in the cavity. An injection-locked cavity operating in the ring configuration and its working principle can be found in detail in [28]. The seed lasers commonly used are external cavity diode lasers. The disadvantage of these diode lasers is their limited tuning ranges. Tunable single-mode ring-type Ti: sapphire lasers allow a broader tuning range and the development of this type of laser is discussed in the chapter 5.

1.3.4 Nonlinear frequency generation techniques

Commonly available tunable lasers cannot produce the full frequency range needed to probe all the atomic transitions. Hence, to generate appropriate frequencies ranging from UV to IR, nonlinear optical techniques are used in

combination with tunable lasers. Frequency doubling and tripling are commonly used to generate the required frequencies matching the energy difference of the excitation and ionization steps for probing the atoms. Basic concepts of nonlinear mixing are discussed here.

Frequency mixing is implemented using nonlinear optical crystals such as beta barium borate (BBO), lithium niobate (LBO), and potassium dihydrogen phosphate (KDP). These crystals exhibit the property of nonlinear susceptibility, providing directly or indirectly second harmonic and third harmonics of the fundamental input beam frequency following a phase-matching condition. When these crystals are subjected to an electric field E, dielectric polarization is induced in the crystal medium and is expressed as [18]:

$$P = \epsilon_0(\chi^{(1)}E + \chi^{(2)}E^2 + \chi^{(3)}E^3 + \dots) = \epsilon_0\chi^{(1)}E + P_{NL} \tag{1.89}$$

where E is the electric field, $\chi^{(k)}$ is a tensor of rank $k+1$ with the k^{th} order dielectric susceptibility. Under a low electric field, the induced polarization is linearly related to the applied electric field. Under high electric field such that of a laser beam, this linearity no longer holds. A nonlinear polarization is induced due to the higher power dependence of the electric field leading to an exchange of energy between the electromagnetic waves traveling through the crystal [27]. Second harmonic generation is one of the nonlinear effects produced by the nonlinear polarization caused by the square of the electric field of the laser beam passing through the crystal. Here a laser beam at frequency ω gets converted to a coherent beam of frequency 2ω. Direct third harmonic generation is challenging and hence is realized by combining second harmonic generation with frequency summing techniques.

In second harmonic generation nonlinear phenomena, the nonlinear behavior of the optical medium higher than second order is negligible such that [18]:

$$P_{NL} = 2dE(\omega)^2 \tag{1.90}$$

where $E(\omega) = E_0\cos(\omega t - kz)$ is the electric field of the fundamental input light. The nonlinear polarization causes the generation of a secondary wave in the crystal with amplitude $E(2\omega)$ and frequency 2ω. For the generation of electromagnetic waves with frequency 2ω with wave vector $k(2\omega)$ from an electromagnetic wave of frequency ω and wave vector k(ω), certain frequency matching and phase matching conditions need to be fulfilled. They are [18]:

$$\omega + \omega = 2\omega \tag{1.91}$$

$$2k(\omega) = k(2\omega) \tag{1.92}$$

The phase matching condition can be fulfilled only using an anisotropic crystal. Due to the anisotropic nature of the crystal, the atoms are organized differently along different axes of the crystal. Hence an electromagnetic wave entering the crystal of length L will experience two refractive indices, an ordinary n_o and extraordinary refractive indices n_e. Due to this difference in refractive indices known as the birefringence, the electromagnetic wave entering the crystal will travel with a phase difference of $\Delta\psi$ to the second harmonic wave at 2ω given by [18]:

$$\Delta\psi = \Delta kL = (2k(\omega) - k(\omega))L \tag{1.93}$$

Phase-matching conditions can be achieved using different methods, depending on which Type I, type II, and quasi-phase-matched crystals exist. Type 1 phase matching can be achieved using a negative uniaxial birefringent crystal ($n_e < n_o$). Here the fundamental wave is an extraordinary wave and the generated secondary wave is ordinary. In order to satisfy the critical phase matching condition, the fundamental/pump wave must propagate in the crystal at an angle θ_{pm} such that [18]:

$$n_e(2\omega, \theta_{pm}) = n_o(\omega) \tag{1.94}$$

The phase matching angle θ_{pm} is given by [18]:

$$\sin^2 \theta_{pm} = \frac{\nu_o^2(\omega) - \nu_o^2(2\omega)}{\nu_e^2(2\omega, \pi/2) - \nu_o^2(2\omega)} \tag{1.95}$$

where $\nu_o = n_o/c$ and $\nu_e = n_e/c$. The adjustment of crystal temperature is also used in some conditions for phase matching to obtain a higher conversion efficiency as the refractive indices along the length of the crystal are temperature-dependent. There are also quasi phase matching techniques where periodically poled nonlinear crystals are used which causes dielectric polarization of the crystal over its length under the influence of an external electric field.

The tuning range of a second harmonic generation crystal depends on the phase-matching constraints and the fundamental laser wavelength. The intensity of the second harmonic wave is proportional to the square of the intensity of the fundamental wave and hence requires high pump powers. The intensity of the SHG wave is given by [18]:

$$I(2\omega, L) \propto I^2(\omega)\omega^2 L^2 \frac{\sin^2 \Delta kL}{(\Delta kL)^2} \tag{1.96}$$

where $I(\omega)$ is the incident power per unit area of the cross-section in the interaction volume. The SHG efficiency thus depends on the incident power and the cross-sectional area of the interaction volume in the crystal. Pulsed laser inputs can provide high peak powers and hence are efficient for SHG. Focusing of the pump laser into the nonlinear medium increases the power density and thus can improve the conversion efficiency. The pump power that can be used is limited by the low damage threshold of the available crystals. Frequency doubling can be performed intra-cavity and in an external cavity where the incoming beam to the crystal is a laser. Intra-cavity doubling is preferred for improved spatial profile of the second harmonic beam compared to the external doubling technique.

CHAPTER 2

Experimental techniques and facilities

With radioactive ion beam (RIB) facilities and the development of techniques related to them, it has become possible to produce and study nuclei with a proton-to-neutron ratio very different from stable nuclei. The main challenges when it comes to the production and study of rare isotopes are their extremely low production rate, the high production rate of the unwanted species in a nuclear reaction, and the short half-lives of the nuclei of interest. One aims for RIB production mechanisms to be fast, efficient, selective, and with significant production rates.

There are two methods for the production of rare isotopes, the Isotope Separation Online (ISOL) technique and the inflight separation technique. ISOL technique uses an accelerated primary beam of light or heavy ions to hit a thick target to produce secondary RIBs through different reaction mechanisms. The nuclei produced are then stopped in a solid/gas catcher which might be the target itself. It is then followed by diffusion from the thick target (in the case of a solid target) and then effusion and ionization to extract the low-energy RIBs. Once the ions are produced, they can be post-accelerated to different experimental setups for spectroscopy. A thin target can also be used where the reaction products ejected out are then stopped in a gas cell. Here the gas cell pressure is adjusted to favor a singly charged ion state which is then extracted out through a nozzle to an electric guiding region and then to experimental setups. ISOL technique can produce intense beams of nuclei with good ion optical quality, timing, and energy characteristics. The inflight technique uses a primary beam of high energy to impinge on a thin target to produce a desired radioactive secondary beam. This technique requires inflight separation from the primary beams using fragment separators and is sent to detector setups for spectroscopy. With the inflight technique, we obtain beams to the most exotic nuclei with the shortest half-lives but with lower ion quality.

Experimental facilities all over the world use different techniques to produce and study radioactive elements using lasers. Some of the leading and established RIB facilities for laser ionization and spectroscopy as mentioned in the introduction chapter include the ISOLDE at CERN (Switzerland), ISAC at TRIUMF (Canada), IGISOL at Jyvaskyla (Finland), CARIBU at ANL (USA), RADRIS

at GSI (Germany), FRIB at MSU (USA) and KISS at RIKEN (Japan). Other facilities are emerging such as the SPIRAL2 at GANIL (France), and FAIR at GSI (Germany).

IGISOL setup at JYU, Finland, uses a Doppler-free collinear laser spectroscopic technique for the study of radioactive isotopes. Their production mechanism is insensitive to chemical or physical properties [29, 30]. IGISOL also uses the ISOL technique for RIB production. The low-energy reaction products produced from a thin target in a buffer gas region are then purged out with the gas flow to an ion guide. The ion beams are mass-separated and then neutralized using a charge exchange cell. The neutralized atoms interact with a laser beam in a counter-propagating configuration to excite them. The excited atoms decay and the fluorescence signal is detected. The laser frequency is fixed while the frequency seen by the ions is Doppler-shifted by the application of a voltage in the interaction region to obtain the spectra. The spectral resolution achievable with this technique is not Doppler limited and a MHz resolution is possible. This is due to the fact that the ion's velocity distribution is narrowed down by their acceleration in the initial stages to tens of kV. This leads to comparable optical line widths to the natural linewidth allowed for atomic dipole transitions. However, the efficiency of fluorescence detection is rather low.

The CRIS setup at ISOLDE, CERN uses a collinear resonance ionization technique where the Doppler-free resolution in collinear geometry is combined with the high sensitivity of resonant ionization technique [31]. The technique follows a similar procedure to the collinear technique until laser interaction where additional laser beams are utilized for efficient ionization. The ions are then sent to a counting station for obtaining the spectra. RAPTOR at IGISOL also uses the same technique which will be capable of producing spectral line width below 1 MHz [32].

Resonant laser ionization is a technique that provides elemental selectivity and in some instances isomer and isotopic selectivity. A detailed description of the technique is given in 2.1. Resonance Ionization Laser Ion Source (RILIS) at ISOLDE uses this technique for producing pure RIBs. Here, the radioactive isotopes are produced using the ISOL technique. To extract RIBs from the target, chemical processes are used and hence are restricted to chemical sensitivity. Here the laser ionization happens in a hot cavity which is explained in detail in section 2.1.1.

The S^3 facility at GANIL uses a mix of ISOL technique and inflight technique for ion beam production. It will use accelerated heavy ions to impinge on a thin rotating target for RIB production. The radioactive beams produced will then enter a recoil separator for primary beam suppression and then be stopped, thermalized, and neutralized in a buffer gas cell region at the S^3-LEB setup. The neutralized species are then ionized in a gas cell or flushed out of the gas cell to a jet environment for laser-atom interaction. S^3-LEB also uses the resonant laser ionization technique. The laser-produced ions are then transported using radio-frequency quadrupole (RFQ) units to detection setups and other experimental setups.

This thesis work is focussed on the commissioning of S^3-LEB setup. A detailed description of the S^3-LEB can be found in this chapter. Before the description of S^3-LEB, basic concepts of resonance laser ionization for laser ion production and spectroscopy and RFQ ion beam manipulation technique used

in S^3-LEB setup are explained.

2.1 Resonance Laser Ionization

The resonance laser ionization technique is an efficient method for laser ion production and spectroscopic studies. The concept of two-step photoionization was first demonstrated by Letokhov *et al.* [33]. In a simple two-step laser photoionization process, a laser is tuned to a frequency corresponding to the energy difference between the ground state of an atom and an excited level at more than halfway to the ionization potential of that atom. A second photon (from the same or another laser) is then used to excite the atoms from the excited energy state for ionization. This can be implemented through a Rydberg state, an autoionizing state, or non-resonantly above the continuum as shown in figure 2.1.

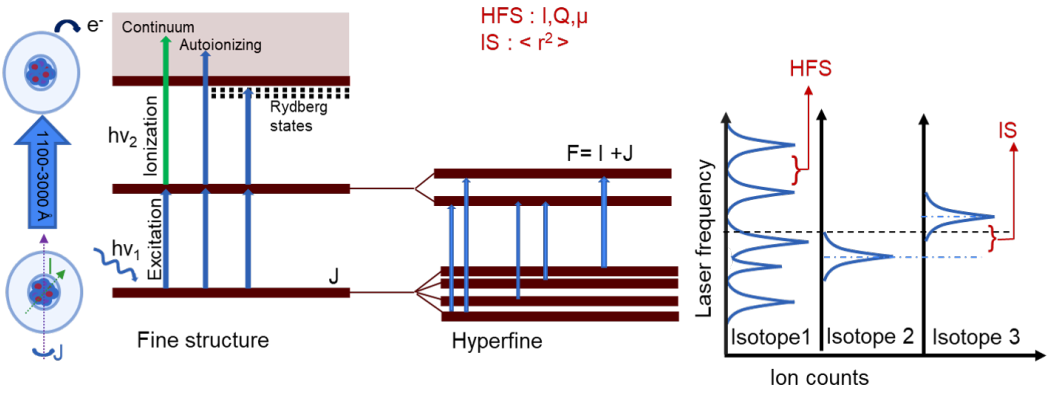

Figure 2.1: Resonance ionization laser spectroscopy schemes to probe hyperfine levels

The cross-section for the non-resonant type excitation is rather low (10^{-19} to 10^{-17} cm^2) and hence the laser photon flux required is higher to satisfy the flux condition compared to a resonant type excitation. The cross-section of a transition through an auto-ionizing state can be as high as 10^{-15} cm^2 which is several orders of magnitude higher compared to non-resonant transition to the continuum [34]. Autoionizing states are efficient energy states above the ionization potential which occur due to several reasons, one of them being the double excitation of valence electrons in a many-electron system. Another type of ionization is through high-lying Rydberg states which can have a cross-section of 10^{-14} cm^2. The latter requires the presence of a sufficiently intense external electric field or via collisions.

For performing resonant laser ionization with saturation of the resonant atomic transition, the lasers have to follow certain requirements. Pulsed lasers are used to overcome the low cross-sections. The laser pulse width should be shorter than the decay time of the excited state to minimize the losses due to spontaneous decay from the excited state. The pulse energy density required for saturation of resonant transition can be deduced from rate equations given by [35] :

$$E_{sat} = \frac{h\nu_1 \Delta\nu_L^1}{2\sigma_{ab}\Delta\nu_t^1} \tag{2.1}$$

where $h\nu_1$ is the resonant photon energy, σ_{ab} is the absorption cross section for the transition, $\Delta\nu_L^1$ and $\Delta\nu_t^1$ are the line width of the laser and the line width of the atomic transition resonance. The linewidth of the laser is required to be greater or equal to the resonance width of the atomic transition to cover the resonance and thus maximize ionization efficiency. The lasers used for excitation are required to be temporally synchronized and spatially overlapped so that the laser can efficiently excite atoms from the excited state to ionization before the decay lifetime of the excited state. Pulsed lasers of repetition rate 10-20 kHz and tens of ns pulse time are more commonly used for step-wise excitation and ionization as they can provide a high peak power of several kW and thus satisfy the photon flux condition (as seen in equation 2.1) to have a high ionization yield. The increase in the number of excitation steps increases the selectivity as the laser frequencies will be resonant to the atomic transitions used for the ionization scheme. Usually, two-step/three-step excitation schemes are used where the transitions matching laser frequencies are mostly available. Multiple steps greater than three-step schemes are challenging in several ways. The increase in the number of laser steps makes it difficult to synchronize and overlap all the laser steps in the laser-atom interaction region.

To perform laser spectroscopy, the atomic fine and hyperfine energy levels are probed using resonant laser frequencies. Two or more lasers are used for step-wise excitation and to finally ionize the atoms. The excitation laser steps are detuned from the atomic transition frequency while detecting the ions to obtain the excitation spectra. Hyperfine transitions are sensitive in the MHz (μeV in terms of energy) range and hence require high-resolution tunable lasers to match the transition line widths. By choosing appropriate resonance ionization schemes, resonances for isotopes and isomers as well as the hyperfine spectra for the odd isotopes can be obtained. From these spectra, atomic observables such as isotope shift and hyperfine parameters can be deduced. These atomic observations can then be used to calculate the nuclear parameters like differences in the charge radii, and nuclear moments. To probe the atomic fine and hyperfine levels, other laser spectroscopic techniques also exist such as the collinear laser spectroscopic technique but they are not in the scope of this thesis work [36, 30, 31].

Thus resonance laser ionization technique has been implemented to produce laser-ionized radioactive beams as well as for laser ionization spectroscopic studies and resonance ionization mass spectrometry. There are several approaches for laser ion sources (LIS) using resonance ionization such as hot cavity ionization and gas cell-based ionization.

2.1.1 Hot cavity laser ion source

In hot cavities, the atoms are created within a high-temperature environment either from reactions (chemical processes) in a thick target like in RILIS ISOLDE or by trapping them onto a solid catcher like in IGISOL, University of Jyvaskyla [35, 37]. Atoms created are extracted from the target using diffusion and effusion processes. Laser then interacts with the atoms effusing out of the hot cavity to create ions. It becomes difficult to diffuse out some atoms such as reactive atoms that form strong bonds with the target material or to the ion source system. The effusion process can be hindered by the long sticking

time of certain atoms with target chamber walls making the extraction of atoms slow. The effusion of atoms from a hot cavity is determined by the source dimension and relative velocity of the atoms. Thus the range of RIB production depends on the production and release properties of the target material used. The hot cavity technique is thus limited when it comes to the study of refractory elements and elements with short half-lives. As the laser-atom interaction will occur in the high-temperature environment of the hot cavities, the atomic spectral resolution is significantly influenced by the Doppler broadening mechanism, which is reduced for heavier atoms compared to lighter ones (see section 1.2.4). For example, ^{170}Er at 2000 °C for an atomic transition $4f^{12}6s^2\ {}^3H_6$ to $4f^{12}({}^3H)6s6p$ at a transition frequency of 24083.16 cm^{-1} will give a Doppler broadening FWHM of $\approx$ 1.9 GHz (using equation 1.74). If the hyperfine structure difference, for example, an isotope/isomer is sufficiently large compared to the achievable atomic excitation resonance widths, hot cavity ion sources can be used. It is usually difficult to resolve the hyperfine structure with small differences due to the Doppler broadening of the resonance widths caused by the high temperature in the hot cavities. The high-temperature environment also causes unwanted thermal ionization of atoms and this causes isobaric contamination which also reduces selectivity. The hot cavity laser ion sources are applicable for the production of ions with elemental selectivity which can in further stages be mass separated for isobaric selectivity for experiments. Techniques such as ion beam gating and separation of ions via time of flight are adapted to tackle the problem [38]. Another technique implemented with the hot cavity approach is the laser ion source and trap (LIST), an RFQ ion trap coupled to the hot cavity where only neutrals are allowed for laser interaction and the surface ions are repelled using electrodes. This allows a significant reduction of contaminant ions as well as improves the laser ionization efficiency. Perpendicularly illuminated laser ion source and trap (PI-LIST) with perpendicular laser configurations allow only atoms of a narrow class of velocity to be probed and thus can reduce the Doppler broadening to a few hundred MHz [39].

2.1.2 Gas cell-based laser ion source

In a gas cell-based laser ion source, the ions are stopped in a gas cell and neutralized. The in-gas laser ionization and spectroscopy (IGLIS) technique is a technique utilizing resonance laser ionization and spectroscopy techniques for the purification and study of radioactive ions. The S^3-LEB setup at SPIRAL2 facility, GANIL Caen, currently under offline commissioning at LPC Caen is implementing this technique [40]. The MARA-LEB, at the University of Jyvaskyla is a similar setup under commissioning using the IGLIS technique [41]. RADRIS and JETRIS setups at GSI, Darmstadt are also very similar to S^3-LEB for gas cell-based laser spectroscopy. In the RADRIS setup, the recoil products from fusion evaporation separated from the primary beam are stopped in a buffer gas environment and then collected on a filament for neutralization. The neutralized atoms from the filament are then re-evaporated for resonant laser ionization and then transported to the detector setup [42]. In JetRIS, the RIBS in the gas cell are transported using an electric field toward a filament where they are neutralized. The filament is heated for the desorption of neutral atoms and the neutral atoms are transported by gas flow to a gas jet region for

laser-atom interaction [43].

In the IGLIS approach implemented at S^3-LEB, the atoms are formed by thermalization and neutralization of ions created from nuclear reactions in a stopping gas cell. The laser-atom interaction will occur inside the gas cell with a buffer gas environment. Here the extraction of the ions is determined by the gas cell dimension and gas flow and thus is not limited to the chemical properties of the atoms. This technique is thus advantageous for the ionization of refractory elements [20, 44, 45]. Inert gases like argon or helium are commonly injected as buffer gases which flow out of the gas cell under pressure to release the ions along with the gas. Ar gas provides improved stopping power and neutralization compared to He gas due to its heavier mass. In cases where neutralization is not a concern but requires faster release time, He can be used. The purity of the gas cell is crucial as a laser ion source. In the presence of impurities mainly water vapor, oxygen, and nitrogen [6], atoms can react with the impurities thus hindering the ionization efficiency. Hence pure gas cell with a very low impurity concentration in the range of ppm to ppb is used.

Laser ionization in gas cells is also affected by Doppler broadening. The Doppler broadening for a gas cell at 320 K for the same Er transition mentioned in the hot cavity section can be calculated using equation 2.11 and is 0.715 GHz. The spectral resolution in gas cell ionization will be additionally affected by pressure broadening due to collisions with the buffer gas atoms (refer to section 1.2.4). The pressure-induced broadening for a gas cell pressure of 100 mbar (atom density: 2.26×10^{18} atoms.cm^{-3}) and 500 mbar (atom density: 1.13×10^{19} atoms.cm^{-3}) at a gas cell temperature of 320 K, for the same Er transition as mentioned in 2.1.1, can be calculated from equation 1.68 to be 1.016 GHz and 5.084 GHz respectively. For the above numerical calculation, γ_{coll} for argon is assumed to be 1.5×10^{-20} cm^{-1}/cm^{-3}, value taken from [20]. γ_{coll} is transition dependent and was not measured previously for the above-mentioned transition. Thus γ_{coll} value for the calculation is taken from literature for similar transitions. The pressure broadening for the particular transition has been measured experimentally as a part of this thesis work and results can be found in 4.4.1.

The spectral resolution in gas cell-based setups can be improved by laser ionization outside the gas cell in a jet environment. For this purpose, atoms are guided along with the buffer gas out of the gas cell through a small exit aperture to create a gas jet. The use of a de Laval nozzle at the exit aperture creates a collimated supersonic jet with low energy spread and velocity spread of atoms. Laser spectroscopy in the gas jet environment reduces the spectral resolution by at least an order of magnitude compared to in-gas cells.

The basic driving force for gas jet formation from the gas cell is the pressure difference between the gas cell (P_0) and the background pressure (P_{bg}) outside the gas cell where the jet is formed. As the gas flows out of the gas cell from high pressure, expansion of gas occurs. The velocity of the expanding gas depends on the gas cell temperature and the temperature at which the gas jet cools down. The gas flow density decreases along the jet stream line inversely proportional to the square of the distance from the exit aperture.

Gas jets can be formed in different configurations. With gas flowing out of the gas cell through an exit aperture, a supersonic-free jet is formed. The free jet is divergent it travels farther away from the aperture. If a de-Laval nozzle

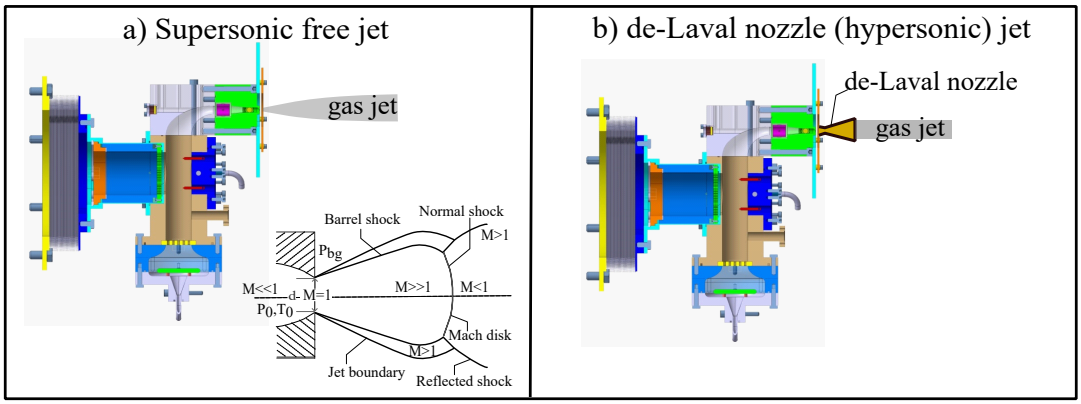

Figure 2.2: Layout of the a) supersonic free jet expansion with inset showing the main attributes of an axisymmetric and supersonic free gas jet and b) de Laval nozzle hypersonic jet expansion from the gas cell. P_0 and T_0 denote the stagnation pressure and temperature in the gas cell and P_{bg} denotes the background pressure in the gas cell chamber.

is implemented at the exit aperture, the nozzle will create an axisymmetric homogenous jet compared to a free jet. Figure 2.2 shows the cross-section of a gas cell with the free-jet and de-Laval nozzle jet expansion. De-Laval nozzles are known for their use in rocket engines and steam turbines to create supersonic velocities of compressible fluids to create thrust. The de Laval nozzle consists of a convergent part followed by a diverging part (see figure 2.3). The converging part causes an increase in the subsonic flow of the gas in the gas cell. The nozzle region with the smallest area is called the throat area where the gas flow reaches the speed of sound. As the divergent portion starts, further acceleration of the gas occurs causing supersonic gas flow by converting the thermal energy of the gas into kinetic energy. As the entropy of the system remains the same, the de-Laval nozzle is said to generate an isentropic flow resulting in the adiabatic expansion of the gas. The gas flow velocity is determined by the boundary

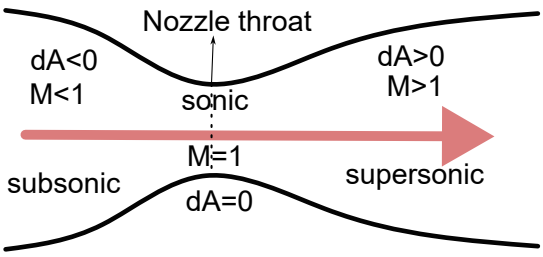

Figure 2.3: Schematic cross-section of a de Laval nozzle showing its different regions of areas.

layers of the nozzle from the area velocity relation expressed as [46]:

$$\frac{dA}{A} = \frac{dV}{V}(M^2 - 1) \tag{2.2}$$

where A is the area of the cross-section of the nozzle, V is the gas velocity and M is the Mach number.

Mach number is defined as the ratio of stream velocity to the velocity of

sound. The stream velocity of the gas jet can be expressed as:

$$u = \sqrt{\frac{\gamma k T_0 M^2}{m(1 + [\gamma - 1/2]M^2)}} \tag{2.3}$$

and the velocity of sound can be express as:

$$a = \sqrt{\frac{\gamma k T}{m}} \tag{2.4}$$

where γ is the buffer gas constant which is the ratio specific heat capacities C_p/C_v, k is the Boltzmann constant, T_0 and T are the temperature in the gas cell and gas jet respectively, m is the mass of the buffer gas atom and M is the Mach number.

In the converging part of the nozzle, $M < 1$ where subsonic flow occurs. At the throat, $M = 1$ where flow is sonic and at the diverging part of the nozzle, $M > 1$ where flow velocity becomes even higher. When the flow velocity is greater than five times the velocity of sound, the flow is known to be hypersonic. Thus the Mach number of the nozzle defines the flow properties of the formed jet. The expansion of the gas in the gas jet will depend on the ratio of the area of the nozzle exit to its throat as seen from equation 2.2. For the gas flow to be choked at the throat area to create supersonic velocities, a certain pressure ratio between the gas cell and background pressure in the jet has to be maintained and is called pressure matching. The gas jet homogeneity is strongly impacted by the background pressure in the jet defined by the equation 2.6. Improper matching will cause the gas jet to undergo over/under expansion which affects the beam divergence and also complete overlap of the laser with the jet.

The temperature, pressure, and density of the gas jet are related to the Mach number by the following formulism [20]:

$$\frac{T}{T_0} = [1 + \frac{\gamma - 1}{2} M^2]^{-1} \tag{2.5}$$

$$\frac{P}{P_0} = [1 + \frac{\gamma - 1}{2} M^2]^{\frac{-\gamma}{\gamma - 1}} \tag{2.6}$$

$$\frac{\rho}{\rho_0} = [1 + \frac{\gamma - 1}{2} M^2]^{\frac{-1}{\gamma - 1}} \tag{2.7}$$

where P_0, ρ_0 and T_0 are the stagnation pressure, density, and temperature in the gas cell, γ is the buffer gas constant (for argon, $\gamma = 5/3$), m is the mass of the buffer gas and M is the Mach number of the de-Laval nozzle. Equations 2.3, 2.5, 2.6, 2.7 show the jet stream velocity, temperature, pressure and density dependence on the Mach number. The stream velocity graph shows an increase with the increase in the Mach number reaching a velocity of about 560 m/s for $M > 5$ for the argon gas jet at a temperature of 320 K. With Mach number, density and temperature can be found to decrease as well as shown in figure 2.5.

The design conditions of the nozzle thus allow the creation of an axisymmetric homogeneous gas jet environment with low temperature and pressure. If laser ionization and spectroscopy are performed in this low-pressure and low-temperature environment, Doppler and pressure broadening are reduced by at

least an order of magnitude compared to in-gas cells, thus improving the spectral resolution [7]. To explain in detail, the velocity distribution of the atoms in the gas cell and gas jet can be considered.

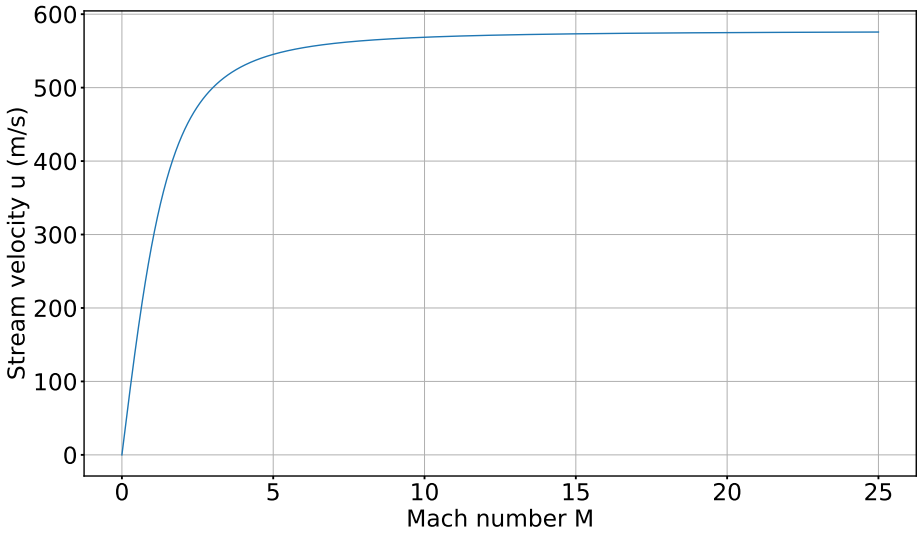

Figure 2.4: Stream velocity of the argon gas jet as a function of Mach number considering gas cell stagnation temperature to be 320 K.

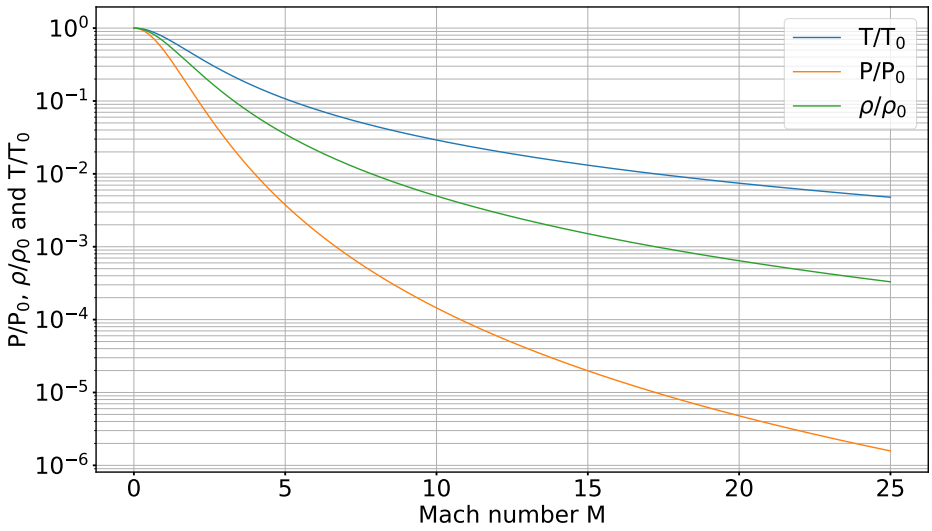

Figure 2.5: Pressure, density, and temperature dependence on the Mach number. Here the y-axis is plotted in log scale using equations 2.5, 2.6, and 2.7.

The thermal motion of the atoms in the gas cell follows the Maxwell-Boltzmann distribution function given by the $F_{th}(v_i)$ function [40]:

$$F_{th}(v_i) = \sqrt{\frac{m}{2\pi k_b T_0}} . \exp(\frac{m v_i^2}{2 k_b T_0}) \tag{2.8}$$

where m is the mass of the atom of interest, k_b is the Boltzmann constant, T_0 is the temperature in the gas cell and v_i is the velocity component in $i = x, y, z$

directions. This equation is the same as equation 1.71 for Doppler broadening. The velocity of the atoms in the gas jet in its direction of flow ($i = z$) is given by a shifted function given by [40]:

$$F_{sh}(v_z) = \sqrt{\frac{m}{2\pi kT}}.\exp(\frac{m(v_z - u)^2}{2kT}) \tag{2.9}$$

where u is the stream velocity of the jet and T is the temperature in the gas jet. The FWHM of the distribution is dependent on the temperature of the jet given by:

$$\Delta_F = 2\sqrt{ln(2)}\sqrt{\frac{2kT}{m}} \tag{2.10}$$

For example, the one-dimensional velocity distribution of the ^{170}Er atoms in the gas cell and supersonic jet of different Mach numbers for argon as buffer gas is shown in figure 2.6. The blue plot shows the calculated velocity distribution from equation 2.8 for ^{170}Er in the gas cell at a temperature of 320 K. The red, green, and yellow plots show the shifted velocity distribution, calculated from equation 2.9, in gas jets for the Mach number values 1, 4 and 8. From the velocity distribution plot, it can be seen that higher Mach numbers give a narrower velocity distribution for the atoms. It means that for higher Mach numbers, the atoms collide less thus reducing the pressure broadening and Doppler broadening.

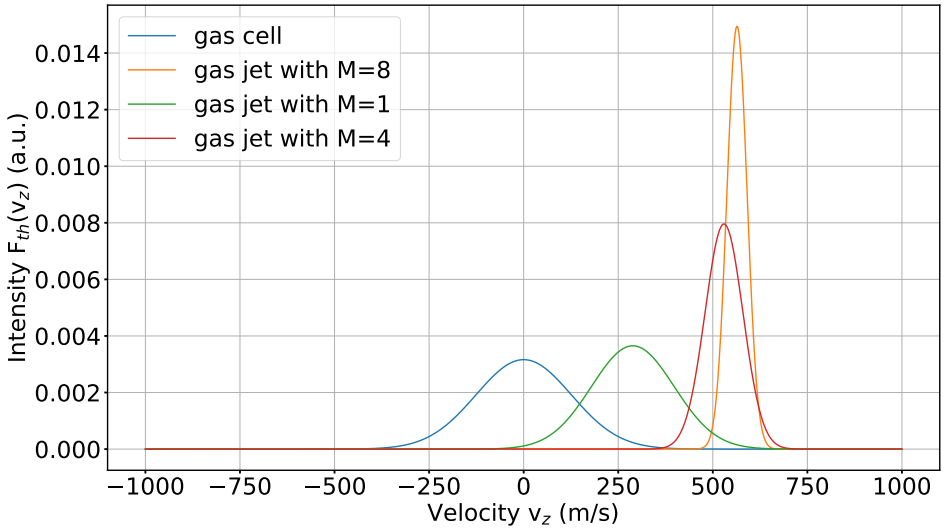

Figure 2.6: One-dimensional velocity distribution of ^{170}Er atoms in the argon injected gas cell and gas jet environment plotted using equation 2.9.

Spectral resolution in gas cell/jet

The spectral resolution obtained for laser ionization spectroscopy using the gas cell/gas jet method, as mentioned before, is mainly determined by two broadening mechanisms: Doppler (Gaussian profile) and pressure broadening (Lorentzian profile). The Gaussian and Lorentzian profile convolute to give the spectral shape a Voigt profile (see section 1.2.4). The Gaussian contribution to

the spectral line shape comes from the Doppler effect on the velocity distribution of atoms. The Gaussian distribution function is given by equation 1.72 [20] and the Doppler FWHM is given by equation 1.73 [20]. In a gas jet, the reduced temperature causes the narrowing of the Doppler width. If the atomic beam in the jet diverges from the axial center of the nozzle it causes additional Doppler broadening given by [20]:

$$\Delta\nu_\theta = \nu_{01} u \sin\theta / c \tag{2.11}$$

where ν_{01} is the atomic transition frequency, u is the stream velocity along the axial center of the nozzle and θ is the angle of divergence of the stream velocity vector from the beam axis. As an example, for a jet with Mach number M = 8, the additional broadening due to a divergence of 5° is around 58 MHz. This thesis work has utilized the IGLIS technique at S^3-LEB for the laser spectroscopic measurements on erbium isotopes and hence the calculations were performed for erbium transition. The Doppler width dependence for ^{170}Er $4f^{12}6s^2\ {}^3H_6$ to $4f^{12}(^3H)6s6p$ transition at 24083 cm^{-1} as a function of Mach number is shown in figure 2.7. The blue line shows the Doppler width at 0° divergence of the jet velocity component compared to the beam axis. The orange line shows the Doppler broadening in the gas jet with a beam divergence of 5°. It can be seen from the graph that the Dopper broadening reduces with higher Mach numbers.

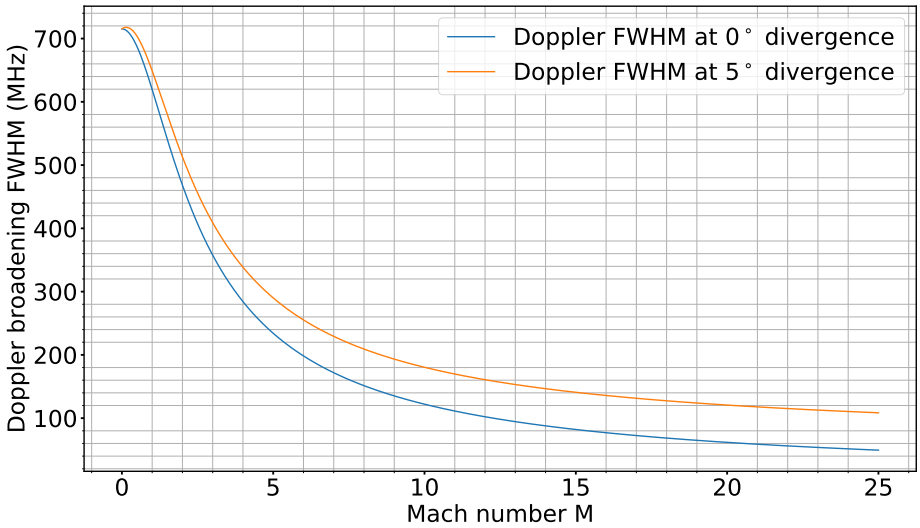

Figure 2.7: The calculated Doppler width as a function of Mach number for the 415.2 nm transition for ^{170}Er is shown in blue when the beam is perfectly parallel to the laser beam. The orange plot shows the Doppler broadening for the same transition for a beam divergence angle of 5°.

The laser linewidth also contributes to the Gaussian contribution of the line profile due to the Gaussian time profile of the laser pulses used for resonance laser ionization [20]. The laser linewidth of the fundamental laser line can be measured using commercially available wavemeters. If the second harmonic generation is used for obtaining the laser frequencies to match the atomic transition, a correction factor can be included in the fundamental line width to obtain the doubled laser frequency linewidth. If σ_ω is the fundamental laser

FWHM line width, the doubled frequency FWHM line width can be deduced as :

$$\sigma_{2\omega} = \sqrt{2}\sigma_{\omega} \tag{2.12}$$

The pressure broadening contribution to the spectral line in the gas cell is a Lorentzian function given by equation 1.67. The total FWHM of the Lorentzian contribution, including natural line width, pressure broadening, and collision-induced shift is defined by equation 1.66 and equation1.69.

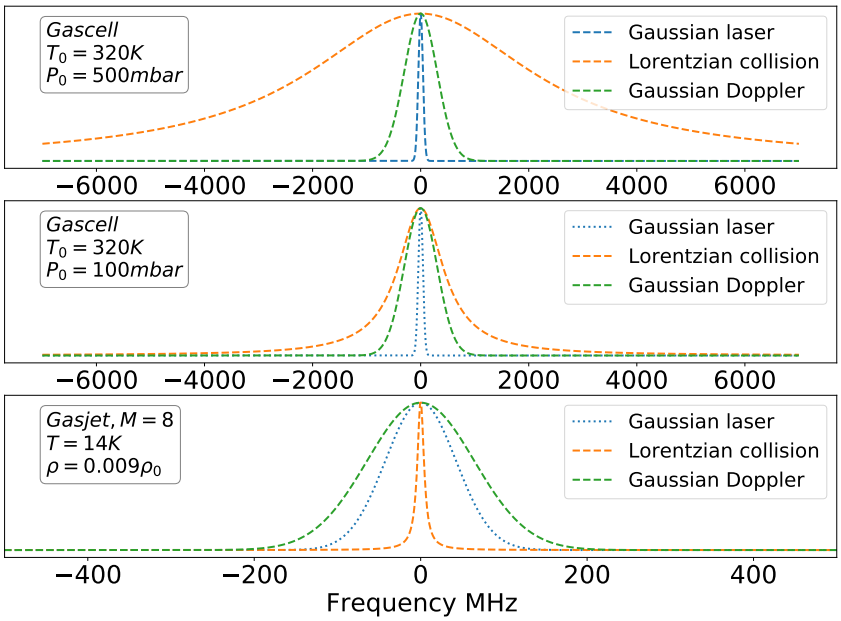

Figure 2.8: The Doppler, pressure, and laser contributions to the spectral line profile for ^{170}Er transition in (top inset) the gas cell at a pressure of $P_0 = 500$ mbar and temperature $T_0 = 320$ K, (middle inset) the gas cell with $P_0 = 100$ mbar, and (bottom inset) gas jet of Mach number $M = 8$, temperature $T = 14$ K and density $\rho = 0.009\rho_0$.

Thus the spectral line profile is the convolution of the Lorentzian and Gaussian profile from Doppler broadening, pressure broadening, and laser linewidth. The FWHM of the Voigt profile can be estimated using the expression 1.75 [20]. The Doppler, pressure, and laser linewidth contribution to the spectral linewidth in the gas cell and jet is demonstrated in figure 2.8. From the graph, it can be seen the spectral broadening in the gas cell at high pressure as in 500 mbar (shown by the top inset) is mainly from the collision with the buffer gas. At lower pressures like 100 mbar in the gas cell (middle inset), the pressure broadening and Doppler broadening are comparable with Lorentzian tails. For the gas jet (bottom inset), with a Mach number M = 8, the jet density decreased down to 0.009 times the gas density in the gas cell (using equation 2.7). The spectral broadening in this condition is significantly reduced as can be seen from the plot. The collision FWHM Γ_{coll} in the gas jet for this condition can be deduced (with equation 1.66) for a 100 mbar stagnation pressure in the gas cell to be $\approx$ 9.55 MHz which is even smaller than the natural line width of the transition considered ($\Gamma_{nat} = 15$ MHz). From this example, it can be seen that

the IGLIS technique in combination with de Laval nozzle provides a spectral resolution sensitive to resolve isotopes and hyperfine structures.

Thus IGLIS technique in combination with the de-Laval nozzle allows the study of nuclei of interest with high selectivity and sensitivity even though the attainable spectral resolution is not as good as in the collinear spectroscopic technique.

The technique of resonance laser ionization can be utilized in many ways for the production of radioactive ions providing Z-selectivity. It can still have isobaric contamination, which then can be minimized using mass separators. Time of flight mass separators allows simultaneous but separate recording of the spectra of different isotopes. The combination of Z selectivity with mass selectivity, along with high sensitivity and fast detection techniques, allows the exploration of short-lived nuclei and nuclides with low production rates with higher accuracy and precision.

2.2 Ion transport, purification and time of flight detection

The laser-produced ions are usually measured using Faraday cups, channeltrons, microchannel plates (MCPs), and MagneTOFs. Faraday cups are less sensitive as they measure the electric current produced as a result of the ion beam hitting the metal surface. Channeltron detectors provide improved sensitivity by producing secondary electron emissions and thus have a higher gain compared to Faraday cups. MCPs are a matrix array of several channeltrons, additionally providing spatial resolution when used with phosphor screen. MCPs have been used in the measurements discussed in section 4.2. If the ions are radioactive, they can also be identified by measuring their alpha, beta or/and gamma emissions with silicon and germanium detectors.

Separation of isobaric contamination before ion detection is crucial for high-resolution laser spectroscopy measurements. The laser-produced ion beams can be sent to detection setups using several ion-guiding techniques. The ions can be mass-separated using mass filters and mass measurements can be performed using a multi-reflection time of flight mass spectrometer (MR-TOF-MS). A MR-TOF-MS requires good vacuum conditions for their operation of the order of ¿10^{-8} mbar. In S^3-LEB, laser ions are produced in the gas cell/jet (at a pressure $>10^{-2}$ mbar) and hence require to be transported to better vacuum conditions for detection and mass measurement. For this purpose, radio frequency quadrupoles (RFQs) are used as simple ion guides for the transportation of ions to higher vacuum regions. This section describes the operating principle of radio frequency quadrupoles as ion guides and as a mass filter. The principle of operation of an MR-TOF-MS is also discussed.

2.2.1 Radio frequency quadrupoles

Once the laser-produced ions are created, they need to be guided to the detection system for further studies. Radiofrequency quadrupole (RFQ) structures have been an established technique to manipulate charged particles ever since its application in quadrupole mass spectrometry [47]. These RFQ struc-

tures are in principle four-rod structures on which electric fields are applied to create a quadrupole field. A simplified schematic diagram of a four-rod RFQ structure is shown in figure 2.9.

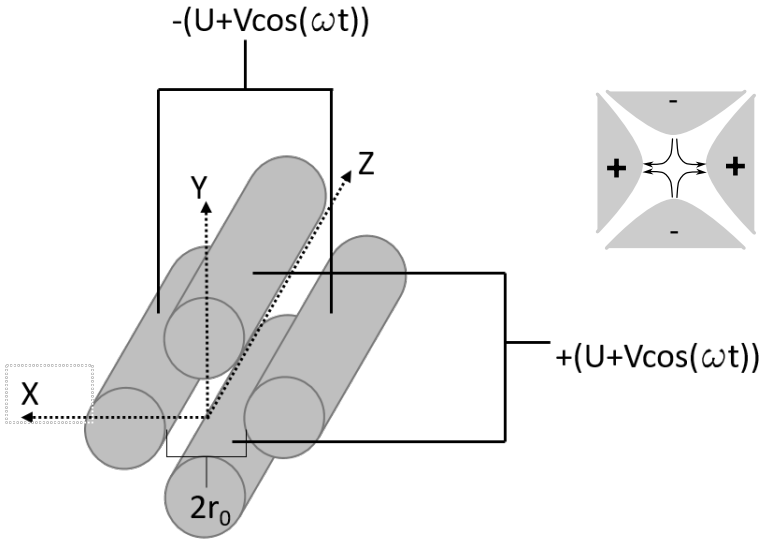

Figure 2.9: Simplified schematic diagram of a radiofrequency quadrupole structure.

Here the ions travel in the z-direction. V is the amplitude voltage of the applied RF voltage oscillating with an angular frequency ω and U is the amplitude of the DC potential applied. If $2r_0$ is the inter-electrode distance, the potential within a quadrupole structure at any given point in the xy plane is given by [48]:

$$\phi_{x,y} = \frac{\phi_0}{2r_0^2}(x^2 - y^2) \tag{2.13}$$

The actual quadrupole potential experienced by the ion is :

$$\phi_0 = 2(U + Vcos(\omega t)) \tag{2.14}$$

where ϕ_0 is the difference between the potential on the positive and negative rods. Hence the potentials applied to the horizontal and vertical pair of cylindrical rods are out of phase with each other. The force acting on the ions in the x and y directions due to the potential is:

$$m\left(\frac{d^2x}{dt^2}\right) = -2e\frac{(U + Vcos\omega t)x}{r_0^2} \tag{2.15}$$

$$m\left(\frac{d^2y}{dt^2}\right) = 2e\frac{(U + Vcos\omega t)y}{r_0^2} \tag{2.16}$$

No force due to the AC field is experienced in the z-direction.

Generally, the motion of the ions in the quadrupole field can be described with the Mathieu equation given by:

$$\frac{d^2u}{d\xi^2} + (a_u - 2q_u \cos t2\xi)u = 0 \tag{2.17}$$

where u is the displacement of the ion, ξ is a dimensionless parameter equal to $\omega t/2$, and a_u and q_u are additional dimensionless parameters describing the stability of the ion's motion. Stability parameters a and q in the x direction are given by:

$$a_x = \frac{8eU}{mr_0^2\omega^2} \tag{2.18}$$

$$q_x = \frac{-4eV}{mr_0^2\omega^2} \tag{2.19}$$

where $a_x = -a_y$ and $q_x = -q_y$.

The solution to the Mathieu equation gives rise to different regions of stability in the x and y trajectories of the ions shown by the Mathieu stability diagram as in figure 2.10. In figure 2.10, region I, II, and III shows regions of simultaneous overlap where both ions in the x and y dimensions are stable. When only RF potential V is applied with DC potential U=0, all a_x, q_x coordinates must lie on the q_x value ($a = 0$) where all ions above a fixed mass to charge ratio will be transmitted through the RFQ structure, thus acting as an ion guide. An additional DC gradient is applied throughout the RFQ segments to push the ions in the z-direction. The upper part of Region I from the stability diagram

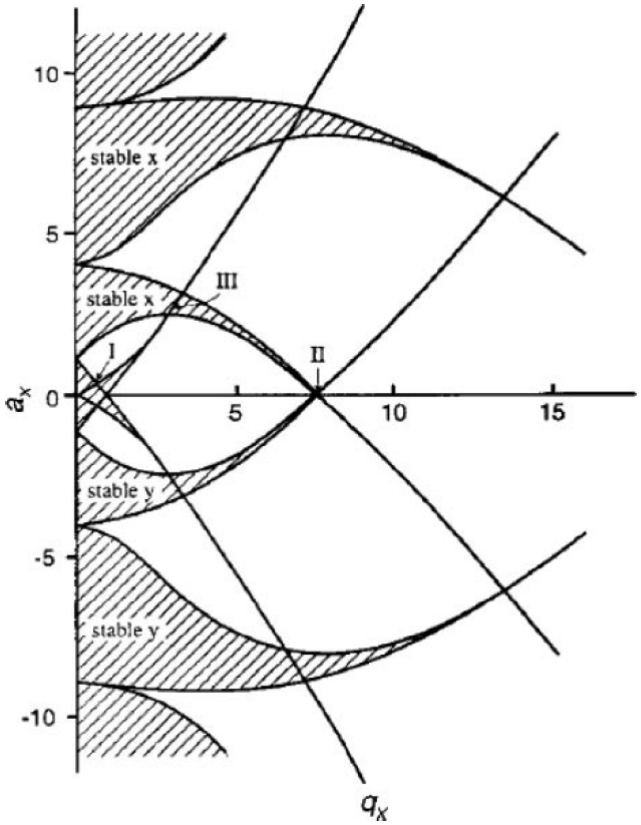

Figure 2.10: Mathieu stability diagram for linear RFQ trap in x and y dimensions(adapted from [49]). I, II, and III show the regions of simultaneous overlap where ions are stable in both x and y dimensions.

2.10 is shown in figure 2.11. Here, ions are bound within the cavity in both the x and y planes.

RFQ as mass filter

The RFQs can operate as a mass filter where the DC(U) and AC/RF(V) voltages are applied such that the stable trajectory for ions is possible for only a certain mass-to-charge range. When r_0, ω, U, and V are fixed, then a and

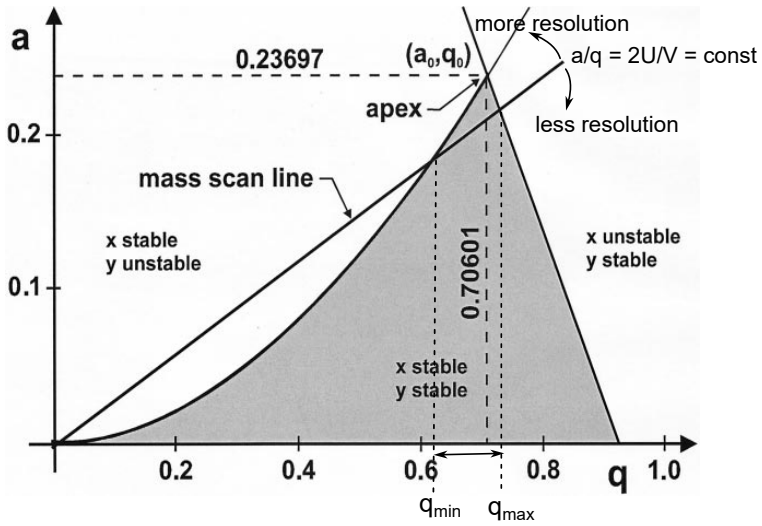

Figure 2.11: First region of stability in the $a - q$ plane in Mathieu stability diagram for ion trajectories in quadrupole mass filter (adapted from [50]).

q parameters are dependent only on the mass-to-charge ratio, i.e., all ions of the same mass-to-charge ratio have the same operating point in the stability diagram. When U and V are scanned, keeping their ratio constant ($a/q = 2U/V$ = const), a mass spectrum is obtained. The scan is performed along the mass can line as shown in figure 2.11. The scan line passes to the apex for each ion of increasing mass-to-charge (A/Q) ratio. As the U/V ratio is increased, the scan line approaches the tip of the stability diagram and only a narrow range of A/Q range can have stable trajectories achieving higher resolution. In ion guiding mode, the RFQ unit will act as a high pass mass filter (with less resolution) where:

$$m > \frac{4eU}{0.908\omega^2 r_0^2} \tag{2.20}$$

where the range of q coordinates can be from 0 to 0.908.

In mass filtering mode (with more resolution), the slope of the scan line determines the range of q coordinates where the mass scan line overlaps with the stability region. The allowed masses in this range of q values can then be expressed by:

$$\frac{4eU_{qmin}}{q_{max}\omega^2 r_0^2} < m < \frac{4eU_{qmax}}{q_{min}\omega^2 r_0^2} \tag{2.21}$$

RFQ for cooling and bunching

In RIB facilities, RFQ structures are also used for cooling and bunching the continuous beam by adding a buffer gas before sending them to a trap-based mass spectrometer [51, 52]. Buffer gas cooling is widely used in low-energy facilities for radioactive ion cooling [53, 51]. The ions are guided along the axial direction by the application of AC and DC voltages to the RFQ structure at the

same time cooled by buffer gas collisions that decelerate the ions. The buffer gas like He is chosen, inert in nature and with high ionization potential, such that the probability of charge exchange with the ion beam is low. Once the ions are decelerated, the ions can be collected to form bunches in an axial electric potential well created by the DC potentials applied in the RFQ segments. The RFQ structure thus needs to be segmented for the application of various DC potentials. The bunched ions can then be extracted by switching on extraction voltages applied to the end segment of the RFQ structure. This kind of ion guide, known colloquially as cooler-buncher, basically has a decelerating, bunching, and extraction part operating in different pressure conditions, thus requiring efficient differential pumping. The design of a cooler-buncher section requires a SIMION or other type of simulation of the ion motion to obtain the highest efficiency. The optimal RF voltage and the bunching and extraction voltages have to be adjusted experimentally to obtain the best bunch parameters, such as emittance and transmission. The bunch properties are crucial when injected into a trap-based detector or mass spectrometer for their optimal performance.

2.2.2 Multi-reflection time of flight spectrometer

A multi-reflection time-of-flight mass spectrometer (MR-TOF-MS) can be used for the inflight separation of the ions according to their mass-to-charge ratios over their time of flight. It can also be used for mass measurement studies of the RIBs. MR-TOF-MS devices are in operation in several facilities including the ISOLTRAP in ISOLDE, CERN [54], CARIBU in ANL, USA [55], TITAN at TRIUMF, Canada, MLL trap in ALTO and many more. At S^3-LEB, a MR-TOF-MS named PILGRIM is installed. The theory of operation of TOF mass spectrometers is well established and one can refer to [47, 48]. The resolving power of such a device is given by:

$$R = \frac{m}{\Delta m} = \frac{t}{2\Delta t} \tag{2.22}$$

where t is the time of flight of the ion inside the spectrometer, m is the mass, Δt and Δm are the time and mass FWHM. A time of flight of several meters to kilometers is required for the separation of the isobars and possible isomers(depending on the lifetime of the isomer state), which requires a resolving power $(m/\Delta m)$ of $10^3 - 10^4$ [8]. This requirement can be realized using an MR-TOF-MS.

MR-TOF-MS is a linear trap consisting of electrostatic plates sandwiching a field-free drift tube. Figure 2.12 shows the schematic layout and operation principle of an MR-TOF-MS setup. The red and blue curves show two masses separating in their time of flight. The red line in the bottom inset shows the total energy of the ions with purple and blue dots showing the switch in potential at the injection and ejection of the ion to and from the trap respectively. Once the ions are injected into the trap, the ions will travel back and forth between electrostatic mirrors until they achieve a flight length of several kilometers. Due to the long flight path, this kind of device requires a good level of vacuum.

Ions are injected into the MR-TOF-MS as bunches. Characterization of the bunch parameters is performed as part of this thesis work and described in detail in the following chapters. The resolving power of an MR-TOF also depends on

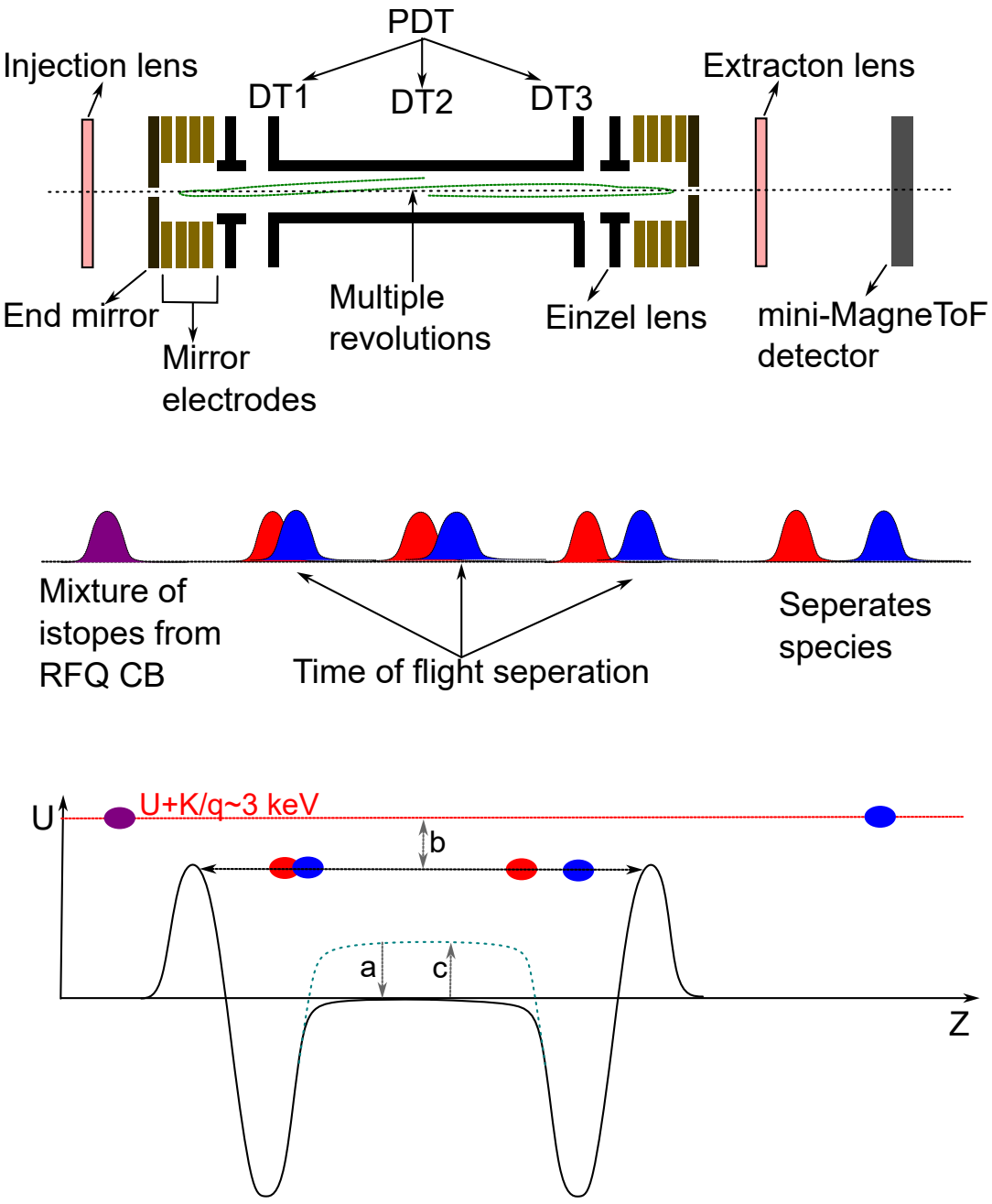

Figure 2.12: Top inset shows the schematic layout and operation of a MR-TOF-MS. The middle inset shows the time of flight separation of ions according to their masses. The bottom inset shows the in-trap lift approach for injection and trapping with a, b, and c labeling injection, trapping, and ejection (adapted from [8]).

the input characteristics of the ion bunches such as the energy spread and initial velocities. The ToF bunch width needs to be as low as possible, directly impacting the dispersion of bunch energy. Due to the energy spread, the time of flight width of the bunched ions will increase over their course of travel. More energetic ions travel faster compared to the less energetic ones. In order to compensate for this spread, a series of electrostatic mirror plates with voltage control are used, such that the ions reaching the mirrors faster are made to travel more distance thus providing a time of flight focus. The time of flight of

the trapped ions depends on the potential of the mirror electrodes and they need to have high stability. Variations in the HV voltage supply connected to the mirrors affect the achievable resolving power and can make mass measurements challenging. DC and RF potentials are applied to the device. The DC potential will form a potential well for trapping of ions in the axial direction. The RF potential allows transversal trapping of the ions in the device.

The ions can be trapped inside using different methods. One approach is to switch down the mirror potential to inject the ions into the spectrometer. Once they are injected the mirror potentials are switched back up for trapping. For the ejection of the ions, the mirror potentials are again switched down. This requires advanced fast-switching voltage supplies at a rate of 100 - 1000 Hz with high voltage stability. Another approach is the injection of the ions with kinetic energy higher than the potential of the mirrors. Once they enter the spectrometer, the pulse drift tube region is pulsed down decreasing the potential energy of the ions and thus trapping them between the mirrors. For ejection, the pulse drift tube is switched back giving energy to the ions to overcome the trap potential. The schematic of the latter method is shown in the bottom inset of figure 2.12. This method is known as in trap lift method and is used in PILGRIM MR-TOF-MS [8]. Here the voltage stability is not as crucial as the former.

2.3 S^3-LEB experimental set up

2.3.1 SPIRAL2

The S^3-LEB setup is a part of the GANIL-SPIRAL2 facility [56]. The Système de Production d'Ions Radioactifs en Ligne de 2^e generation (SPIRAL2) facility consists of a superconducting linear accelerator (SC-LINAC) that can deliver high-intensity stable ion beams from H to U with energies ranging up to 14 MeV/u [56]. It consists of two electron cyclotron resonance (ECR) ion sources with currently an $A/Q = 3$ injector with which the SC-LINAC can deliver deuteron beams of intensity up to 5 mA as well as heavy ion beams up to 1 mA (See figure ??). A new $A/Q = 7$ injector project is underway which will be able to produce heavy ion beams of higher intensities than what is available currently, in the mass range $A = 40$ to 238 [57, 58]. These high-intensity stable ions beams are currently equipped to be sent to two experimental halls, the Neutron for Science (NFS) setup [59] and the Super Separator Spectrometer (S^3) setup [60]. The NFS facility is currently in operation. At NFS, experiments with deuteron and other beams producing high-intensity neutron beams for fundamental and applied physics research are ongoing.

S^3 experimental setup is being constructed with the aim to study exotic nuclei usually difficult to produce due to their low production cross section and very short lifetimes. Figure 2.14 shows the schematic of S^3 installation. It is a high-resolution inflight separator where the SPIRAL 2 heavy ion beams can impinge on a rotating wheel target, that can withstand high beam power, to induce a nuclear fusion evaporation reaction. The recoil products will have relatively low energy of a few MeV/u and large angular and momentum distributions. The S^3 setup has been designed to provide a large acceptance angle of $\pm$ 50 mrad and a momentum acceptance of $\pm$10% with transmission of up to

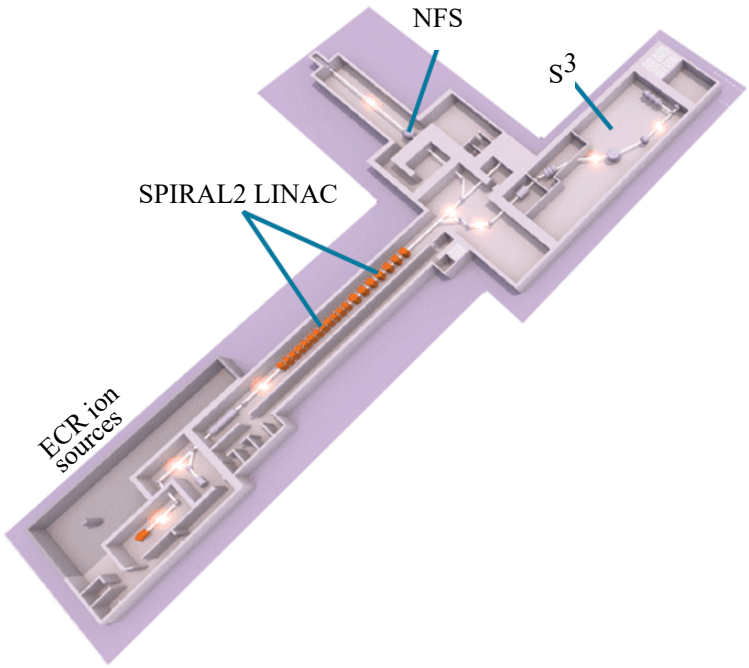

Figure 2.13: Schematic of the GANIL SPIRAL2 facility

60% in the $N = Z$ region [61]. The S^3 optical design is a complex setup mainly consisting of a momentum achromat part and a mass spectrometer part. The momentum achromat part serves for primary beam rejection and refocusing of produced ions of interest. The mass spectrometer part provides selectivity and capability to inflight mass separation according to the charge-to-mass ratio with a mass resolving power of $m/\Delta m > 450$. The optical structure of S^3 is $Q^3DQ^{3'}Q^3DQ^3Q^3EQ^3Q^3DQ^3$ where Q^3 is the superconducting multipole triplets, $Q^{3'}$ is the room temperature multipole triplets, D is the magnetic dipole and E is the electric dipole. They allow beam manipulation and optical corrections.

The S^3 can operate in two modes, a converging mode, and a high-resolution mode. In converging mode, most of the charge states of ions of interest are focused on a plane providing larger acceptance but with no mass selectivity. In high-resolution mode, up to three charge states of the desired ion are allowed with A/Q selectivity but at the cost of lower transmission rates. For tuning of the S^3 beam, several diagnostics have been installed at different sections of the S^3 chamber. Particularly, for the tuning of the S^3 and identification of the fusion evaporation residues, a diagnostic box has been implemented at the end of S^3. It consists of secondary electron detectors (SEDs), double-sided silicon strip detectors (DSSD), and Ge detectors to measure the position, time of flight, energy, alpha decay of the incoming beam, and the gamma emissions respectively.

The primary beam characteristics of SPIRAL2 beams along with suppression of the primary beam at S^3 thus allow the production and study of nuclei with low production rate and very short lifetime. The produced nuclei can then be delivered to various experimental setups such as the S^3 - low energy branch (S^3-LEB), a laser ionization and spectroscopy setup, and a state-of-the-art detector system for decay spectroscopy studies such as the proton, alpha, electron, and

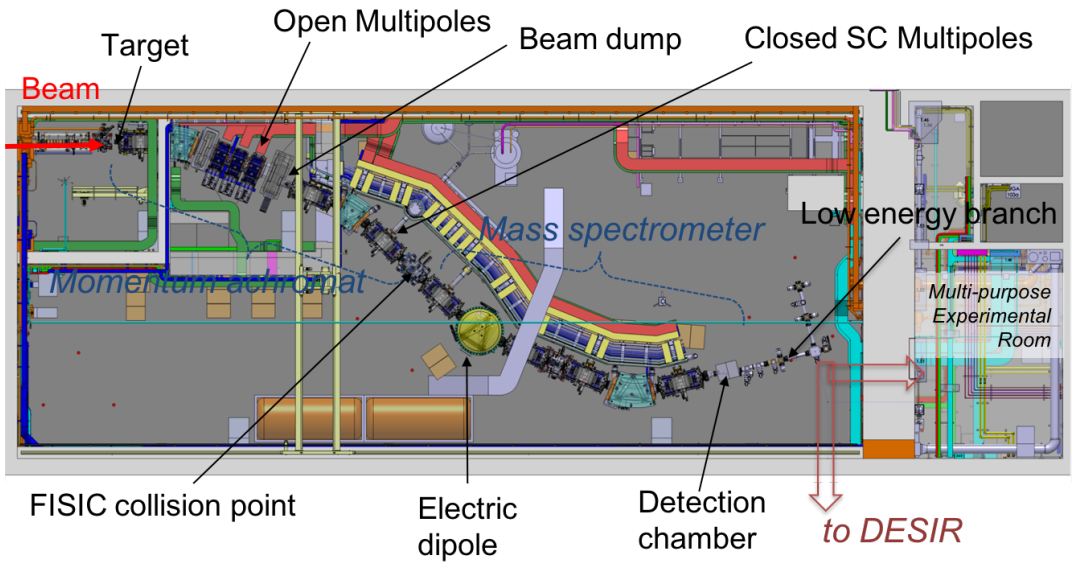

Figure 2.14: Schematic of the installation at S^3 showing the different components. At the focal plane, the S3-LEB setup and the SEASON detector installation can be implemented [62].

gamma spectroscopy (S^3-SIRIUS) [63]. S^3-LEB will be the focus of this thesis work. The S^3 will operate in converging mode for delivering ions to S^3-LEB, thereby allowing maximum transmission of all nuclei without mass selectivity.

2.3.2 S^3-LEB

The work mentioned in this thesis work is the offline commissioning tests with resonant laser ionization spectroscopy that have been performed with the S^3-LEB setup. S^3-LEB is a collaborative project with several partner institutes. This project is supported by a large international collaboration including KU Leuven (Belgium), GANIL (France), LPC Caen (France), IJCLab-Orsay (France), the University of Mainz (Germany), and the University of Jyvaskyla (Finland).

The S^3-LEB setup will make use of the in-gas laser ionization and spectroscopy (IGLIS) technique (discussed in section 2.1) in combination with an MR-TOF-MS to produce and study high-purity radioactive beams. This dedicated setup is a flexible tool for the production of high-purity radioactive ions for mass spectroscopy, laser spectroscopy, and decay spectroscopy. The main physics motivation for the S^3-LEB setup is:

- Extraction of the nuclear ground state and possible isomeric state properties of nuclei using laser spectroscopy in the neutron deficient region and the heavy regions of the nuclide chart of elements as shown in the figure 2.15. As there are no chemical processes used for the extraction of the atoms, it can be used for studying refractory elements.
- Isobaric purification and mass measurements of ions using a multi-reflection time of flight spectrometer(MR-TOF-MS)
- Coupling to the Spectroscopy Electron Alpha in Silicon bOx couNter (SEASON) detector for decay spectroscopic studies.

- Delivering beams, in the future, to the DESIR facility for high-precision measurements and collinear laser spectroscopy studies.

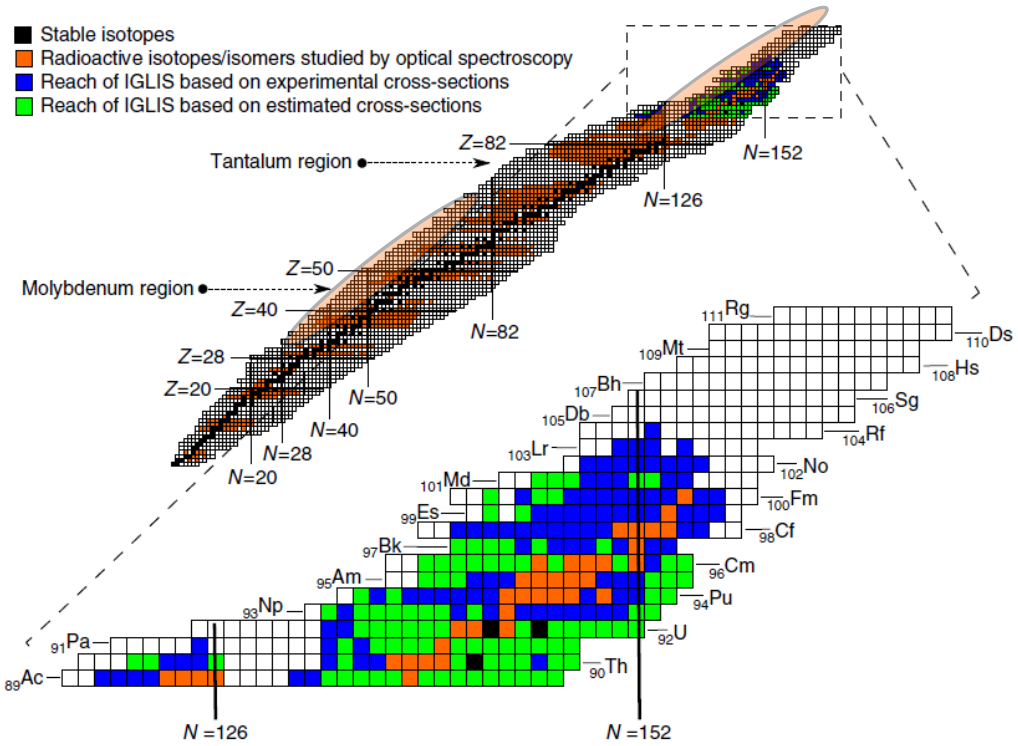

Figure 2.15: Nuclide chart showing the reach of IGLIS technique(taken from [21]).

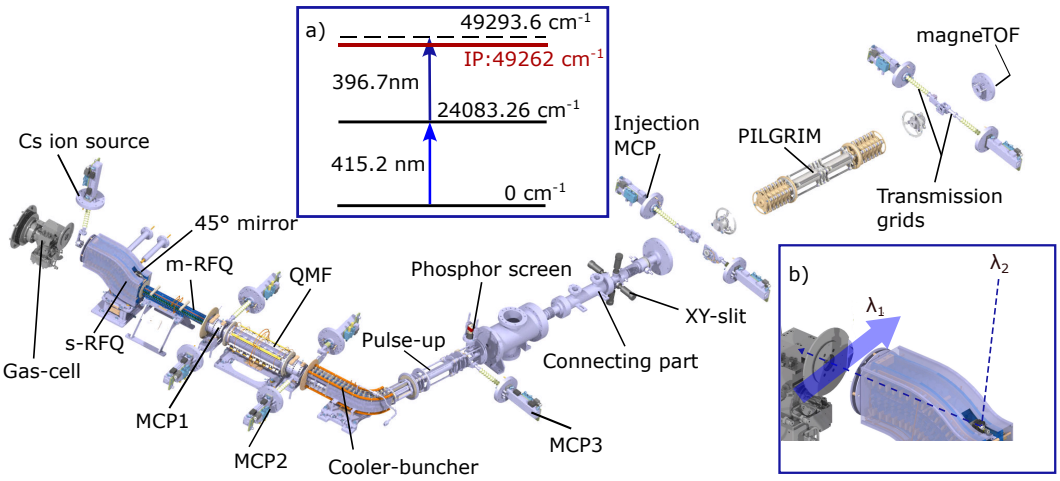

Figure 2.16: Layout of S^3-LEB setup is shown and *a*) shows the applied laser scheme for resonance ionization of the erbium atoms, *b*) zoom of the gas jet portion in the setup with λ_1 and λ_2 indicating the first step and second step laser paths.

The complete layout of the S^3-LEB in its current configuration is shown in figure 2.16. In online conditions at SPIRAL2, the ion beam produced and selected by S^3 will enter the gas cell through a titanium or Mylar entrance window of a few micrometers thickness. The gas cell will be filled with ultrapure

argon buffer gas under constant flow, reaching a pressure of 200 - 500 mbar for efficient stopping of the atoms. The entrance window will separate the vacuum region of S^3 from the higher-pressure region of the gas cell. The radioactive ions reaching the gas cell will stop in the buffer gas cell, thermalize, and neutralize in the buffer gas. The neutralized ions will then be flushed out of the gas cell along with the buffer gas to form a gas jet. The lasers will interact with the atoms either in the gas cell or in the gas jet to ionize the neutralized species with Z-selectivity via resonant laser ionization. The ions are then transported through a series of radio-frequency quadrupoles (RFQs) to detection setups such as MCPs placed at different stages of the RFQs or to an MR-TOF-MS for mass purification and mass measurements. A deflector can then bend the purified ions to future experimental setups such as the decay station, SEASON, or DESIR facility.

The main highlights of the S^3-LEB setup are its efficiency in studying nuclei of very low cross-sections owing to high-intensity primary beams available from SPIRAL2, its Z-selectivity due to resonant laser ionization technique, mass selectivity provided by the mass separator coupled to it with a mass resolving power in the order of 10^5 and its achievable spectral resolution down to the order of 200 MHz due to in-gas-jet laser-atom interaction (refer to section 2.1.2). A detailed description of each component of the S^3-LEB is given in the following subsections.

Gas cell

In S^3-LEB, the S^3 beams entering the gas cell through a thin entrance window will be stopped by collisions with the buffer gas. Since S^3 will be in converging mode for maximum transmission efficiency, the ion beam distribution will be large. To send the entire beam through, the gas cell entrance has an opening of 50 mm diameter. The S^3-LEB is currently installed with a shadow-shaped gas cell. Shadow gas cells were originally designed to separate the reaction region and ionization region and thus improve selectivity such as in the LISOL facility [6]. This gas cell has the stopping region and laser-ionization region separated with a 90° bend [6]. This separation helps in improving the laser ionization efficiency which otherwise might re-neutralize in the plasma formed in the stopping region. The initial design of the gas cell is from KU Leuven. The S^3-LEB gas cell design was adapted from [64].

The gas cell mainly has an inlet for buffer gas injection, a cell body part for stopping and thermalization of the ions, and a conical-shaped converging part for laser atom interaction and gas jet creation. The cross-section of the 3D drawing of the S^3-LEB gas cell is shown in figure 2.17. The geometry of the gas cell has been designed for maximal flow rate and minimal evacuation time of the atoms [65]. The stopped ions neutralize inside the gas cell with the electrons created in the plasma during thermalization and the neutralized atoms are flushed out along with the buffer gas through a small exit aperture. The gas cell design can have two exit aperture holes of diameters 1 mm and 1.5 mm. The cell body has an oval-cylindrical portion with a stopping region cross-section option of 30 mm by 70 mm (wide gas cell) as well as 20 mm by 60 mm (narrow gas cell) [46]. The wide gas cell will be used when S^3 is in converging mode for maximum transmission. The wide gas cell is currently installed at S^3-LEB. The narrow gas cell could be used in the high-resolution mode where

only one charge state of the ion beam is of interest is selected, however with low transmission. With the current exit aperture configuration of 1 mm, the currently installed 'wide' S^3-LEB gas cell has an average evacuation time of ≈ 600 ms. The evacuation time can further be reduced by using the narrower gas cell configuration and an exit aperture of 1.5 mm to ≈ 190 ms.

The inlet of the gas cell consists of a conical tube to feed the buffer gas to the gas cell. The injected gas then enters a chamber with an obstacle reducing its velocity and then flows through a honeycomb structured grid made of 51 tubular arrays to enable a uniform flow in the gas cell [65, 64]. The argon buffer gas is injected into the gas cell from the gas cylinder through a gas handling system that allows for purging, additional purification, and controlled flow to the gas cell. Additional purification is performed to avoid any molecule formation in the gas cell with contaminants that can reduce the ionization efficiency in the gas cell. The gas handling system consists of a purging pump, valves, a getter gas purifier model Saes PB4-MT3-R-2, a flow controller, and a pressure gauge. Figure 2.19 shows the injection system control GUI. It can be operated in manual mode as well as in injection mode where it starts with an automatic cycle of purging and then injection of the gas.

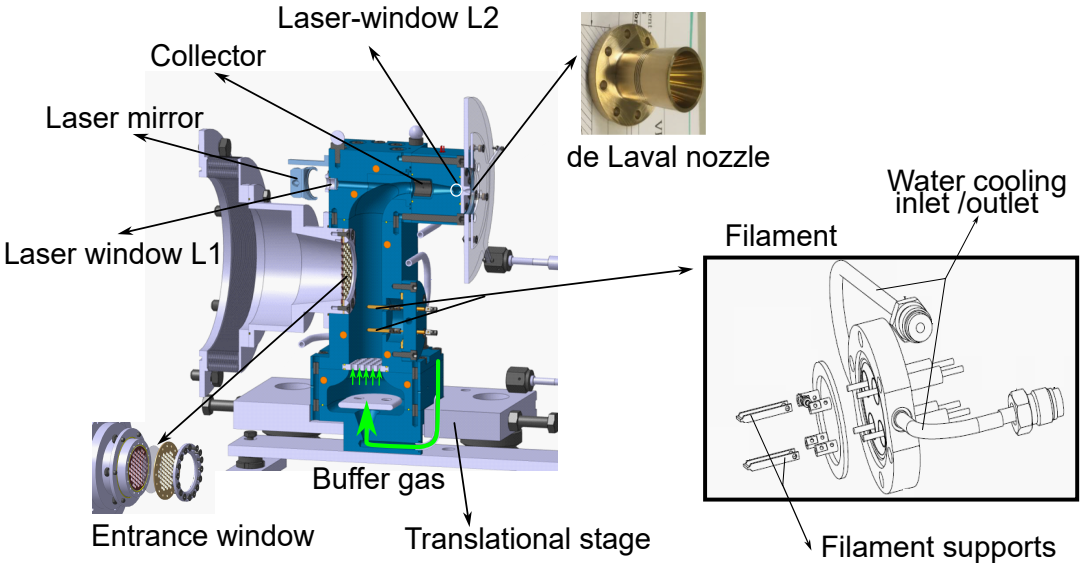

Figure 2.17: Image of the gas cell and the tantalum filament installed in the S^3-LEB setup.

The gas cell consists of two laser windows made of fused silica for the passage of laser light into the gas cell. One window allows the transport of laser light along the axis of the jet marked as L1 (see figure 2.17) and the other marked as L2 allows laser light interaction to be perpendicular to the direction of propagation of the atoms. The laser paths are shown in figure 2.18.

The gas cell contains two filament feed-throughs opposite to the entrance window side. In online conditions, these filaments are used to create additional electrons for improving the neutralization process in the gas cell. For offline measurements, these feed-throughs are used to apply resistive heating to stable or long-lived sources to create atoms. A drawing of the filament flange is shown in the inset of figure 2.17. The gas cell and the filaments are cooled by water with their inlet and outlet for the water flow circuit shown in figure 2.17. The

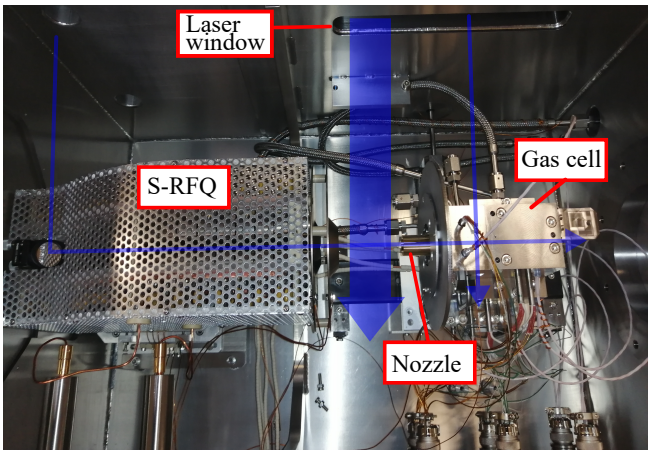

Figure 2.18: Image of the gas cell coupled to the RFQ ion guide. The arrow lines in blue shows the laser paths for in-gas cell and gas jet laser ionization.

gas cell can be baked using the heating element unit connected to it. The heating element consists of eight units whose locations are marked with the orange dots in the figure, two of them for the injection chamber, three for the gas cell body, one for the ion collection chamber, and two for the turning block. The heating elements are regulated using the MINI8 controller (Eurotherm) and can be heated up to 150 °C. The non-neutralized species after the thermalization process have to be suppressed for which two collector electrodes are installed in the gas cell before the exit. Only one collector electrode is used at a time and the other is grounded during experiments.

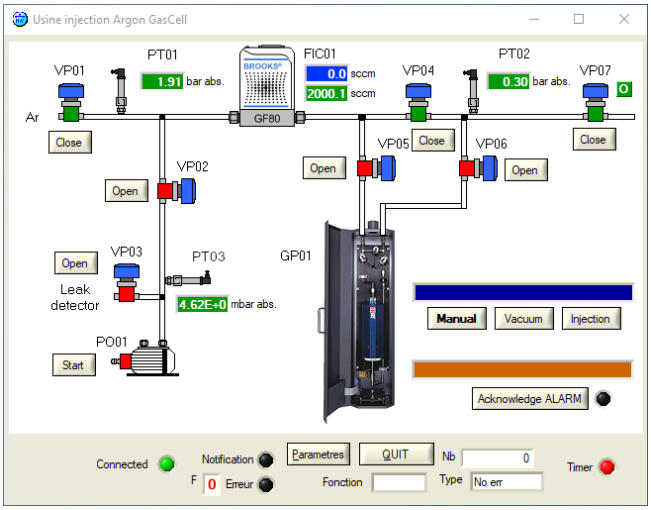

Figure 2.19: Control GUI for buffer gas injection into the gas cell. Labels: VP(1-7)- gas valves, GP- gas purifier, PT(1-2)- pressure gauge, PO-primary pump, FIC- gas flow controller.

Before the coupling of the gas cell, the RFQ units were tuned individually using a thermionic ion source [16]. The thermionic source is installed in the gas cell vacuum chamber between the gas cell exit and the first RFQ unit such that it can be inserted in/out before the ion guides for offline measurements. For this thesis work, the gas cell was commissioned and aligned to the RFQ units.

Gas cell entrance window

The window separating the S^3 side and gas cell is mounted on an adapter piece with a grid as shown in the figure 2.20. The connecting part will be coupled to the S^3 side using the bellows. The entrance windows considered for

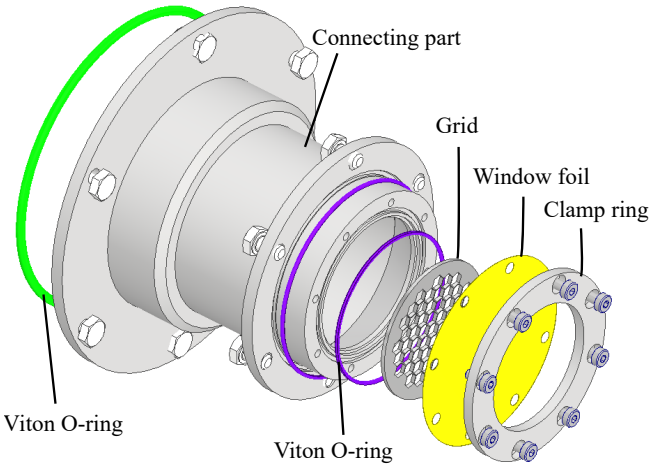

Figure 2.20: The 3-D design layout of the S^3-LEB gas cell entrance window adapter.

S^3-LEB are titanium and Mylar foils. The window material and thickness are chosen such that they should provide sufficient gas-vacuum separation as well as good ion propagation. The materials for the entrance window should be able to provide low attenuation of the S^3 beams as the ions enter the gas cell. For low Z-value materials essentially, the loss of the ion beam at the window would be less. Al would be a good choice in this aspect but it easily breaks when made thinner. The fragileness of the foils thus also needs to be considered. Ti is also a good window material due to its high heat resistance. Mylar foils can be prepared with < 1 µm thickness but it is less resistant to high temperature. Window foils of different thicknesses were tested to see if they could withstand the pressure difference between the vacuum side and buffer gas side of the gas cell. Detailed studies of the entrance windows are presented in chapter 4.5.

Gas jet

The atoms along with the buffer gas exiting from the gas cell form a homogenous supersonic gas jet with a de-Laval nozzle installed at the exit aperture of the gas cell. A de-Laval nozzle of Mach number M = 8.2 manufactured in KU Leuven is currently installed at the S^3-LEB. The nozzle design was performed by Von Kerman Institute for Fluid Dynamics (VKI, Belgium). The flow mapping of the M = 8.2 nozzle for its characterization was performed in KU-Leuven and University of Jyvaskyla with resonance ionization flow mapping and planar laser induced fluorescence method respectively [64, 65]. The jet velocity for M = 8.2 nozzle will be $\approx$ 565 m/s (see equation 2.3). For all the atoms coming out of the nozzle, to interact with the laser pulses of 10 kHz at least once, for in-gas jet laser ionization, the jet distance has to be a minimum of 50 mm. For in-gas jet laser ionization in free jet configuration (see section 2.1.2), the distance between the gas cell exit and the first RFQ has to be as minimal as possible

for maximum ion extraction efficiency. To adjust the distance between the gas cell/nozzle exit and the first RFQ, the gas cell is placed on a translational stage with a movable range of 0 - 120 mm.

For in-gas jet laser ionization and spectroscopy, the laser beam is expanded to illuminate the entire jet region. The lasers can be sent collinear/counter-propagating as well as transversal to the jet axis via the laser paths shown in figure 2.18.

The pressure in the gas cell and the background pressure in the gas cell chamber are crucial in having optimum gas jet conditions (see section 2.1.2). To ensure pressure matching between the stagnation pressure in the gas cell and the gas cell/jet chamber, efficient pumping speed has to be ensured in the gas cell chamber. For this purpose, the gas cell chamber is pumped using a GXS 450/4200 screw pump with a pumping speed of 875 l/s.

Radio frequency quadrupoles

The gas jet with the laser-produced ions, enters a series of radio-frequency quadrupole (RFQ) units to guide them to detection units and to other experimental setups. These RFQ-based ion guides will transfer the laser-produced ions from low vacuum conditions in the gas cell chamber of the order 10^{-1} - 10^{-3} mbar to a region of high vacuum of the order 10^{-7} - 10^{-8} mbar. The ion beams can be manipulated by the ion guides to have low beam emittance required for better spectral resolution. The RFQ ion guides installed at S^3-LEB in the order of propagation of the beam are the S-shaped RFQ (S-RFQ), mini-RFQ, quadrupole mass filter (QMF), and RFQ cooler-buncher (RFQ-CB). For the control and monitoring of RFQ parameters, EPICS software will be used at S^3-LEB to be compatible with S^3. However, for the initial offline commissioning tests, a CVI control system with a Python GUI was used. Figure 2.23 shows the 3-D layout of the RFQ units of S^3-LEB.

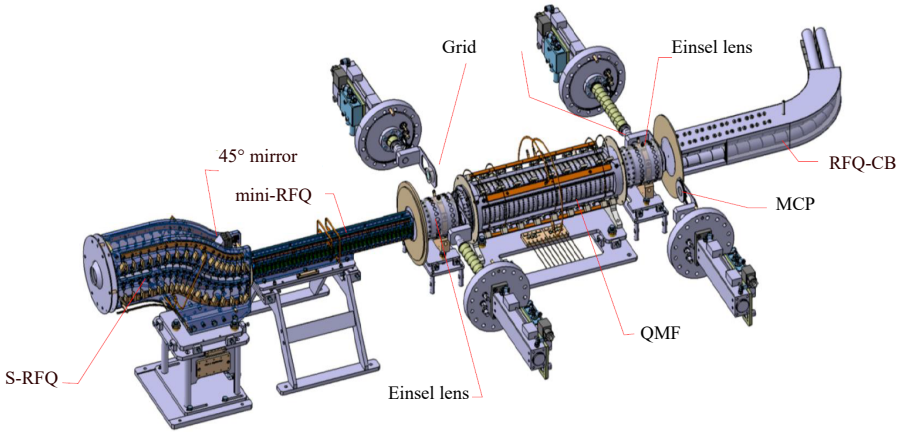

Figure 2.21: CAD drawing of the RFQ components for S^3-LEB (Drawings from LPC Caen).

The first RFQ unit is the S-RFQ which decouples the laser axis from the propagation axis of the ions in case of counter-propagating laser interaction as shown in figure 2.16. The gas cell and the S-RFQ are hosted in the same chamber with a pressure matched to the gas jet. The S-shape of the RFQ with two 45° bends is used to avoid direct pumping of the jet to the differential pumping

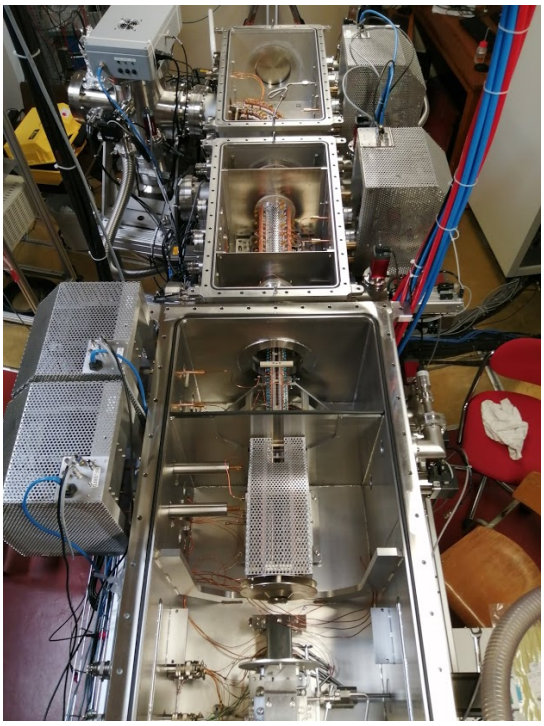

Figure 2.22: Image of coupled S^3-LEB RFQs.

diaphragm. The design is similar to the S-RFQ used in the IGLIS setup at KU Leuven [66]. At the first bend portion, a 45° laser mirror is also installed to allow laser interaction with the jet in anti-collinear geometry. The S-RFQ rods are divided into 20 segments to which DC potentials can be applied. The DC voltage gradient along the segments guides the ions through the longitudinal axis of the RFQ. DC voltages can be applied along four segments (1^{st}, 7^{th}, 14^{th}, and 19^{th}) along the direction of propagation of the ions. The DC voltage across the rest of the segments is provided through voltage dividers. The S-RFQ is operated at 500 kHz RF frequency with a maximum peak-to-peak voltage of 150 V. The RFQ rods were spaced with a radius of 9 mm with the first three RF segments at an enlarged radius according to the SIMION simulations for optimum ion transmission [67].

The mini-RFQ is housed in a chamber separated from the gas cell chamber with a differential pumping diaphragm having a small opening at its entrance and exit. Thus the purpose of mini-RFQ is to enhance differential pumping, transporting the ions from the high pressure of the gas cell chamber to the next RFQ unit which is a quadrupole mass filter (QMF). For this purpose, the mini RFQ chamber is independently pumped using a turbo pump and a GXS 160 screw pump with a pumping speed of 40 l/s. The mini-RFQ chamber is pumped to a pressure of 10^{-3} - 10^{-4} mbar. The mini-RFQ is operated at an RF frequency of 500 kHz with a peak-to-peak voltage of 35 V. It consists of 40 RF rod segments with an inner radius of 3 mm. DC voltages can be applied to the first, 20^{th}, and 39^{th} segments. DC voltages can be separately applied to each of the four rods of the 40th segment.

The QMF serves for preliminary filtering of the ions according to their charge-to-mass ratio (A/Q). The theory behind stable trajectories in QMF has been discussed in section 2.2.1. The RF rods are kept at a radius of 10 mm. It

operates at an RF peak-to-peak voltage of 700 V and a frequency of 500 kHz. The QMF has 9 segments of RF-rods with its first and 9^{th} segments acting as Brubaker lenses. Brubaker lenses are quadrupoles acting as a high pass filter with RF only field to guide the ions into the QMF and thus improve transmission. Without Brubaker lenses, there might be losses due to defocusing from the RF-DC fringing fields [68]. Segments 2-4 and 6-8 are connected together. Additional DC potential along with RF AC potential allows the QMF-RFQ to perform mass scans and act as a mass filter. It has two Einzel lenses installed before the QMF rods for axial focussing of the ions into the QMF. The QMF has two modes of operation: an ion transmission mode and a filtering mode (refer to section 2.2.1). In the transmission mode, the QMF will act as a basic ion guiding RFQ without any DC potential applied along with the RF potential. In the filtering mode, QMF acts as a mass separator with a mass resolving power $m/\Delta m > 100$. The additional DC voltage can be scanned along with the RF potential keeping their ratio constant to perform a mass scan. In the filtering mode, the mass selectivity is improved but with reduced transmission. The QMF is operated at a pumping pressure of 10^{-7} - 10^{-8} mbar.

The ions from the QMF are then sent to an RFQ-CB to improve the emittance of the ion beam and to inject the ions as bunches into PILGRIM MR-TOF-MS. The CAD drawing with the layout of the RFQ-CB is shown in figure 2.23. RFQ-CB has two sections with a 76° bend (the bend was for space considerations in S^3-LEB). The cooling section operates with a continuous flow of buffer gas like He, with a high ionization potential (26.4 eV) to minimize any exchange of charge and with low mass for cooling most of the ion species. He being inert in nature also minimizes the chances of laser-produced ions forming molecules. Compared to Ar, He would require more cooling time. The ions are slowed down by collisions with the He atoms reducing their axial velocity and thus cooling them. Once the ions are cooled, they are trapped in an electric potential well by creating radial minima using RF and axial minima using the DC voltages applied to a set of DC electrode plates known as bunching voltages (VB). The RFQ-CB for the S^3-LEB is operated at an RF voltage of 1000 V at a frequency of 1000 kHz. After the required bunching time, the ion bunches are released by switching the potential on the DC segments referred to as extraction voltages (VE). The switching of voltages between bunching and extraction is performed at specific time intervals called bunching cycles. Figure 2.26 shows the ion extraction in an RFQ-CB. The extraction ramp contributes to the energy spread of the ions as well as to the spatial dispersion of the ion bunches.

The bunched ion beams are reaccelerated using a Pulse-Up unit for their injection into PILGRIM. The Pulse-Up unit consists of a pulse-up lens followed by a cylindrical electrode tube to which acceleration voltages can be applied. There are four deflector electrodes installed after the pulse−up unit for correcting any spatial drift along the XY plane. The pulse-up lens voltage applied is -180 V. The ion bunches are accelerated to $\approx$ 3 keV. A high-voltage switch is used to first apply the potential of the electrode to roughly -1.5 kV as the ion enters the electrode tube and then switch it to +1.5 kV after a predefined time delay pushing the ion bunches out of the pulse up with a total energy of roughly 3 keV. The acceleration field and the spatial distribution of the ejected bunches play a crucial role in the initial time of flight width of the ions thereby

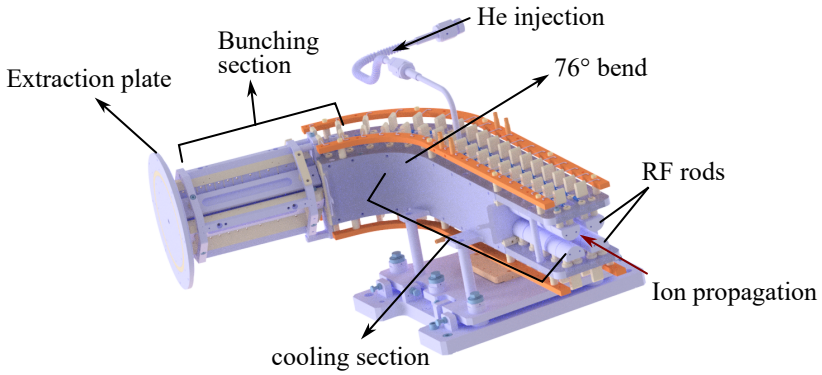

Figure 2.23: CAD drawing of the S^3-LEB cooler buncher unit (Drawings from LPC Caen).

affecting the resolving power of PILGRIM.

PILGRIM

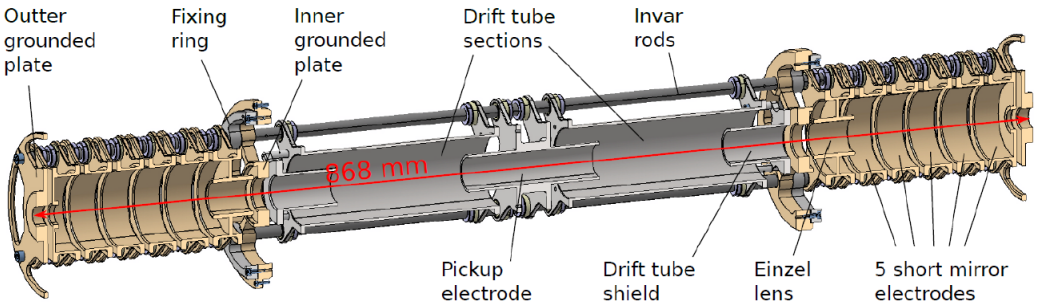

Figure 2.24: Layout of PILGRIM multi-reflection time of flight mass spectrometer.

Figure 2.25: PILGRIM coupled to the RFQs

At the end of S^3-LEB, the MR-TOF-MS named PILGRIM is installed for isobaric purification of the ion contaminants that might tag along with the laser-produced ions and for mass measurement studies. The initial design of the MR-TOF-MS was from Giessen University. The bunched ion after reacceleration

using Pulse-Up unit can be trapped in PILGRIM and extracted using the in-trap lift method discussed in section 2.2.2.

PILGRIM is housed in three sections of a vacuum chamber pumped with turbomolecular pumps to achieve the high vacuum conditions of 10^{-8} - 10^{-9} mbar (See figure 2.25). PILGRIM has five mirror electrodes and three Einzel lenses supplied with high voltage from ISEG (See figure 2.24). The pulse drift tube (PDT) of PILGRIM has three sections referred to as DT1, 2, and 3 at the entrance, center, and exit of the PDT. All of the drift tube sections can be individually switched using high-voltage switches controlled with TTL signals from an external pulse generator. The bunches from RFQ CB follow a cooling and extraction cycle of 20 Hz. At the beginning of each bunch cycle, a source pulse of 50 ms period is started. A pulse delay is then defined as a trigger for the acquisition using FASTER in PILGRIM [69]. The pulse delay is the same as the trapping time for a given number of turns. The PDT implements ion trapping. Figure 2.26 shows the schematic of ion bunching, injection, and extraction from PDT. At the falling edge of the PDT pulse, the potential of the drift tube is switched from 1.2 keV to ground for trapping the ions. On the rising edge of the pulse, the potential is switched back to 3 keV, and the ions are ejected.

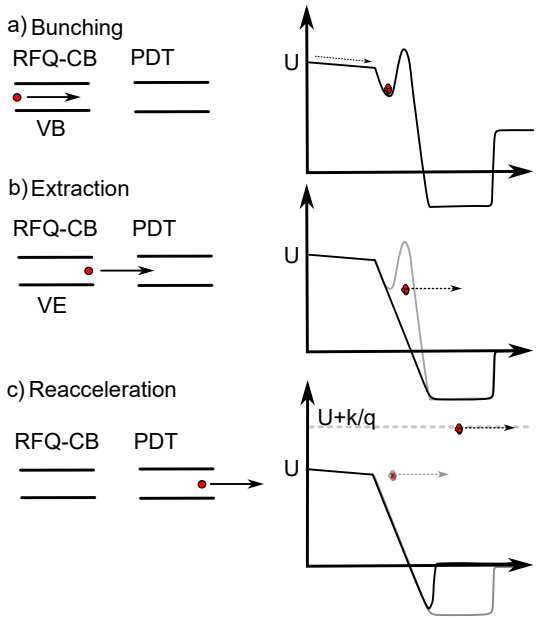

Figure 2.26: Schematic showing the a) cooling and bunching of the ions b) extraction and injection of the bunches to pulse drift tube (PDT) and c) ejection of the ions from PDT.

For the extraction of contaminants, extra pulses are applied individually to DT1, 2, or/and DT3. This will allow the release of the unwanted ions from the injection side of PILGRIM after a specific number of turns without disturbing the ions of interest. PILGRIM design, simulation, and previous tests are reported in [8, 70]. PILGRIM is currently coupled to the pulse up unit via a connecting rod at S^3-LEB and the tests and results with laser-produced ions from the gas jet are discussed in this thesis work in section 4.3. In order to perform the spatial profiling of injected beams, a set of XY-slits is installed in front of PILGRIM.

Deflector

A deflector will be additionally installed between the Pulse-UP unit and PILGRIM to inject the purified RIBS from the RFQ-CB or beams exiting from PILGRIM spectrometer to be sent to other detection setups. The future layout for the deflector is shown in figure 2.27. It will be a multi-directional 90° electrostatic deflector. It will have focussing electrodes and bending electrodes in a geometric configuration aiming for minimum beam divergence and time of flight spread. The design and simulation work for the geometric optimization of the deflector is ongoing.

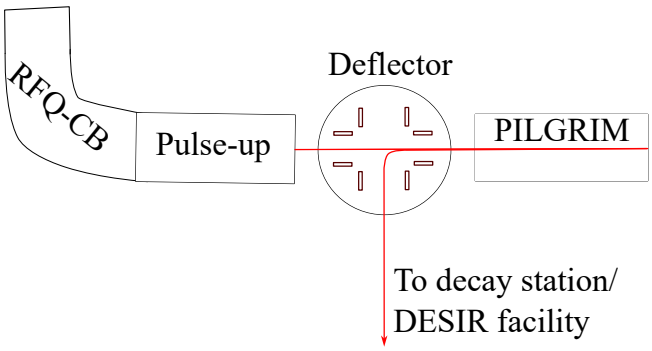

Figure 2.27: Future layout of the planned deflector at S^3-LEB facility.

Detector setups

Charged particle detection is performed with microchannel plates (MCPs), Faraday cups, and a MagneToF-Mini detector installed at different stages of the S^3-LEB. There are three sections for charged particle detection. Figure 2.28 shows a schematic layout of the S^3-LEB showing the vacuum chamber sections and the positioning of different detector systems. MCP 1 and MCP 2 detect the ion counts after the mini-RFQ and QMF. MCP 1 and MCP 2 are biased to -3600 V when in operation. A voltage of -100 V is applied to the 10% transmission grids in front of them. The accelerated ion bunches can be monitored using MCP 3 after the Pulse-Up unit. MCP 3 has two attenuation grids in front of them with 10% transmission each. The first grid is grounded. A 45° mirror can be inserted in the transmission path after the MCP 3 detection stage to record the ion bunch images in a CCD camera, reflecting light from a phosphor screen for spatial profiling. Before PILGRIM, an injector MCP (inj-MCP) is installed. The schematic of the detection after pulse up is shown in figure 2.29. A mini-magneToF is installed for counting ions after PILGRIM with two movable attenuation grids of 10% transmission each. Previously an extraction MCP was installed instead of the MagneToF-Mini and the characterization work of RFQ-CB was performed with detection using this MCP.

Dedicated detector setups with a sensitivity of a few particles per second will be required to explore nuclei in the N = Z region and superheavy regions. The ions from PILGRIM can be implanted in a thin carbon foil surrounded by a segmented silicon array for decay measurements. As a future possibility, Spectroscopy Electron Alpha in Silicon bOx couNter (SEASON) detector, under construction at IRFU (Saclay) can be coupled to the S^3-LEB setup [9]. Simple ion counting as well as decay spectroscopy through electron and α-radiation

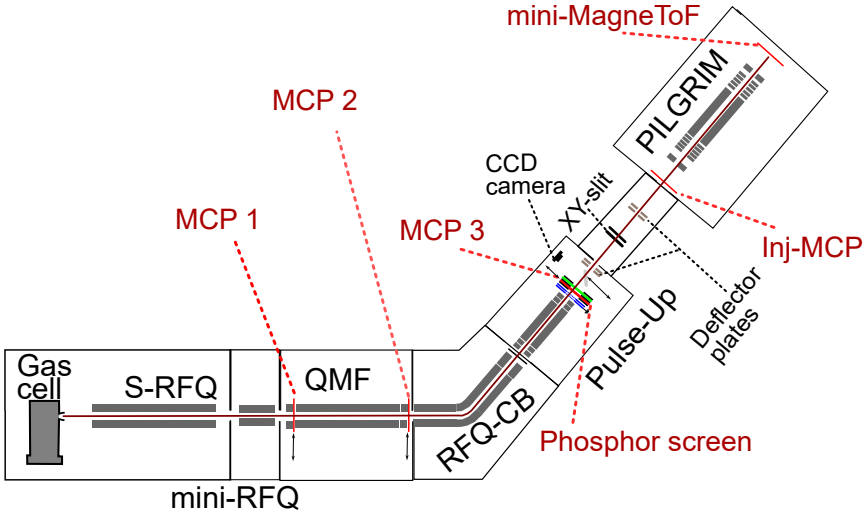

Figure 2.28: Schematic layout of S^3-LEB showing the vacuum sections and detector stages

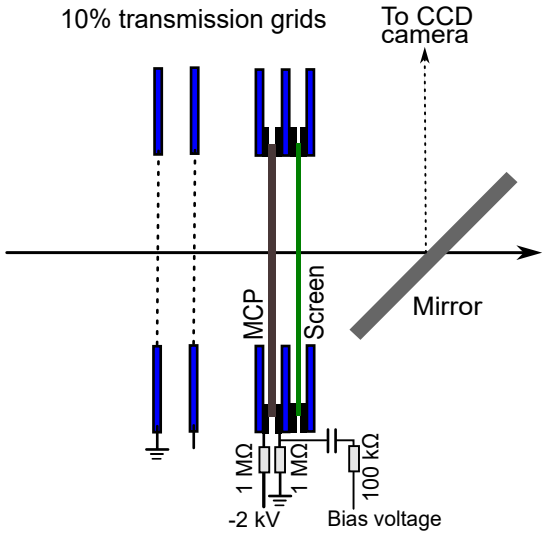

Figure 2.29: Schematic layout of MCP 3 detection stage with the phosphor screen

will be handled by a new generation of electronics with automatic gain switching. The detector will aim for high efficiency and resolution with a low energy threshold. Two germanium detectors can be integrated for registering coincident γ-rays. The addition of a tape station for β-decay studies is also foreseen. However, SEASON is not in the scope of this thesis work. DESIR facility is also in the future plan for high-precision studies of the radioactive ion beams. It will be dedicated to studies of very low-energy beams with traps, laser spectroscopy, and decay spectroscopy.

CHAPTER 3

Laser systems and frequency conversion units for S^3-LEB

For optimum ionization efficiency and the best spectral resolution, the laser systems to be used as ion sources need to be flexible and powerful. Tunable pulsed dye lasers and solid-state Ti: sapphire lasers have been commonly used for resonant laser ionization and spectroscopic purposes. S^3-LEB aims to use both Ti: sapphire and dye laser systems to cover all possible wavelength ranges. Figure 3.1 shows the wavelengths covered by available Dye and Ti: sapphire lasers. The Ti: sapphire laser and the dye laser will act complementary to each other and a comparison of the performance of these laser systems for S^3 can be found in [71].

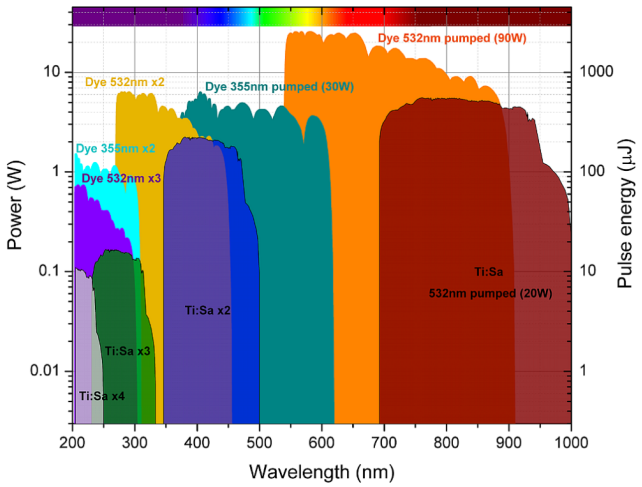

Figure 3.1: Wavelengths covered and available maximum output power with Dye and Ti: sapphire lasers (picture is taken from [71]).

The laser prerequisites for spectroscopic investigations are their pulse energy, tunability, and narrow linewidth operation. For laser ionization inside a gas cell, the atoms move slowly at the rate of a few m/s and hence require lower repetition rate lasers of 200 - 300 Hz for efficient ionization of the atoms. Also, due to the collisional broadening in the gas cell at high pressures, the spectral resolution is limited to a few GHz. Hence broadband lasers of a few GHz linewidth can be

used for gas cell ionization. However, for gas jet ionization, the atoms move at velocities of 500 - 600 m/s and hence require high repetition rate lasers of 10 - 15 kHz for optimum temporal overlap. The reduced temperature and pressure in the gas jet provide spectral resolution in the range of a few hundred MHz and hence the laser linewidth needs to be less than 100 MHz. At the LISOL facility in Louvain-la-Neuve, as a joint collaboration between the University of Mainz and GANIL, experiments were done using a gas cell-based laser ion source to compare a 200 Hz LISOL dye laser system pumped by 15ns pulsed excimer laser and a 10 kHz Ti: sapphire laser system pumped by 100- 200 ns pulsed Nd: YAG laser [72] in gas cell and in-gas jet ionization. The laser systems showed similar performances with regard to ionization efficiency in the gas cell. Thus for in-gas cell and in-gas jet ionization, the Ti: sapphire laser systems are now operated at a 10 kHz repetition rate.

For the commissioning of S^3-LEB, only the Ti: sapphire lasers will be installed. This chapter presents the Ti: sapphire laser systems installed and characterized for S^3-LEB.

3.1 Ti: sapphire laser system for S^3-LEB

The laser system consists of two or three broadband (BB) cavities for in-gas cell laser spectroscopy and a narrowband (NB) cavity for in-gas jet laser spectroscopy pumped by a frequency-doubled Nd: YAG laser. Figure 3.2 shows the layout of the Ti: sapphire laser systems that will be installed at S^3-LEB. The Ti: sapphire lasers were developed at the Johannes Gutenburg-Universität, Mainz for ultra-trace analysis application [73]. Improved versions of the then-developed BB Ti: sapphire system were made over the years with better pump geometry, output power, and frequency conversion techniques [26, 74]. Single mode (SM) or NB Ti: sapphire lasers were also developed over the years for high-resolution laser spectroscopy applications [75, 76, 77]. An injection-locked laser provides a narrow linewidth of a few tens of MHz and their use was reported in [28, 78]. The Ti: sapphire laser system for the S^3-LEB are upgraded

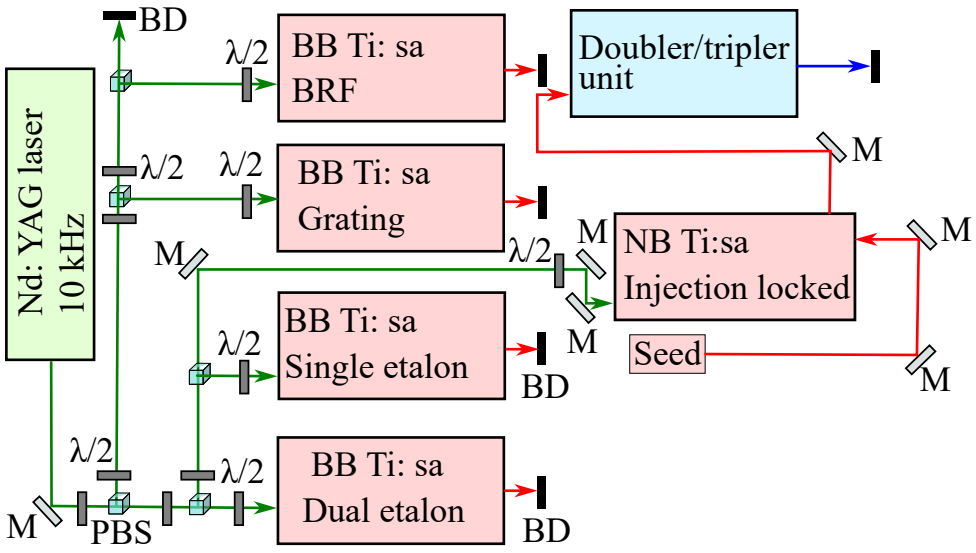

Figure 3.2: Ti: sapphire laser systems for S^3-LEB. Labels: PBS - polarizing beam splitter cube, $\lambda/2$ - half wave plate, M - mirror, BD - beam dump

versions delivered from Institut für Physik (JGU, Mainz), TRILIS (TRIUMF), and IGISOL (University of Jyvaskyla). These laser systems were first commissioned at GISELE lab with laser ionization of erbium in an atomic beam unit under a vacuum of 10^{-8} mbar and this work has been published in [67]. Further developments on the Ti: sapphire laser systems are ongoing at the GISELE lab. Installation and commissioning of a new injection-locked Ti: sapphire system from Mainz is in progress. This laser system will use a single-mode (SM) continuous wave (CW) Ti: sapphire laser system for seeding and its development work is mentioned in the following sections. Dye laser installation is planned in the future and preparation of the laser room for the dye system is ongoing. The preparation of the laser room for Ti: sapphire lasers at S^3 is almost complete. The different Ti: sapphire laser systems currently installed for S^3-LEB are:

Broad band (BB) Ti: sapphire laser

This laser utilizes a configuration with a Z-shaped resonator. It uses a 20 mm Ti: sapphire crystal between two curved mirrors (CM) at a folding angle of 17.5°. The cavity is closed using a high-reflecting (HR) mirror on one end and a partially reflecting mirror acting as an output coupler (OC) on the other end. It is pumped using a 120 ns (FWHM) pulsed 532 nm laser with a repetition rate of 10 kHz at 10 - 20 W. The pump beam is focussed into the Ti: sapphire crystal using a 75 mm focussing lens. The Ti: sapphire crystal is water-cooled to avoid thermal lensing effects. The resulting Ti: sapphire laser has an output pulse-time width (FWHM) $\approx$ 35 - 50 ns and is shown to have an average power of up to 3W for 12 W pump power at the maximum of the gain profile. The wavelength tunability of the laser is a crucial requirement when broad-band scanning is required and for obtaining resonance spectra. It depends on the mirror sets and frequency-selective elements in the case of Ti: sapphire lasers. Layertec mirror sets SP - 0, 1, 2, 3, and 4 sets are commonly used. The SP-0 set has a coating in the broadband range covering 650 - 1040 nm. The SP- 1, 2, 3, and 4 sets cover 655 - 755 nm, 780 - 850 nm, 840 - 940 nm and 920 - 1000 nm respectively. Mirror sets alone cannot provide the wavelength selection required for laser spectroscopy and other frequency selective elements are used. The frequency selection in BB Ti: sapphire cavities is performed using a birefringent (BRF) filter and etalons (E) in the cavity. The working principle of these elements has been presented in section 1.3. Based on frequency selection broadband Ti: sapphire laser systems are classified into BRF, single etalon, and dual etalon systems. The BRF laser systems operate in a fixed range with wavelength scanning possible over $\approx$ 10 nm [76]. The birefringent filter used in the BB system is made of parallelly spaced four plates with varying thicknesses to achieve a wider tuning range (determined by the thinnest plate) and better selectivity (determined by the thickest plate).

A single-etalon Ti: sapphire laser system has an etalon in addition to the BRF filter for finer wavelength selection (see figure 3.3). A thin solid etalon is installed in the system resulting in a line width FWHM = 5 GHz. The thin etalon is motorized and continuous tuning is possible remotely by changing the etalon angle to the incident light. Single etalon Ti: sapphire lasers can be used for resonance ionization scheme developments and excitation/ionization step lasers in BB spectroscopic applications. Piezo-actuated air-spaced etalons can also be used instead of solid etalons for comparatively stable power and

stable operation. For air-spaced etalons, the length between air-spaced etalons is adjusted by the application of voltage to a piezo-actuator for tuning the wavelength of the laser system [18].

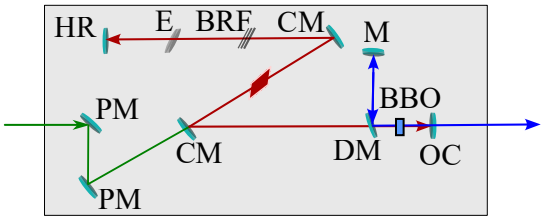

Figure 3.3: BB Ti: sapphire laser with a single etalon. Labels: PM - pump mirror, CM - curved mirror, HR - high reflecting mirror, OC - output coupler, E - etalon, BRF - birefringent filter, BBO- doubling crystal, DM - dichroic mirror, M- mirror

A dual-etalon Ti: sapphire laser system uses a combination of thin and thick etalon allowing even fewer laser modes to survive in the cavity and thus a narrower linewidth (see figure 3.4). A thin etalon of 0.3 mm and a thick etalon of 6 mm are installed in the current dual etalon cavity commissioned for S^3-LEB. This gives the dual etalon to operate with a linewidth of 1 - 2 GHz. Both the etalons are motorized. For tuning the dual etalon laser, the thick etalon angle is scanned. To maintain the optimum linewidth while scanning, the thin etalon angle needs to be adjusted (to be in the center of its transmission peak) in sync with the thick etalon angle to guarantee mode hop-free tuning. This gives a two-dimensional stable region of operation for the thick etalon and thin etalon motor positions for wavelength tuning(can be found in detail in [76]). The motor positions of the thin etalon are controlled to obtain the optimum line width, using a closed loop based on a calibration performed prior to the measurement. The thick etalons motors are tuned to obtain the desired wavelength.

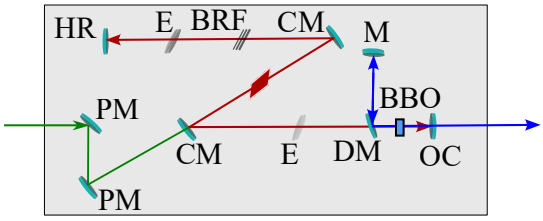

Figure 3.4: BB Ti: sapphire laser with dual etalon. Labels: PM - pump mirror, CM - curved mirror, HR - high reflecting mirror, OC - output coupler, E - etalon, BRF - birefringent filter, BBO- doubling crystal, DM - dichroic mirror, M - mirror

Grating Ti: sapphire laser

The Grating Ti: sapphire laser system is used for wide continuous wavelength tuning and is required for laser ionization scheme search. It has the same configuration as that of the BRF Ti: sapphire cavity except for the high-reflecting mirror. Here the HR mirror is replaced by a diffraction grating in the Littrow configuration [79] (see figure 3.5). For tuning the wavelength, the

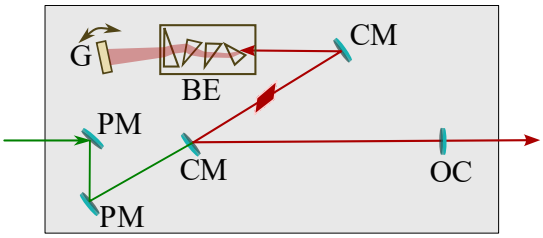

Figure 3.5: BB Ti: sapphire laser with grating. Labels: PM - pump mirror, CM - curved mirror, OC - output coupler, G - grating, BE - beam expanding prisms

grating position mounted on a rotational stage is scanned remotely. The change in the orientation of the grating adjusts the wavelength according to the grating equation for first-order diffraction:

$$2d \sin\theta = \lambda \tag{3.1}$$

where θ is the angle of the rotation of the grating, d is the groove spacing of the grating and λ is the wavelength of the reflected light. Here the linewidth of the laser is determined by the groove spacing and number of grooves in the grating. The resolving power R is related to the groove density N as $R = \lambda/\delta\lambda = mN$. In order to illuminate the entire surface of the grating, the resonating light is expanded by a factor of 17 before the grating using a set of four prism expanders. Currently, a gold-plated grating is installed with Soloist Aerotech rotational motor control providing linewidth in the range of 2 - 7 GHz with tuning capability over 150 nm [16].

Injection locked Ti: sapphire laser

The injection-locked cavity follows a bow-tie resonator geometry such that the light passes twice through the Ti: sapphire crystal in one round trip (see figure 3.6). The crystal length and the folding angle are similar to the BB laser system. The cavity length is designed such that a single round trip length in this cavity is roughly half the round trip in the BB cavities. Thus the pulse duration and buildup time remain comparable to the BB cavities [74]. Here, the Ti: sapphire crystal is water-cooled with an additional option of Peltier cooling. The Ti: sapphire crystal is pumped using a pulsed 532 nm laser of 10 - 15 W. The laser system operates on the principle of pulsed amplification of a narrow linewidth continuous wave laser known as the seed laser. The seed laser can be external cavity diode lasers or SM CW Ti: sapphire laser or dye lasers. The amplifier bow-tie cavity allows several round trips and the multifold amplification of the few mW CW seed input. The resonator cavity is actively locked to the seed laser using feedback control electronics. The resonator length is adjusted by controlling a piezo-actuated cavity mirror for locking the cavity. Thus injection-locked cavity gives several kW of power per pulse and a narrow linewidth of a few tens of MHz.

Frequency conversion units

The frequency conversion units use non-linear optical crystals for the second and third harmonic generation and frequency mixing of the Ti: sapphire output.

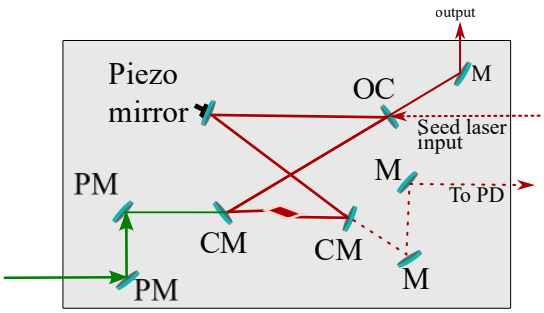

Figure 3.6: SM Ti: sapphire laser cavity. Labels: PM - pump mirror, CM - curved mirror, OC - output coupler, M - mirror, PD - photodiode

The frequency conversion units mainly include frequency doubling and tripling units. External doubling and tripling unit for S^3-LEB allows only a single pass of the fundamental light with a maximum conversion efficiency of 50%. In the BB cavities and in the new injection-locked cavity from Mainz, intra-cavity doubling is possible giving increased second harmonic output power and improving the SH light beam spot quality compared to external cavity doubling. The intra-cavity doubling adds the etalon effect of the BBO crystal which can introduce wavelength instabilities. The layout of the external doubling/tripling unit used at S^3-LEB is shown in figure 3.7. It uses the same layout as in [76]. The fundamental light is sent through BBO crystals for the second harmonic generation or for frequent mixing in the third harmonic generation. The second harmonic beam is passed through a focussing lens (L) and dichroic mirrors (DM) to obtain a parallel circular beam shape separated from the fundamental light. The half-wave ($\lambda/2$) plate can alter the polarization direction of the blue light. Doubled light is superimposed with the primary red/IR light to generate the third harmonic. The crystal angle is tuned until the phase-matching condition is satisfied. The principle of frequency conversion based on nonlinear optics is explained in section 1.3.

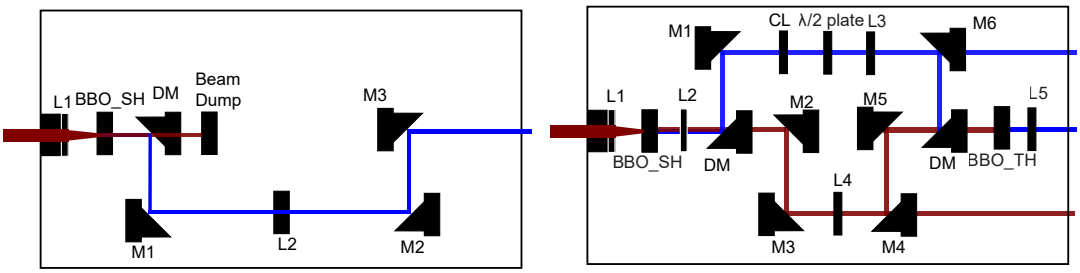

Figure 3.7: Schematic diagram of the external frequency doubling/tripling unit. The left image shows the doubling configuration and the right shows the tripling configuration. Labels: DM - dichroic mirror, M - reflecting mirror, L - lens, BBO - beta barium borate crystals for second (SH) and third harmonic (TH) generation, $\lambda/2$ - half-wave plate, CL - cylindrical lens.

Laser monitoring and control

For optimum ionization efficiency, another prerequisite for the lasers is the spatial and temporal overlap of the laser pulses used in the resonance ionization

scheme. Spatial overlap can be achieved using mirror optics and beam mergers/splitters. For temporal overlap of pulses, Pockel cells can be added in the resonator cavities. The high voltage applied to the Pockel cell will introduce losses in the cavity thereby restricting the cavity from lasing. High voltage can be switched off after the required delay time allowing the cavity to restart lasing. Thus temporal overlap by pulse synchronization can be performed [74]. However, for the offline commissioning tests, Pockels cells were not used. As the lasers were located more or less close to the laser table, slight adjustments of the pump power distribution and pump focussing in the Ti:sa crystal were sufficient for the temporal adjustments of the laser pulses. For monitoring the laser pulses the reflected light from the BRF plates or a leak out from the cavity end mirror is coupled to a fiber to send the light signal to a switch box. The switch box splits 10% of the light signal to be sent to a photodiode and the rest is sent to the wavemeter.

The laser wavelength can be measured using HighFinesse WS6 or WS7 wavemeters. The laser powers were measured using Coherent PM 100-19C, Coherent PM-10, and Thorlabs S410C power sensors. For remote monitoring and controlling of the laser systems and devices, the LabVIEW environment was used. EPICS control system will replace the LabVIEW environment in the future to be compatible with the S^3 system. The LabVIEW drivers run on the same PC to which the wavemeters are connected. The driver can take the wavemeter reading from the wavemeter software and allow the averaging of values and calculation of uncertainties during data collection. Wavelength regulation is performed for fixed wavelengths by actively adjusting the angle of the etalon as the wavelength drifts from the target wavelength. For the injection-locked system, wavelength regulation is performed by regulating the seed laser wavelength using a proportional control system regulating the voltage applied to the piezo actuator of the seed laser grating. This is the case when the seed laser is a grating-based external cavity diode laser. Laser powers can also be monitored using the LabVIEW program.

3.2 Ti:sa laser installation at LPC Caen

For the offline commissioning of S^3-LEB, Ti: sapphire-based laser systems were set up at LPC Caen. The layout of the laser setup for S^3-LEB installed at LPC Caen is shown in figure 3.8. The laser table is mainly composed of a pump laser, Ti: sapphire lasers, frequency conversion units, and monitoring and control systems. A pulsed Nd: YAG laser Amplitude Model MESA 532-60-M of 532 nm output wavelength with a repetition rate of 10 kHz was used to pump three Ti: sapphire lasers. The laser pulses were synchronized using an external 10 kHz trigger from a function generator. The Nd: YAG laser is operated at a maximum current of 37 A giving an average output laser power of 60 W (measured using PM100-19C) and a pulse width of FWHM = 120 ns. The pump power was distributed among the Ti: sapphire lasers using polarising beam splitter cubes (PBS) and half-wave plates as shown in the figure 3.8.

The Ti: sapphire lasers included two BB cavities and an injection-locked Ti: sapphire laser seeded with an external cavity diode laser. One of the BB lasers was installed with a dual etalon assembly for finer wavelength selection [76] and the other one with a single etalon assembly. The former gave a line

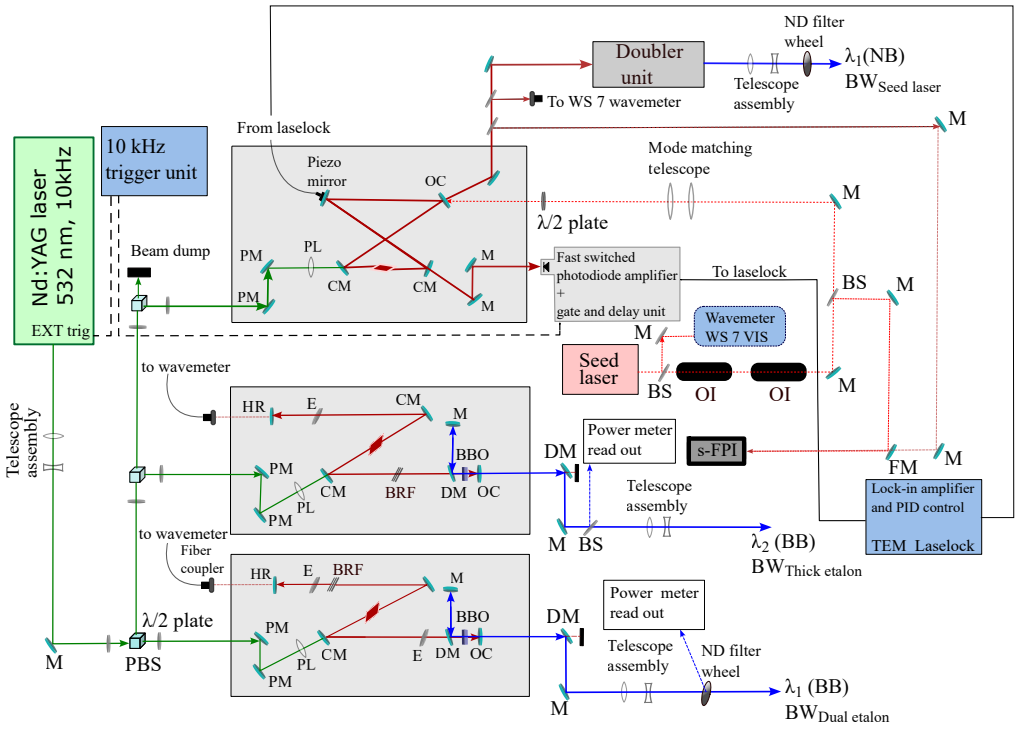

Figure 3.8: Layout of the laser table at LPC Caen is shown. Labels: PM -pump mirror, PL - pump lens, CM - curved mirror, HR - high reflector/end mirror, OC - output coupler mirror, M - guiding mirrors, E - etalon, PBS - polarising beam splitter cubes, $\lambda/2$ plate - half-wave plate, OI - optical isolator, DM - dichroic mirror, BS- beam sampler, BBO - beta barium borate doubling crystal.

width of average FWHM = 1.8 - 2 GHz fundamental and the latter gave a fundamental linewidth of average FWHM = 5 GHz measured using the High Finesse WS7 wavemeter. For the dual etalon laser, the thick etalon of 6 mm was tuned to obtain the desired wavelength while the thin etalon of 0.3 mm was adjusted to keep a constant linewidth and power. Synchronized movement of the etalons was performed remotely using a closed loop configuration for thin etalon following a calibration curve and an open loop configuration for thick etalon with LabView. For the single etalon cavity, the thick etalon stepper motor was operated in an open control loop configuration. Both z-geometry cavities were frequency doubled internally using BBO crystals. The BBO crystal was installed in between the CM and OC (refer to figure 3.8). A dichroic mirror and reflection mirror were also set up in the cavity to feed the reflected doubled light back to the output.

Injection locked cavity characterization

The injection-locked cavity was pumped by the same Nd: YAG laser for pulsed operation and higher power. The seed laser, which is an external cavity diode laser (ECDL), was injected into the cavity such that the Ti: sapphire amplifier cavity would follow seed laser modes. The ECDL was a grating tunable single-mode diode laser of Model Toptica DL100. A lens telescope system was installed prior to the injection of the seed into the amplifier cavity to overlap

the mode diameter of the ECDL output to the TEM_{00} mode of the cavity for the optimum injection efficiency. BB SP-0 mirror sets were installed in the amplifier cavity. For cavity stabilization, a TEM Messtechnik lock-in amplifier was used to control the cavity length by providing HV control signals to the piezo-actuated mirror of the cavity. The input signal for the LaseLock was the transmission of the seed laser through one of the curved mirrors in the cavity using a photodiode attached to the preamplifier /gate box. In order to avoid saturation of the photodiode due to the 10 kHz pump pulses, a fast-switching amplifier box is used to switch down the amplifier every time the pump pulse is triggered. The performance of the injection-locked cavity is sensitive to the environment and hence locking electronics is required. For this purpose, the signal from the amplifier box is sent to a preamplifier unit of TEM Messtechnik and then to the Laselock unit. The LaseLock generates a proportional-integral-derivative (PID) control signal for adjusting the cavity length to match the seed laser modes. The Lock-in amplifier of the LaseLock unit generates a dithering signal and multiplies it with the detected input signal with a phase difference to generate an integral signal that can average out the noise contributions from the detected signal. The first derivative of this signal is then used to generate an error signal which is used by a PID control loop to regulate the amplifier cavity length. This allows the stable locking of the amplifier cavity modes to the seed laser modes. Full commissioning of the injection-locked cavity is reported in [80]. The injection-locked cavity locked to the seed wavelength can be seen in figure 3.9 showing the interferometer transmission pattern from HighFinesse wavemeter WS7. Signal 2 (red) and 3 (green) shows the transmission from the injection-locked laser and the ECDL respectively. The wavemeter readings show that the injection-locked laser modes are following the seed laser modes.

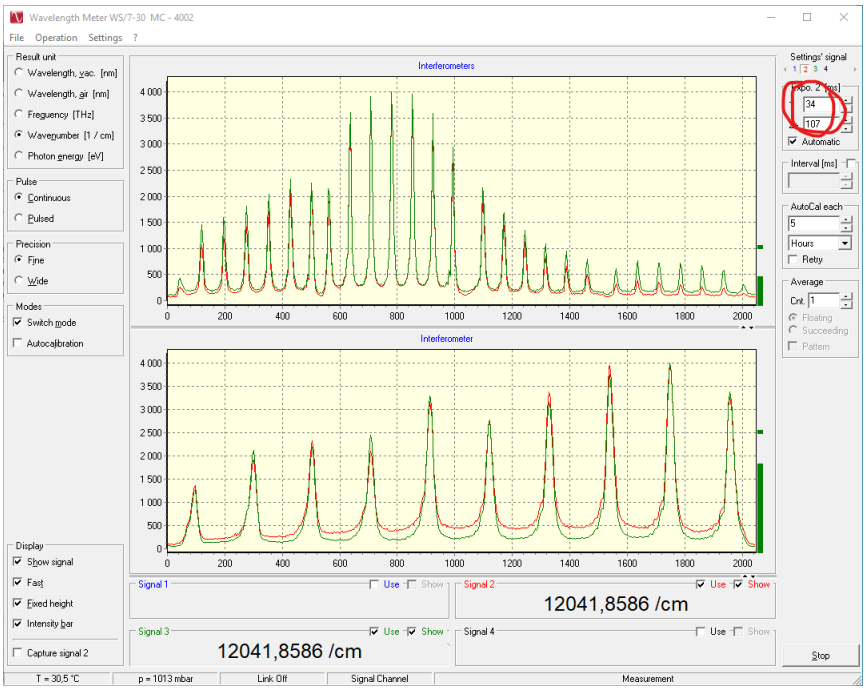

Figure 3.9: Wavemeter signals of the seed laser (green) and injection-locked laser (red) recorded with HighFinesse WS7 wavemeter.

The injection-locked laser output was then frequency doubled externally

using the doubler unit (refer to section 3.1). The doubler unit consisted of a BBO crystal with an operating center wavelength of 850 nm. Pick-ups of the fundamental laser light from all three lasers were used for pulse, wavelength, and power monitoring (refer to section 3.1). Figure 3.10 shows the pulse signals from the Ti: sapphire outputs (shown by oscilloscope channels 2, 3, and 4) temporally overlapped. Channel (yellow) 1 shows the Nd: YAG pulse signal with FWHM $\approx$ 120 ns and earlier than the Ti: sapphire output pulses. The ringing noise in the green channel is an artifact of some electronic noise coupling to the channel. The signals from channels 2 (cyan)and 3 (magenta) show small sids bumps which are residual green light leaking into the photodiodes.

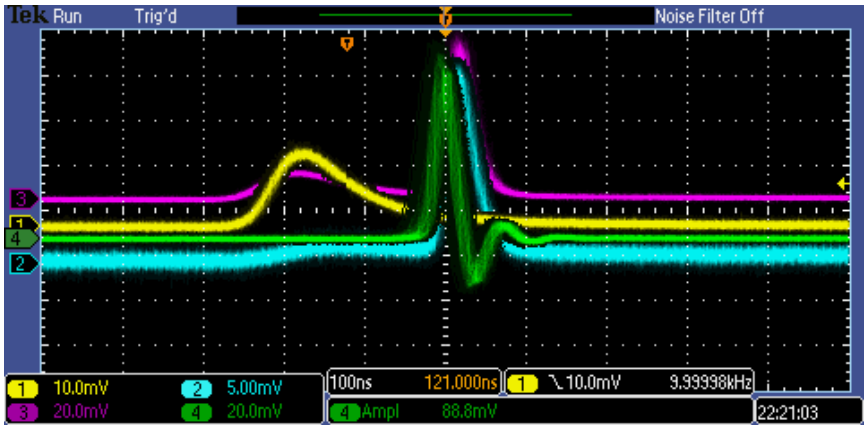

Figure 3.10: The Nd: YAG laser and Ti: sapphire lasers output pulses recorded using an oscilloscope. Channels 1 (yellow), 2 (cyan), 3 (magenta), and 4 (green) show the Nd: YAG, dual etalon, single etalon, and injection-locked laser pulse signals respectively.

A commercial scanning Fabry-Perot Interferometer (Toptica FPI 100) with 1 GHz FSR was installed to measure the linewidth of the seed laser and the pulsed injection-locked cavity. Figure 3.11 and 3.12 show the transmission maxima of ECDL light and the injection-locked cavity respectively obtained by applying a scanning voltage ramp to the FPI's piezo mirror. The transmission signal of the ECDL shows equally spaced and clear peaks showing single-mode operation with no side bands. The transmission peaks from the injection-locked cavity also show four equally spaced peaks within the scan range with a constant background from the pump laser. Since the FSR in the frequency and time domain of the FPI is known, the line width of both ECDL and injection-locked cavities in the frequency domain could be calculated by measuring the line width in the time domain. For this purpose, one of the transmission peaks from the FPI was fitted with a Gaussian profile to obtain the FWHM in the time domain. The FWHM line width of the ECDL and the injection-locked cavity were thus calculated to be $\approx$ 11 MHz and 35 MHz respectively.

The wavelength tuning range of the injection-locked cavity depends on the tuning capacity of the ECDL. The ECDL tuning depends on the specifications of the laser diode used and the careful alignment of the ECDL cavity for single-mode tuning. The cavity houses a Toptica/Eagleyard diode gain chip with a central wavelength of 850 nm. It is tuned by a piezo-actuated grating with a maximum range (including manual tuning) usually around 10 - 50 nm. The diode wavelength is adjusted using an ECDL control unit Toptica Photonics

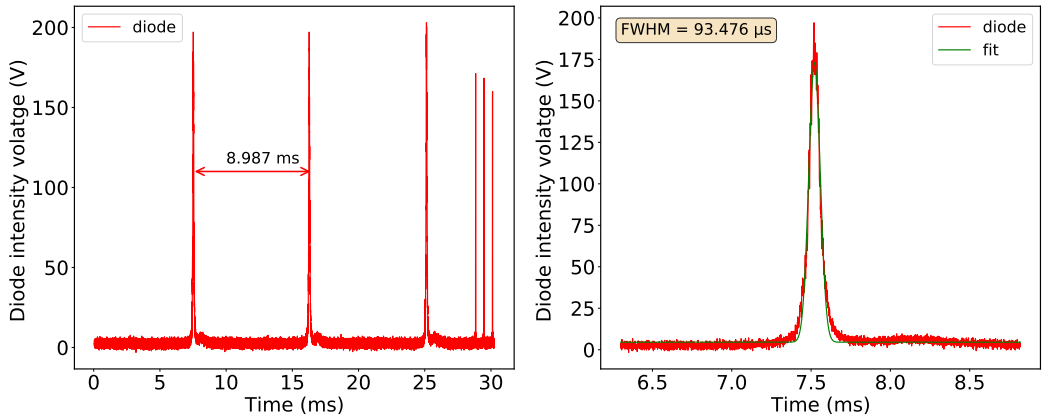

Figure 3.11: Transmission peaks in the scanning FPI for ECDL output giving an averaged FWHM line width of 11 MHz. The red color shows the recorded data points and the green shows the Gaussian fit of a single transmission peak from which FWHM in time is calculated.

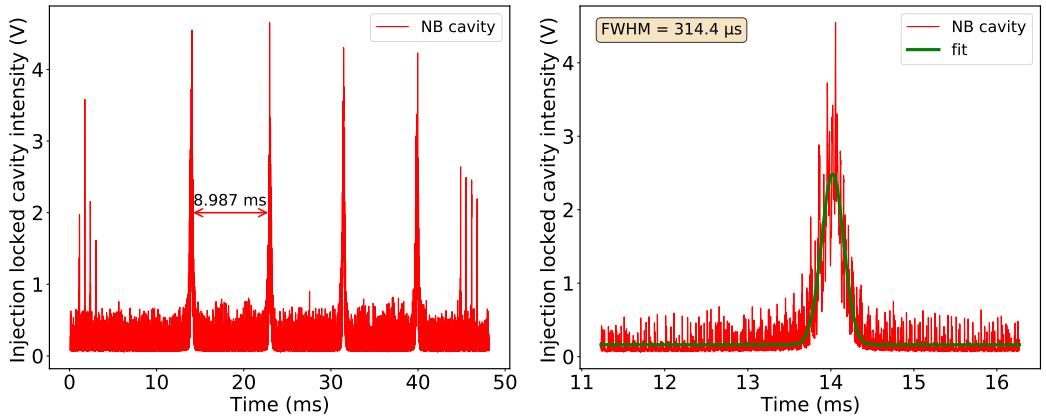

Figure 3.12: Transmission peaks in the scanning FPI for the injection-locked cavity output giving an averaged FWHM line width of 35 MHz. The red color shows the recorded data points and the green shows the Gaussian fit of a single transmission peak from which FWHM in time is calculated.

Model 110 with current, temperature, and grating scan control. The seed laser gave a maximum power of 50 mW measured with a PM10 power meter. Two optical isolators were added to the ECDL laser path (see figure 3.8) to prevent the amplifier cavity laser light from reaching the ECDL and damaging the diode. After the mode-matching telescope (with focal lengths, f_1 = 50mm and f_2 = 75mm), the ECDL power was measured to be 35 mW. The mode-hop free continuous tuning range after alignment was lower than the specifications within a range of 0.2 cm^{-1} or 6000 MHz. The diode cavity was initially optimized for a 780 nm diode and the choice of the cavity components might improve the range. the tuning range also depends greatly on the simultaneous adjustment of the diode current with the grating voltage. An optimized setting for the diode current and grating voltage could improve the tuning range. The reduced tuning capability might also be due to the mechanical wear and tear of the alignment screws of the grating preventing the fine alignment of the grating

of the ECDL. The laser was housed in a noisy environment as well causing fluctuations and temporal drifts in diode temperature which in turn affected the diode current and diode wavelength.

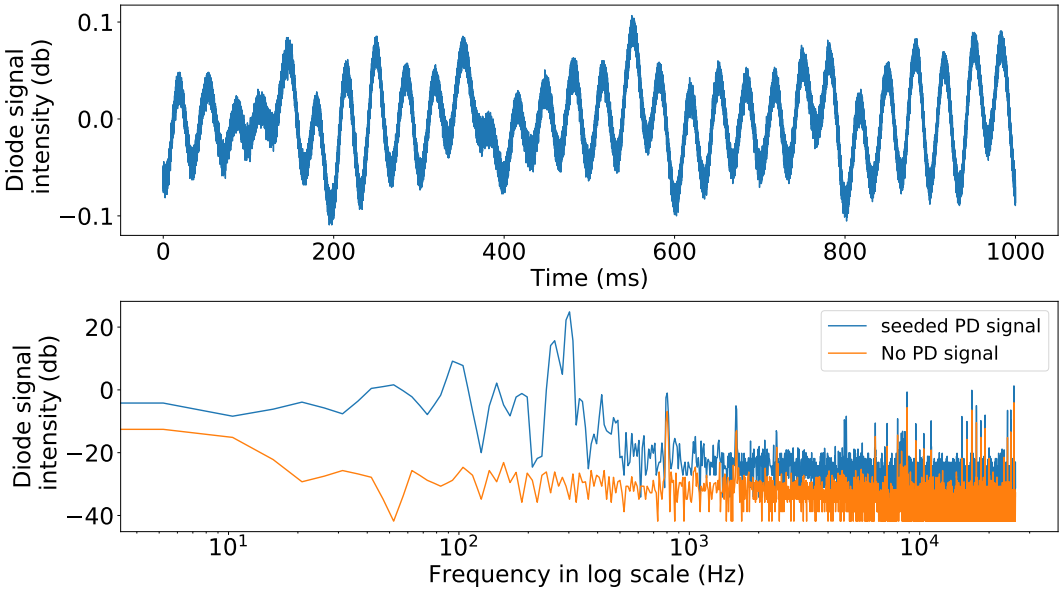

Figure 3.13: The photodiode signals from the passive resonator amplifier cavity. The blue signal shows the photodiode signal when the seed laser modes match the transmission maxima of the cavity. The orange signal shows the photodiode signal from the amplifier cavity without the seed laser injected into it. See text for details.

In order to find the optimum parameters for the locking, the passive resonator stability of the cavity at LPC Caen was measured. The measurements were done similarly to the commissioning work at GISELE [16] and [74]. For this, the photodiode signal of the seeded Ti: sapphire cavity without locking was recorded using an oscilloscope while the wavelength of the ECDL was manually matched to the transmission maximum of the Ti: sapphire cavity. The top inset of figure 3.13 shows the photodiode (PD) signal of ECDL light seeded into the Ti: sapphire cavity at resonance. The bottom inset shows the same signal (blue) as well as the signal without any seed laser sent to the cavity (unseeded), in the frequency domain by applying the fast Fourier transform (FFT) functionality in the oscilloscope. The mechanical vibrations induced in the cavity will be seen as fluctuations in the transmitted intensities from the photodiode. The FFT of these intensity signals thus gives the frequencies of the mechanical vibrations in the cavity. The mechanical noises induced in the cavity can be detected using this method. Compared with the unseeded signal, it can be seen that the noise from the passive cavity is contributing to the peaks at 200 - 300 Hz similar to what was observed in [16] as well as to a 5 kHz peak. The laser surrounding significantly affected the passive stability of the cavity which includes the vibrations from other components in the laser table, operation of the chillers, pump, and even the surrounding light. The other peaks found in both seeded and unseeded conditions include the noise from the 10 kHz pump and other electronic noises. These passive vibrations can make the input signal to Laselock noisy and can cause difficulties in obtaining a reliable

feedback signal from the Laselock for cavity stabilization. By identifying the mechanical resonances of the cavity, signal filtering parameters in the LaseLock unit can be chosen to limit the feedback signal's output range frequencies to be far away from these resonances.

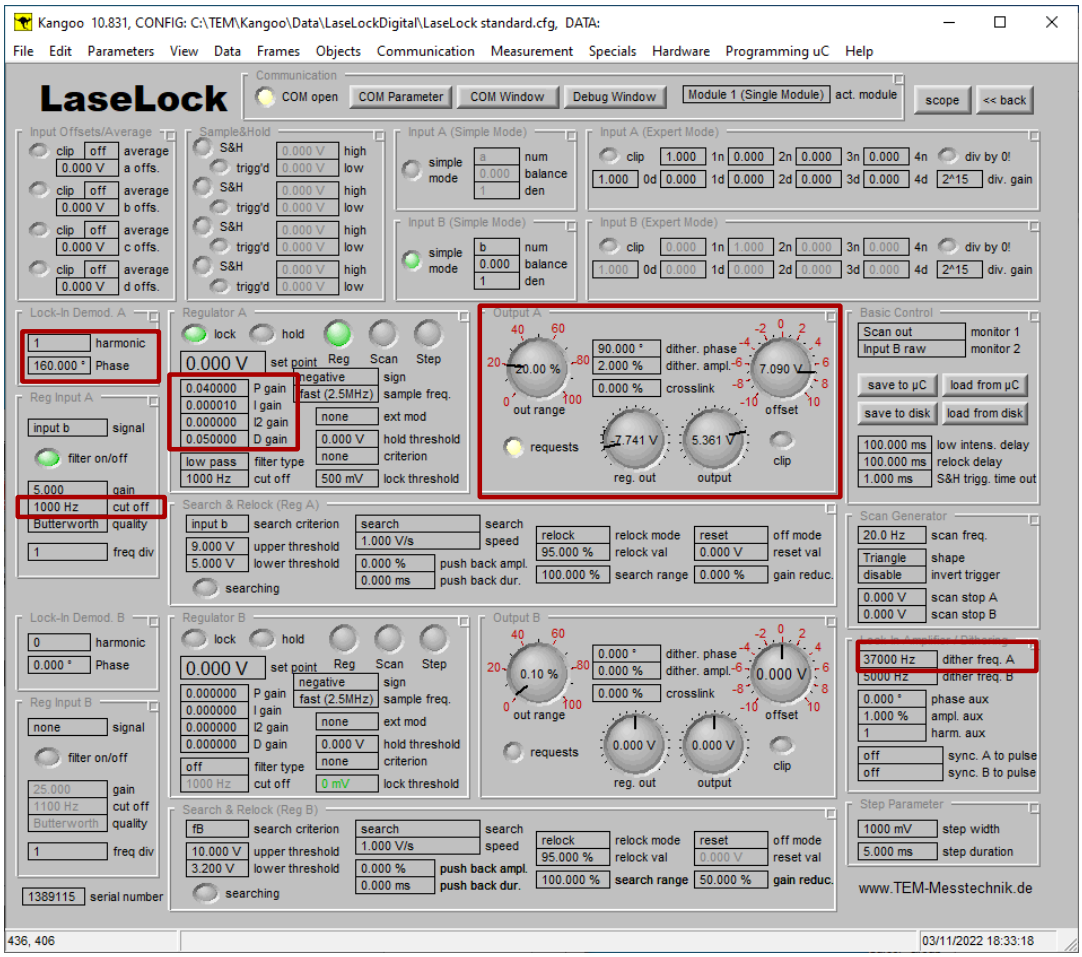

Figure 3.14: LaseLock settings from the Kangoo software used at LPC for the injection-locked cavity.

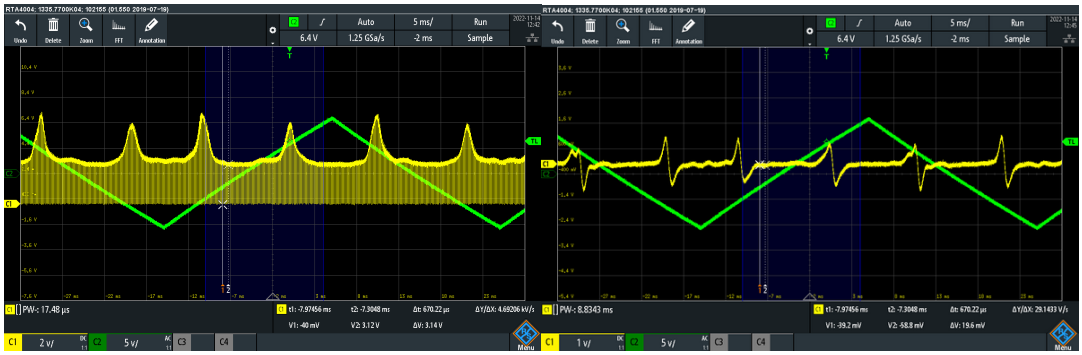

(a) Raw input signal (yellow) and scanning ramp (green) to the LaseLock.

(b) Demodulated signal (yellow) and scanning ramp (green) from the LaseLock.

Figure 3.15: Photodiode signals from the injection locked cavity recorded for active stabilization using the LaseLock unit. See text for details.

For active stabilization, the length of the amplifier cavity is locked to one

of the transmission peaks of the seed light from the amplifier cavity sent to a photodiode and then to Laselock (see figure 3.8). While scanning the piezo-actuated mirror in the injection-locked cavity, the LaseLock parameters were tweaked to achieve optimum locking conditions. The procedure was followed according to the user manual from the TEM Messtechnik LaseLock unit. The LaseLock control GUI called 'Kangoo', with the laselock settings used at LPC Caen is shown in figure 3.14. A top-of-fringe locking technique was used. Figure 3.15a shows the raw transmission signal from the laser cavity while scanning. The signal in green shows the scanning ramp and the signal in yellow shows the photodiode signal. The peak in the photodiode signal corresponds to the cavity length matching the transmission conditions for a given wavelength. Hashed pattern can be seen in the photodiode signal which is the 10 kHz noise from the gated amplifier. This raw input signal is filtered and demodulated using the LaseLock electronics. The demodulated signal is shown in the right inset of figure 3.15b. The low pass filter cutoff for the Laselock input was kept at 500 Hz to eliminate the low-frequency noises. A demodulated signal from the filtered input is chosen by selecting the first derivative ('harmonic = 1') in the Kangoo interface (See figure 3.14). The zero-crossing of this demodulated signal (see figure 3.15a) corresponds to the peak maxima of the raw input signal (see figure 3.15b). The demodulation phase was set to 160° where the maximum amplitude for the demodulated signal was obtained. Whenever the cavity deviates from its locked wavelength due to some noise, the intensity of the raw input signal varies which in turn shifts the zero-crossing of the demodulated signal. This generates an error 'lock-in' signal from which the Laselock electronics generate a PID control signal to regulate the cavity length to the transmission peak. The dither frequency was set at 37 kHz as several mechanical resonances in previously reported measurements of modulation strength of the piezo were observed between 10 kHz and 30 kHz for this cavity (refer to [16]). This can strongly vary the gain and phase of the feedback signal driving the piezo-mirror. For locking, the scanning mode was switched to the regulation mode using the 'Reg' option (See figure 3.14). The P, I, and D parameters of the PID regulator were tweaked until stable long-term locking of the Ti: sapphire wavelength to the ECDL wavelength was achieved (See figure 3.9). Locking could be maintained for continuous scanning while in-gas jet laser spectroscopy measurements were performed.

3.3 CW Ti: sapphire laser development

A CW Ti: sapphire laser is an alternative to external cavity diode laser (ECDL), providing a much wider tuning range. This section describes the implementation of a compact-design CW Ti: sapphire using diode lasers for pumping as a cost-effective alternative to a commercial CW pump laser.

The commercially available CW Ti: sapphire laser is too expensive for small laboratories. A comparison of the commercial master lasers with an ECDL can be seen in the table 3.1. The commercial availability of inexpensive blue-green diode lasers ($<$ 100 €) of up to several W power makes it possible to implement a diode-pumped Ti: sapphire cavity which can be cost-effective. In this thesis work, the upgrade, implementation, and characterization of such a cavity are reported. The system was designed by Volker Sonnenschein at

Nagoya University and manufactured in GANIL. An initial version of this laser cavity has been reported in [81].

Table 3.1: A comparison of the properties of different commercial master laser systems.

Properties	ECDL	CW Ti:sa
Cost (€)	10 - 30 K	>100K
Power (mW)	10 - 100	500-5000
Wavelength tunability (nm)	10 - 50	300
Mode-hop free scanning (GHz)	30	10 - 50
Linewidth (MHz)	≈ MHz	30 kHz - MHz

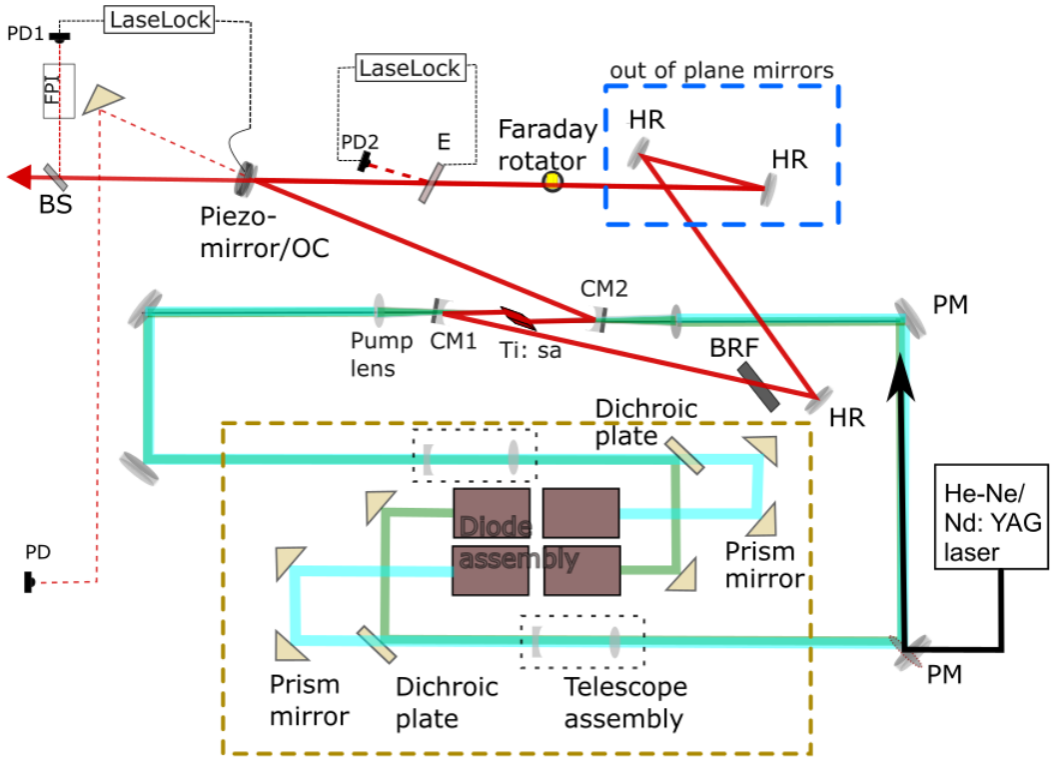

Figure 3.16: Design layout of the diode-pumped CW cavity. The laser pump assembly is marked in a yellow frame. Labels: HR - high reflecting cavity mirror, OC - output coupler mirror, BRF - birefringent plate PD - photodiode, E - etalon, CM1, 2 - curved mirrors, PM - pump mirror, FPI - Fabry-Perot Interferometer, BS - beam sampler.

The layout of the CW cavity being implemented in the GISELE lab at GANIL is shown in figure 3.16. Green-blue combination of diode lasers used for pumping the Ti: sapphire crystal gives higher pumping power (blue diode lasers) as well as good absorption (green diode lasers) efficiency in the gain medium [81, 83]. Figure 3.17 shows the reported p-polarized absorption data in the visible wavelength region with the plot in brown (labeled as CT1a) showing the absorption strength for a highly doped Ti: sapphire crystal for a wavelength range of 300 - 750 nm [82]. The Ti: sapphire crystal was chosen to be CT1a, which gives the maximum absorption efficiency for the green and blue diode lasers.

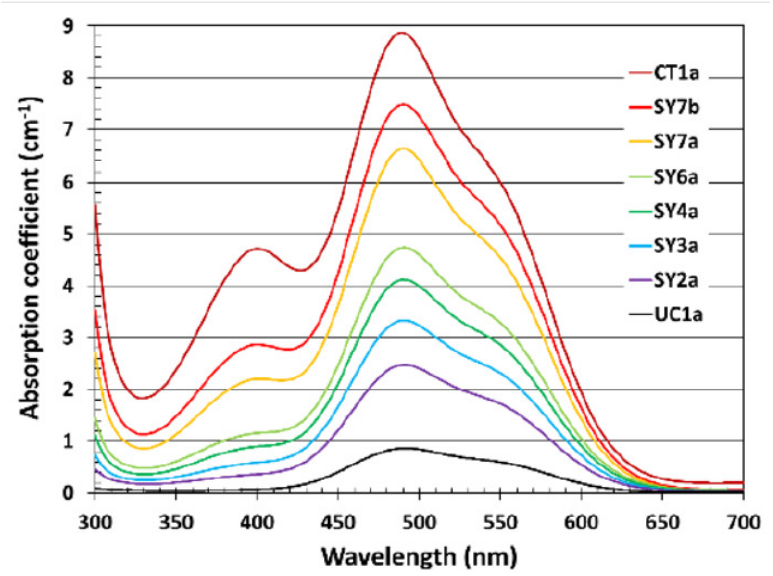

Figure 3.17: Absorption spectra for p-polarised light in different doping concentrations of the Ti: sapphire crystal taken from [82].

Four InGaN diode lasers (from Lasertack) are used as pump lasers, two of them blue and two of them green. They are installed on a water-cooled copper block for temperature stabilization. The diode lasers are controlled by the Lasertack iLD series driver units. Two blue diode lasers of 465 nm with a maximum power close to 3 W and two green diode lasers of wavelength 520 nm with a maximum power close to 1 W were installed. An additional pumping path for a CW Nd: YAG green laser was added to the design and it can also be used for coupling in an alignment laser (See the laser path in figure 3.16). This gives the option to switch from pumping with multiple laser diodes to a traditional CW green laser pump though it will be more expensive. Using a combination of prism mirrors and dichroic mirror plates, the diode lasers are aligned into the Ti: sapphire crystal in both directions. One green diode laser and one blue diode laser enter the cavity from each direction. The quality of the diode lasers can be defined by their beam propagation ratios (M^2) and their output power. M^2 value defines the degree of variation of the beam from an ideal Gaussian beam. A laser beam of $M^2 = 1$ represents a perfectly Gaussian (TEM_{00} mode) beam. The laser beam diameter during propagation can be expressed, in relation to the (M^2) value, by the equation [84]:

$$W(z) = W_0\sqrt{1 + M^4\left(\frac{\lambda}{n\pi W_0}\right)^2 (z - z_0)^2} \tag{3.2}$$

where $W(z)$ is the 4σ-D beam diameter from the beam waist, W_0 is the beam waist diameter at z_0, z_0 is the distance in z-direction from a reference point to where the beam waist is located, M^2 is the beam propagation ratio, n is the refractive index of the propagation medium (for air, $n = 1$) and z is the direction of the beam axis. The 4σ-D beam diameter or second-moment width is used according to the ISO1146 standard for beam width measurements. It gives beam diameter as four times the standard deviation of the intensity distribution of the beam. The diode laser beams are far from Gaussian with an M^2 value

nearly equal to 3 - 15. The M^2 value for blue diode lasers is slightly worse than the green diode laser. The diode laser beam spots are not circular but elliptical with its major-axis length approximately 6 mm. In order to ensure parallel beams from these diode lasers, the pump transport includes telescope assembly with a combination of cylindrical N-BK7 plano-concave and plano-convex lenses of focal lengths 13.7 mm and 150 mm respectively. The telescope assembly combination provides six-fold magnification of the pump beams before reaching the pump focussing lenses.

The cavity uses an off-axis bow-tie geometry consisting of six cavity mirrors: two curved mirrors (CM1 and CM2), one output coupler (OC), and three high-reflecting (HR) cavity mirrors (CM) (See figure 3.16). The gain medium is a highly doped Brewster-cut Ti: sapphire crystal of 6 mm diameter and 4 mm length cooled using water circulating in the copper block on which the crystal rests. The two curved mirrors have a coating with high reflection at 650 - 1000 nm. The output coupler is a BB dielectric-coated mirror with a reflectivity of 98% for the wavelength range 660 - 920 nm. The OC is mounted on a 15 μm stroke piezo-ring stack (Thorlabs PK44M3B8P2). The HR mirrors are Layertec mirrors with $\geq$ 99% reflectivity for 750 - 1100 nm. The two curved mirrors allow spatial mode matching and also restore a parallel beam in the cavity in each round trip. The cavity in its basic bow-tie configuration with all mirrors in the same plane lases in two directions. Out of the three high reflecting mirrors, two of the mirrors are mounted out of the plane, i.e. in a different beam height. This allows the beam to slightly rotate the polarization direction of the beam which in combination with the Faraday rotator allows for defining the beam direction (See more details of ring cavity operation in 1.3). A homemade Faraday rotator was thus installed for unidirectional operation. It was built using a TGG crystal mounted in an Nd ring magnet giving axial magnetization. A birefringent filter, (Sirah Lasertechnik BIFI 550 - 650 nm, 850 - 1040 nm) composed of three parallel plates, is used for the first stage of wavelength selection. The cavity also houses an air-spaced etalon for further mode selection and its installation is detailed in section 3.3.3.

Active stabilization and continuous wavelength tuning of the CW cavity are performed by implementing two Laselock loops. In the first loop, a small fraction of the laser output is sent through a scanning Fabry-Perot cavity to a photodiode PD1, and the PD1 signals are sent to the TEM Messtechnik LaseLock unit. The Laselock signal controls the piezo actuator of the output coupler thus regulating the CW cavity length using the LaseLock electronics. The scanning FPI will act as a reference cavity to which the Ti: sapphire cavity will be locked. The frequency of the laser can then be scanned by tuning the piezo-actuator mirror of the FPI. This changes the transmission wavelength of the FPI which in turn will change the output wavelength of the CW cavity locked to the FPI. For the second loop, the reflection from the etalon is sent to a photodiode PD2 which gives the input signal to the LaseLock. For this, an air-spaced etalon is installed and one of the mirrors of the etalon is piezo-actuated. The etalon length is modulated at a high frequency. While scanning the wavelength of the CW cavity using the FPI, any fluctuation in the modulation intensity will be detected in the transmission peaks detected by the photodiode PD2 which in turn changes the error signal generated by the Laselock. Error signal will generate an HV signal which will adjust the length of the etalon to remain locked to the

amplifier cavity while wavelength tuning is performed. This ensures maximum transmission intensity of the etalon while wavelength tuning is performed.

3.3.1 Pump laser diode assembly

The four pump laser diodes were assembled in the pump laser system in such a way that two of them overlapped their paths to reach the Tisa crystal from both ends (see figure 3.16). The diode lasers of the same wavelength are powered in series and thus all four diodes are controlled using two Lasertack diode drivers/controllers. The diode control connection layout is shown in figure 3.18. The diode drivers are powered using two 30 V DC power supply RSD3305P. A voltage of 13.5 V is applied in parallel to the two drivers such that for each diode laser, the supply voltage $Vin = V_{LD} + V_{Drop} = 6$ - 6.5 V. This fixed supply voltage powers the laser diodes. The drivers have their own interlock loops and these interlock circuits are closed during operation. The drivers can be started once the start signal in the driver is set. They have a certain power-up delay of 5 seconds. For the diode lasers to lase, a modulation voltage greater than the threshold voltage of the diode lasers is required to be applied. The modulation voltage is applied to vary the diode current and thereby the laser diode output power. The maximum modulation voltage applicable to each of the diodes was 5 V. All four diode lasers were tested and the threshold modulation voltage for lasing was found to be 0.2 V - 0.3 V. The green and blue diode

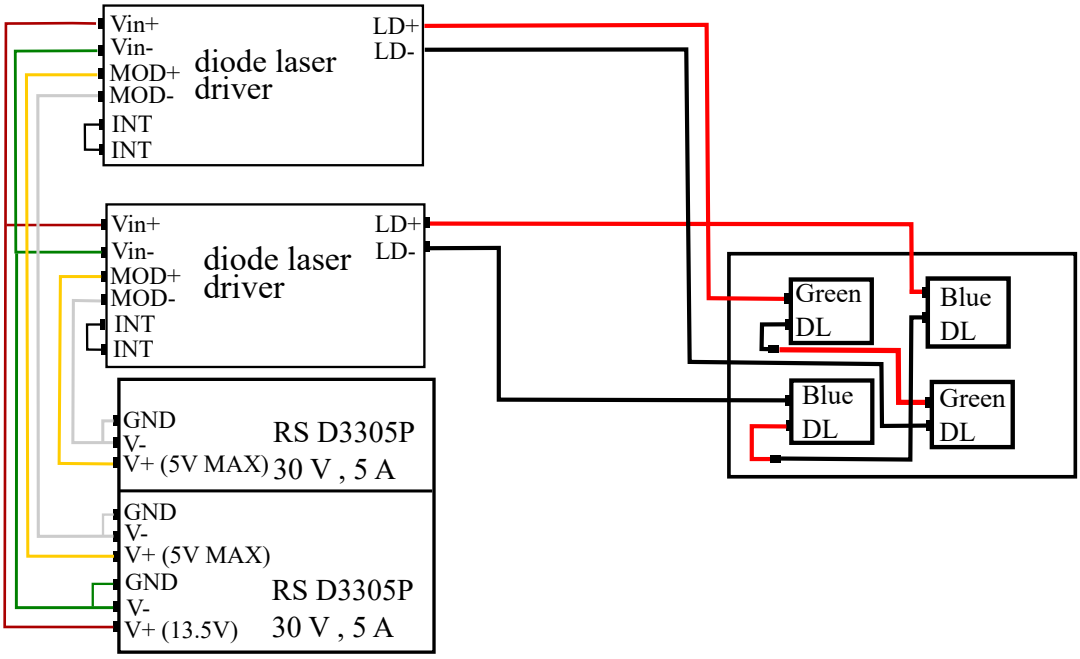

Figure 3.18: Layout of the diode connection used for the pump laser system in CW cavity. Labels: DL - diode lasers, MOD+ and MOD - modulation voltage connections, INT - interlock connections, GND - ground connections and V+ and V- - power supply voltage connections.

laser power measurements were performed for this purpose. The output power vs voltage characteristics for the blue and the green diode are shown in figure 3.19. After a threshold voltage of ≈ 0.25 V, the outpower increases almost linearly with the modulation voltage. For the green laser diode, the modulation

voltage was slightly increased above the maximum voltage of 5 V but could not obtain more laser output power. The modulation voltages were kept at their maximum values for the Ti: sapphire cavity alignment procedures.

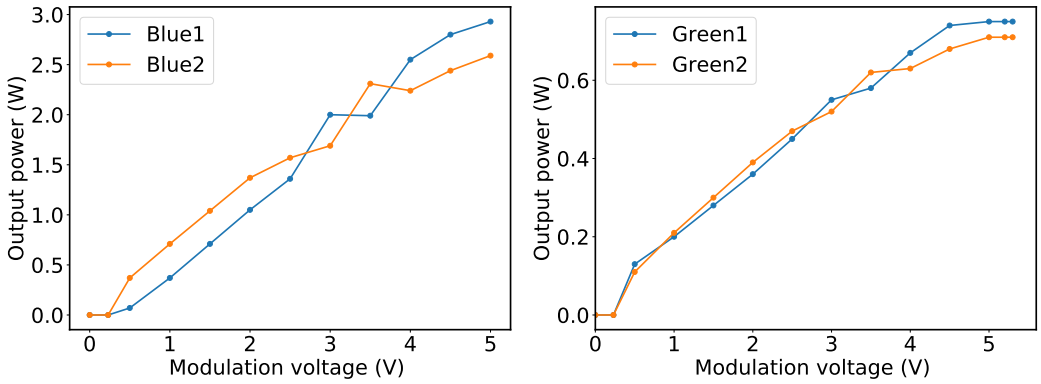

Figure 3.19: Diode laser output power versus modulation voltage

The transverse/radial mode structure of the laser diodes was also measured using a beam profiler to obtain the M^2 values. For the beam profile measurements, the laser diode first passing through the cylindrical telescope in the pump assembly was sent through a convex lens of 150 mm focal length installed outside the cavity. The convex lens was kept at approximately the same distance to cover the pump path to the Ti: sapphire crystal from the cylindrical lens. In order to send diode lasers outside the cavity, the second pump mirror mounts were removed from the diode laser transport paths (see figure 3.23). The 4σ-D beam diameter for each of the laser diodes was measured by recording the beam spot images using a CMOS camera Optoprim-CMOS-1202. The 4σ-D beam diameter across the tangential and sagittal plane is obtained from the CMOS camera software. Figure 3.20 and figure 3.21 show the 4σ-D sigma beam radii of one of the blue and green laser diodes, measured over the beam z-range. The beam radius at the dip gives the beam waist. The resulting beam radii curve was fitted using the equation 3.3. Table. 3.2 shows the resulting M^2 values of all the diodes used for pumping the Ti:sa cavity obtained from the fit following the equation 3.3. The M^2 values indicate that the green and the blue diode beams have several radial modes, with blue laser diodes being farther from the Gaussian nature compared to green laser diodes. The beam waist for the tangential and sagittal plane can be seen slightly shifted. The use of an aspheric lens as a pump-focusing lens in the CW cavity can reduce astigmatism and other optical aberrations caused by the multimode blue-green diode lasers.

Table 3.2: Determined values of M^2 from the beam profile measurements

Laser	M^2 in tangential plane	M^2 in sagittal plane
Blue left arm	18.1(10)	12.00(12)
Blue right arm	18.3(8)	12.02(10)
Green left arm	6.9(3)	4.63(7)
Green right arm	5.4(3)	2.2(5)

For the alignment of the diode lasers to the Ti: sapphire cavity, one had to make sure that the diode paths were overlapped. The prism mirrors and

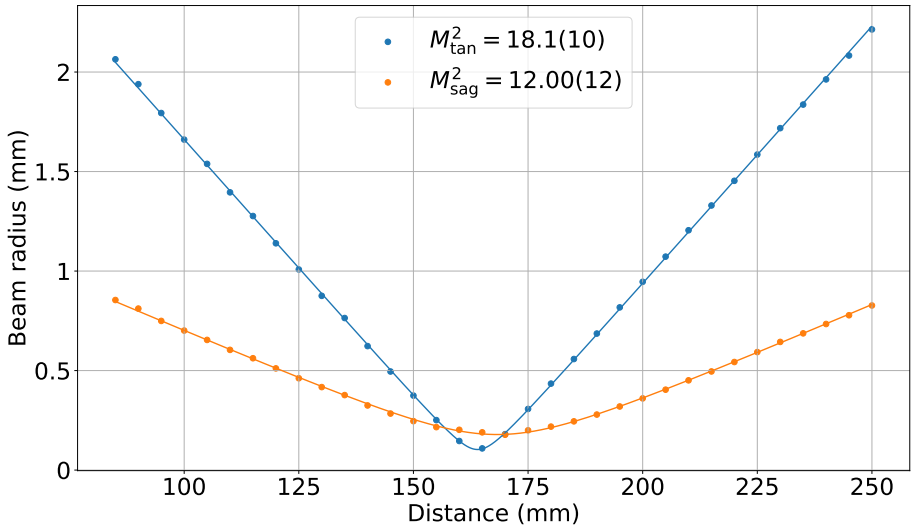

Figure 3.20: Beam profile measurement of one of the blue diode lasers showing beam waist diameter in tangential (blue) and sagittal (orange) planes.

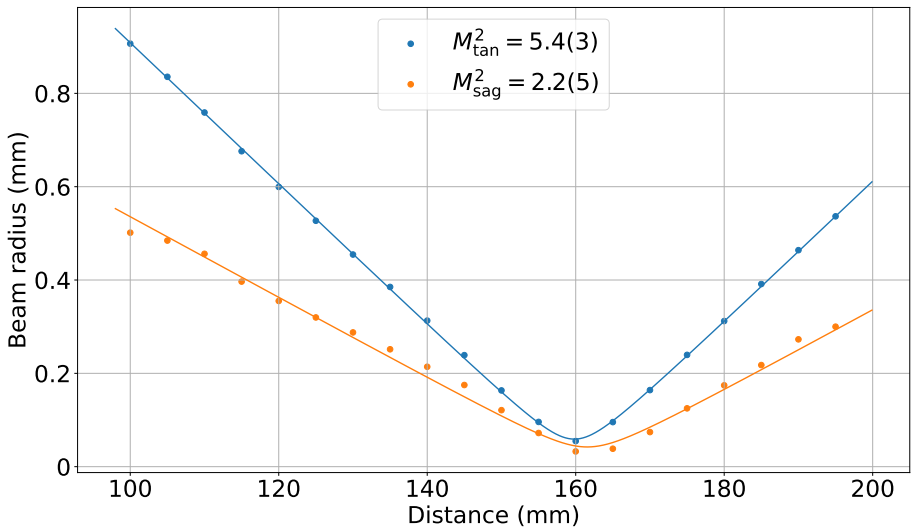

Figure 3.21: Beam profile measurement of one of the green diode lasers showing beam waist diameter in tangential (blue) and sagittal (orange) planes.

dichroic plate (see figure 3.16) were roughly adjusted to overlap the blue and green laser paths and to center them on the pump mirrors. The pump mirrors were then tuned to overlap all four laser spots in the Ti: sapphire crystal. The prism mirrors as well as the pump mirrors are iteratively tuned to overlap the laser diode spots onto the cavity mirrors. Figure 3.22 shows overlapped laser diodes in the Ti: sapphire crystal.

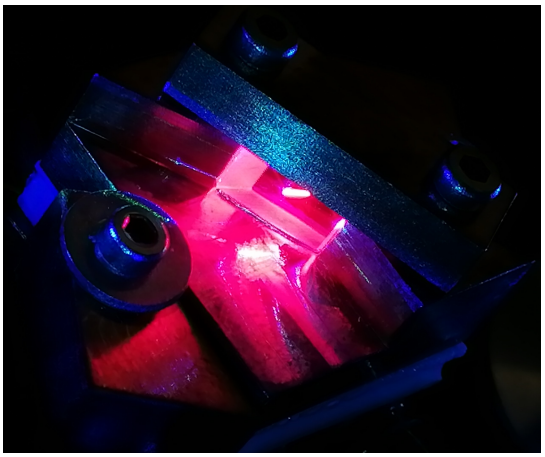

Figure 3.22: Aligned laser diodes focussed along the same path in the Ti: sapphire crystal

3.3.2 Cavity assembly and alignment

The rendered image of the CW cavity design is shown in figure 3.23a. The cavity was built from scratch including the assembly of all the components. The cavity houses the diode pump system as well in the design, unlike the older versions.

For the first alignment, only the six cavity mirrors, the Ti:sa crystal and the BRF were installed. The initial assembly of the cavity mirrors and alignment was performed using a CW He: Ne alignment laser. He - Ne laser beam was sent through the output coupler mirror. All the cavity mirrors were roughly positioned such that the He-Ne laser beam spot was roughly centered on the mirrors. The He-Ne alignment was performed with the BRF in the cavity as it significantly shifts the beam compared to the bare cavity. Once the cavity mirrors were roughly aligned, each of the pump diode lasers was sent to the cavity centering the laser diode spots in each of the mirrors using the four pump mirrors. The fluorescence from the Ti: sapphire cavity was finally monitored using a photodiode coupled to an oscilloscope. Fine-tuning of each of the cavity mirrors was performed to obtain lasing conditions. The first alignment was performed with all the cavity mirrors at the same height. Once lasing was achieved, two of them (marked in blue frame in figure 3.16) were mounted at different heights to implement the off-axis geometry. The cavity installation with lasing in both directions is shown in figure 3.23b. Maximum output power measured in one direction was 65 mW giving a total of 130 mW in both directions.

A home-built Faraday rotator was installed for unidirectional operation. It consisted of a Brewster-cut TGG crystal, with a path length of 3 mm and diameter of 5.8 mm, mounted in a neodymium ring magnet (inner diameter - 6.3 mm) with axial magnetization. TGG crystal was chosen as it operates in the near-infrared spectral region having a large Verdet constant which defines the strength of the Faraday effect [85]. The principle of operation of the Faraday rotator in a ring cavity is presented in section 1.3. The losses in the cavity increased with the addition of the Faraday rotator and hence the output power was reduced to roughly 100 mW. The one-directional output power was stable and switching of lasing direction was not observed. Long-term power measurement in unidirectional operation was performed to measure power stability over

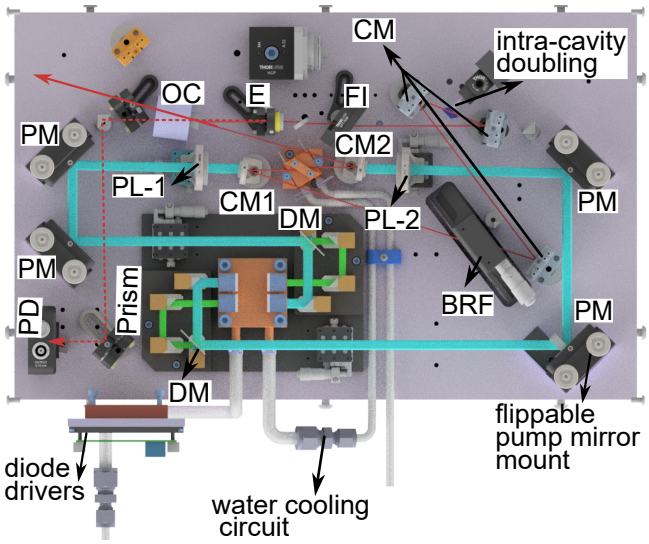

(a) Top view from the 3D drawing of the CW Ti: sapphire cavity.

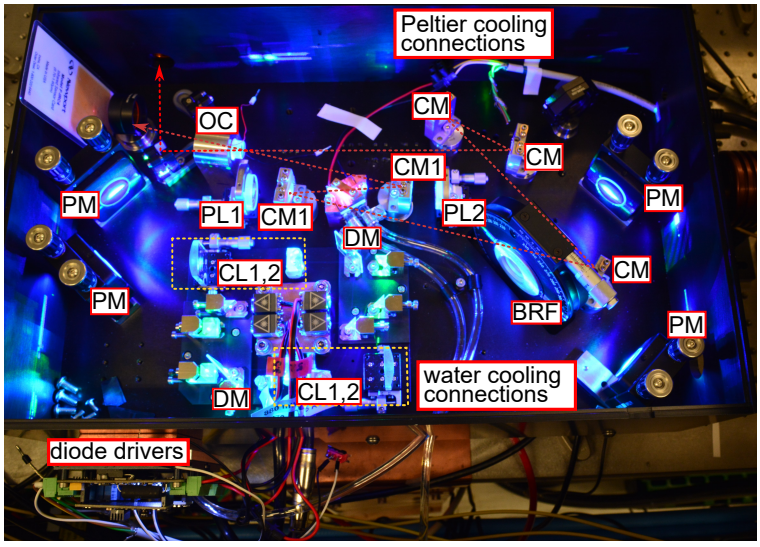

(b) The CW cavity installation at GISELE lab. Without the Faraday rotator, lasing in two directions can be seen.

Figure 3.23: The CW Ti: sapphire cavity layout and installation for GISELE lab. Labels: PM - pump mirror, CM1, 2 - curved mirrors, CM - high reflecting cavity mirrors, OC - output coupler, DM - dichroic mirror, BRF - birefringent filter, E- etalon, FI- Faraday rotator, PL-1, 2 - pump lens, CL1, 2 - cylindrical lenses. See text for details.

time as shown in figure 3.24. No active stabilization is implemented and the fluctuations in the output power might be due to noises induced by the vibration of the CW cavity.

To monitor the output wavelength of the cavity, a small portion of the output beam was split using a 10% beam sampler and sent to a fiber coupler coupled to a High Finesse WS6 wavemeter. The wavemeter readout from the CW cavity in the off-axis configuration without any stabilization can be seen in figure 3.25. The wavemeter signal does not show any side modes but mode jumps were seen over time in the wavemeter readings. To eliminate this mode hops, active stabilization is required. The transversal mode structure of the

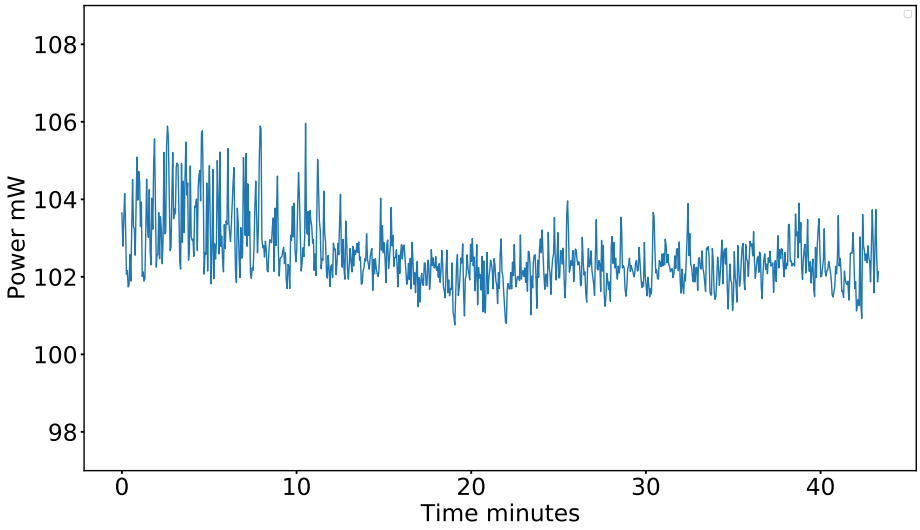

Figure 3.24: Long-term power readout of the CW Ti: sapphire laser in unidirectional operation without active stabilization.

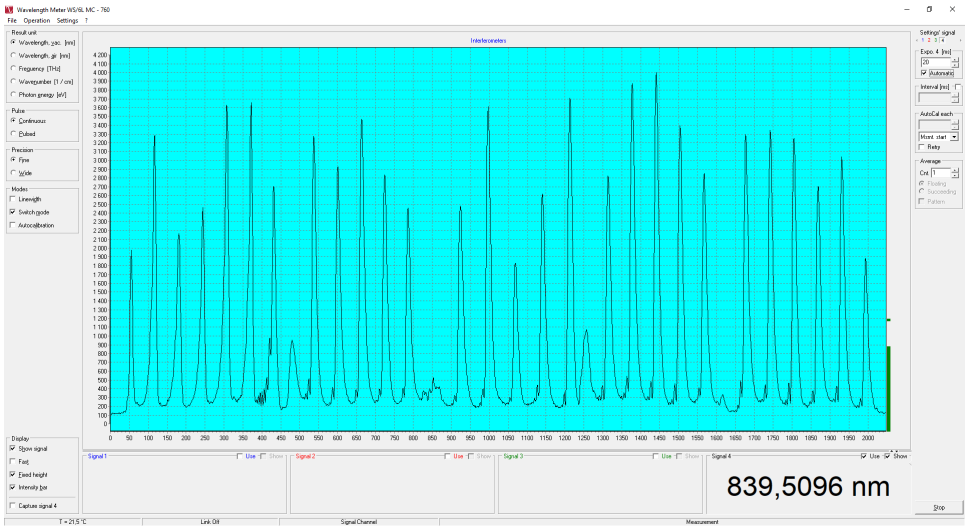

Figure 3.25: Wavemeter (High Finesse WS6) readout of the cw cavity.

cavity was also recorded using beam profile measurements. Figure 3.26 shows the beam waist profile of the CW cavity. The M^2 value obtained from the fit for the tangential and sagittal plane is 1.032(4) and 1.369(9) respectively showing a single transversal mode operation.

For cavity stabilization, an air-spaced etalon was constructed (construction and tests of the air-spaced etalon are presented in 3.3.3.) and installed in the cavity but the losses in the cavity were too high for the cavity to lase. In order to stabilize the cavity, a thin solid etalon was used instead of the air-spaced etalon. The cavity output with a 2 mm solid etalon installed was sent to a scanning FPI (Toptica, FSR 1 GHz) to measure the line width. The linewidth was measured to be 80 MHz.

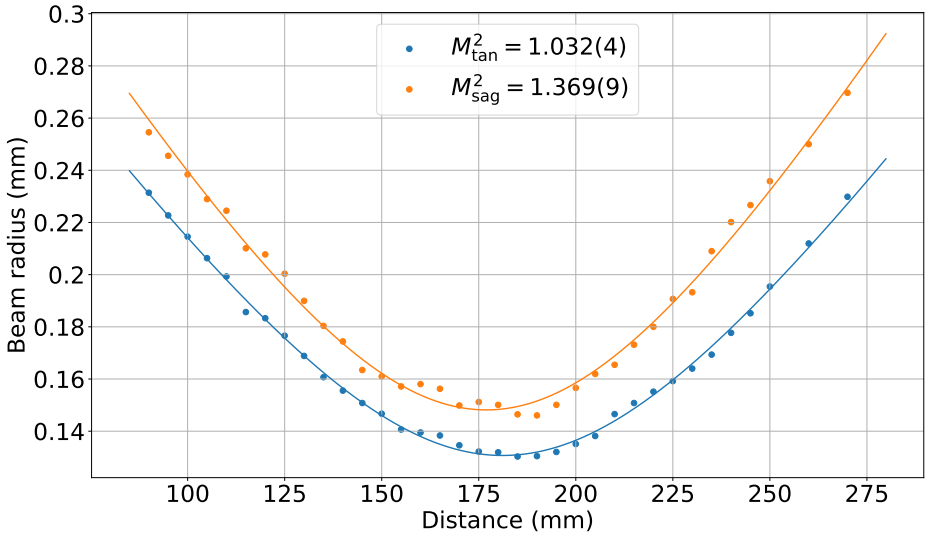

Figure 3.26: Beam profile measurements of the CW cavity with 2 mm solid etalon

3.3.3 Air-spaced etalon

Once unidirectional operation was achieved, another optical element to be added to the laser cavity is a home-built air-spaced etalon. It consists of two partially reflecting window surfaces such that the light beam passing through it will undergo multiple reflections and transmissions. The transmitted light beams from the surfaces will undergo constructive and destructive interference depending on their accumulated phase after reflection within the surfaces. The schematic of the ray propagation in air-spaced etalon is shown in figure 3.27.

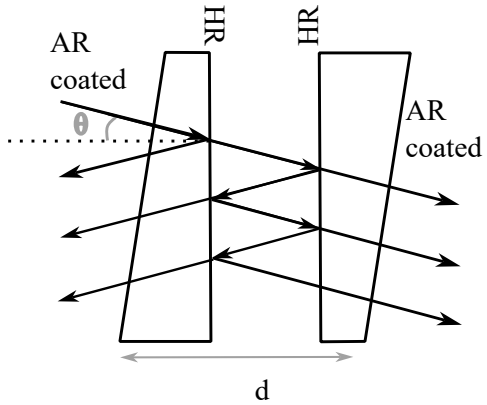

Figure 3.27: Ray propagation in air-spaced etalon. Labels: AR - anti-reflection, HR - high reflection

For the construction of an air-spaced etalon for the CW Ti: sapphire cavity, two Thorlabs BSF05-B beam samplers were used as the parallel plate windows with wedges of ≤ 30 arc mins. One side of these beam samplers is antireflection coated for the cavity spectral range and wedged. The wedge shape minimizes etalon effects between the two sides of the beam sampler. The anti-reflection side is coated with $< 0.5\%$ reflectance for 650 - 1050 nm wavelength ranges at

45° angle of incidence. The high reflection sides of the beam samplers were glued to both sides of a piezo ring-actuator Throlabs PA44M3KW having a length of 3.2 mm ± 5 μm. An additional spacer of roughly 2 mm width was added in between the beam samplers such that the distance between the two beam samplers is of the order of 5 - 5.2 mm. This distance should ideally provide an FSR of 29 GHz according to the equation 1.85. The quoted reflectance for the beam sampler BSF-05B is 4% for an incident angle of 0 - 10°. The coefficient of finesse can then be obtained from equation 1.86 to be 0.65. The spectral width or bandwidth is then ideally ≈ 44.6 GHz according to equation 1.86.

The parallelism of the high reflecting surfaces of the beam samplers is crucial in the alignment of the air-spaced etalon. A He-Ne laser was used for the construction and alignment of the air-spaced etalon. Two methods were adapted for the alignment of the air-spaced etalon, a fast alignment procedure and a scanning procedure. The fast etalon alignment method was adapted from [86, 87], and the setup used for construction is shown in figure 3.28. In this method, the He-Ne laser was first sent through a 1 mm aperture. The two surfaces are mounted on a translational kinematic cage mount. A focusing lens was added in between the aperture and the etalon surfaces. The back reflection from both surfaces gives two or more spots on the aperture screen. The intensity of the back reflected spots indicates whether it is from the AR-coated surface or from the other. Since one of the surfaces is wedged, One etalon is kept fixed and the other etalon is rotated such that the wedged surfaces are parallel to each other. The back reflections from both the samplers are overlapped by fine adjustment of the etalon surfaces. Piezo-actuator is attached to the inner side of one of the samplers and the spacer to the other. The samplers are brought close until they touch and are glued. Before curing the glue, the fine adjustment of the second beam sampler was performed till clear interference fringes were seen as shown in figure 3.28. The circular and equally spaced fringes ensure the parallelism of the etalon surfaces.

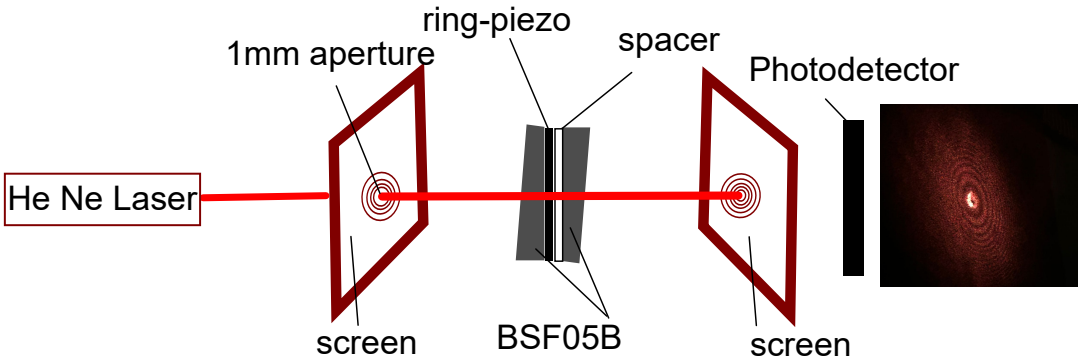

Figure 3.28: Air-spaced etalon alignment setup. The right shows the circular fringes seen after the fast alignment procedure ensuring parallelism of the etalon surfaces.

For the scanning method, the alignment setup is similar to figure 3.28 and was used to check the first alignment method. A Toptica miniScan generator was used to provide a voltage scan ramp to the piezo attached to the etalon. The transmission from the air-spaced etalon was sent to a photodiode coupled to an oscilloscope. The resulting transmission fringes can be seen in the figure 3.30. A maximum of 150 V scan ramp can be applied to the piezo and a scan

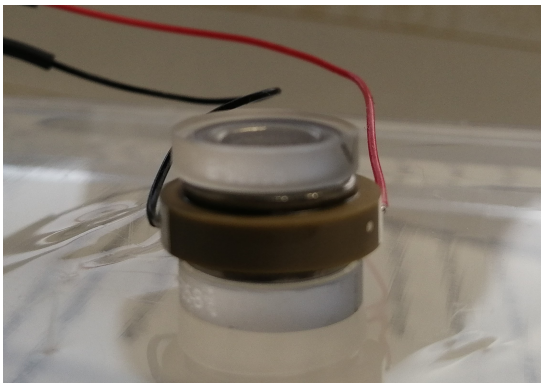

Figure 3.29: Construction of air-spaced etalon with two BSF05B beam samplers at a distance of ≈ 5.2 mm.

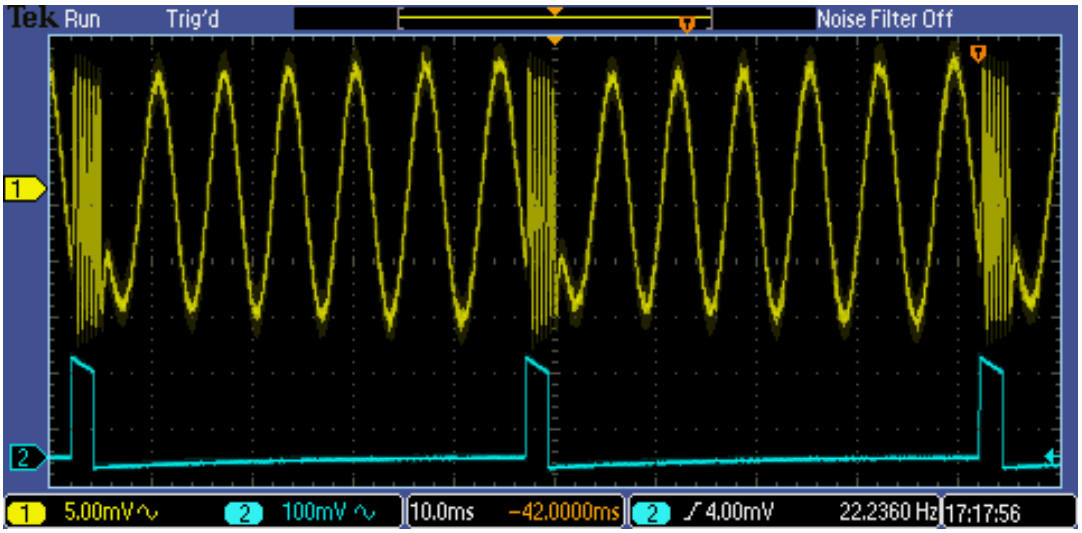

Figure 3.30: Transmission fringes from the air-spaced etalon.

frequency of 100 mHz to 200 Hz. Figure 3.30 shows the trigger output from the scan generator in blue at a frequency of ≈ 25 Hz and the transmission from the etalon in yellow. Voltage ranges between 10 - 50 V are chosen for scans to avoid non-linear behavior [88]. The assembled and aligned homemade etalon is shown in figure 3.29.

The air-spaced etalon can be used in the CW cavity for active mode stabilization. However, the losses in the cavity are increased with the addition of the air-spaced etalon. This caused the CW cavity to stop lasing and hence alignment of the etalon to the cavity without lasing was not possible. However, to check the performance of the constructed etalon, it was installed in a commercial CW Ti: sapphire ring cavity operating in the 850 - 1000 nm range from Hubner Photonics GmbH. The air-spaced etalon provided a mode hope free tuning of roughy 22 GHz. The etalon was locked to the ring cavity for this purpose and the piezo of the etalon was scanned to tune the cavity. This was without stabilization using an FPI. The mode hop-free tuning with air-spaced etalon can be seen in the figure. 3.31. Roughly 22 GHz (0.7 cm^{-1}) mode-hop-free tuning was obtained as can be seen from the figure.

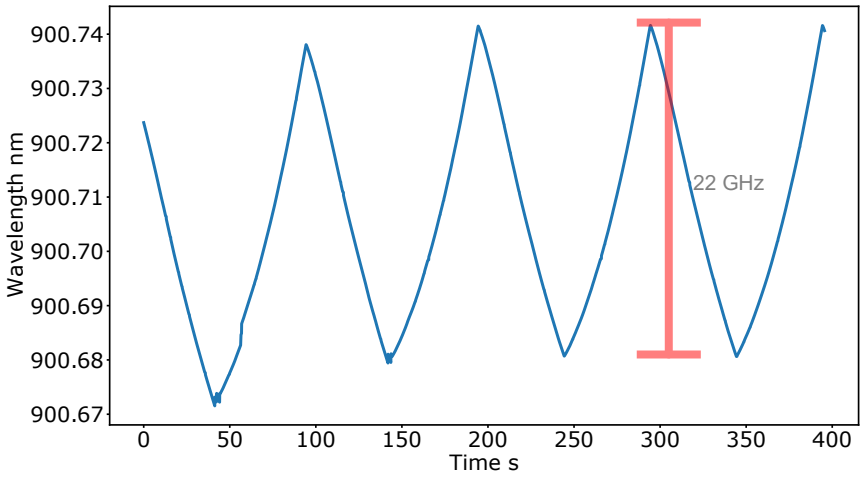

Figure 3.31: Mode-hop free wavelength tuning with the air-spaced etalon in the CW cavity.

3.3.4 Ongoing work and perspectives

Currently, the cavity losses are so high that with the addition of the air-spaced etalon, the cavity cannot lase. The reason for the losses might be insufficient pumping power and misalignments of the optical components in the cavity. To tackle the problem of insufficient pumping, the commercial Laser-tack laser diodes have to be replaced with ones that can provide higher output power. For normal operation of the CW cavity, the total laser diode power needs to be at least 8 - 10 W and the currently installed diode lasers provide a maximum pumping power of 6 W. It might be that the cavity is just above the threshold condition for lasing. The overlap and fine alignment of the four diode lasers play a very crucial role. Slight misalignment can reduce the CW output power as it can induce additional thermal lensing effects in the Ti: sapphire crystal. The laser diodes have to be individually aligned carefully overlapping their focusing points in the crystal using a beam profiler.

With the current setup, lasing was not possible with the addition of air-spaced etalon, and hence active stabilization could not be implemented. A solid etalon of 2 mm thickness was installed in the cavity as a trial check and lasing was possible. Locking of the cavity was tried with the installation of the solid etalon. The first-order reflection from the etalon was sent to a photodiode and then to LaseLock. Any vibrational noise in the CW cavity should cause fluctuation in the intensity of the photodiode signal. These fluctuations are recognized by the Laselock unit to generate a control signal for the piezo mirror of the CW cavity. Locking was achievable using this method. However, it was a trial check and in reality locking mechanism is different which requires the air-spaced etalon as well as a reference FPI cavity to be installed. With the previous method, the cavity has shown its capability to stabilize which is crucial for laser spectroscopic applications.

The cavity also requires a more efficient cooling mechanism of the crystal. Now the copper block assembly holding the Ti: sapphire crystal does not allow efficient cooling of the crystal. The crystal needs to be at approximately 20

°C. With the current mount, the crystal temperature is roughly near body temperature. The Peltier current cannot be increased in the current stage as it starts condensing the copper plates which can cause damage to the crystal as well.

Thus the current version of the CW Ti: sapphire laser requires more conditions to be fulfilled for its use in high-resolution laser spectroscopy. A part of the development work has been completed and characterized as shown in this chapter. The continuous tunability option still needs to be implemented for which a scanning FPI of high Finesse and an FSR of 5 - 10 GHz is required. For active stabilization of the cavity, both the air-spaced etalon and the scanning FPI are required. The challenges to overcome and the solutions have been recognized. The construction of FPI, re-installation of the laser diode, and fine alignment are ongoing to achieve the best lasing conditions. With a pumping power of 8-10 W and optimum alignment, an output power of roughly 100 mW is expected with the addition of all optical components. For seeding an injection-locked cavity, the laser output power required is only a few mW. The cavity with its upgrades does show its potential to be used as a seed laser for high-resolution laser spectroscopy.

CHAPTER 4

Offline measurements at S^3 -LEB

The offline commissioning of the S^3-LEB setup has been ongoing at Laboratoire de Physique Corpusculaire (LPC) Caen and the related measurements performed are described in the following sections. Stable erbium has been used for the commissioning tests as it will be the first case to be studied at S^3. For the online commissioning of the S^3-LEB, Er is chosen as the first test case as it can be produced with a high production cross section and hence will be an easy case in terms of production. ^{152}Er is also an alpha emitter and hence can be detected unambiguously while performing commissioning of S^3. Physics can be extracted as well by laser spectroscopy of ^{151m}Er which has not been measured yet.

4.1 Previous measurements

For the preparation of offline studies, the Ti: sapphire laser systems to be used in S^3-LEB were separately commissioned and high-resolution Er laser spectroscopy was performed in an atomic beam unit (ABU) at the GANIL Ion Source using Electron Laser Excitation (GISELE). This work is described in detail in [16].

For the initial commissioning of the S^3-LEB RFQs, simulation, and optimization of the RFQs were performed individually till the RFQ-CB. This work is also reported in [16]. The transmission in S-RFQ and mini-RFQ was performed in the reported work using a Cs source and a relative transmission of 95(5)% was achieved. The transmission was deduced by comparing the current measured in the grid placed in front of the source and a faraday cup after the mini-RFQ. The QMF transmission and filtering characterization tests were performed with a Rb surface ion source placed just before the QMF unit. Relative ion transmission > 90% (ion guiding mode) and 80% (filtering mode) was achieved for the Rb source measured using MCP installed before and after the QMF. ^{85}Rb and ^{87}Rb masses could be completely resolved. The ion transmission through the RFQ-CB was tested under similar conditions to QMF. To test bunching mode efficiency, a beam gate of 1 ms was used to bunch the ions, and

a cooling time of 10 ms. The transmission through the RFQ-CB was measured to be 30%.

The PILGRIM performance was optimized using alkali sources ^{23}Na, ^{39,41}K, ^{85,87}Rb, ^{133}Cs and was reported in [8, 70]. The ion beam source was placed in front of the PILGRIM unit and was chopped using the Bradbury-Nielson (BN) gate. A transmission of $> 80\%$ and a resolving power of 150000 was achieved for these tests. For the mass measurement tests, mass accuracy of the order of 10^{-7} was achieved.

4.2 First in-gas laser ionization of Er and transmission

For this thesis work, Er ions were produced, both in the gas cell and gas jet, by resonant laser ionization for the first time at S^3-LEB. The complete RFQ components were aligned, additionally coupling and aligning the RFQ cooler buncher and PILGRIM. The S^3-LEB gas cell was also newly coupled and aligned to the RFQs. The complete S^3-LEB setup used for the offline measurements has been described in detail in chapter 2.3.2. A laser room with two pulsed broadband and one injection-locked Ti: sapphire laser system with a 10 kHz repetition rate was prepared adjacent to the S^3-LEB setup. The laser installation and alignment work is described in detail in chapter 3. The ion transport through the complete setup was optimized. Laser spectroscopy studies were performed in the gas cell and gas jet and compared with the previous laser spectroscopy results from ABU and other literature works. The following section details the offline ion guide optimization as well as laser ionization and spectroscopy tests performed with the setup and the results achieved.

Figure 4.1: Tantalum filament mounted on the filament flange of the S^3-LEB gas cell.

For offline in-gas cell/jet laser ionization, the gas cell was operated as it will be in online conditions, except that the entrance window was replaced by a blind flange. The entrance windows are currently being tested in a dedicated offline test bench to develop a protocol for their installation and to verify their leak tightness. The design of the test bench, test protocols, and initial tests are described in section 4.5. In order to create atoms in the gas cell, two tantalum filaments were installed in the gas cell (see gas cell set up in section 2.17), on which stable isotopes of the Er were deposited in solution form, allowing their evaporation as neutral atoms directly into the gas cell through resistive heating. A thin rectangular strip of Ta foil was hand-cut to prepare the filaments. Figure 4.1 shows the installed Ta filament. To ensure that the Ta filament was properly installed, the voltage-current (V-I) characteristic was measured for the Ta filament on resistive heating as shown in figure 4.2.

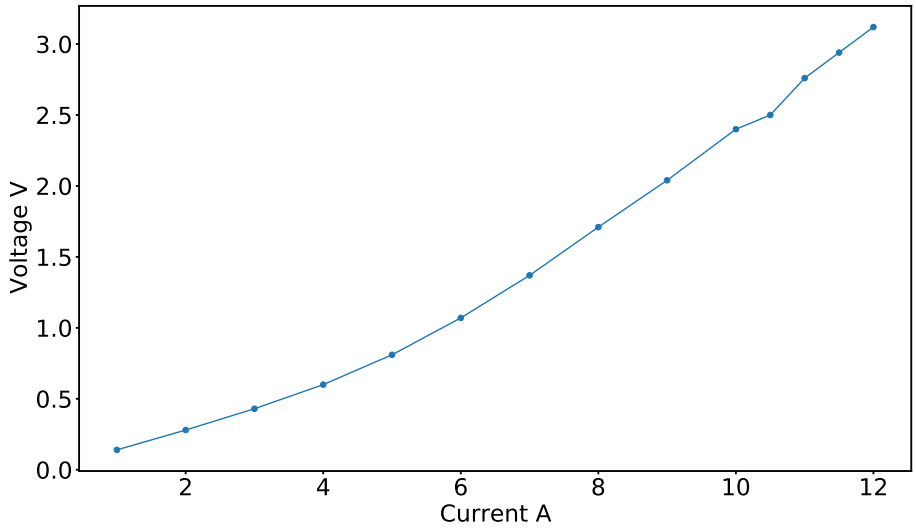

Figure 4.2: V-I characteristics of the Ta filament installed in the gas cell for offline measurements.

A 30 μL Er_2O_3 in HNO_3 solution was deposited on each of the two tantalum filaments installed in the gas cell. One of the filaments was resistively heated by $\approx$ 13 A (4 V) current to form Er atomic vapors. At the exit aperture of the gas cell, a de-Laval nozzle of Mach number $M = 8.11(12)$ was installed to create a hypersonic gas jet [7]. Details on the calculations and design of $M = 8.11(12)$ nozzle can be found in [64, 65]. The distance between the nozzle and the first entrance electrode of the S-RFQ was kept at about 5-6 cm which is the minimum distance required for the atoms in the jet to interact with 10 kHz laser pulses at least once. For gas-cell ionization, the first-step and second-step lasers were sent transverse and counter-propagating to the atomic beam, respectively.

The laser ionization of the Er isotopes was performed with the two-step laser scheme, developed and reported in [89], and is indicated in figure 2.16. The Er atoms were promoted from the ground state $4f^{12}6s^2\ {}^3H_6$, $J = 6$ to the first excited state (FES) $4f^{12}({}^3H)6s6p$, $J = 5$ by a laser tuned to 415.2 nm vacuum wavelength and then ionized via an auto-ionizing state above the ionization potential (IP), $4f^{12}({}^3H)5p^6 6s_{1/2}$ $J = 13/2$, by a laser tuned to 396.6 nm. For

the first excitation step in gas-cell ionization, we used a frequency-doubled, dual-etalon Ti: sapphire laser cavity, with an average fundamental linewidth of 1.8 GHz FWHM. For the same step in gas-jet ionization, we used a frequency-doubled, injection-locked Ti: sapphire laser seeded by an external-cavity diode laser (ECDL) Toptica Photonics DL100 [75]. The ECDL was installed with an 840 nm gain chip. An average fundamental linewidth of about 35 MHz was obtained for the laser. For the ionization step, we used a frequency-doubled, single-etalon Ti: sapphire laser of average fundamental linewidth $\leq$ 5 GHz FWHM. The first step and second step laser pulses were temporally overlapped by adjusting the pump power distribution and the focusing point of the pump beam into the Ti: sapphire crystal thereby varying the gain. Temporal overlap of the laser pulses was ensured by monitoring them using the photodiode signals collected from the pick-ups of the lasers.

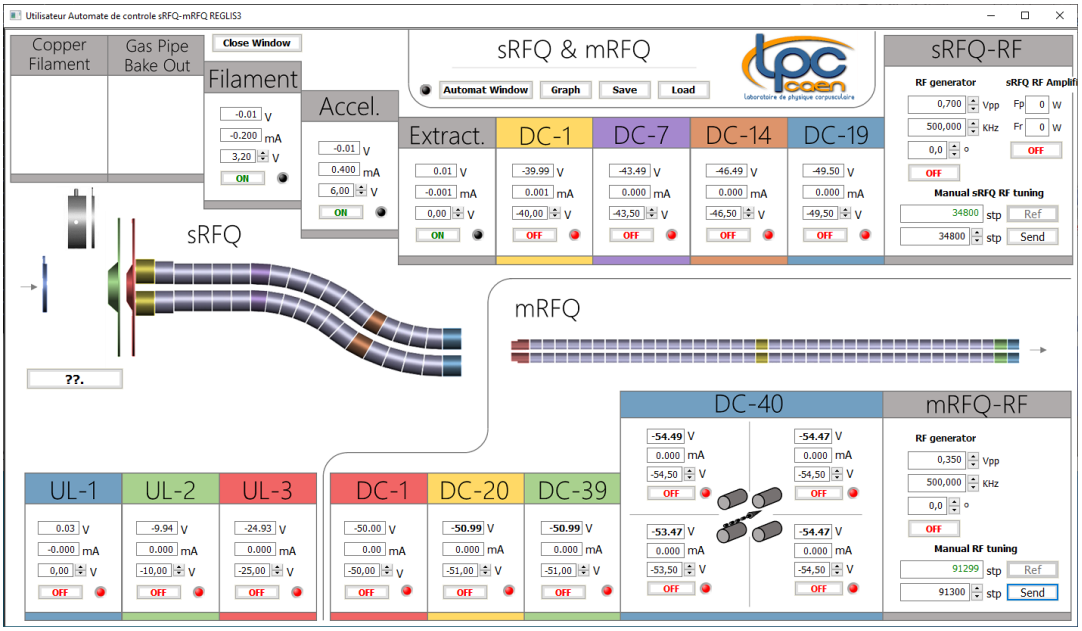

Figure 4.3: GUI for the S-RFQ and mini-RFQ with the current settings optimized for transport of Er ions.

Following Er ionization, the resulting ions were extracted through the S-RFQ and mini-RFQ from the residual pressure of the gas cell chamber into the high-vacuum ion-transport region. The voltages used in this work for the S-RFQ, mini-RFQ, and QMF are adapted from those reported in [67] while adjusting the overall bias of the transport line to the lower initial energy of the ions produced in gas. The graphical user interface (GUI) settings for the S-RFQ and mini-RFQ are shown in figure 4.3.

The combined efficiency of the S-RFQ and mini-RFQ had already been measured to be close to 100% using the Cs source placed approximately at the jet position, although having a much larger emittance than the laser ions produced in the jet [67]. The gas jet ions are assumed to have 100% transmission as well through the S-RFQ and mini-RFQ. This is yet to be proven experimentally to see if the collisions in gas affect the laser-produced ions. After passing through the S-RFQ and mini-RFQ, the laser-produced Er ions were sent through the QMF in transmission mode to obtain close to 100% transmission. A minimum ion-collector voltage of -40 V in the gas cell was required to completely suppress

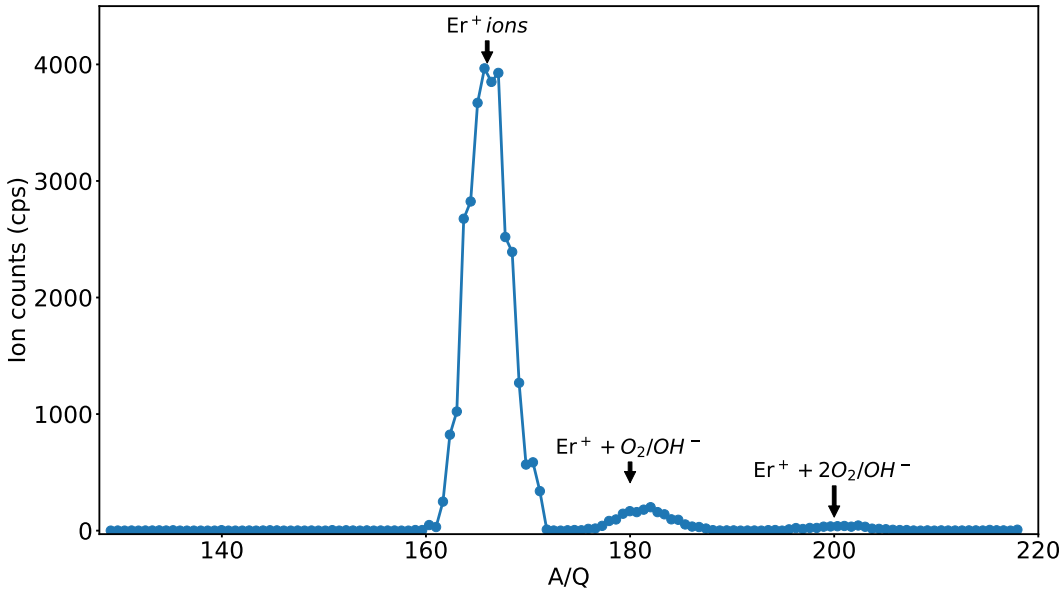

Figure 4.4: QMF mass scan of gas-cell ions obtained by scanning the RF and DC voltage in filtering mode, with the gas cell ion-collector voltage ON.

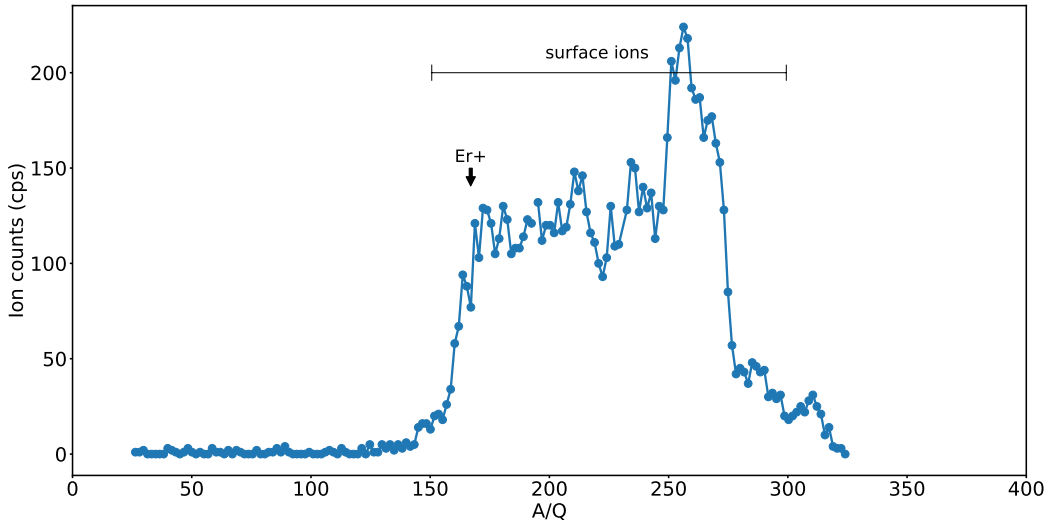

Figure 4.5: QMF mass scan of gas-cell ions obtained by scanning the RF and DC voltage in filtering mode, with the gas cell ion-collector voltage OFF.

the surface ions produced by the filament. The filament current was adjusted to obtain around 6300 cps at MCP 2 after the QMF. A mass scan was then performed with the QMF in filtering mode, by scanning the RF and DC voltages such that, for the requisite masses, Mathieu parameters $a = 0.225$, and $q = 0.706$ would be obtained, with an RF frequency of 500 kHz (knowing the QMF field radius of 10 mm). Figure 4.4 shows the resulting mass spectrum, where only ions in the Er mass range can be seen along with a small side peak which corresponds to adducts of Er forming oxides and hydroxides after laser ionization. Figure 4.5 shows the mass spectrum of ions formed after laser ionization without the application of collector voltage. It shows that without the collector, a large number of surface ions, produced by the filament in the gas cell during resistive heating along with the laser-produced Er ions, are reaching

the ion transport system. Figure 4.4 compared to figure 4.5 shows that collector electrodes efficiently suppress the surface ions formed in the gas cell. The baking of the gas cell and heating of the filament over time gradually reduce the surface ion contamination and could be even operated at a lower collector voltage.

In the filtering mode (used for the mass scan), the QMF transmission was 60%, with respect to the maximum number of ion counts detected in the non-filtering mode. Individual Er isotopes could not be resolved after the QMF as it can be seen in figure 4.4, which however is capable of selecting a range of about 10 mass units without a major loss in efficiency as seen from the test with Rb source [16]. This is important for online measurements where isobaric contaminants will be higher compared to the offline test and identification of the contaminants would be crucial to separate them from the ions of interest. For the rest of the tests, the QMF was kept in transmission mode. The GUI settings used for the transport through QMF are shown in figure 4.6.

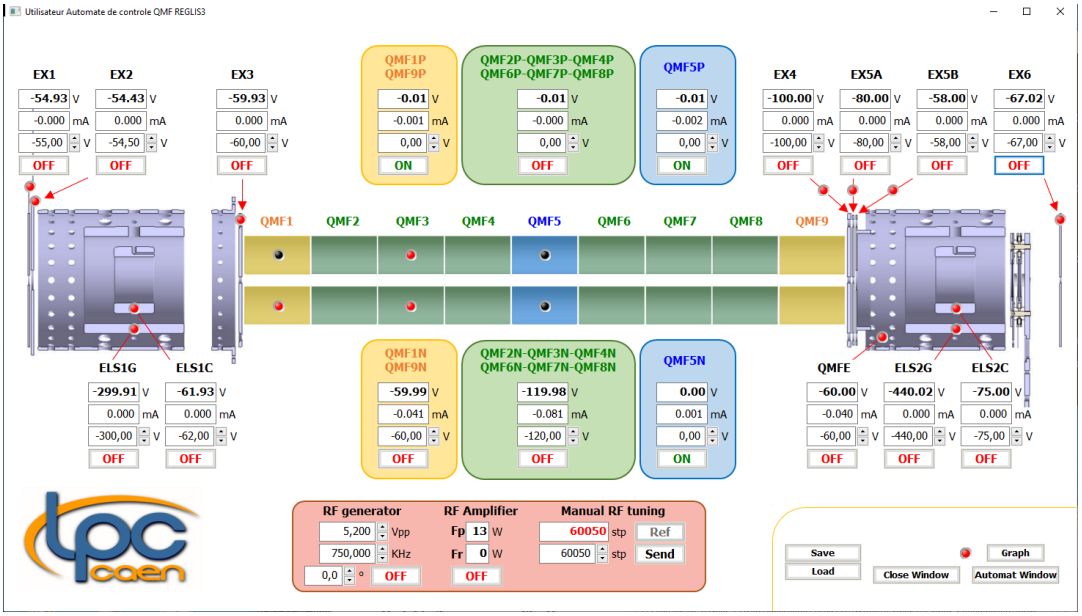

Figure 4.6: GUI for the QMF with the current settings optimized for transport of Er ions.

4.3 Buncher optimization

The continuous ion beam from the QMF was then sent to the RFQ-CB. A study of the bunching parameters was performed to obtain the optimum spatial and energy distribution of the bunches for injection into PILGRIM. The preliminary buncher transmission efficiency in the bunching configuration was 40(10)%. A rough estimate of 10% tolerance is given to the transmission efficiency considering the contribution of pile-up and MCP efficiencies. The relatively low transmission was due to an observed misalignment of the buncher. After correcting the misalignment of the buncher, transmission efficiency of $\geq$ 80(10)% was achieved.

Figure 4.7 shows the graphical user interface of the S^3-LEB cooler and buncher section in its current settings. A RF peak-to-peak voltage of 1.2 kV

with a frequency of 1000 kHz was applied to the cooler-buncher. The RF voltages are applied on separate electrodes from the DC voltages and the former are biased to -60 V. RF tuning was performed with which the capacitance of the impedance matching circuit could be adjusted to have maximum forward power coupling. This was performed for all RFQs. The timing trigger for bunches was provided by an external function generator. For optimization of the buncher performance, a characterization study of the RFQ buncher parameters was performed for maximum transmission and TOF resolution. The transmission through the buncher was investigated for different bunch parameters including the He pressure, the RF voltage, and the bunching voltages.

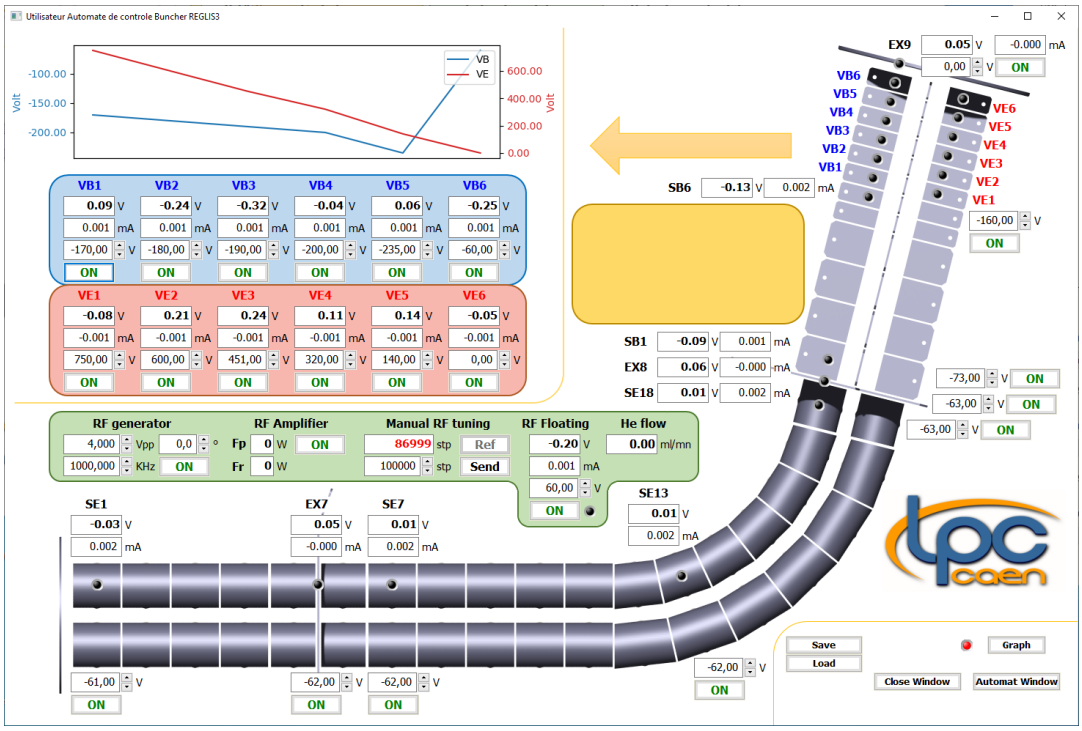

Figure 4.7: GUI of the cooler buncher section of S^3-LEB, showing the different electrode segments with VB and VE representing the bunching/trapping and extraction voltages respectively.

Transmission and TOF characterization

For the characterization of the RFQ-CB, the bunched ions from the RFQ-CB were sent through PILGRIM without trapping, and the TOF spectra were measured with the MCP installed after PILGRIM. Figure 4.9 and figure 4.10 show the transmission and TOF FWHM for ^{170}Er isotope at different a) buncher pressure, b) RF voltage and c) voltage of the bunching trap segment defining the depth of the potential well, at 10 Hz and 20 Hz bunch cycle respectively. To obtain the transmission rate and the TOF width, the ^{170}Er peak from the time of flight spectrum was fitted using a Gaussian profile as shown in figure 4.15. The fit function is given by:

$$G(x) = b + ae^{(-0.5(\frac{x-\mu}{\sigma})^2)} \tag{4.1}$$

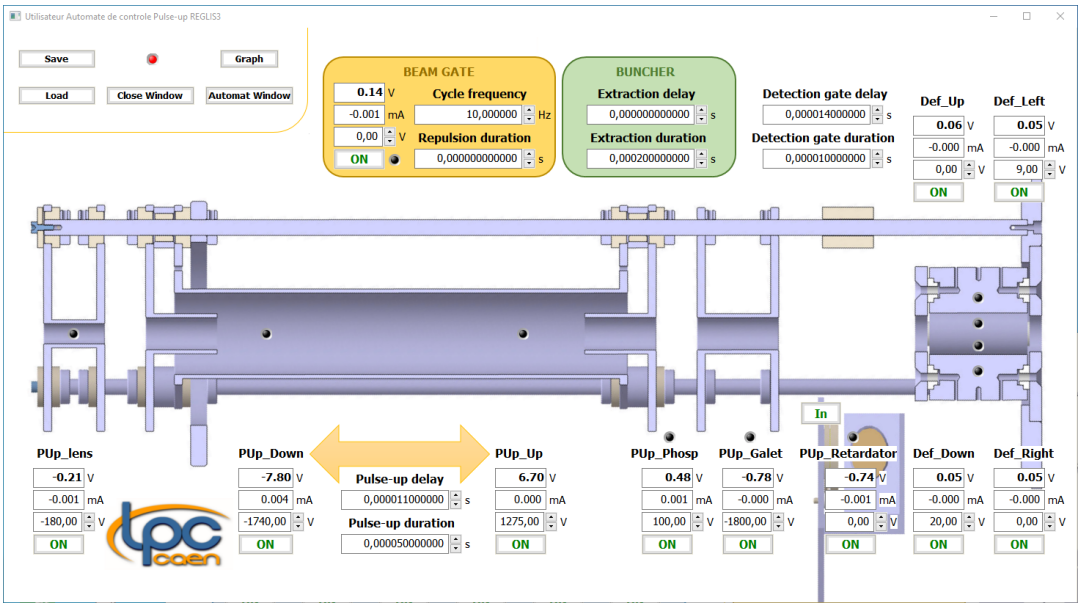

Figure 4.8: GUI interface for the PUP system before injection into the PILGRIM.

where b is the offset, a is the fit constant, μ is the mean value and σ is the standard deviation. The data for the two bunch cycle frequencies were taken on consecutive days and hence the count rates cannot be compared. However, both settings showed a similar trend in transmission and TOF focus with the change in bunch parameters. The 20 Hz bunch cycle in general gave an increased TOF FWHM compared to 10 Hz. The fact that bunching at 20 Hz provides less time for cooling of all the ions, compared to the 10 Hz cycle can be the reason for an increased TOF width for the same buncher conditions.

The He buffer gas pressures corresponding to a flow rate from 40 - 110 mL/min for both bunch cycles were investigated to obtain optimum transmission and TOF FWHM. Inset a) and b) of figure 4.9 and 4.10 shows that with increasing pressure in the investigated range, the transmission is increased due to better cooling in both cycles. For the 10Hz cycle, the TOF width remains mostly the same within the range of a flow rate of 75 - 110 mL/min (buncher pressure 1.18×10^{-3} to 2.6×10^{-3} mbar) showing that lower pressure was enough for cooling all the ions in the bunch. The pressure gauge was calibrated for air and hence a correction factor of 5.9 was multiplied to obtain the He pressure in the buncher. For 20 Hz, TOF width was decreasing showing that due to less cooling time, more pressure was required to cool the bunch.

Inset c) and d) of Figure 4.9 and 4.10 shows the dependence of transmission and bunch width on the RF voltage. An increase in RF voltage increased the transmission while the TOF remained mostly the same considering 1-σ of the error bars. RF voltage contributes to the radial confinement of the ions. An increase in the RF voltage might be causing better radial confinement of ions, increasing the number of ions reaching the detector. Radial confinement of ions should not affect the ions' time of flight thus giving a similar time of flight FWHM. Insets e) and f) show that increasing the bunching voltage VB5 improved the TOF width and at the same time reduced the transmission. By increasing VB5 voltage, one increases the depth of the electric potential well, for collecting the ions per bunch. This causes fewer ions with similar energy to

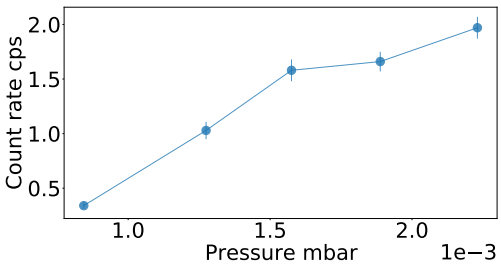

(a) Count rate vs buncher pressure

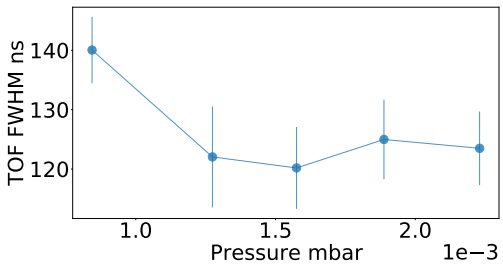

(b) TOF FWHM vs buncher pressure

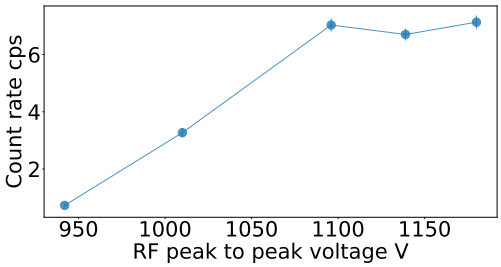

(c) Count rate vs RF voltage

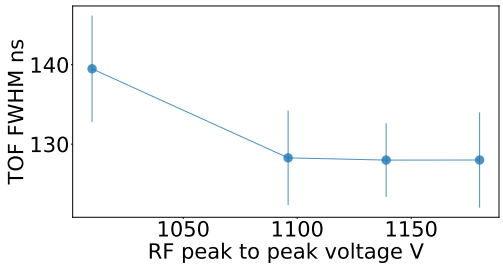

(d) TOF FWHM vs RF voltage

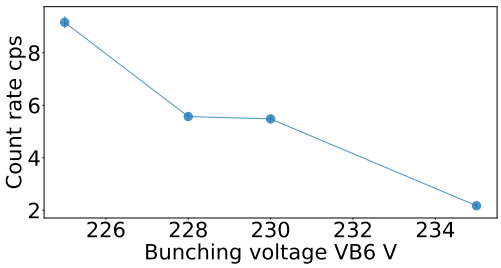

(e) Count rate vs bunch voltage VB6

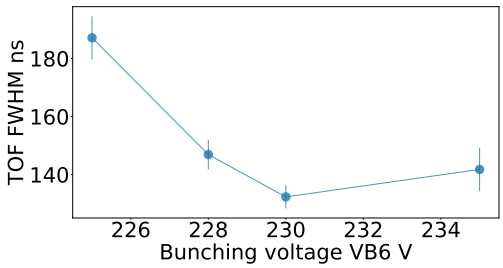

(f) TOF FWHM vs bunch voltage VB5

Figure 4.9: Tranmission and TOF width of ^{170}Er isotope at 10 Hz bunch cycle.

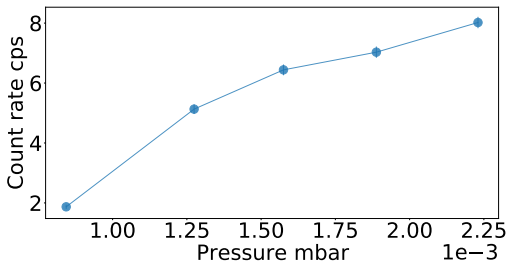

(a) Count rate vs buncher pressure

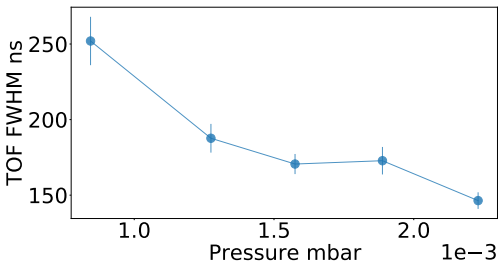

(b) TOF FWHM vs buncher pressure

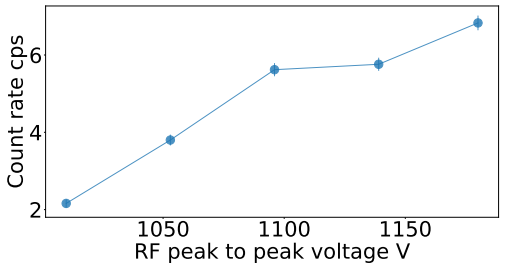

(c) Count rate vs RF voltage

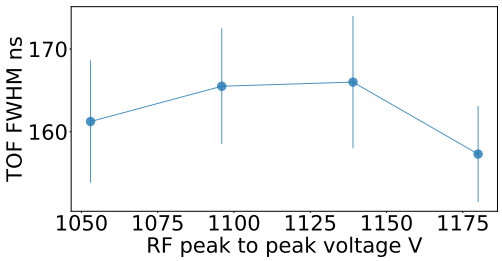

(d) TOF FWHM vs RF voltage

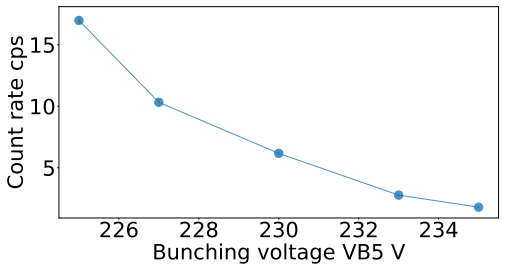

(e) Count rate vs bunch voltage VB5

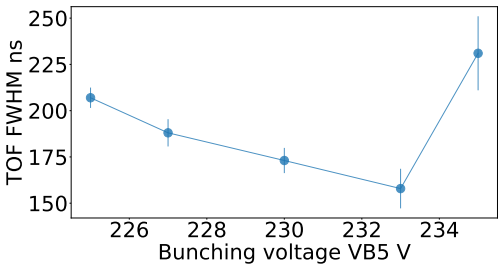

(f) TOF FWHM vs bunch voltage VB5

Figure 4.10: Tranmission and TOF width of ^{170}Er isotope at 20 Hz bunch cycle

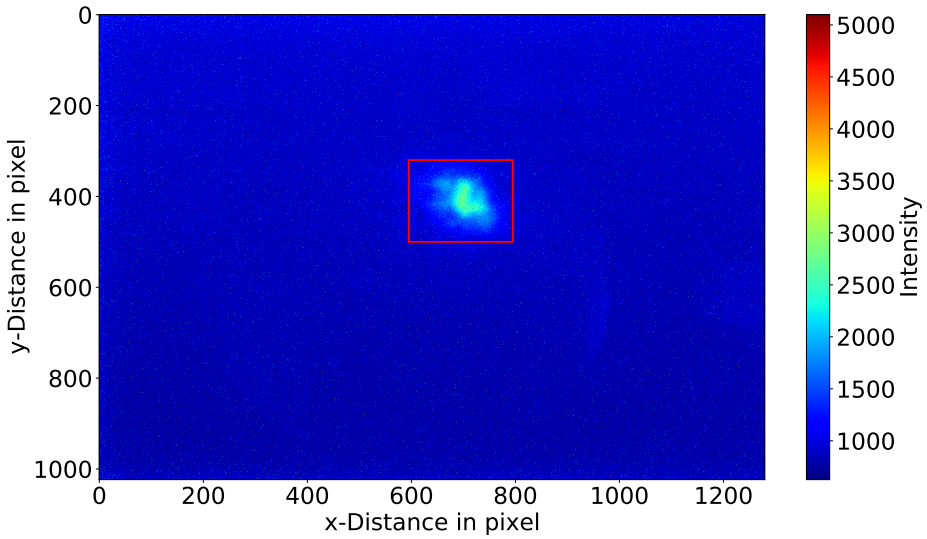

Figure 4.11: Spatial profile of the bunched beam intensity in pixels at 20 Hz bunch cycle. The color legend shows the intensity scale from maximum to minimum (red to blue).

be collected thus reducing the transmission while improving the TOF width.

Optimum bunch properties were obtained at 10 Hz and 20 Hz bunch cycles. At 20 Hz bunch cycle, a He flow rate of 110 mL/min and an RF voltage of 1.2 kV, the voltage settings for bunching and extraction are shown in GUI (see figure 4.7). In order to eliminate the chances of pile-up, a 20 Hz bunch cycle was chosen for further measurements.

Spatial and energy distribution of the bunches

Buncher spatial profile and bunch energy distribution were also measured. To obtain the buncher spatial profile, phosphor screen images were recorded using the phosphor screen installed after the pulse-up unit (refer to chapter 2). Figure 4.11 shows the spatial profile of the bunched beam at 20 Hz bunch cycle in pixels. Multiple images were recorded and the intensities were summed to obtain the spatial profile of the ion bunch as shown in figure 4.11. Figure 4.12 shows the Gaussian fit of image intensity for the X and Y-projections of the image recorded using a CCD camera. To perform the fit, the pixel distance was converted to distance in mm by multiplying with a conversion facor. From the image, the position of the edge of the mirror is obtained in pixels. The distance in pixels and the known 1-inch dimension of the mirror were used to calculate the conversion factor. Then a Gaussian fit was used to obtain the spatial dispersion. The fit function is given by equation 4.1). The tuning of the Einsel lens and pulse-up voltages were performed while recording these images to ensure there was no spatial drift of the ion bunches while optimizing pulse-up unit parameters. The spatial profile FWHM at the optimum buncher setting was measured to be 1.2(2) mm on the horizontal axes and 1.5(4) mm on the vertical plane as seen from the phosphor screen. The measurement shows that the ion bunches are spatially focussed roughly symmetrical along the XY planes. Due to the misalignment of the optics after RFQ, the bunches arrived

at the side of the detector. However, the ions were centered in the RFQ at extraction.

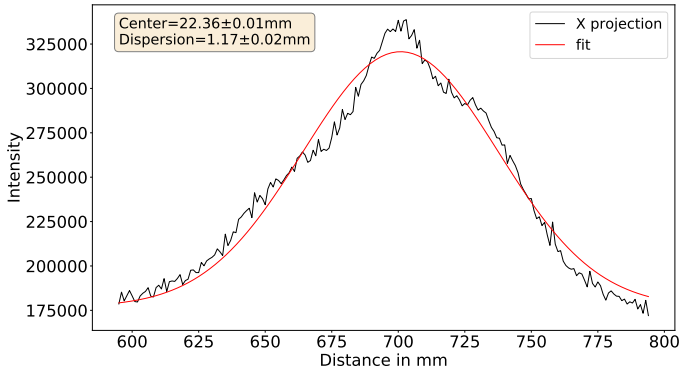

(a) X-projection

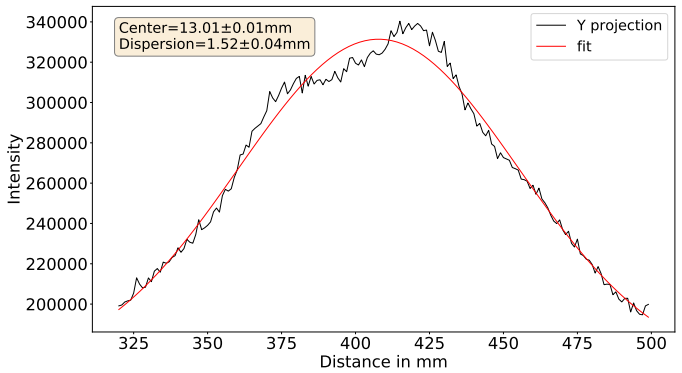

(b) Y-projection

Figure 4.12: XY projection of the image intensities from the phosphor screen

To obtain the bunch energy distribution, the pulse up retarding voltage(see figure 4.8) was scanned from maximum to minimum transmission. This voltage is applied on one of the grids of the MCP 3 installed after the pulse-up unit. An error function fit was performed with the resulting transmission data to obtain the energy dispersion as it is the cumulative distribution function of a Gaussian energy distribution profile. The error function fit equation is given by:

$$f(x) = \frac{a}{2}\left(1 + erf\left(\frac{x-\mu}{\sigma\sqrt{2}}\right)\right) + b \tag{4.2}$$

where a and b are the fit constants, x are the energy values, μ is the mean, σ is the standard deviation. For the set buncher parameters, the energy distribution obtained is shown in figure 4.13. The energy distribution of the ion bunch was measured with its mean at 3 keV kinetic energy resulting in an FWHM = 13(1) eV after the pulse-up electrode. It can be seen that the measured mean energy of the bunches from figure 4.13 is larger than the sum of V^+ and V^- applied in the Pulse-Up which is due to the initial kinetic energy of the ions before Pulse-Up acceleration.

The buncher characterization was performed prior to the re-alignment of the buncher. Hence, optimizing the cooler buncher parameter is still in progress to

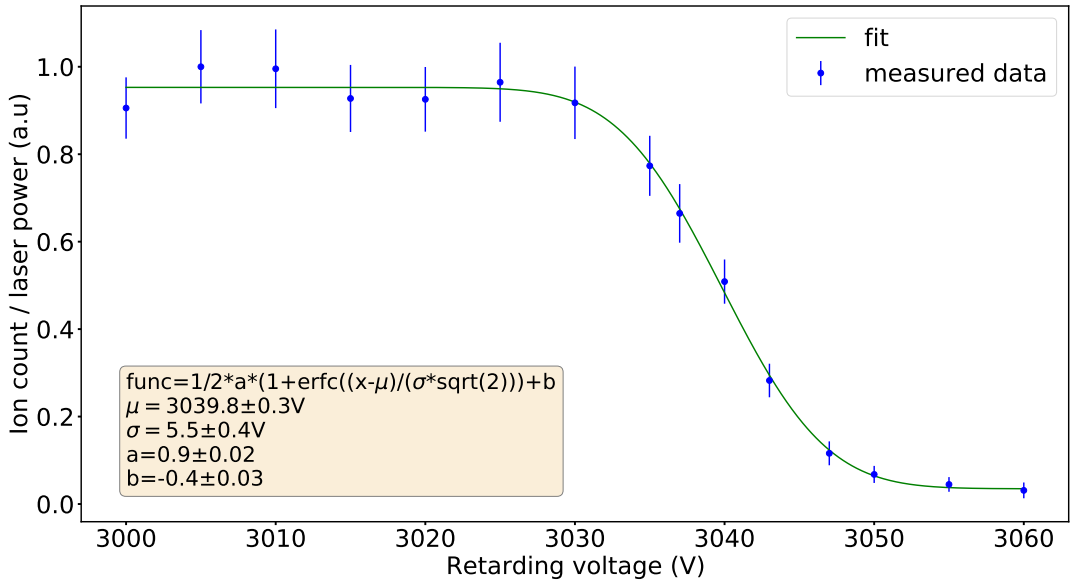

Figure 4.13: Gaussian cumulative distribution function fit performed to obtain the FWHM of the energy distribution of the bunched beam at 20Hz bunch cycle. The ion counts are normalized with laser power and scaled to unity. Each data point is averaged for the measured time of 100 s with the error bar showing the standard deviation from the average value.

obtain the optimum initial temporal spread and kinetic energy distribution for optimum injection to PILGRIM. The currently achieved bunch properties do not give the best achievable resolving power (¿ 100000) in PILGRIM but good transmission which was needed for the in-gas jet laser spectroscopy measurements. The transmission test measurements shown in 4.9 and figure 4.10, will be reconfirmed. The measurement performed in this work has shown that a clear compromise has to be found between the transmission and resolution and the misalignment might make it more critical. It was observed that the shape of the electric potential for the extraction of the bunches had a significant impact on the bunch profile. A spatial shift in bunches was also observed with tuning of the last extraction plate EX9. This might have been because of the mechanical misalignment observed and corrected later. The EX9 and the pulse-up lens voltages were optimized to make sure that the ions were reaching the center of the phosphorous screen.

PILGRIM injection

The laser ions were injected into the PILGRIM for the time of flight detection and PILGRIM optimization. The high voltage switch was applied to the pulse-up tube such that the ion entering the tube first sees -1740 V and thus gets accelerated from a few eV to about 1750 eV. As the ions reached the center of the tube, the voltage was switched to 1275 V pushing the ions out as well as accelerating them to have nearly 3 keV of kinetic energy. After the pulse-up unit, deflector voltages were tuned to obtain the maximum transmission to PILGRIM. The deflector voltage settings are presented in table 4.1.

At the entrance of the PILGRIM, another set of XY-deflectors, a transfer lens with two electrodes, and an Einzel lens are installed. The entrance de-

Table 4.1: Deflector voltages setup after pulse up unit.

Deflector	Voltage V
Up	0
Down	20
Left	9
Right	0

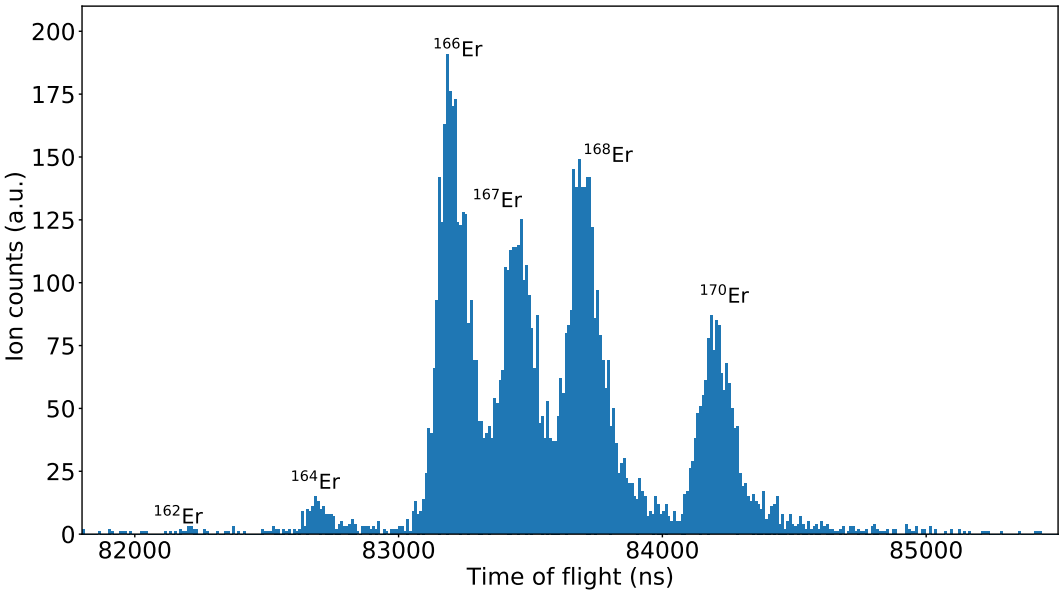

Figure 4.14: Time-of-flight spectra of laser-produced Er ions in a shoot-through mode of the MR-TOF MS with the ion-flight path length of ≈ 4.2 m from the buncher extraction.

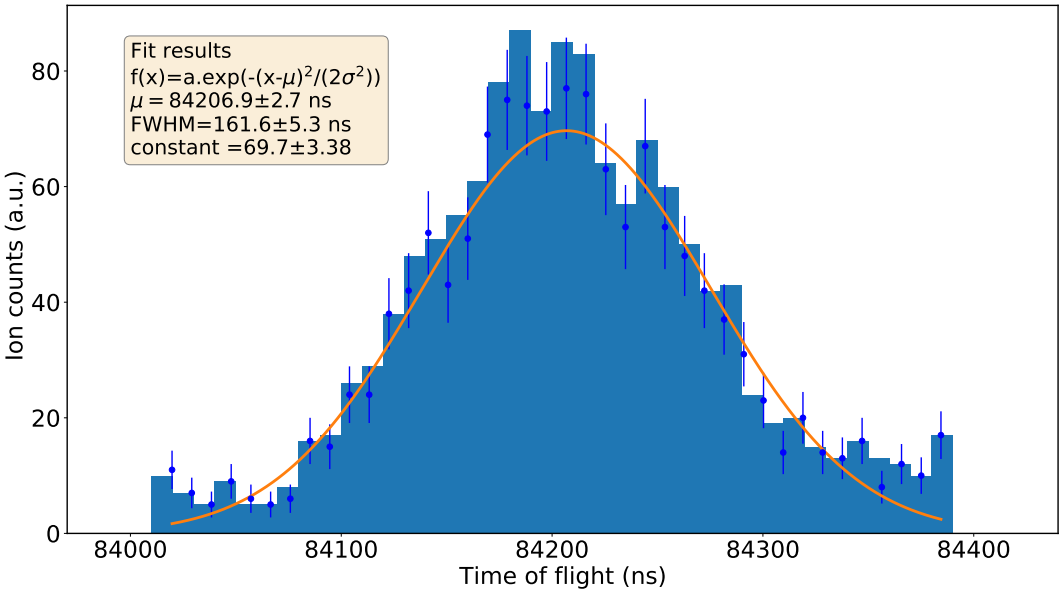

Figure 4.15: Time of flight spectrum of ^{170}Er at a bunch cycle of 20 Hz with mean TOF = 84.2 μs and TOF FWHM = 162(6) μs.

flectors and lens voltages were tuned and set to have maximum transmission through PILGRIM. The X-deflectors had to be tuned to 30 V whereas the Y

deflector was almost set to 0 V showing that the ion path was drifting from the buncher to PILGRIM in one plane and had to be corrected. The lens voltages were fixed at 1150 V and 610 V where maximum transmission was obtained. There is an injection lens as well as an extraction lens before and after the mirror electrodes which were set to -2500 V and -1500 V respectively. The mirror electrodes of the PILGRIM were kept at the same voltage as it was for the test settings with the alkali source as mentioned in section 4.1. After the optimization, the transmission from the buncher (in bunching configuration) to the end of PILGRIM without trapping was found to be 80(20)% with bunch setting as shown in figure 4.7. Figure 4.14 shows the obtained PILGRIM shooting-through time-of-flight (TOF) spectrum of all the stable Er isotopes, with first-step and second-step lasers kept at a fixed frequency, agreeing roughly with the natural isotopic abundance (^{162}Er-0.139%, ^{164}Er - 1.6%, ^{166}Er - 33.5%, ^{167}Er - 22.9%, ^{168}Er - 27%, ^{170}Er - 14.9%). The obtained TOF width for ^{170}Er without trapping was with mean TOF ≈ 84.2 μs from the buncher extraction to the end of PILGRIM and FWHM of 157(6) ns, with optimization still in progress. The preliminary resolving power obtained is $R \approx 80,000$ for 1000 revolutions which can be improved to the order of $R \approx 10^5$ as seen from the tests with alkali elements [90, 70, 8] (See section 4.1).

Supression of contaminants with PILGRIM

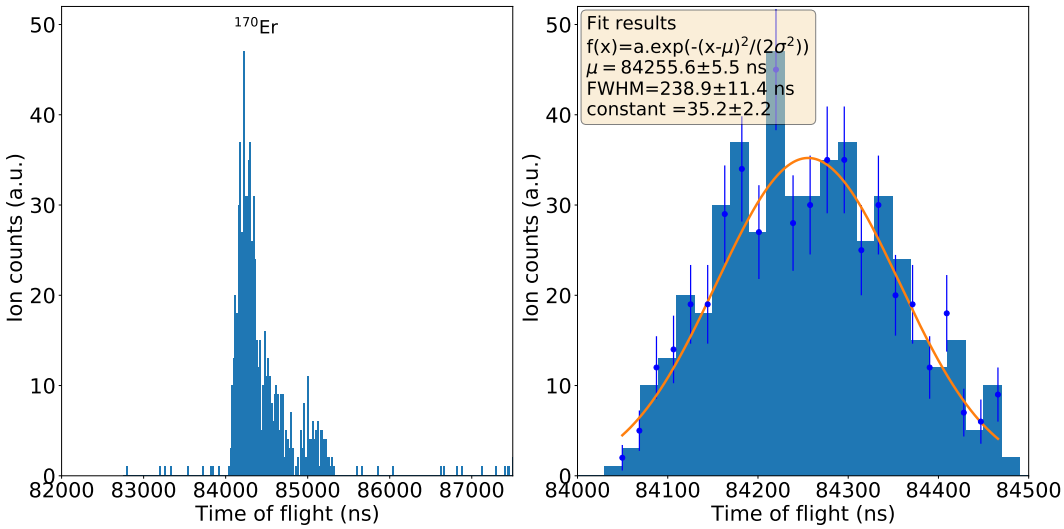

Figure 4.16: Time of flight spectrum of ^{170}Er at a bunch cycle of 20 Hz after trapping for 1072 revolutions. The left inset shows the ^{170}Er with a side tail of contaminant. The right inset shows the Gaussian fit giving a TOF FWHM = 239(11) ns.

For the efficient suppression of contaminants, an appropriate number of revolution/ trapping times can be chosen such as to extract only the ions of interest. The extraction of ^{170}Er after 1072 turns is shown in figure 4.16. This is because, at this particular number of turns, only ^{170}Er is at the center of the PDT due to increasing TOF separation. The TOF width of the ^{170}Er shown in figure 4.16 is broader compared to the peak obtained without trapping (see figure 4.15). This might be due to voltage fluctuations which make the

bunches have slightly different TOFs together giving a broadened TOF after a certain number of turns. Another reason can be the optical aberrations which might cause the ions to have slightly long or short TOF in each turn. These effects become more crucial with the increase in the number of turns. Thus an unoptimal TOF focus and voltage fluctuation/aberrations can lead to broader TOF peaks.

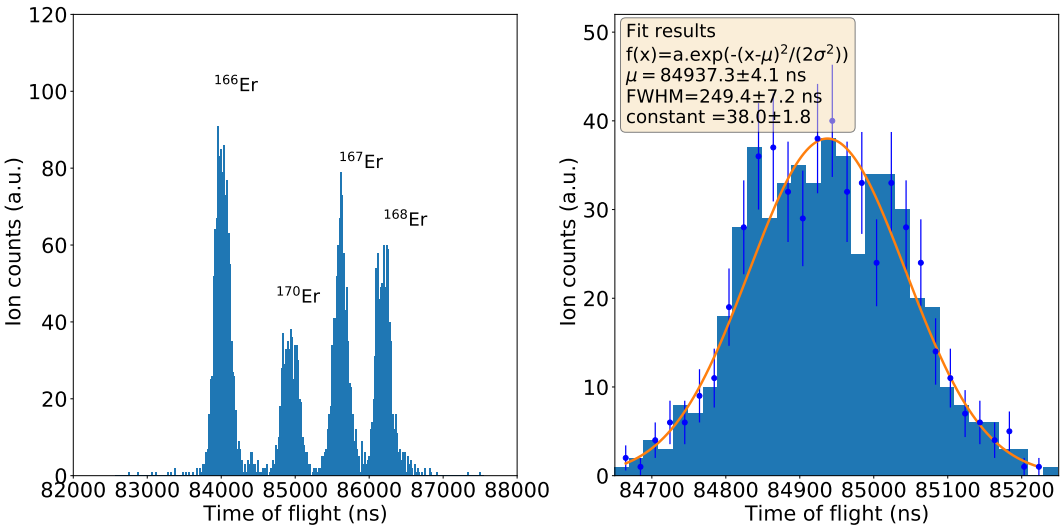

Figure 4.17: Time of flight spectrum (with offset) of Er isotopes at a bunch cycle of 20 Hz after trapping for 1000 revolutions for ^{170}Er. The right inset shows the Gaussian fit for ^{170}Er giving a TOF FWHM = 249(7) ns. The offset is because the trigger to the FASTER acquisition is shifted by the trapping time and hence does not give the total TOF of the ions but the TOF with the trapping time subtracted.

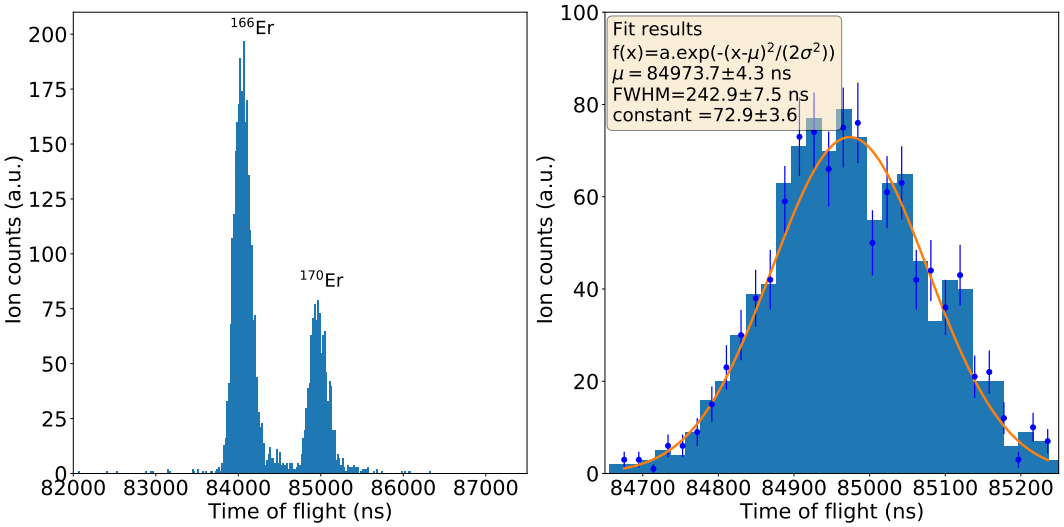

Figure 4.18: Left inset: Time of flight spectrum of Er isotopes at the same conditions as figure 4.17 with DT1 extraction of ^{167}Er and ^{168}Er. Right inset: shows the Gaussian fit for ^{170}Er giving a TOF FWHM = 243(8) ns.

Another technique used in PILGRIM is by utilizing the segmented sections of the PILGRIM pulse drift tube (PDT). The drift tube consists of three sec-

tions DT1 at the entrance, DT2 at the center, and DT3 at the exit of the PDT (refer to figure **??**). The DT1 can be switched to extract the contaminants at a different number of revolutions without affecting the ions of interest. Due to the difference in the time of flight between the ions of interest and the contaminants, the contaminants can be extracted from DT1 at a turn when the ions of interest are not in that drift tube section but only the contaminants. The switching of the drift tube sections was tested and efficient suppression of contaminants was achieved. The ions of interest were extracted at 1000 revolutions. The contaminants were extracted using DT1 at a lesser revolution which escaped out somewhere to the chamber. This method was tested by the extraction of ^{167}Er and ^{168}Er as contaminants by DT1. The time of flight spectra without suppression at 1000 turns for ^{170}Er is shown in figure 4.17. The time of flight spectra of ^{166}Er and ^{170}Er with ^{170}Er at 1000 turns after the extraction of ^{167}Er and ^{168}Er using DT1 is shown in figure 4.18. In order to identify the possible contaminants as well as to obtain their position in the MR-TOF-MS with respect to the ions of reference, a Python-based software tool was developed as reported in [90] which could provide the time of flight of the ions at a specific number of turns. The details of the work performed on the PILGRIM optimization with Er ions can be found in [90]. It can be seen from fits of ^{170}Er (from figure 4.17 and figure 4.18) that the mean TOF is slightly shifted indicating TOF drifts. This might be because of the drifts in the mirror electrode voltages. PILGRIM optimization is still in progress and future prospects include adding voltage stabilization to the mirror electrodes to minimize any drift in TOF as well as to improve the resolving power.

With the optimization still in progress, the transmission has been improved significantly from the QMF to PILGRIM compared to the previous measurement, especially in the buncher unit. With the optimization work performed, a total relative transmission efficiency of 80(20)% is achieved. Here, 20% uncertainty is given considering factors such as pile up, and the detector efficiencies.

4.4 Laser spectroscopy of Erbium

Apart from the laser ionization and transmission studies of the ions through S^3-LEB, resonance-ionization laser spectroscopy of stable Er isotopes in the gas cell/gas jet was also performed. For the in-gas cell studies, the first step laser used was a dual etalon Ti: sapphire laser. For the in-gas jet studies, an injection-locked Ti: sapphire laser laser was used as the first step. The second step laser for both studies was a single etalon BB Ti: sapphire laser. Laser setups used are discussed in detail in section 3.2. For the laser-spectroscopy measurements in the gas cell and gas jet, ion counts were measured using the MCP detector after QMF and the MagneToF detector after PILGRIM respectively. The ion counts were digitized with respect to time with a resolution of 4 ns/bin using a time-to-digital (TDC) converter developed by KU Leuven and synchronized to the 20 Hz cycle of the buncher.

4.4.1 In-gas-cell laser ionization

For in-gas cell ionization laser spectroscopy measurements, the first-step laser and the second-step laser were sent transversal and counter-propagating

to the axis of propagation of the atoms, respectively. The ions were detected and measured using MCP 2 after the QMF. At MCP 2, the individual isotopes are not resolved owing to their small isotope shift. Hence the gas-cell measurements are performed for all isotopes together without mass separation at MCP 2. However, this should not affect the measured values as the isotope shift between the different isotopes is in the order of 100 MHz, whereas the broadening of the gas-cell spectra is several GHz. The ion counts were recorded while scanning the first step laser power to obtain Er resonances. As the first test, Er ionization was performed in the gas cell with the first-step laser at full available power. Er ions were successfully produced and the resonant excitation spectra obtained can be seen in figure 4.19. It can be seen that the spectral FWHM is more than tens of GHz. This is because the spectrum is largely power-broadened.

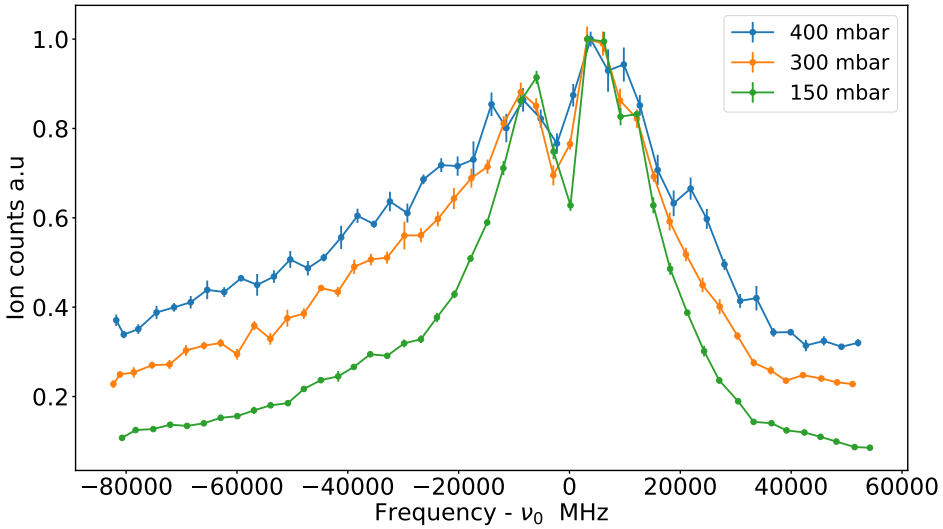

Figure 4.19: Resonance ionization laser spectroscopy for different gas cell pressure at full first-step laser power of 40 mW and fundamental FWHM line width 1.8 GHz, resulting in broadening as well as a dip in the resonance peak. Here the offset $\nu_0 = 721995050$ MHz.The counts are scaled to unity for comparison of resonances at different gas cell pressures. The error bars show the standard deviation of the mean counts for an averaging time of 5 s.

To reduce power broadening, a saturation test was performed by recording the ion counts at different laser powers measured before the gas cell chamber. The saturation curve for the first step is shown in figure 4.20 where the data was fitted with a least-square method using lmfit model from Python programming. The curve function used for fitting was :

$$I(P) = a + b \times \frac{(P/P_0)}{(1 + P/P_0)} \tag{4.3}$$

where I(P) is the intensity of the ions as a function of laser power P, P_0 - saturation power of the laser, a - offset due to background/non-resonant ions, and b - the maximum counts. The saturation laser power obtained from the fit was 2(1) mW with an offset of 2.36(57) cps and a constant of 1498(147) cps. The saturation curve for the first-step transition was thus measured and the

laser power was kept below 0.15 mW until no more power broadening of the spectrum was observed (refer to section 1.2.4). Power saturation with collisional de-excitation effects can also cause a loss in ionization efficiency. Figure 4.19 shows a dip in the resonance peak which is suspected to be a combined effect of pressure and power broadening. This resonance dip was also observed in the gas cell ionization of Thorium experiments in JYU [91, 92]. The exact nature of this collisional de-excitation phenomena in heavier mass regions is not completely understood and requires dedicated characterization studies as performed in [93]. At a considerably low laser intensity of 0.15 mW, the dip in the resonance was not observed as can be seen in figure 4.21 for the different gas cell pressures studied. The saturation test for the second step was also performed and it was seen that the second step at its maximum available power was not saturating the transition. The second-step laser power was kept at 50 mW.

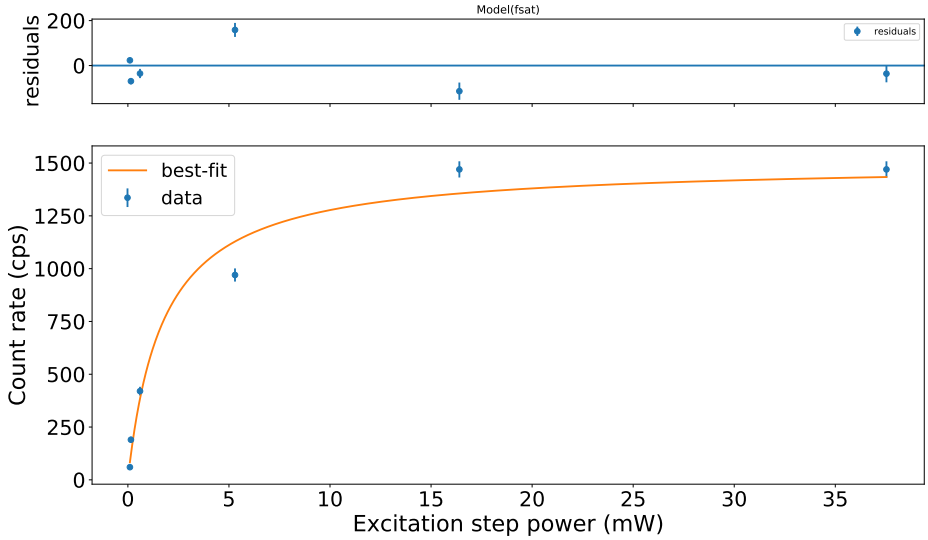

Figure 4.20: Power saturation curve fit for first step transition using a dual-etalon laser in gas-cell laser ionization giving a saturation power of 2(1) mW. The residuals are the difference between the data and the fit model. Error in the Er counts is calculated from the square root of the counts at each first-step laser power.

In-gas cell characterization

In the gas cell, the collisions of the atoms with buffer gas cause pressure broadening of the spectrum as explained in section 2.1.2. The pressure broadening can be several GHz wide, which limits precise measurements of atomic isotope shifts and hyperfine constants. In order to quantify these broadening effects, in-gas-cell resonant laser ionization of Er atoms was performed and characterized for different gas-cell pressures. The broadening of the Er excitation spectral lines was studied by scanning the laser frequency over the FES transition resonance peak. Figure 4.21 (top panel) shows the gas cell FES transition spectra as a function of argon gas cell pressures from 90 - 500 mbar, compared to a single resonance measured for ^{170}Er in the gas jet. Considering only the gas cell resonances, it can be seen that the resonances broaden and experience

a centroid shift to lower frequencies with an increase in the gas cell pressure [20]. This phenomenon has been explained and a theoretical calculation of the broadening and shift for the same transition is shown in section 2.1.2. It can be seen from the measurements that the resonance peak centroid measured in the gas jet measurement is slightly shifted. The gas jet measurement is only for ^{170}Er and the gas cell measurement is for all isotopes. Also, the laser frequency measurements for the in-gas cell spectroscopy were performed with a HighFinesse WS6 wavemeter with an accuracy of 600 MHz (fundamental) in a single day whereas the gas jet measurements were performed, on a different day, with a WS7 version, having an absolute accuracy of 30 MHz. The reference transition frequency corresponds to the in-jet resonance of ^{170}Er which is measured to be ν_{01} = 721,995,054(60) MHz. The value is within the wavemeter accuracy of the transition frequency deduced from the atomic beam unit (ABU) measurements (ν_{01} = 721,995,048(60) MHz) [80].

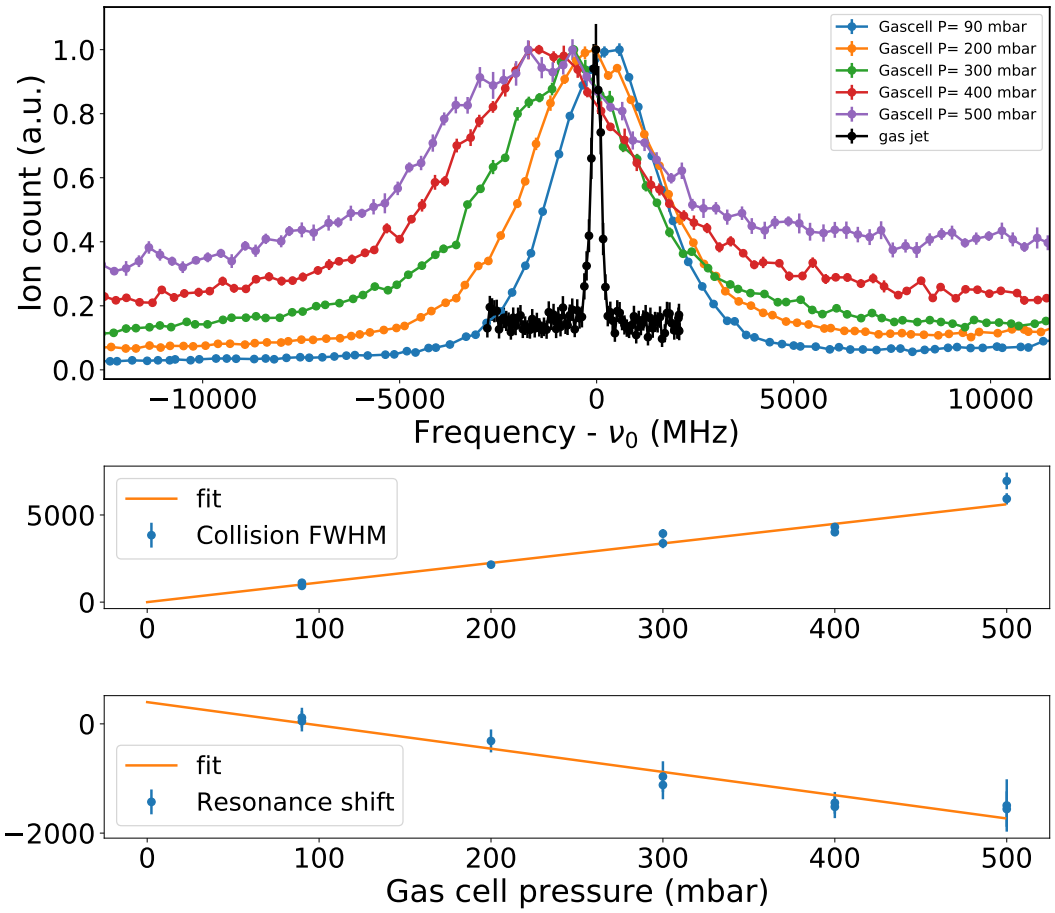

Figure 4.21: (Top) Resonance ionization spectroscopy of Er in the gas cell for different gas pressures (color) compared to the gas-jet spectroscopy of ^{170}Er (black) for the FES transition relative to ν_0 = 721,995,050 MHz. (Middle and bottom) Collision FWHM and centroid shift were determined for the spectra as a function of pressure. A linear fit is applied to the data to extract the pressure broadening and pressure shift coefficients discussed in the text.

To quantify the collisional broadening and shift, spectra for the different gas cell pressures were fitted with a Voigt profile, using the Statistical analysis toolbox for laser spectroscopy (SATLAS) package [94]. The fit for 300 mbar gas

cell pressure is shown in figure 4.22. Several scans were performed and fitted for each gas cell pressure. The rest of the fits are added in the appendices (See figure A.1). The Lorentzian and Gaussian contributions can be individually estimated

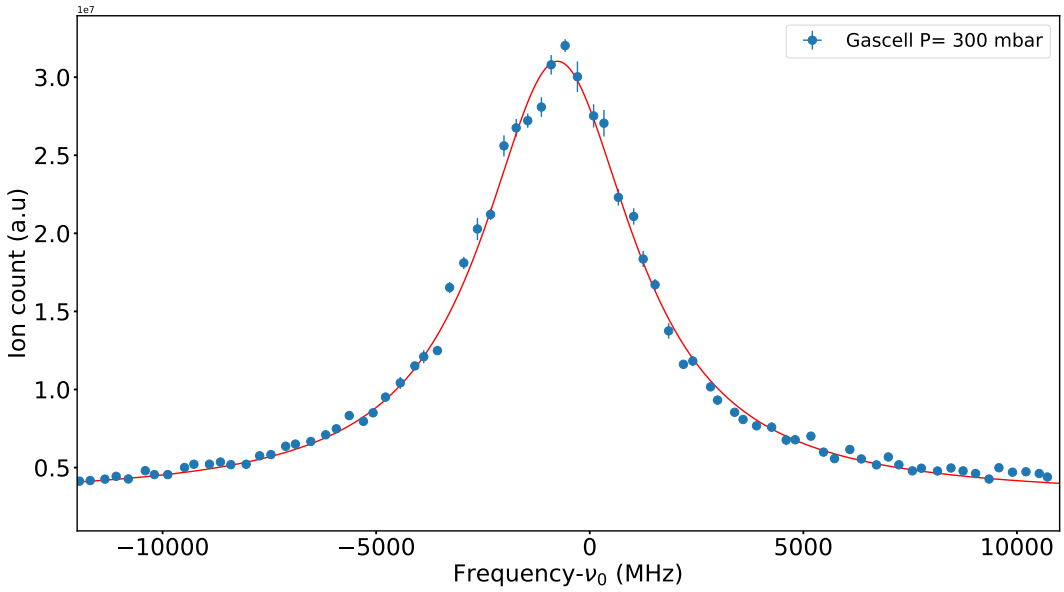

Figure 4.22: Voigt fit(red) for the resonance excitation spectra (blue) performed in the gas cell at 300 mbar gas cell pressure.

from the Voigt profile using the equation 1.75. The Doppler FWHM for the FES transition at an estimated gas cell temperature of $T = 353(16)$ K was calculated to be 0.75(2) GHz (according to equation 1.74) [20]. The estimation of the gas cell temperature is from the gas jet measurements and is explained in section 4.4.2. The first-step laser linewidth for gas-cell ionization was an average of 1.8 GHz FWHM obtained from the wavemeter readout. Then the total Gaussian FWHM could be calculated from the square root of the sum of the squares of Doppler FWHM and the laser FWHM linewidth. Thus the Gaussian FWHM was estimated as $\Delta_G = 2.6(2)$ GHz. The uncertainty involves the statistical error from Doppler width calculation and the wavemeter uncertainties. For individual gas cell pressures, the Gaussian FWHM was fixed to the calculated value in the fitting procedure to obtain the resonance center and the Lorentzian FWHM, the latter being entirely due to the collisional broadening and the natural transition linewidth. The natural spectral linewidth depends on the transition probability (9.6×10^7 s^{-1}) and can be calculated to be 15.3 MHz (according to equation 1.61) which is negligible compared to the collisional broadening effect [95]. A linear least-squares fit was applied to the resulting collisional FWHM and resonance shift data as a function of different gas cell pressures from which the collisional broadening coefficient (Γ_{coll}) and the shift coefficient (Γ_{sh}) were deduced to be 11(1) MHz/mbar and -4(1) MHz/mbar, respectively. The data (blue) and the resulting fit (orange) are shown in the lower two panels of figure 4.21). The centroid shift from the fit line extrapolates to -398(143) MHz for zero gas cell pressure. This could be a residual isotope shift effect because the reference frequency in gas jet measurements is for ^{170}Er. Since argon is used as the buffer gas, the shift coefficient has a negative sign, i.e., the centroid is red-shifted [96]. The spectral FWHM for a gas cell pressure

of 300 mbar was measured to be on average 4.5(2) GHz. The experimentally deduced value is comparable with the estimated value for this Er transition (refer to section 2.1.2).

Calculation of uncertainities

For the calculation of the uncertainties for the collisional FWHM and shift, the Voigt fit for an individual scan was performed by fixing the Gaussian FWHM values and extracting the Laurentzian FWHM. The collisional FWHM was extracted by subtracting the natural atomic transition line width from the resulting Lorenztian FWHM. For an individual scan, the Gaussian FWHM values were fixed to the calculated value Δ_G, as well as $\Delta_G + \sigma_{\Delta G}$ and Δ_G - $\sigma_{\Delta G}$ where $\sigma_{\Delta G}$ is the uncertainty obtained for the estimated Gaussian FWHM. The Voigt fit for each gas cell pressure for the excitation spectra was performed with all three fixed Gaussian contributions. If the collisional FWHM values obtained from fixing $\Delta_G + \sigma_{\Delta G}$ and Δ_G - $\sigma_{\Delta G}$ are Γ^+ and Γ^-, a total propagated uncertainty value was calculated from them as:

$$\sigma_{prop} = 0.5 * (\Gamma^+ - \Gamma^-) \tag{4.4}$$

The σ_{prop} was added to the uncertainty obtained from the fit (σ^2_{fit}) to obtain the total uncertainty as:

$$\sigma_{tot} = \sqrt{\sigma^2_{prop} + \sigma^2_{fit}} \tag{4.5}$$

Ionization step transition

Like the first excitation step transition, the second transition also undergoes collisional broadening and shift of the resonance centroids. For the second-step transition, a frequency scan over the resonance was performed to obtain the broadening coefficient but several nearby autoionizing states along with collisional de-excitation make it difficult to quantify the collisional broadening effect. Figure 4.23 shows the resonance scans over the peaks for the second step transition at different gas cell pressures. The resonances can be seen with several small resonances or side peaks and dips which are effects of the collisional quenching. The second-step transition was also not saturated and hence slight fluctuations in the laser power while scanning influenced the laser ionization efficiency. Even though quantifying the resonance was challenging, it can be seen from the figure 4.23 that the maxima of the highest peak shifts to lower frequencies as well as experience broadening.

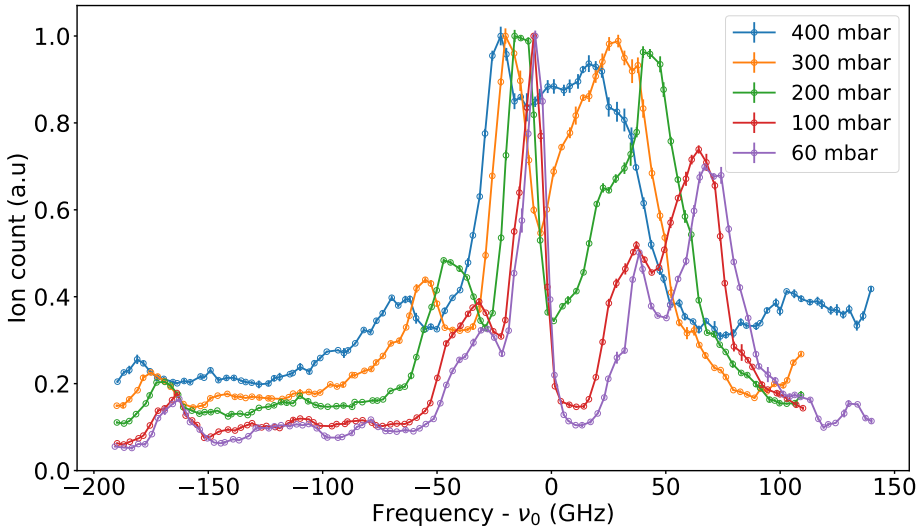

Figure 4.23: Resonance scan of the second-step transition for different gas pressures (color). Here the offset $\nu_0 = 755786.97$ GHz. The ion counts were normalized on power and scaled to unity for comparison of different gas cell pressures. The error bars are the standard deviation of the averaged count for a time of 5 s normalized on power.

4.4.2 In gas jet laser ionization and spectrosocpy

To perform resonance ionization spectroscopy in the gas jet, the gas-jet chamber was pumped to a pressure of 1.25×10^{-1} mbar for a gas cell pressure of 300 mbar. This was to match approximately the background pressure with the gas jet pressure in order to obtain a homogenous jet for laser spectroscopy studies according to the equation 2.6.

Two laser configurations were used and characterized, with the first-step laser aligned both counter-propagating or transverse to the gas jet, while the second-step laser was transverse and counter-propagating, respectively. For the transverse laser path in the jet, a laser beam sheet of width 2 mm and length 50 mm was prepared using a combination of two cylindrical lenses (focal lengths, f_1 = -20 mm and $f_2 = 250$ mm). A saturation curve for the FES transition with the injection-locked laser was measured as shown in figure 4.24. For the transverse configuration, the first-step laser power was kept below 1 mW (measured before the laser sheet) to minimize the power broadening. The second-step laser power was kept around 170 - 200 mW. The second-step laser was reoptimized to obtain higher count rates for gas-jet spectroscopy measurements and hence the higher power compared to the gas-cell spectroscopy measurements.

Several scans were performed in the gas jet for both laser configurations and all of them gave a spectral resolution of less than 300 MHz FWHM. Figure 4.21 (top panel) shows a comparison of the gas cell (color) and gas jet spectra (black). The values are scaled to 1 for comparison. The obtained gas jet ion counts were more than triple compared to the gas cell ion counts for the same second-step laser powers. The increased count rate in the gas jet compared to the gas cell could possibly be due to the collisional quenching effects occurring inside the gas cell causing the de-excitation of atoms from the intermediate state

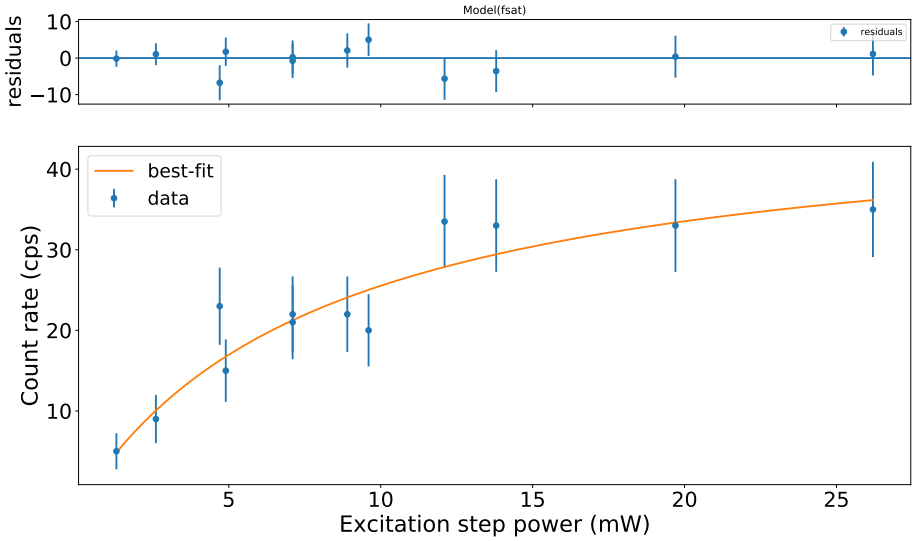

Figure 4.24: Power saturation curve fit (performed using the equation 4.3) for first step transition of ^{170}Er isotope using the injection-locked laser in gas-jet laser ionization giving a saturation power of 8(4) mW.

reducing the chances of ionization.

Data analysis procedure

To perform the laser spectroscopy measurements in a gas jet, the laser frequency was scanned over the resonances for the individual isotopes, and the MagneTOF counts after PILGRIM were recorded using the Leuven TDC. The TDC spectrum for a single laser frequency scan is shown in figure 4.25. For this scan, the time resolution of the TDC was chosen to be 12 ns/bins. From the TDC spectrum, specific regions of bins were selected for plotting the individual isotopes' excitation spectrum. The bunched ions were trapped for three revolutions in PILGRIM to have an increased time-of-flight allowing separation of the Er isotopes. The representative spectra are shown in figure 4.26. The spectra were fitted with a Voigt profile, using the SATLAS package as shown in figure 4.26, fixing the relative intensities of the hyperfine components by the corresponding Racah coefficients for ^{167}Er (See section 1.2.2). A chi-square fitting routine was followed for individual scans. Several scans were performed for the measurements and a weighted average of the fit results were calculated. The total uncertainties were estimated following the approach detailed in [80], considering the statistical uncertainties, the scattering of the values from the individual scans, and the systematic errors of the wavemeter.

Calculation of uncertainities

In order to calculate the values and uncertainties mentioned for the isotope shifts and hyperfine constants, scattering of the fit values for several scans was taken into account to obtain a weighted average. If x_i are the values and σ_{xi} the uncertainty obtained from fitting individual scans, then the weighted average is

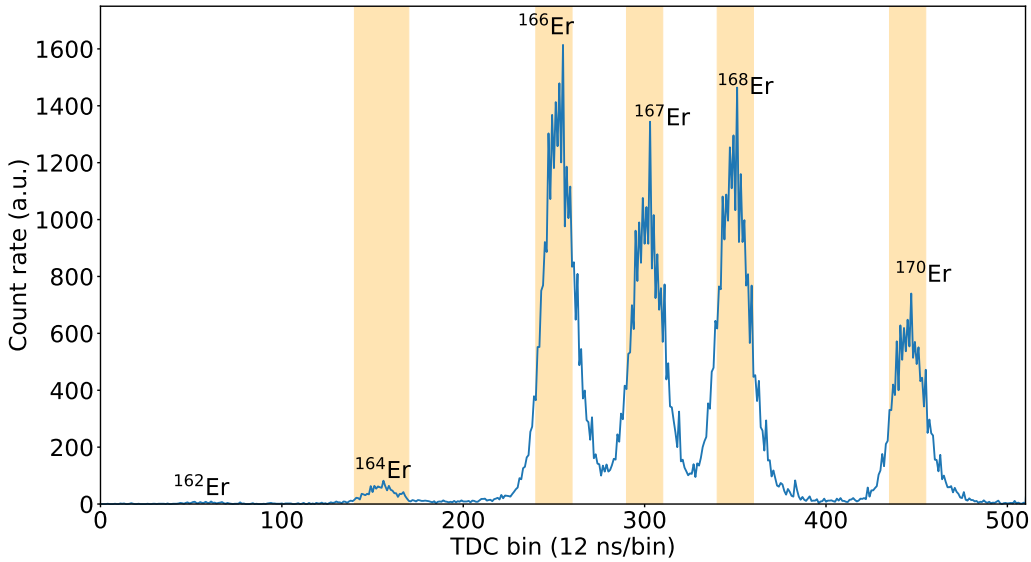

Figure 4.25: TDC spectrum showing the integral counts with isotopes in their respective bins. The shaded regions of the bins were selected for analysis of individual isotopes (see text).

:

$$\bar{X} = \frac{\sum \frac{x_i}{\sigma_{x_i}^2}}{\sum \frac{1}{\sigma_{x_i}^2}} \tag{4.6}$$

and

$$\frac{1}{\bar{\sigma}_X} = \frac{1}{\sigma_{x_i}^2} \tag{4.7}$$

The obtained uncertainty is then multiplied with the reduced χ^2 value if $\chi^2 >> 1$ obtained from the fit. Reduced χ^2_{red} is calculated as :

$$\chi^2_{red} = \frac{\sum \frac{(x_i - \bar{X})^2}{\sigma_{x_i}^2}}{N-1} \tag{4.8}$$

where N is the number of scans taken into account.

Results

The weighted average of the fitted spectral FWHM was found to be 281(5) MHz. The isotope shifts (IS) for $^{170-164}$Er with ^{170}Er as the reference isotope as well as the hyperfine A and B constants of the odd isotope ^{167}Er were determined (see Table 4.2). The hyperfine A and B constants were determined in two ways, firstly by keeping the A and B parameters for the $4f^{12}\ 6s^2\ ^3H_6$ ground state free and secondly, by fixing them to literature values, leaving free only the parameters of the excited state, for the fit. The results of both methods of fitting are in agreement with the literature [97, 80, 98, 99]. The results from [80] are from high-resolution laser spectroscopy in an ABU. Since ABU measurements are performed in vacuum conditions, the broadening effects are in the order of 100 MHz. Hence the spectrum is very well resolved as can be seen in figure 4.27 [16].

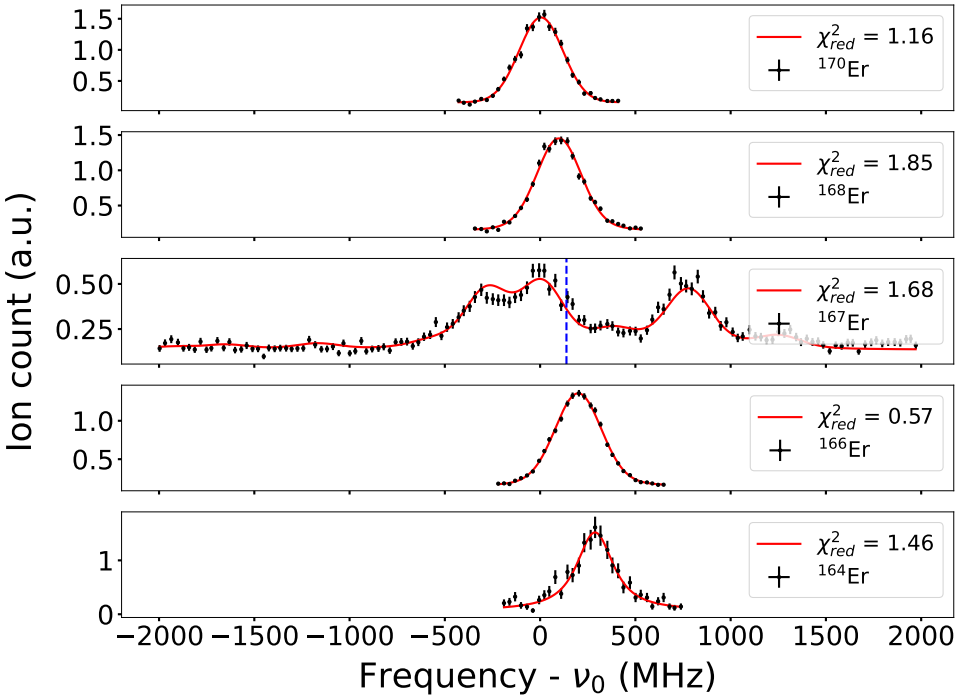

Figure 4.26: Resonance peak scan of the excitation transition for the isotopes of stable Er in the gas jet with ν_0 = 721,995,050 MHz. The measured data points are normalized with laser powers of both steps which are shown in black and the fit is shown in red. The reduced χ^2 values for the fits are labeled as χ^2_{red}. The centroid for the ^{167}Er is marked as the blue dotted line.

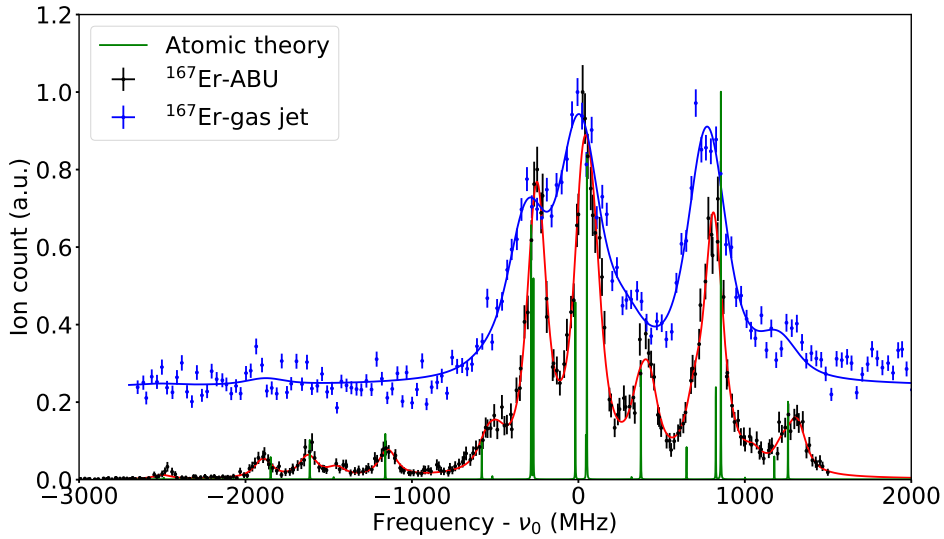

Figure 4.27: Resonance peak scan of the excitation transition for the isotopes of stable Er in the gas jet (blue) and in an ABU (black) with ν_0 = 721,995,050 MHz. Their respective χ^2 fits are also shown. The measured data points are normalized with laser powers of both steps. The green plot shows the spectra expected theoretically, obtained by fixing I, J, and hyperfine A and B constants and fitting with a fixed spectral resolution of FWHM = 0.25 MHz to a Voigt function.

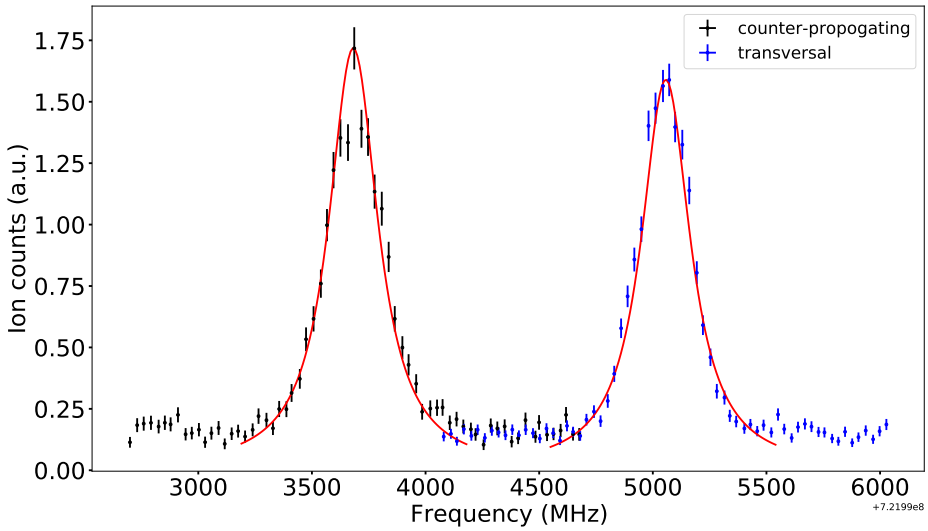

Figure 4.28: Resonance peak scan of the excitation transition for the ^{170}Er isotope. The measured data points are normalized with laser powers of both steps which are shown in black for the counter-propagating first step and blue for the transversal first-step laser configurations. The chi-square Voigt fit is shown in red. The counter-propagating laser alignment causes a Doppler shift of the centroid as shown by the black data points.

From the deduced isotope shift measurements for the specific Er transition,

Table 4.2: IS values $\Delta\nu^{A',170} = \nu^{A'} - \nu^{170}$ of stable $^{168-164}$Er isotopes with respect to ^{170}Er and hyperfine A and B constants, for the $4f^{12}6s^2\ ^3H_6$ and $4f^{12}(^3H)6s6p$ $J = 5$ atomic states of ^{167}Er deduced from the gas jet measurements, are shown and compared with the literature values reported in [80, 98, 99]. Fit values with A and B for the ground state kept free and fixed are shown. $\sigma(\Delta\nu^{A',170})$, $\sigma(A)$, and $\sigma(B)$ indicated in parenthesis represents the total uncertainties [80].

$\Delta\nu^{A',170}$ (MHz) $4f^{12}6s^2\ ^3H_6 \rightarrow 4f^{12}(^3H)6s6p\ J = 5$			^{167}Er HFS coefficients				
			$4f^{12}6s^2\ ^3H_6$			$4f^{12}(^3H_5)6s6p\ J = 5$	
Mass number	gas jet	ABU [80]	Method	A (MHz)	B (MHz)	A (MHz)	B (MHz)
168	96(6)	97(8)	gas jet	-122(3)	-4847(237)	-148(4)	-2230(200)
167	138(8)	132(10)	gas jet	-121.8(fixed)	-4563(fixed)	-147.1(7)	-1936(24)
166	196(7)	193(8)	ABU [80]	-121.80(75)	-4563(53)	-147.66(83)	-1888(58)
164	283(7)	298(7)	[98, 99]	-120.487(1)	-4552.984(10)	-146.6(3)	-1874(16)

it can be seen that they are in the order of a few hundred MHz. These small isotope shift values are not sensitive to the changes in the charge radii and hence different transitions are required to be considered for extracting information on this nuclear parameter. For this purpose, other Er transitions (another ongoing Ph.D. work) are currently under study. A 400.8 nm, 408.8 nm, and 393.7 transitions from the ground state have been shown in the literature to possess isotope shift values on the order of a few GHz and hence could be used for online studies for extracting the differences in the charge radii of the isotopic chain in the neutron deficient region [100, 101]. These transitions are currently being studied offline with the S^3-LEB setup, probing the atoms both in the gas cell as well as in the jet region. With the optimizations performed from this thesis work and later work, the spectral resolution for these transitions could achieve less than 200 MHz and the data collected are under analysis for deduction of broadening coefficients, isotope shifts, and hyperfine constants.

4.4.3 Estimation of Mach number of the jet

For estimating the Mach number of the jet, calculations based on [20, 64] were performed. A weighted average of the centroid and FWHM values from the SATLAS fits were considered for the ^{170} Er resonance. The transverse first-step laser configuration was used to deduce the centroid from the fit. This gave the atomic transition frequency (ν_{01}) of the ^{170}Er atom ν_{01} = 721,995,054(60) MHz. The local temperature of the gas jet was determined from the Doppler FWHM and atomic transition frequency according to the equation 1.74. The Doppler FWHM was calculated from the fitted FWHM of the ^{170}Er resonance after subtracting the contribution of the natural and laser line widths. The resulting value was 268(5) MHz from which the local temperature of the jet was deduced to be 46(2) K. The atoms flushed out with the buffer gas in the jet are assumed to have the same velocity and temperature as that of the buffer gas atoms. The counter-propagating first-step laser configuration was used to measure the Doppler shifted centroid of the ^{170}Er resonance ν_{02} = 721,993,693(60) MHz (shown in figure 4.28). The stream velocity of the jet u = 565(35) m/s was calculated from the Doppler shift according to the equation 2.11.

The Mach number was calculated to be $M = 4.5(3)$ from the stream velocity (u) and speed of sound (a) derived from the temperature of the gas jet according

to equations 2.3 and 2.4. The deduced temperature in the gas cell is T_0 = 353(16) K for the deduced Mach number according to the equation 2.5. The deduced Mach number is lower than the value reported in [64] which might be due to a possible misalignment in the laser path, inhomogeneity of the jet, or power broadening.

The conclusion from the Mach number estimation required the flow characteristics of the jet to be studied more systematically. The resonance ionization flow mapping method was used to study the jet characteristics in collaboration with KU Leuven and the detailed analysis of the test will be part of another thesis work. The atoms in the jet were locally probed at different areas of the jet for this purpose and the excitation spectra recorded are under analysis. The first estimation from the tests showed a slight misalignment of the counterpropagating laser path from the jet axis. This can lead to probing the atoms in low Mach number regions of the jet. This was corrected although it did not impact the spectral resolution significantly. Other possible reasons for the low Mach number estimated were the power broadening effect and improper jet-matching conditions. The jet homogeneity could be improved by correcting for increasing the pumping at the gas cell chamber. The current gauge used for measuring the gas cell pressure was calibrated for nitrogen and hence the pressure reading was later corrected for the Argon gas. The laser power even though shown in the linear region of the saturation curve is still estimated to cause power broadening due to the very strong Er transition used. The delay of the second pulse by more than 40 ns could improve the spectral resolution. The first results from the RIS mapping showed that spectral resolution can be improved down to 200 MHz. The laser power realistically cannot be reduced to very low powers to obtain the ideal spectral resolution as it would reduce the ion rate as well. For online cases with very low production cross-section, this would be not practical. The use of weak transition could help in reducing the power broadening at the cost of ionization efficiency.

4.5 Entrance window and gas cell pressure optimization

The use of a gas cell for stopping ions requires knowledge of the stopping power and range of the various nuclei of interest that are planned to be studied using the S^3-LEB technique. For different physics cases, to isolate the S^3 spectrometer under vacuum from the gas cell, entrance window materials to the gas cell considered are titanium and Mylar foils as mentioned in section 2.3.2. The S^3-LEB gas cell has a depth of 30 mm. The gas cell can run at 100 - 500 mbar argon gas pressure. The entrance window and gas cell pressure are chosen such that the ions can stop in the middle of the gas cell. The windows should also prevent strong leakage of the argon gas from the gas cell to the S^3 side. To obtain the best window thickness and gas cell pressure combinations, four reactions that cover all the kinematics of fusion evaporation reactions planned as day-1 cases have been studied here using LISE++ code. LISE ++ is a code that allows to simulate spectrometer models to calculate the transmission and yield of fragments produced and transmitted via the spectrometer [102]. It also allows us to calculate the energy loss for $1 \leq Z \leq 130$ with energies from 10 keV

in material from H to U [102]. S^3 optical model is incorporated in the LISE++ code which was used for the calculation of the production, transmission yield, and energy distribution of the recoil nuclei at the focal plane of S^3. The stopping range of the nuclei of interest at S^3-LEB is then studied and compared using both SRIM and LISE++ codes [102, 103]. SRIM is a group of programs commonly used for stopping range calculations of ions into matter from 10 eV to 2 GeV/A [103]. It uses analytical formulas for determining atom-atom collisions and the concept of a free flight path between two collisions. SRIM uses sophisticated computational methods for its calculations in terms of considering the various effects occurring when ions are transported through matter.

For the stopping range calculation using the LISE++ code, the following settings for the production mechanism were chosen. The reaction for the production of ions of interest was set as fusion-residual. The energy loss model used for the production mechanism is from [104] as it incorporates low-energy beams. The energy straggling was calculated using ATIMA version 1.2 (LS theory)/LISE++. The charge states of the recoil products from the reaction are calculated using [105]. Monte-Carlo calculation of fragment transmission tool was used to calculate the ion transmission of a specific charge state to obtain the total average kinetic energy (TKE) and its distribution in FWHM before the gas cell entrance window and the range and its FWHM in the gas cell. The method used in LISE code for range straggling calculations is the so-called 'interpolation from table' where a table with range straggling calculations from 10 keV to 3 GeV/A is used [102].

Reaction 1

This reaction is aimed to produce erbium for the commissioning of S^3-LEB. The reaction uses ^{40}Ar as projectile on ^{116}Sn target (0.5 mg/cm^2) at an energy of 4.3 MeV/u and an intensity of 2 pμA. Figure 4.29 shows the LISE++ simulation of the nuclei produced from the reaction. The dashed blue line shows the limit of known laser spectroscopy data. Figure 4.30 shows the Monte Carlo transmission plot for one of the recoil ions ^{151}Er, giving the total kinetic energy distribution at the focal plane of S^3 and the range in the stopping range in the gas cell for a gas cell pressure of 300 mbar when the entrance window is Ti of 3 μm thickness.

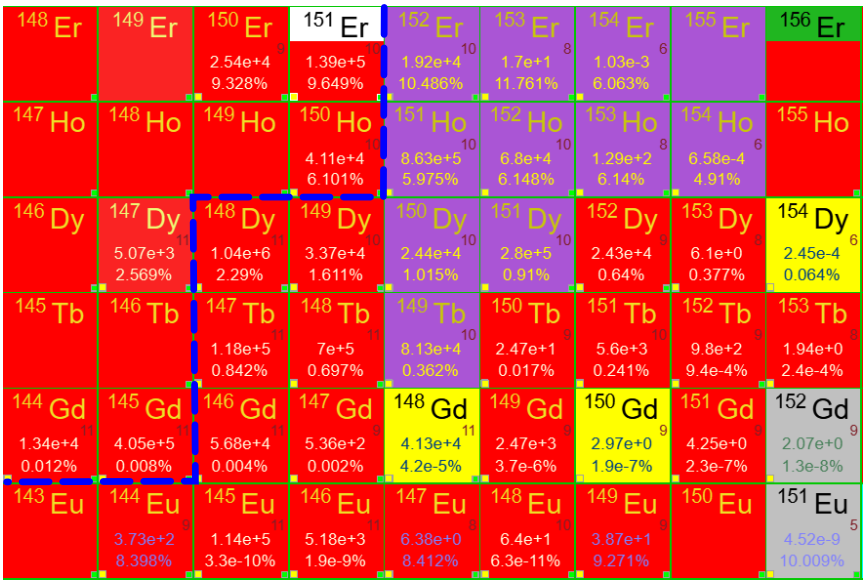

Figure 4.29: Reaction 1: LISE++ simulation for nuclei produced at the focal plane of S3. The reaction is ^{40}Ar on ^{116}Sn target (0.5 mg/cm^2) at an energy of 4.3 MeV/u and an intensity of 2 pμA.

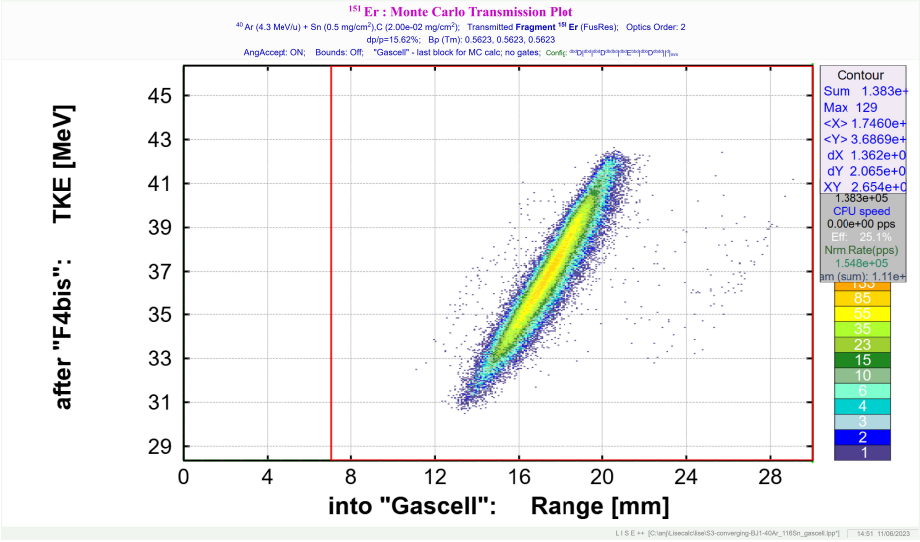

Figure 4.30: Monte Carlo transmission plot for the ^{151}Er recoil from ^{40}Ar + ^{116}Sn reaction. Y-axes give the total kinetic energy at the focal plane of S^3 and X-axes give the stopping range in the gas cell.

Reaction 2

The second reaction considered uses a projectile beam of ^{40}Ar on ^{175}Lu target (0.5 mg/cm^2) at an energy of 3.75 MeV/u and an intensity of 2 pμA. This reaction will produce actinium isotopes and the LISE++ simulation of all the nuclei produced from the reaction is shown in figure 4.31. This reaction will be used to evaluate the S^3 capabilities in the heavier mass regions. Figure 4.30

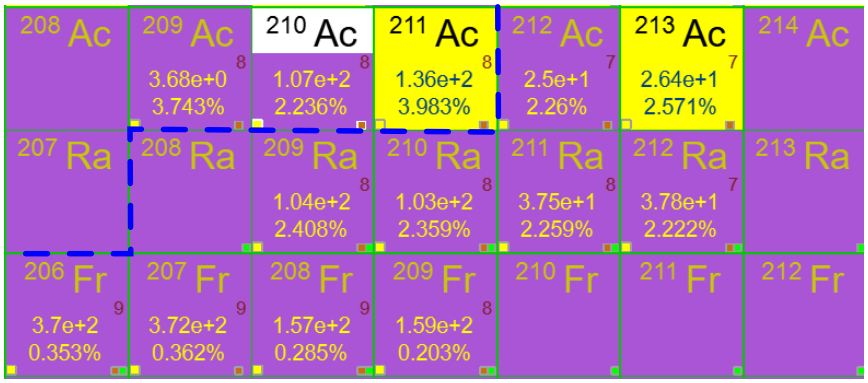

Figure 4.31: Reaction 2: LISE++ simulation for nuclei produced at the focal plane of S^3. The reaction is ^{40}Ar on ^{175}Lu target (0.5 mg/cm^2) at an energy of 3.75 MeV/u and an intensity of 2 pμA.

shows the Monte Carlo transmission plot for one of the recoil ions ^{210}Ac, giving the total kinetic energy distribution at the focal plane of S^3 and the stopping range in the gas cell for a gas cell pressure of 200 mbar when the entrance window is Ti of 2 μm thickness.

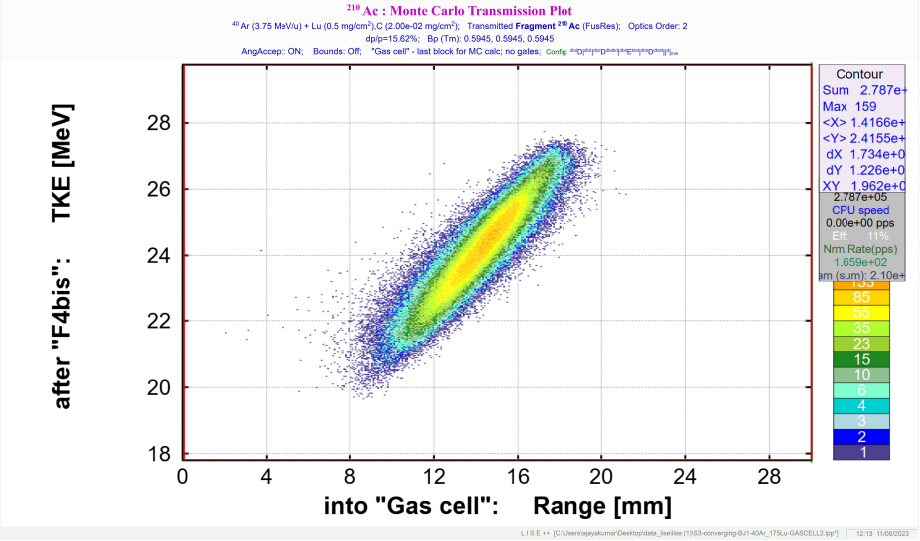

Figure 4.32: Monte Carlo transmission plot for the ^{210}Ac recoil from ^{40}Ar + ^{175}Lu reaction. Y-axes give the total kinetic energy at the focal plane of S^3 and X-axes give the stopping range in the gas cell.

Reaction 3

The third reaction also produces actinium isotopes similar to reaction 2. It uses a ^{20}Ne projectile beam on ^{197}Au target (0.25 mg/cm^2) at an energy of 7 MeV/u and an intensity of 2 pμA. The reaction is very asymmetric and puts stringent constraints on the S^3 spectrometer and thus can be used for evaluating the performance of the spectrometer and a direct comparison with reaction 2

can be made producing nuclei in the same mass regions. This reaction will produce very low-energy reaction products and hence would require a very thin entrance window and low gas cell pressure at the S^3-LEB. Figure 4.33 shows the LISE++ simulation of nuclei produced. Figure 4.30 shows the Monte Carlo

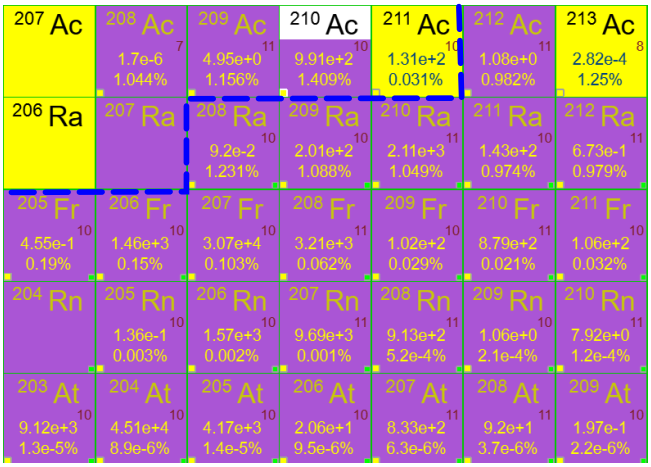

Figure 4.33: Reaction 3: LISE++ simulation for nuclei produced at the focal plane of S^3 for the reaction is ^{20}Ne + ^{197}Au.

transmission plot for one of the recoil ions ^{210}Ac, giving the total kinetic energy distribution at the focal plane of S^3 and the stopping range in the gas cell for a gas cell pressure of 100 mbar when the entrance window is Mylar of 1.5 μm thickness.

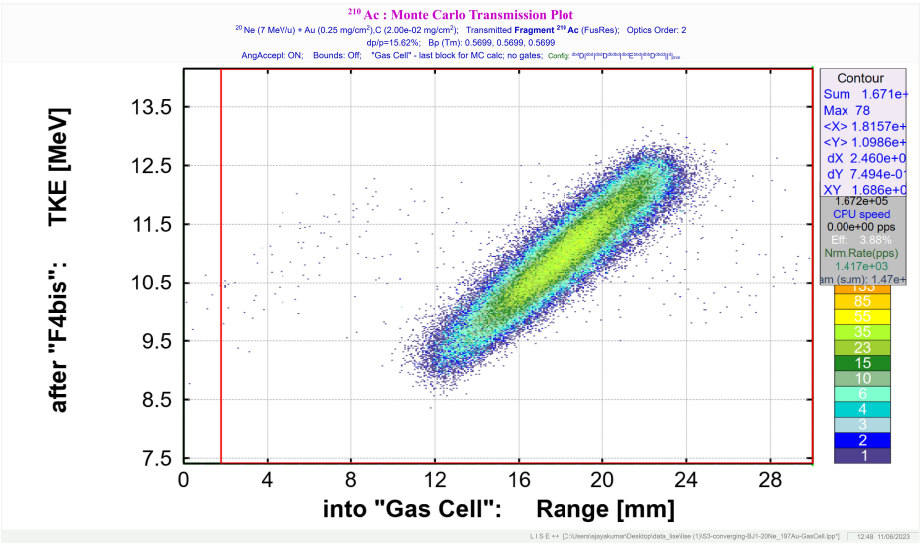

Figure 4.34: Monte Carlo transmission plot for the ^{210}Ac recoil from ^{20}Ne + ^{197}Au reaction. Y-axes give the total kinetic energy at the focal plane of S^3 and X-axes give the stopping range in the gas cell.

Reaction 4

This reaction uses ^{50}Cr on ^{58}Ni target (1.2 mg/cm^2) at an energy of 5.11 MeV/u and an intensity of 2 pμA. It is aimed at producing nuclei near the $N = Z$ region in the nuclide chart. Figure 4.35 shows the LISE++ simulation of the nuclei produced. Figure 4.30 shows the Monte Carlo transmission plot

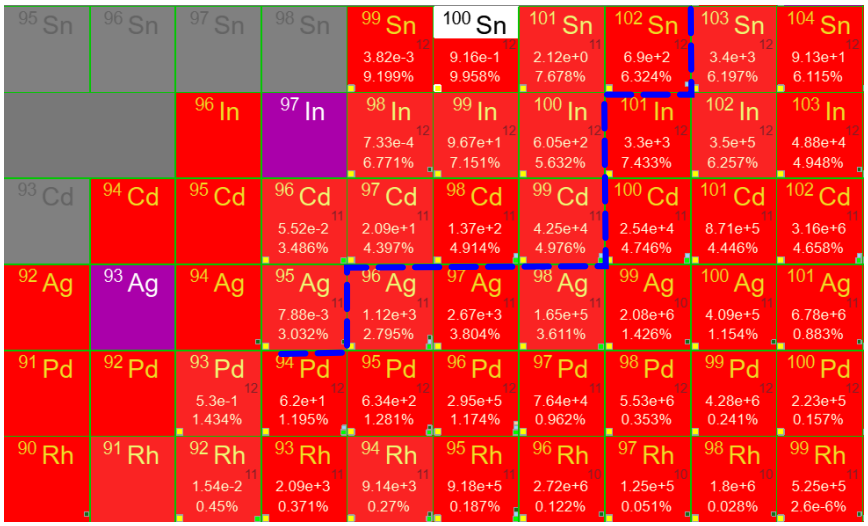

Figure 4.35: LISE++ simulation for nuclei produced at the focal plane of S^3 for the reaction ^{50}Cr + ^{58}Ni

for one of the recoil ions ^{100}Sn, giving the total kinetic energy distribution at the focal plane of S^3 and the stopping range in the gas cell for a gas cell pressure of 500 mbar when the entrance window is Ti of 5 μm thickness.

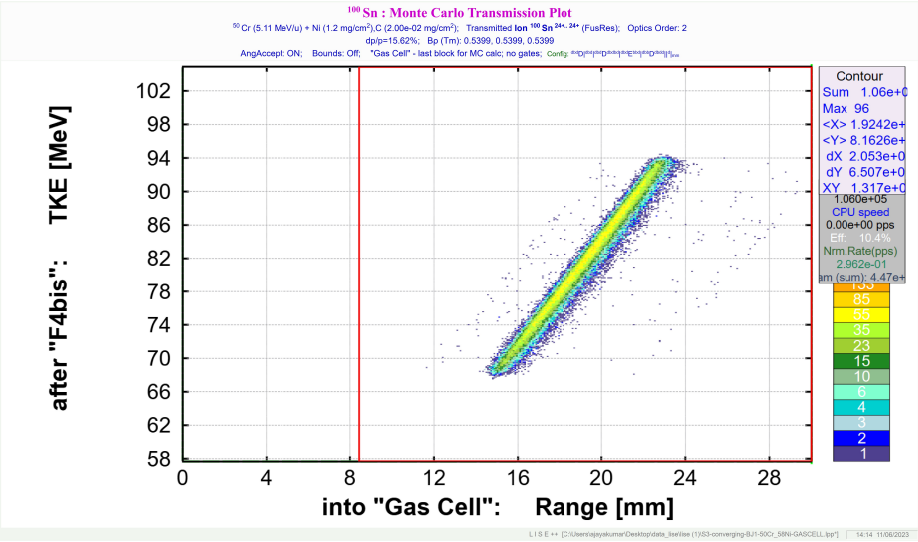

Figure 4.36: Monte Carlo transmission plot for the ^{100}Sn recoil from ^{50}Cr + ^{58}Ni reaction. Y-axes give the total kinetic energy at the focal plane of S^3 and X-axes give the stopping range in the gas cell.

Table 4.3 presents the resulting production rate (at the focal plane of S^3), the total kinetic energy (TKE), and FWHM of the energy distribution for a specific recoil ion and of specific charge state. For the range calculations using the SRIM code, the TKE before the gas cell from the LISE++ code was used as an input to the SRIM code. The window thickness and the argon gas density in the gas cell were set to obtain the range in the gas cell as shown in figure 4.37. To obtain the uncertainty in range for SRIM calculation, the range was calculated for the mean TKE, mean TKE + FWHM/2 and mean TKE - FWHM/2. Figure 4.37 shows the calculated stopping range values in different gas cell pressures for the four reactions producing $^{151}Er^{19+}$, $^{210}Ac^{12+}$ and $^{100}Sn^{24+}$ using LISE++ and SRIM codes.

Table 4.3: Production rate and total mean kinetic energy obtained for each ion of interest studied using LISE++ code

Reaction	A	Production rate (pps)	Mean TKE (MeV)	FWHM (MeV)
1	$^{151}Er^{19+}$	1.39E+05	37.1	5.8
2	$^{210}Ac^{12}$	1.07E+02	24.4	1.4
3	$^{210}Ac^{12+}$	9.91E+02	11	1.9
4	$^{100}Sn^{24+}$	9.16E-01	81.6	20.4

Table 4.4: Window-gas cell pressure combinations used to stop the desired nuclei in the middle of the gas cell.

Reaction	A	Ti thickness (μm)	Mylar thickness (μm)	Ar pressure (mbar)
1	$^{151}Er^{19+}$	3	-	300
2	$^{210}Ac^{12+}$	2	-	200
3	$^{210}Ac^{12+}$	-	1.5	100
4	$^{100}Sn^{24+}$	5	-	500

The resulting range obtained using the LISE++ code is comparable with that of the SRIM calculations. This shows that an estimation of the window thickness required can be obtained from LISE ++ code. Thus LISE++ can be used as a complete package for the calculation of S^3 reactions such as yield and transmission as well as the stopping range in the gas cell. Table. 4.4 shows the resulting optimum thickness of entrance windows and gas cell pressure required for the four reactions. For stopping Er and Sn nuclei, the Ti foil of thicknesses 3 and 5 μm can be used at 300 and 500 mbar gas cell pressures respectively (see figures 4.37a and 4.37e). For actinide elements like actinium, the total kinetic energy before the gas cell is lower and hence requires a very thin window so that ions will not be entirely stopped on the window surface. From the LISE++ and SRIM calculations, it is seen that Ti 2 μm window foil and a gas cell pressure of 200 mbar can stop the actinium ions for the ^{40}Ar + ^{175}Lu reaction near the center of the gas cell (See figure 4.37b). To compare, a Mylar foil of 1.5 μm was also calculated showing that a higher gas cell pressure of 400 mbar which the thin foil cannot hold (See figure 4.37c). The ^{20}Ne + ^{197}Au reaction for Ac production requires very thin windows such as 1.5 μm Mylar and low gas cell pressure (See figure 4.37e) to stop the ions in the middle of the gas cell.

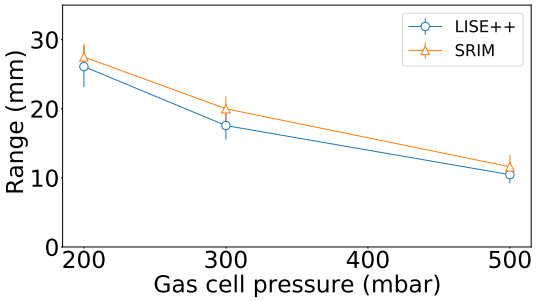

(a) ^{151}Er with Ti 3 μm window with reaction 1

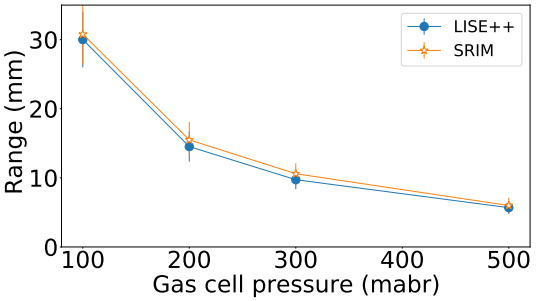

(b) ^{210}Ac with Ti 2 μm window with reaction 2

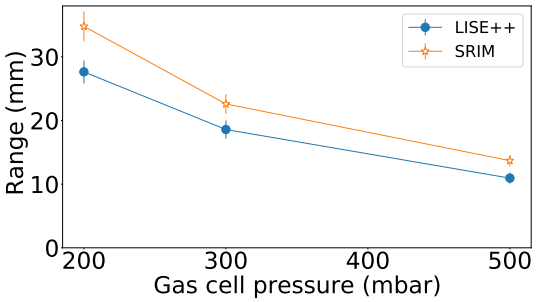

(c) ^{210}Ac with Mylar 1.5 μm window with reaction 2

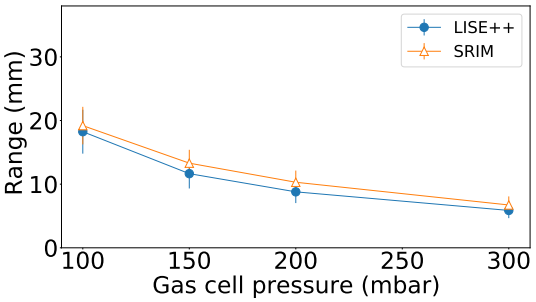

(d) ^{100}Ac with Mylar 1.5 μm window with reaction 3

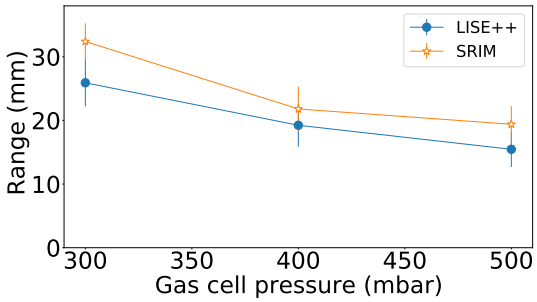

(e) ^{100}Sn with Ti 5 μm window with reaction 4

Figure 4.37: Range for Er, Ac, and Sn ions of specific charge states vs different gas cell pressures.

This is technically challenging as it can be seen from the thin window tests discussed in the next section. For the heavier elements in actinide regions, at low energies, disagreements between experimental data and SRIM calculation of stopping power and ranges have been reported [106]. The experiments with nobelium reported in [106] show an underestimation of the stopping range by SRIM from the experimental data and is more pronounced in the argon gas (by nearly 50%) than in the Mylar foil (by nearly 13%) which they have used. This variation is due to the scarce experimental data available for heavy ions at very low energies which are needed for the SRIM to provide reliable estimates. This shows that, in reality, the gas cell pressure might need to be adjusted from the calculated values to compensate for this disagreement.

In order to maintain good vacuum condition at S^3, the leak of argon gas to S^3 through the thin windows should also be minimum ($<10^{-5}$ mbar L/s) as mentioned before. To test if the calculated window material and thicknesses can be reliably used, a new test bench was designed and implemented. Figure 4.38 shows a layout of the new test bench installed. The window foil is mounted on a window holder. The window holder can be coupled to the gas cell chamber using an adaptor piece as mentioned in section 2.3.2. The test bench has a 3-way cross on one side of the entrance window to which helium gas is injected. This side acts as the gas cell side. Helium gas was used for the tests instead of argon gas. Helium with its lower molecular size can detect small leaks and gives the worst-case scenario. A gauge is connected to the three-way cross to monitor the pressure at the gas cell side of the test bench. The other side of the window has the adaptor piece connected to a four-way cross. This side acts as the vacuum side or the S^3 spectrometer side. Through the four-way cross, the S^3 side of the test bench is pumped to vacuum using a scroll pump. A leak tester is connected to this side for measurement of the leak rate and the contribution of impurities from the O rings. Pumping options at both sides of the window are made possible through the bypass connection. Each of the foil was mounted onto the window holder for resistance tests and leak rate measurements. Once all the foils are tested in the test bench, final tests will be done in the gas cell itself. Figure 4.39 shows the installed test bench.

In order to compare the results from the tests and to avoid any damage to the foil during its mounting, a reliable test procedure was developed for the entrance window tests. The test procedure step by step is:
1) Punch screw holes using the designed piece. (see figure 4.39)
2) Properly mount the window foils to the window holder. (see figure 4.39 for Ti foil)
3) Pump both sides of the window with the bypass valve open.
4) Close the bypass valve and gradually inject He to the gas cell side of the window. Close the injection valve when specific gas cell pressure is reached.
5) Close the valve to the pump and open the valve to the leak detector for absolute leak rate measurements.
6) To vent, open the bypass valve again and disconnect the leak detector side to reach atmospheric pressure on both sides of the window.
8) test for several cycles of pumping and venting to test the resistance of the foil.
8) Test several foils of the same type for reliable leak rate measurements.
9) Monitor gas cell side pressure using a gauge connected to the LabView control

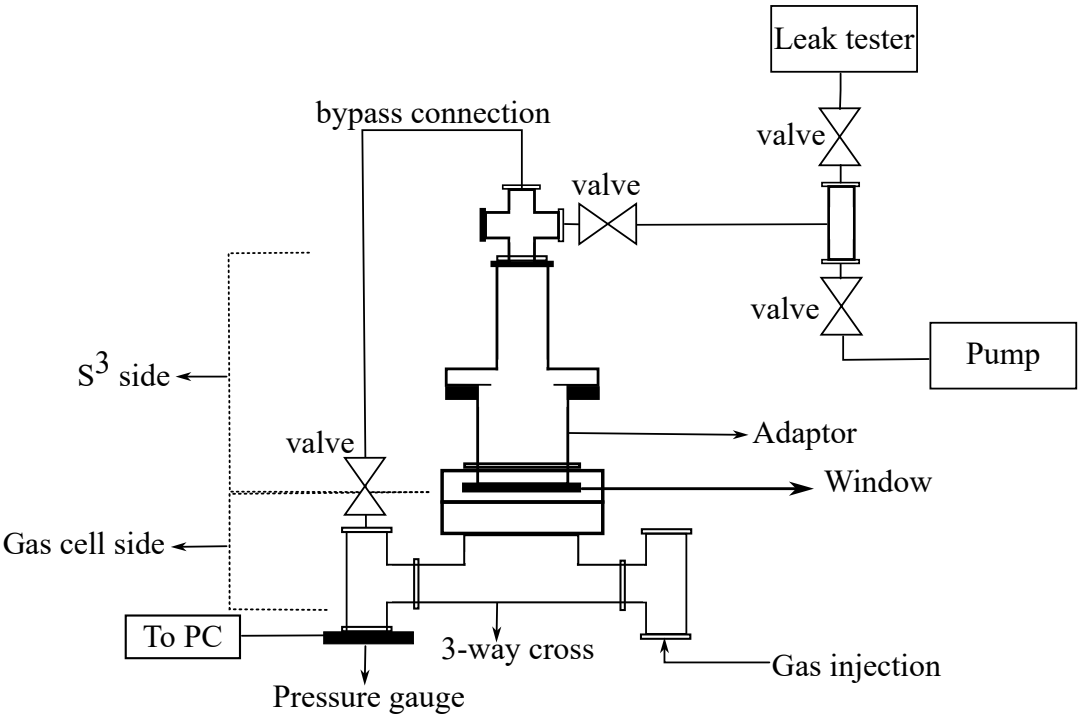

Figure 4.38: New testbench design layout for absolute leak rate measurements.

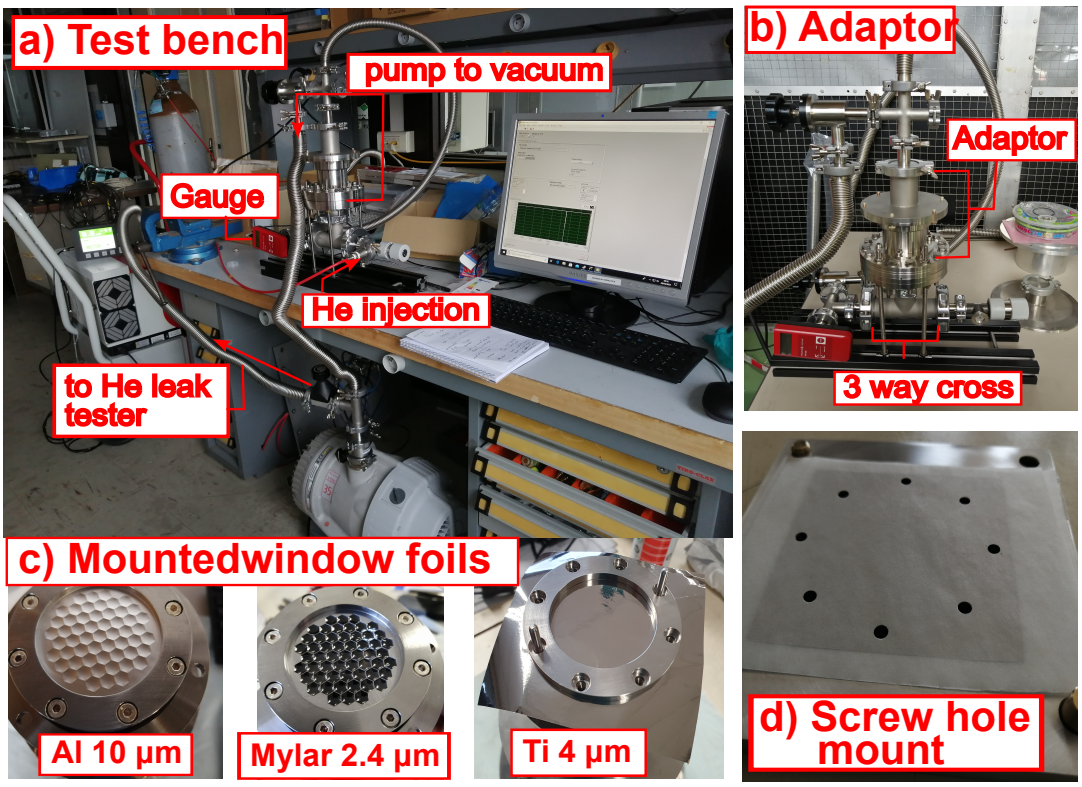

Figure 4.39: Test bench for window foil tests. a) shows the window test bench with the paths to the primary pump, leak detector, and He gas injection. b) shows the adaptor piece mounted onto the test bench. c) shows the different windows mounted on the adaptor piece and d) shows the mount designed for punching screw holes to the window foils.

software.

Foils of different materials and thicknesses were tested. Three foils were tested for each case. The leak tests were performed for different gas cell pressures of 100 mbar, 300 mbar, and 500 mbar as well as for different cycles of pumping and venting. The long-term pressure measurement at the gas cell side was also measured to see if pressure in the gas cell side was leaking over time as well as to see outgassing effects. Figure 4.40 shows the long-term pressure reading for two cycles of pumping for 11 μm Al foil. A small period fluctuation of 2% in the pressure reading over day and night can be seen which might be an effect of surrounding temperature or noises. The pressure reading shows that the foil can be used multiple times after careful venting and repumping without affecting the mechanical resistance and porosity of the foil. Table 4.5 shows the absolute leak rate measured using He leak tester with values corrected for argon gas for the window foils of various thicknesses. For the correction from the He leak rate to the Ar leak rate, a choked flow is considered where the flow throughput is inversely proportional to the square root of the atomic mass of the gas [65, 107]. A conversion factor of 0.316 is thus multiplied by the measured He leak rate. From the tests, it could be concluded that Ti foils of thickness down

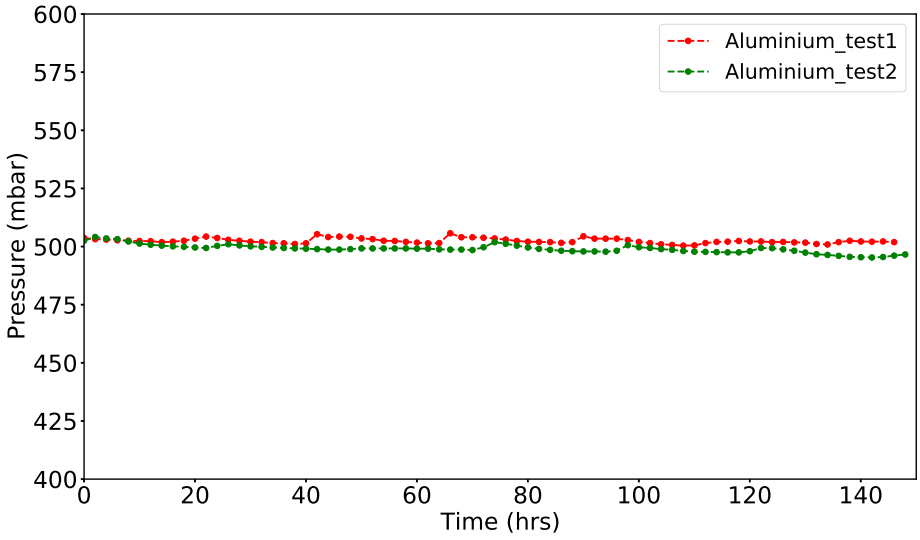

Figure 4.40: Long-term pressure reading in the gas cell side with the same Al foil as entrance windows for two cycles of pumping.

to 4 μm have strong mechanical resistance towards the pressure difference and can hold without breaking even up to 1000 mbar. Thinner Ti foil and Mylar foils could withstand up to 300 mbar but the grid that is used for the entrance window was found to have poor surface quality which easily damaged the foil with higher pressure differences causing the leak rate to be high. However, for the commissioning case Er and most of the day-1 cases, the initial tests have proved that the entrance windows could maintain the pressure difference and perform reliably for at least two to three cycles of pumping and venting cycles. For actinides, a very thin foil of 1 - 2 μm would be required which did not provide the desired leak rate so far. Even though a Mylar foil of 2.4 μm might not give the ideal condition, leak rate measurement at 100 mbar pressure shows

that it could be used for actinide studies in S^3-LEB. Grid designs are currently in progress for further tests on the very thin foils. For actinides, with very thin foils, an additional turbopump at the S^3 side might solve the issue.

Table 4.5: The absolute leak rate values of different window foils tested in the test bench at helium pressures 100 - 500 mbar measured using He leak tester. The leak rates mentioned are corrected for argon gas (see text for details).

Foil type	Foil thickness (μm)	Pressure (mbar)	Leak rate (mbar L/s)
	10	500	0.6×10^{-8}
Al	10	500	1.1×10^{-7}
	5	100	0.7×10^{-6}
Ti-test1	5	300	2.2×10^{-6}
	5	500	0.6×10^{-5}
	5	100	0.3×10^{-6}
Ti-test2	5	300	1.3×10^{-6}
	5	500	0.6×10^{-5}
	4	100	1.3×10^{-8}
Ti-test1	4	313	1.5×10^{-8}
	4	500	0.4×10^{-5}
	4	100	3×10^{-8}
Ti-test2	4	300	0.7×10^{-7}
	4	500	1×10^{-7}
	4	100	3×10^{-8}
Ti-test3	4	300	0.3×10^{-7}
	4	500	0.5×10^{-7}
	4	1000	1×10^{-7}
	6	100	0.8×10^{-5}
Mylar-test1	6	300	1.7×10^{-5}
	2.4	100	2.8×10^{-7}
Mylar-test1	2.4	300	0.5×10^{-4}
	2.4	500	1.4×10^{-4}
	2.4	83	1.6×10^{-5}
Mylar-test2	2.4	500	1.6×10^{-4}
	2.4	100	1.6×10^{-6}
Mylar-test3	2.4	280	0.5×10^{-4}
	2.4	300	2.5×10^{-4}

CHAPTER 5

Laser spectroscopy measurements on U and Am

The actinide and transactinide regions in the nuclide chart possess fascinating nuclear phenomena such as octupole deformation, formation of bubble nuclei, and the presence of K-isomers. In addition, strong relative effects and electron-electron correlations are expected at the atomic level. The LISA (Laser Ionization and spectroscopy of actinides) training network focuses on ion beam research and applications, laser technologies, and their application in spectroscopic studies on the radioactive elements in the actinide region. The aim of the project is to have a better understanding of the atomic and nuclear properties of the actinides on which studies are difficult due to their dense electronic levels, radioactivity, and short lifetimes. The actinide data measured from laser spectroscopy are very scarce as they require the identification of suitable atomic transition schemes and high-resolution techniques. As a part of the LISA network, laser spectroscopic studies on natural uranium in search of a suitable RIS scheme have been performed with the Ion Guide Isotope Separation On-Line (IGISOL) group at the University of Jyvaskyla (JYU). Also, laser spectroscopy on long-living americium isotopes at RISIKO in the Johannes Gutenberg University (JGU) has been performed. The studies were done as proof of the principle for laser developments completed for high-resolution measurements with actinides. The details of the spectroscopic studies and the setups used are discussed in this chapter in the following sections.

5.1 Uranium scheme tests at JYU

In the actinide regions, several nuclei from radon to uranium isotopes are predicted to show the existence of octupole deformation [108, 109]. The presence of octupole deformation can be inferred by measuring the ground state properties with high-resolution laser spectroscopy. By quantifying the charge radii odd-even staggering, the existence of octupole collectivity was hinted for ^{226}Ac and the measurement of magnetic moments indicated the presence of octupole deformation in the ground states of ^{225,227}Ac [110]. Studying the ground state properties of actinide isotopes using laser spectroscopy is thus of interest as well at S^3-LEB. One of the proposed online experiment cases in S^3-LEB is

the laser spectroscopic study of uranium isotopes in search of octupole deformation and their evolution with N and Z using the IGLIS technique (Letter of intent by Marine Vanderbrouck, DRF/IRFU/CEA). The uranium isotopes will be produced via fusion evaporation reaction, ^{208}Pb(^{22}Ne,xn), $^{230-x}$U, separated from the primary beam by traversing through the S^3 in-flight separator and sent to the S^3-LEB set up. A suitable resonance ionization scheme is then used to ionize the uranium isotopes and to obtain high-resolution spectra.

The IGISOL group at JYU is also motivated to study uranium isotopes. One of their goals is to develop a gas cell-based laser ion source with filament-based dispensers of long-living actinide isotopes to study the detrimental effects of buffer gas collision while performing resonance ionization spectroscopy of actinide elements. In lighter elements, these collisional processes have been mostly studied where theoretical modeling is also computationally less expensive. Theoretical modeling of this kind of effect is not present for the heavier elements due to their complicated atomic structure. As a part of this study, strong collision-induced effects were seen in plutonium atoms studied using gas cells filled with He buffer gas [93]. The gaseous environment in the gas cell suffers from spectral pressure broadening and shifts while performing laser resonance excitation and ionization. The pressure broadening and shift effects in a gas cell were demonstrated in this thesis work as well using laser spectroscopy of erbium. Apart from the broadening and shift, laser ionization efficiency is also affected by the collisional-deexcitation effects which are more prominent in the lanthanide and actinide regions due to their high atomic-level densities. In the gas cell, due to buffer gas pressure, atoms collide with one another and affect the population of the electronic levels. Due to this, resonant excitation of electronic ground states and excited states to a specific higher-lying level might become ineffective. Collisional de-excitation can cause spontaneous decay of an excited state to some metastable states such that the lasers can no longer probe them. Resonance laser ionization schemes proved efficient in a vacuum system and thus might show decreased performance in terms of ionization due to the strong collisional de-excitation occurring in the gas cell. A focused work on this collisional de-excitation is hence required while considering laser spectroscopic studies on heavy/superheavy elements in the gas cell-based setups.

5.1.1 Tests in ABU

As preparation for the investigation of collisional de-excitation effects, two three-step RIS schemes of uranium available from the literature were tested in an atomic beam unit (ABU). These schemes were then also tested for in-gas cell laser ionization. The following section discusses the observations from the tests, the difficulties encountered and to be considered in future studies. No laser spectroscopic results are obtained from the tests but interesting observations and evidence for the collisional effects.

In order to prepare for the in-gas cell laser ionization of uranium at IGISOL JYU, different resonance ionization laser schemes were investigated in the FURIOS lab by performing laser ionization of a uranium sample in an ABU. Figure 5.1 shows the ABU in the FURIOS lab of the IGISOL facility used for the tests. The ABU design and operation can be found in detail in [28]. For the scheme studies, a natural uranium sample of ^{234}U: 0.0054%, ^{235}U: 0.7204%,

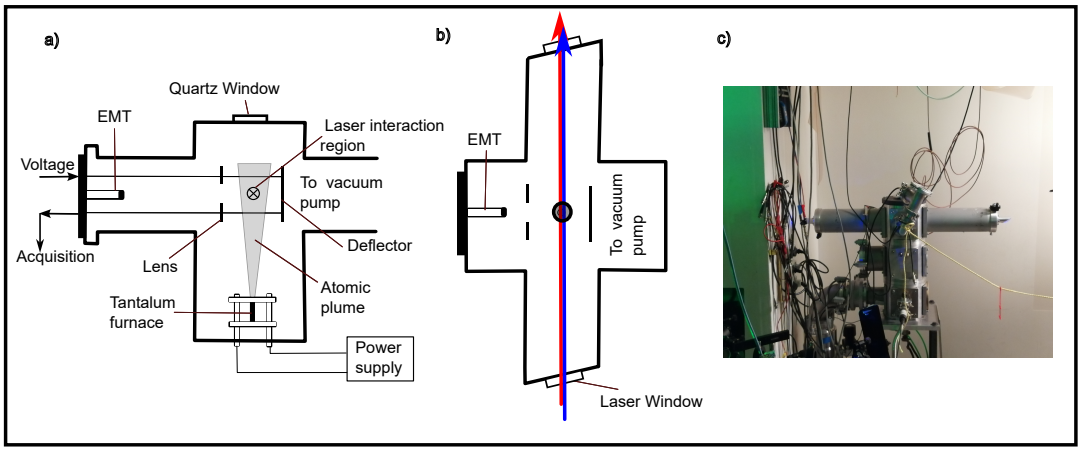

Figure 5.1: The ABU setup in FURIOS laboratory, University of Jyvaskyla is used for offline laser spectroscopic studies with insets a) showing schematic layout in side cross-sectional view b) Top cross-sectional view and c) Image of the ABU. EMT- Electron Multiplier Tube

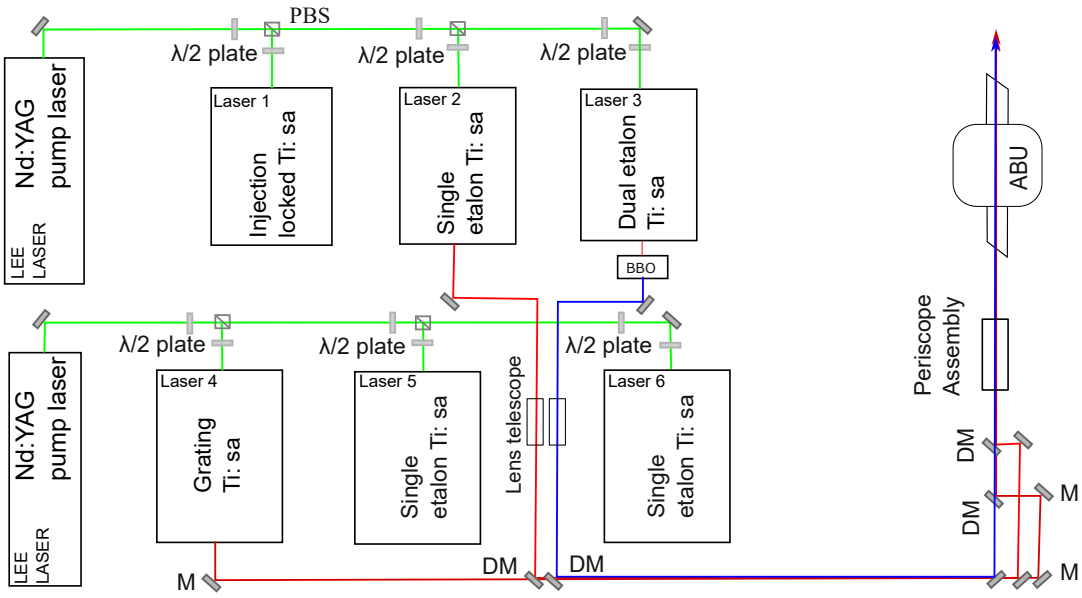

Figure 5.2: Layout of the offline test system at FURIOUS lab in JYU. The laser paths to the ABU for the Uranium scheme tests are shown.

^{238}U: 99.2742% (Manufacturer: Good Fellow) in its metal form was installed in a tantalum tube and thermoelectrically heated up to 65% of the maximum oven current to evaporate the uranium isotopes inside the ABU's oven. The created atomic beam was then collimated through an orifice at the exit of the oven. The laser beams were sent to the interaction region of the ABU through Brewster-angled fused silica windows where they resonantly excite the atoms. The perpendicular laser beam geometry to the atomic beam was used to reduce the Doppler broadening. The laser-produced ions are guided using ion optics to be detected using an electron multiplier tube (EMT). The resulting EMT signals are amplified and counted in coincidence with the laser trigger to achieve sensitive detection and background suppression.

Ti: Sapphire lasers were used for the excitation and ionization of ^{238}U. The layout of the laser systems used for uranium scheme tests in the FURIOS lab

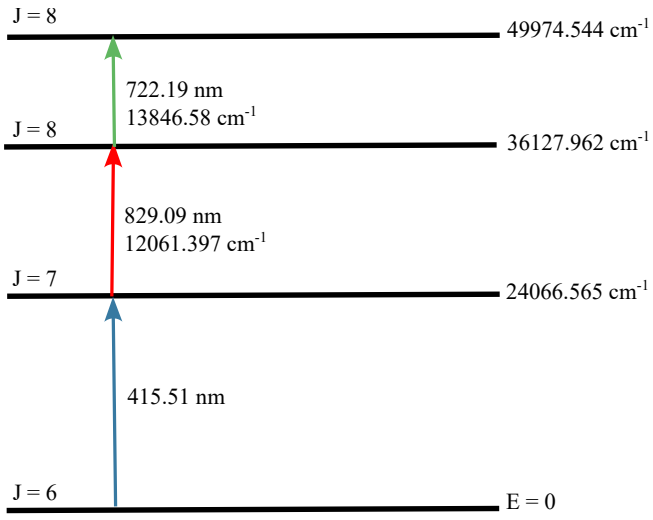

Figure 5.3: Scheme 1: Three-step resonance laser ionization scheme for stable ^{238}U developed in the literature [111].

is shown in figure 5.2. The laser path from the used laser system to the ABU is also shown. The Ti: sapphire lasers were pumped by pulsed Nd: YAG lasers (manufacturer: Lee Lasers) of 532 nm doubled frequency output. Two different three-step laser schemes from [111, 112] were tested.

The first laser scheme investigated was developed by Isselhardt and reported in [111]. The layout of this three-step laser scheme is shown as scheme 1 in the figure 5.3. The first excitation step is a blue transition of vacuum wavelength 415.51 nm with a transition probability of $1.931\times\ 10^7$ s^{-1} [113] from the ground state $5f^3\ 6d\ 7s^2\ ^5L_6$ (J = 6). A dual-etalon Ti: sapphire laser system was externally doubled using a BBO crystal to set up the first excitation/blue transition step. The dual etalon system uses a thick etalon of 6 mm and a thin etalon of 0.3 mm thicknesses giving a FWHM linewidth $\approx$ 1 GHz at the fundamental wavelength. Due to the heated environment in the oven of the ABU, Doppler broadening would be in the GHz range and hence the use of a narrow linewidth laser would be inefficient for resonance excitation of atoms. The second excitation transition step was tuned to 829.09 nm vacuum wavelength using another single etalon laser with fundamental FWHM line width 2-5 GHz. The third/ionization step was set to 722.19 nm to reach an auto-ionizing state using a single etalon Ti: sapphire laser (etalon thickness: 0.3 mm) of linewidth similar to the grating laser. The ionization potential of U is at 6.19 eV (49958.4 cm^{-1}). All three laser beams were spatially overlapped before sending them to the ABU. The three laser pulse timings were also synchronized. The fundamental laser wavelengths were monitored using commercial HighFinesse WS6 and WS10 wavemeters. The pulse timing was monitored using a photodiode placed after the ABU to pick up the transmitted laser light from the ABU arm.

The first step laser frequency scan was performed using a synchronized dual etalon scanning software. This allows scanning of the two etalon in sync using a pre-generated lookup table ensuring a constant laser linewidth and power throughout the scan. The maximum first, second, and third-step laser powers measured before the ABU were 120 mW, 450 mW, and 2 W respectively. The saturation curves for the different laser steps can be seen in figure 5.4. During measurements, the counting rates were decaying over time. The U source was

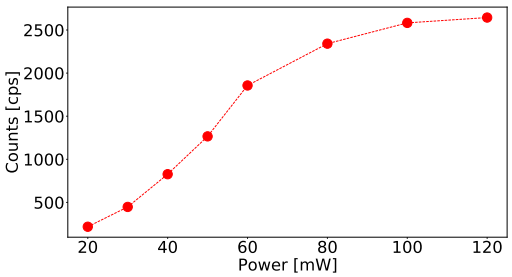

(a) FES: First excitation step

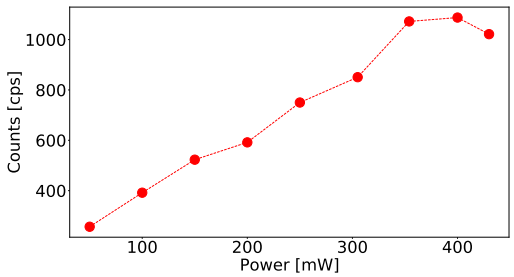

(b) SES: Second excitation step

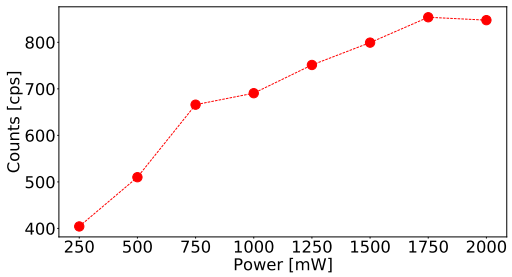

(c) TES: Third excitation step

Figure 5.4: Scheme 1: Saturation curves for first, second, and third laser steps

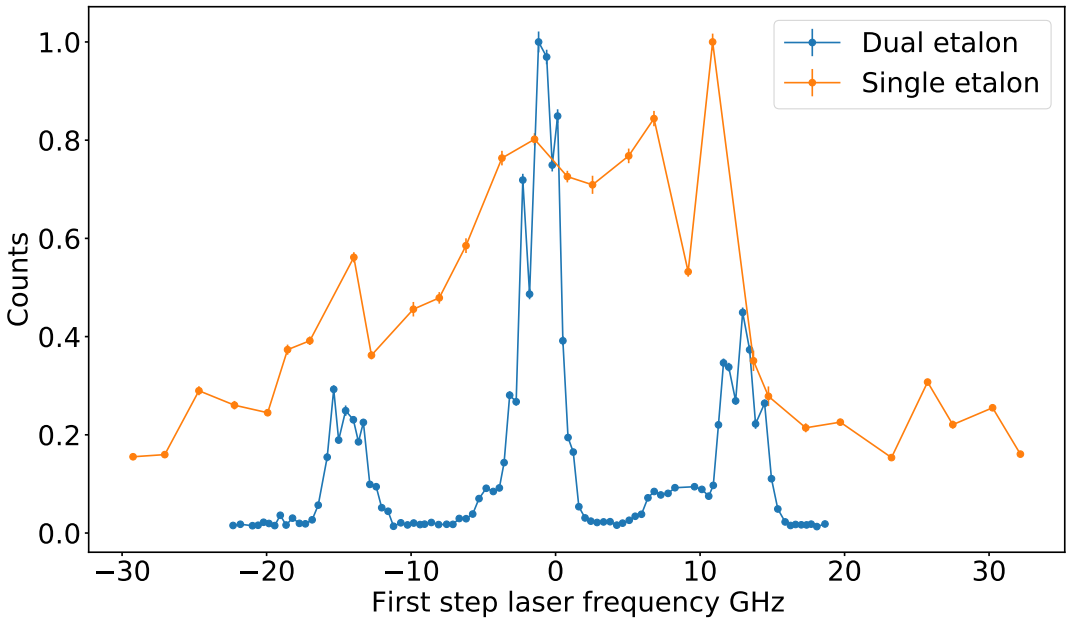

Figure 5.5: Scheme 1: RIS of ^{238}U with first-step laser scanning. Plot in blue is the excitation spectra with dual etalon and in orange is the excitation spectrum with thick etalon removed. The offset is the center laser frequency at 721497.4676 GHz. The data is binned with a step size of 0.2 GHz to obtain the mean data and the error bars shown are the standard deviation from the mean.

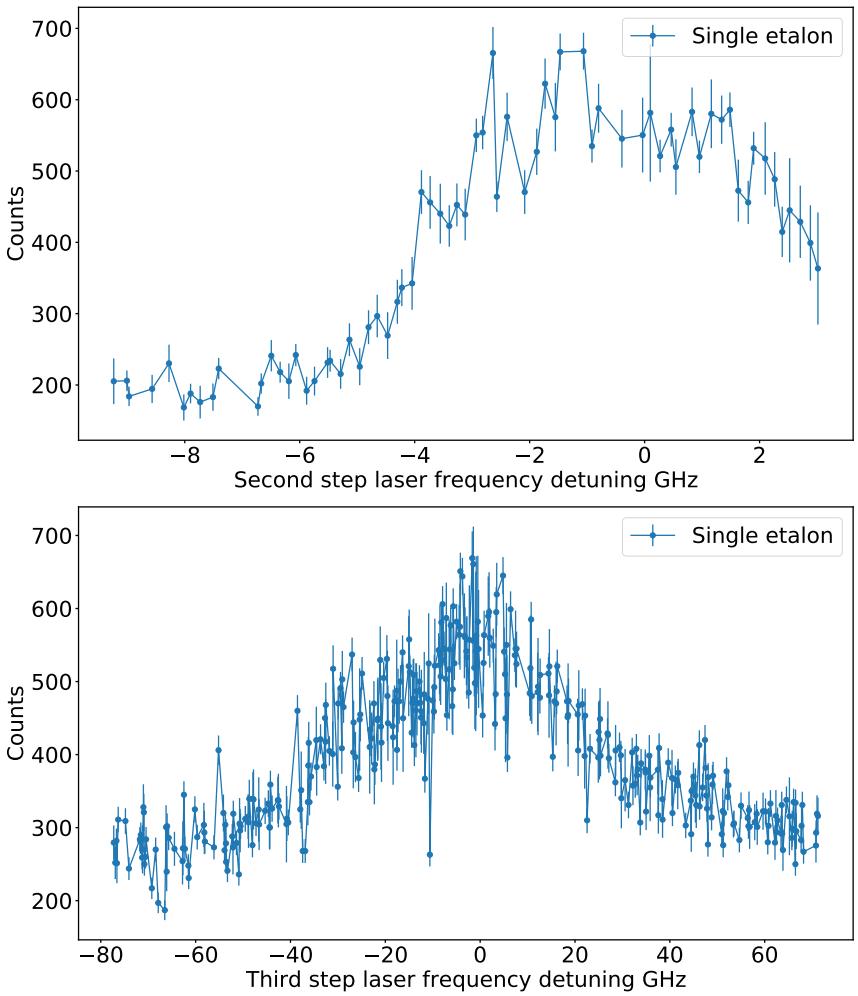

Figure 5.6: Scheme 1: Resonance peak scan of the second and third step laser.

from an older target source material and it might have degraded over time, possibly causing a faster decrease in uranium counts. For the saturation curves, the count rate data were binned to obtain the mean and rescaled to correct for the decreasing count rate over time (assuming a linear decrease for the measured time). The raw data and correction procedure can be found in the appendices (See appendix B). On top of the decreasing count rate, there was a count rate fluctuation due to filament instability. For the first-step dual etalon laser frequency scans, the first-step laser power was attenuated using an ND filter wheel to reduce any power-broadening effects.

The excitation spectrum obtained by scanning the first step transition is shown in figure 5.5. The uncertainties in the data points are the standard deviation of the mean of the binned data. Binning was performed for a step of 0.1 GHz. The plot in orange shows the scan performed with only a single etalon (thick etalon was removed from the dual etalon laser step) giving a broad resonance structure. The blue plot shows the excitation spectrum from the dual etalon scan. The spectrum obtained shows two side peaks along with resonance instead of showing a single resonance peak. These two smaller side peaks correspond to the arising side modes of the thick etalon. To ensure that side peaks were multimodal effects from the dual etalon, the dual etalon alignment was adjusted and measurements were repeated giving shifted side peaks with different intensities. This multimoding could not be eliminated completely for any of the scans performed. The resonance scans of the second and third transition steps were also performed by the respective laser frequency scans to ensure that all the lasers were contributing to the ionization process resonantly. The second and third step laser scans are shown in figure 5.6. The data points are binned with step sizes of 0.05 GHz and 0.01 GHz for the second and third-step scans respectively and the mean value is plotted. The error bars shown are the standard deviation from the mean value.

Scheme 1 tests, despite the count fluctuations and decaying count rate (due to issues with the uranium source and filament instabilities), showed that it is able to ionize uranium atoms resonantly. A cleaner source could reduce the signal-to-background ratio. The multimodal effects in dual etalon will be covered by the pressure broadening of the first step transition when performing in-gas cell ionization. The nonresonant uranium ionization from the laser steps (see figures 5.6) would still be present when performing in-gas cell ionization.

The second scheme tested (Scheme 2) was also from the ground state ($J = 6$) with the first step at 24066.57 cm^{-1} ($J = 7$) similar to scheme1, the second step at 37096.5 cm^{-1} ($J = 7$), and the third step at 50443.4 cm^{-1} ($J = 6, 7, 8$) above the I.P (See figure 5.7). This scheme was reported in the RILIS database [114]. For the first step, the same dual etalon laser was used, the second step was set up using a grating-based Ti: sapphire laser with a linewidth of 3 - 5 GHz FWHM, and the third step was step using the same single etalon laser as of scheme 1. Uranium was resonantly ionized using scheme 2 and the excitation spectra were recorded. Large fluctuations in the count rates were observed similar to the tests in Scheme 1. The excitation spectra measured are shown in the figure 5.9. It shows the resonance peak scan measured by scanning a dual etalon laser as well as a single etalon laser (with thick etalon removed). The second and third-step transitions were also scanned and the resonances are shown in the figure 5.10. The data points are binned with a stepsize of 0.01

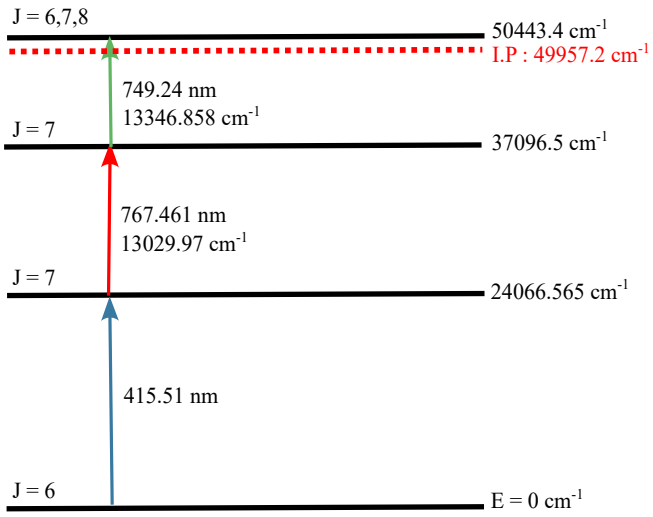

Figure 5.7: Scheme2: Three-step resonance laser ionization scheme for stable ^{238}U developed in [114].

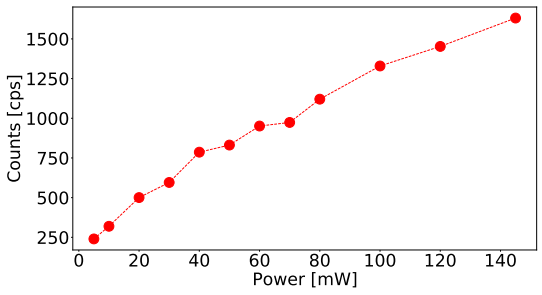

(a) FES: First excitation step

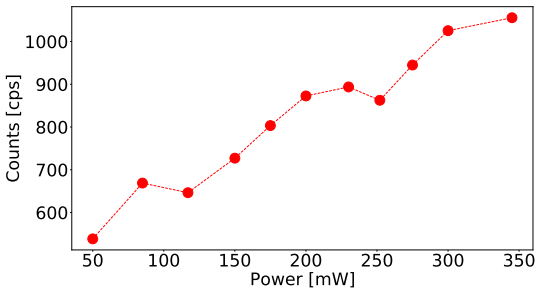

(b) SES: Second excitation step

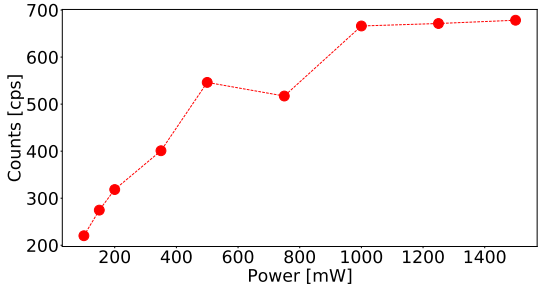

(c) TES: Third excitation step

Figure 5.8: Scheme 2: Saturation curves for first, second, and third laser steps

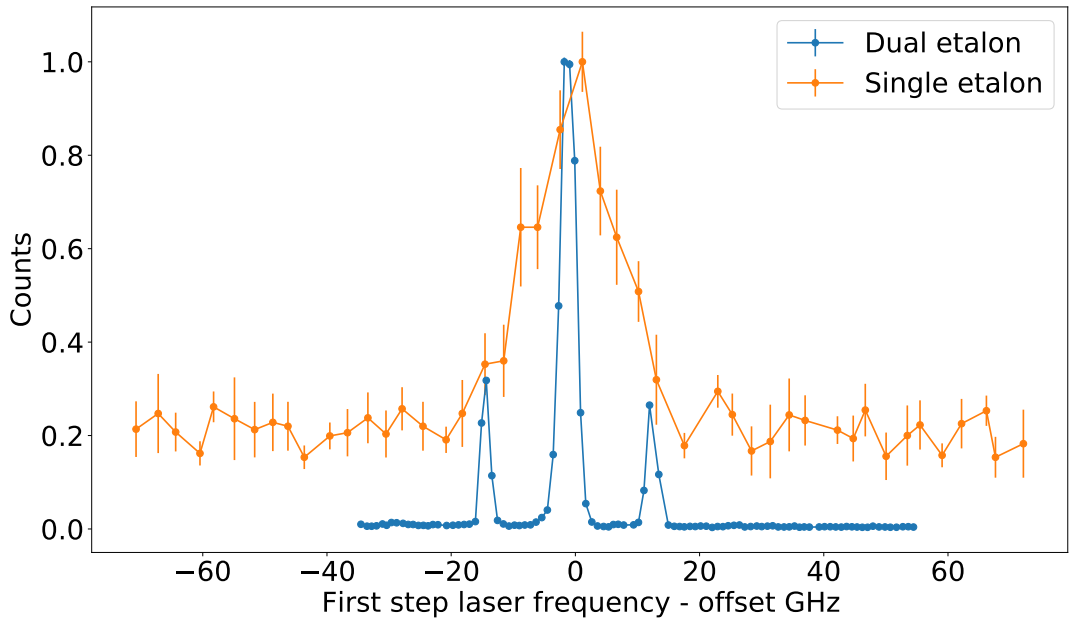

Figure 5.9: Scheme2: The first step resonance excitation spectra for uranium using the RIS scheme from [114]. The blue plot shows the scan with the dual etalon laser and the orange plot shows the scan with the thick etalon removed. Here the offset is 721497.4676 GHz. The plotted values are binned data points similar to scheme 1.

GHz and the mean values are plotted. The error bars shown are the standard deviations of the mean values. For the measurements, the second and third-step lasers were kept at a power of 345 mW and 1.5 W respectively, measured just before the ABU. In the first step, laser power was attenuated to nearly 40 mW. The saturation tests and binning of data were performed similarly to scheme 1.

The saturation scans for scheme 2 are shown in the figure 5.8. To ensure that the pulse timings are synchronized, the first-step laser was delayed with respect to the second and third-step lasers, and the corresponding count rates were recorded. The timing scan measurements can be seen in the figure 5.11. Maximum count rates were obtained when laser pulses were completely overlapped. Due to the fluctuations in the count and decaying count rate while measurements, a quantitative conclusion on the goodness of the scheme is challenging. However, qualitatively, we can conclude that the tested schemes 1 and 2 gave comparable ionization efficiency in the ABU. Further precise studies will be performed by replacing the dual etalon laser with a double grating Ti: sapphire laser to provide a continuous and wide scanning range in the blue transition wavelength region.

Another scheme of interest is a three-step scheme reported in [112]. This scheme involves a transition from a metastable state at 620.3 cm^{-1} ($J = 5$) near the ground state. Atoms from thermoelectrical heating would excite to the metastable state and from the metastable state they can be excited using a laser to an excited level at 25349 cm^{-1} ($J = 6$). From the first excited level, the electrons can be further excited to 37412.2 cm^{-1} and then ionized above the ionization potential of 49958.4 cm^{-1}. In the literature [112], this scheme has been efficiently used for resonant laser ionization. There are also two-step schemes with transitions in the blue wavelength range developed such as the

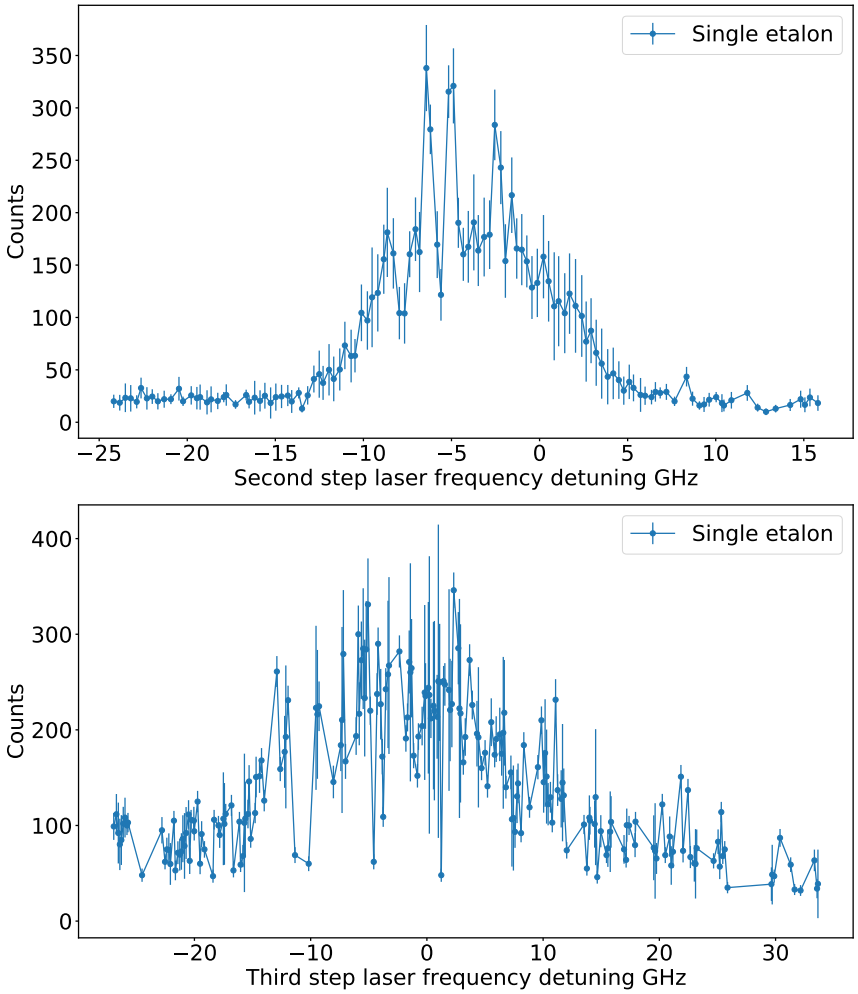

Figure 5.10: Scheme2: Resonance peak scan of the second and third step lasers.

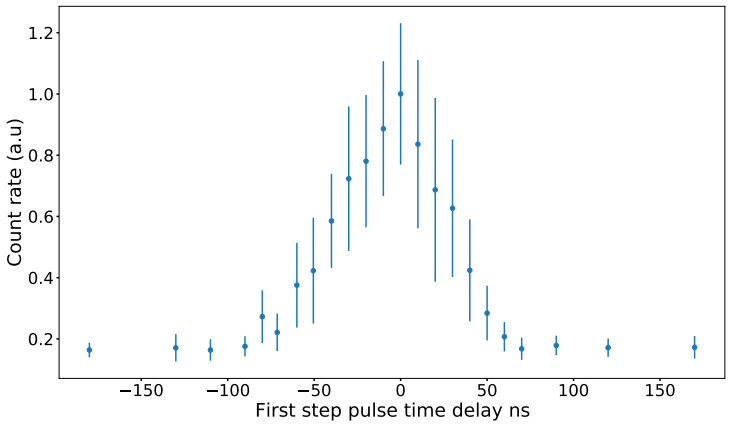

Figure 5.11: Pulse timing scan performed by delaying the first step laser pulse with respect to the second and third step using RIS scheme (Scheme 2) from [114].

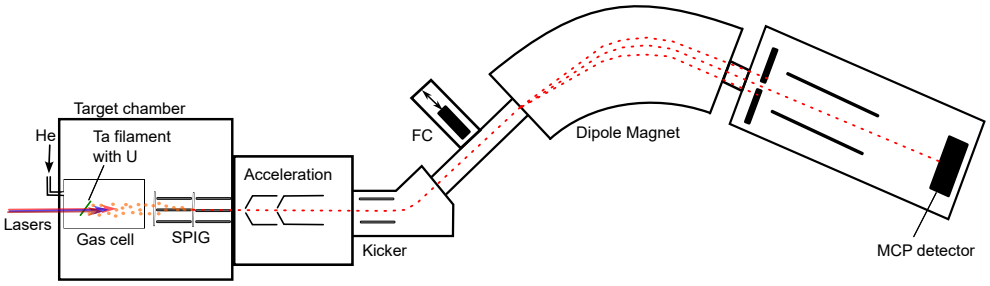

Figure 5.12: The layout of the IGISOL set-up for offline gas cell tests with U(The image is adapted from [93]).Labels are SPIG-Sextupole ion guide, FC-Faraday cup, MCP- michrochannel plate

one used in [115] for ultra-trace analysis and [116] for mass spectrometry. The scheme from [116] is two-step transitions of the same wavelength of 396.3 nm and hence will not be able to distinguish the resonant counts from the nonresonant background. The scheme from [115] uses two-step blue-blue transitions of slightly different wavelengths of 396.2 nm and 403.9 nm that could be used for resonance ionization laser spectroscopy of uranium. Two-step schemes would be easier to set up and control and are of interest for the S^3-LEB measurements. However, to test these schemes we would require proper scanning of resonances of the blue transition, which is currently not possible with laser setups available. It can be implemented using a doubled grating-based Ti: sapphire laser system.

5.1.2 Tests with the gas cell

For the preliminary gas cell tests, scheme 1 was implemented [111]. The layout of the gas cell laser ionization setup at IGISOL is shown in figure 5.12. The gas cell is housed inside the target chamber. Laser ionization of uranium atoms occurs inside the gas cell filled with He as buffer gas at around 120 mbar pressure. The ions with He are flushed out from the gas cell. The ions are then guided through a sextupole ion guide (SPIG) and accelerated toward a mass separator. The dipole magnet is set for mass-selection of ^{238}U with a mass resolving power $m/\Delta m = 400$. An MCP detector is located at the focal plane of the separator to measure the ion count rate. More details on the IGISOL setup and gas cell can be found in [93]. For the tests with U, the first step transition was set with a dual etalon laser at an average power of 75 mW measured before the gas cell window. The second and third-step lasers were set to an average power of 300 mW and 870 mW respectively. A U sample was wrapped in a Ta foil and clamped onto the holder inside the gas cell chamber. The filament was heated to $\approx 1700^\circ$ (measured with a pyrometer) which required a filament current of rough 3 - 4 A. A positive voltage was applied at the entrance plate of the SPIG to verify that the ions were formed inside the gas cell. As the ions were mostly formed in the gas cell, the positive voltage gave a drop in the count rate repelling the ions coming out of the gas cell at the entrance of SPIG.

The first step laser scan is shown in figure 5.13. The second step did not contribute to the ion counts. The resonance structure with multiple peaks is laser-produced ions only from the first step. With the first step-laser OFF,

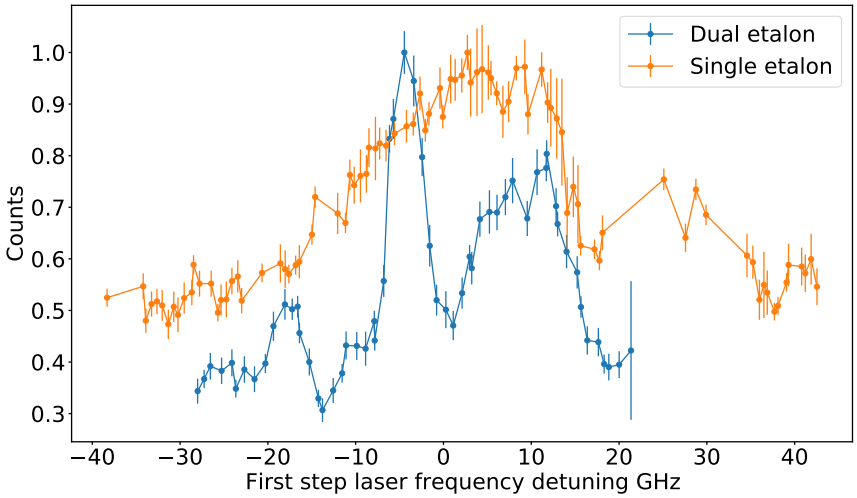

Figure 5.13: First step laser scan for laser ionization of ^{238}U inside the IGISOL gas cell. The orange plot shows the first-step laser scan with a single thin etalon of 0.3 mm. The blue plot is the resulting spectra for scanning a dual etalon (with a thin etalon of 0.3mm and thick etalon of 6mm thickness) as the first step showing the resonances with a dip at the center of the peak. The data is binned with a step size of 0.01 GHz to obtain the mean and the error bars are the standard deviation from the mean value.

the ion count reduces to half. Even though a two-photon excitation does not reach the ionization potential of U, the blue laser step alone contributes to the ionization of U. With the second step blocked, no effect was seen on the counts. Blocking and unblocking the third step showed that it affects only the background. The fact that the second step and third step do not contribute to the ionization process unlike the case in ABU indicates possible collisional de-excitation processes in the gas cell as it was seen in [93]. From the figure 5.13, it can be seen that a dip is present at the center of the resonance peak-like structure. A similar trend with the dip at the center of the resonance peak was observed with laser ionization of Er in the gas cell ionization (See section 4.19). This dip was however not seen for very low powers in gas cell ionization with Er indicating a combined effect from collision and power broadening.

In order to define the contribution from the different laser steps, mass scans were performed at different laser configurations. Long-range mass scans showed the formation of UO (an order of magnitude more than the uranium signal itself) and UO_2 (half of that of U signal) molecules (See Appendix B.6). The presence of oxygen might be through the injected gas in the gas cell. Figure 5.14 shows the mass spectra in the mass range of stable uranium with the blue plot showing the mass spectra with the first and third laser steps in, the orange plot showing the spectra with the first excitation step detuned, and the green plot showing the spectra with first step detuned and the third laser step blocked. From the mass spectra, it could be clearly observed that the first laser step was contributing to the laser ionization of ^{238}U. The side peaks at mass 235 are not ^{235}U as it does not match the natural isotopic abundances. Also when the first step laser is detuned, only the ^{238}U signal counts are reduced and the side peak remains the same. The contribution of the third laser step to ionization was also investigated. From the mass spectra, it could be seen that when the third

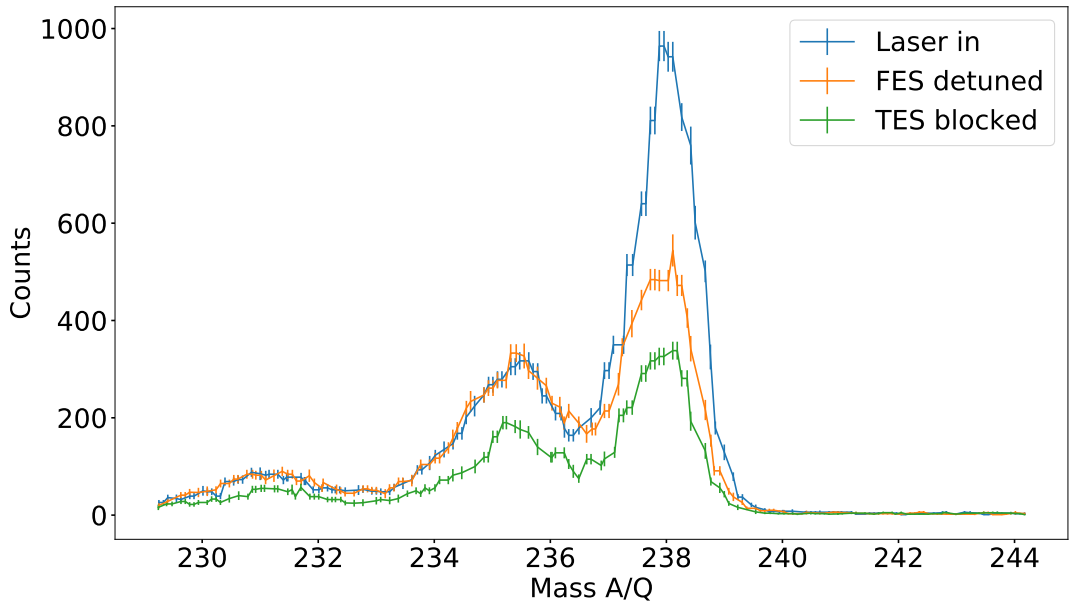

Figure 5.14: Mass scan performed for the laser-produced ions in the gas cell

excitation step (TES) was blocked, the ^{238}U peak and the side peak counts were reduced by the same amount. This means the third step contributes only to the background and not to the laser ionization. The background contamination is from the impurities in the gas cell ablated by the first and third step laser forming molecules. With the first and third steps blocked, these backgrounds are no longer present (see appendix B.7).

Further systematic studies are required to quantify these effects which was challenging due to the count rate fluctuations and instability of the filament. For future studies, more reliable filament such as the ones used in gas cell studies of thorium at IGISOL (reported in [92]) is required. Here, the actinide elements are electrolytically deposited on a substrate (like Ta) and then covered with a layer of reducing agent (like Ti). These so-called actinide sandwiches result in stable sources of atoms. When performing resonant laser ionization in a gas cell at S^3-LEB, similar problems will be encountered and have to be tackled. However, for high-resolution spectroscopy laser atom interaction will be in the gas jet and hence the tested laser schemes can be used efficiently. For prior offline tests, stable filament sources have to be developed, as mentioned above, for reliable and systematic studies. In IGISOL JYU, for collinear laser spectroscopy hyperfine structure measurements on ^{235}U isotope, spark sources were used (ongoing thesis work). The future perspective to these tests in regard to S^3-LEB will be to study these collisional deexcitation effects systematically in the gas cell to improve the resonance laser ionization efficiency in the gas cell.

5.2 Laser spectroscopy of Americium at RISIKO

For high-resolution laser spectroscopy, laser developments and the upgradation of existing laser systems have been ongoing in the Department of Physik, JGU Mainz. As a part of the laser developments, a CW Ti: sapphire laser was upgraded to be used as a seed laser for an injection-locked laser system. With

this laser system as the first step excitation laser, high-resolution resonance ionization laser spectroscopy of the long-living isotopes ^{241}Am and ^{243}Am was conducted with the Resonance Ionization Spectroscopy in Collinear geometry (RISIKO) setup. The test was performed as a part of the training to develop and evaluate the performance of the diode-pumped CW laser system in high-resolution spectroscopy applications. The americium measurements discussed below were also part of a master thesis work at JGU where two laser ionization schemes for americium were studied [117]. Here measurements with one resonance laser ionization scheme are discussed in the scope of demonstrating the applicability of the JGU CW laser system.

Americium was chosen for the tests as it is one of the elements in the actinide series on which only a few laser spectroscopic studies have been performed and hence several information regarding its atomic and nuclear structure are missing. Americium has applications used as radionuclides, and as a neutron source. The half-life of longest living isotopes, ^{241}Am and ^{243}Am are 432.2 years and 7350 years. Resonance ionization laser spectroscopy studies on americium isotopes have been previously reported in [118, 119, 120, 121].

The general layout of the RISIKO setup is shown in the figure 5.15. The setup consists of a hot-cavity ion source with a reservoir and an atomizer made of tantalum. Americium in solution form was dried on a foil made of zirconium (used as a reducing agent) and was installed in the sample reservoir. The sample reservoir and the atomizer were heated resistively for the atomization of americium isotopes. It has a laser ion source and trap (LIST) module that has two repeller electrodes to suppress the surface ions. Laser ionization of the atoms is performed in the LIST module.

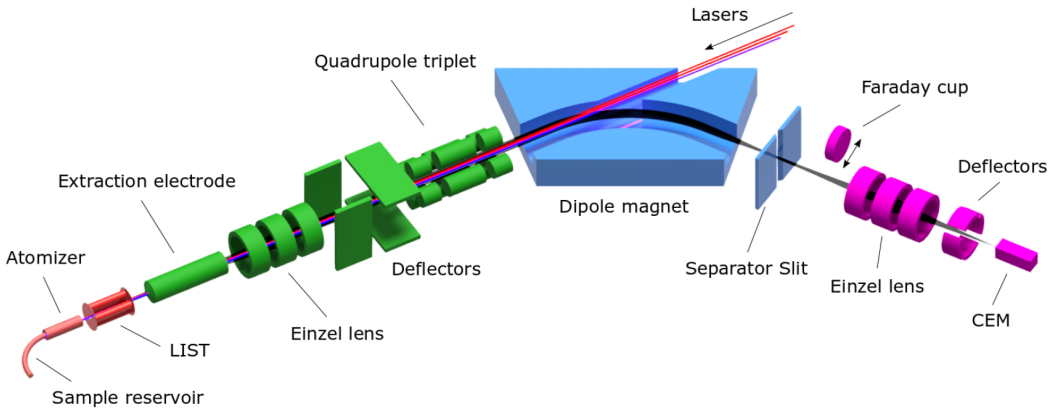

Figure 5.15: The layout of different components of RISIKO setup taken from [89].

For laser ionization of the Am atoms, a two-step ionization laser scheme was used as shown in figure 5.16. The laser scheme implemented was taken from [115]. The first step laser was set up using a frequency-doubled injection locked Ti: sapphire laser seeded by a diode-pumped CW Ti: sapphire laser developed in JGU Mainz [75, 81]. The CW Ti: sapphire laser currently being built in GANIL (presented in section 3.3) is an updated design of the CW cavity used in JGU, Mainz. The layout of the CW cavity in Mainz is shown in the figure 5.17. It is a double-sided diode laser-pumped Ti: sapphire laser system with a basic bow-tie geometry. It incorporates two curved mirrors, an output coupler,

and a high-reflecting mirror, all of them having broad-band wavelength coatings of 620 - 1100 nm. The operation of this laser cavity is similar to the GANIL CW laser (refer to section 3.3). Unlike the GANIL CW cavity, the JGU CW cavity has all the mirrors aligned in one plane. Hence an additional half-wave waveplate (WP) is required for polarization rotation to achieve unidirectional operation. The high-reflecting mirror is the piezo-actuated mirror compared to the piezo-actuated output coupler mirror in the GANIL CW laser (see section 3.3). It was observed that with this cavity, while continuous wavelength tuning of the cavity, the angle of the etalon varies and causes a flip in the direction of lasing hindering continuous measurements during experiments. To avoid this problem, the GANIL CW cavity uses off-axis geometry with additional two cavity mirrors. This might increase the losses in the cavity but still give enough seeding power. The JGU CW cavity also has the diode pump laser setup outside the cavity requiring more space, and pump alignment to the crystal is different from the GANIL CW cavity. The full characterization of the JGU CW cavity can be found in detail in [117]. For the GANIL CW cavity, the provision of an internal frequency doubling unit is also added to obtain CW output in the blue wavelength region. The doubling can be of use for planar laser-induced fluorescence measurements [64] if needed for gas jet flow characterization in S^3-LEB.

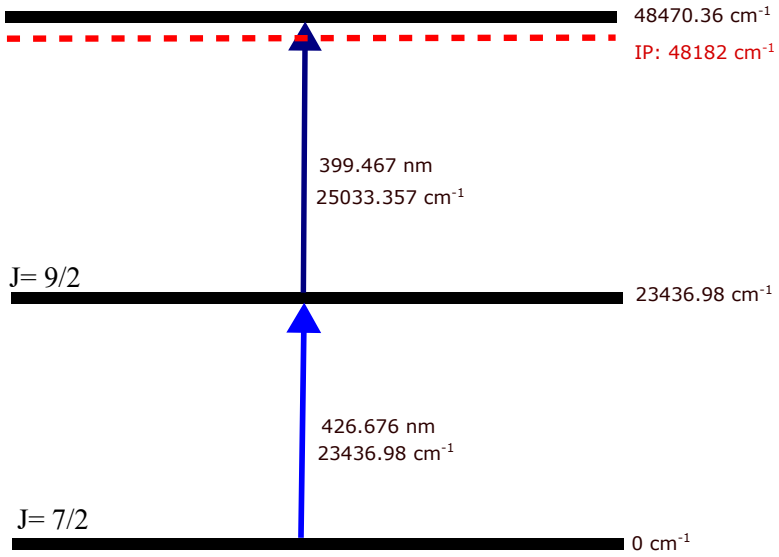

Figure 5.16: Two-step laser scheme used for resonance ionization laser spectroscopy of americium isotopes reported in [115].

For the Am tests, the CW laser output was kept at a few mWs which was sufficient to seed the injection-locked laser. The cavity output beam quality was evaluated by measuring the M^2 value of the output beam spot in both tangential and sagittal planes as shown in figure 5.18. For the measurement, a small portion of the CW laser output at a wavelength $\lambda = 834$ nm was sent through an achromatic focusing lens of focal length 60 mm to a CMOS camera (Cinogy Technologies CMOS-1202) to measure the 4σ-D beam diameter. The measured data was fitted (using the least-square method) to the equation 3.3 to obtain an $M^2 = 1.347(17)$ and $M^2 = 1.274(17)$ in the tangential and sagittal planes respectively. The uncertainties mentioned are the standard deviation of

the measurements from the fit results. The M^2 values in both planes are close to unity indicating that the transversal mode of the CW laser output is preferably TEM_{00} or Gaussian. This can also be observed from the beam waist overlap of the beam diameter measurement in both planes which otherwise indicates a spatial dispersion. The linewidth of the CW laser was measured to be 2.95(33) MHz using a scanning FPI as reported in [117].

The CW cavity was then used to seed the injection-locked cavity. The CW laser output was fiber coupled to the injection-locked cavity. The injection-locked cavity wavelength was tuned by scanning the wavelength of the CW cavity. The wavelength of the JGU CW- cavity was coarsely adjusted around the resonance wavelength range using a BRF filter. For scanning the injection-locked cavity wavelength and for fine-tuning the cavity, a small portion of the CW-cavity output was sent to a Fabry-Perot cavity and the corresponding peak from the transmission fringe pattern of the FPI was scanned by application of a scanning ramp signal. The variation in the transmission intensity generates the control signal for the piezo-actuated mirrors thereby finely adjusting the cavity length. Thus the cavity length, being locked to the FPI transmission, follows the transmission length variation, thereby tuning the wavelength of the cavity. For the JGU CW cavity stabilization, the etalon in the cavity was also piezo-actuated and a technique called dither-locking was implemented. The operation of the injection-locked cavity is similar to the one used in S^3-LEB and is explained in chapter 3.

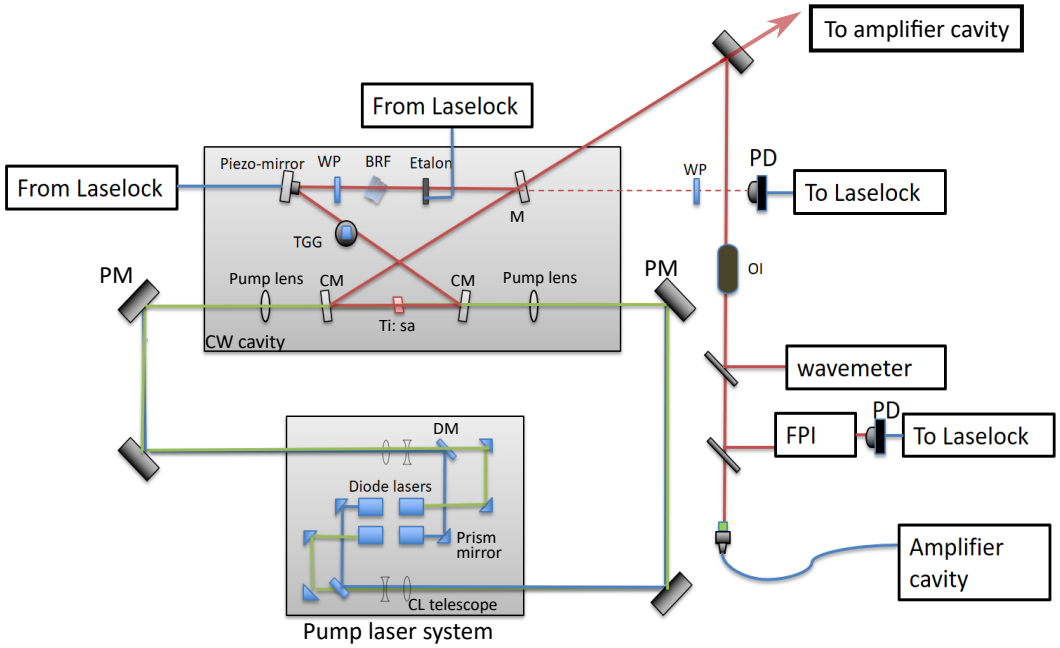

Figure 5.17: Layout of the JGU continuous-wave Ti: sapphire cavity used as a seed laser for the injection locked Ti: sapphire laser for the americium measurements. Labels: DM - dichroic mirror, PM - pump mirror, CL - cylindrical lens, CM - curved mirror, TGG - Faraday rotator, WP - half-wave plate, BRF - birefringent filter, M - high reflecting mirror, PD - photodiode, FPI - Fabry-Perot interferometer.

The second step laser was set using a frequency-doubled dual-etalon Ti: sapphire laser. Both the dual etalon and the injection-locked Ti: sapphire lasers

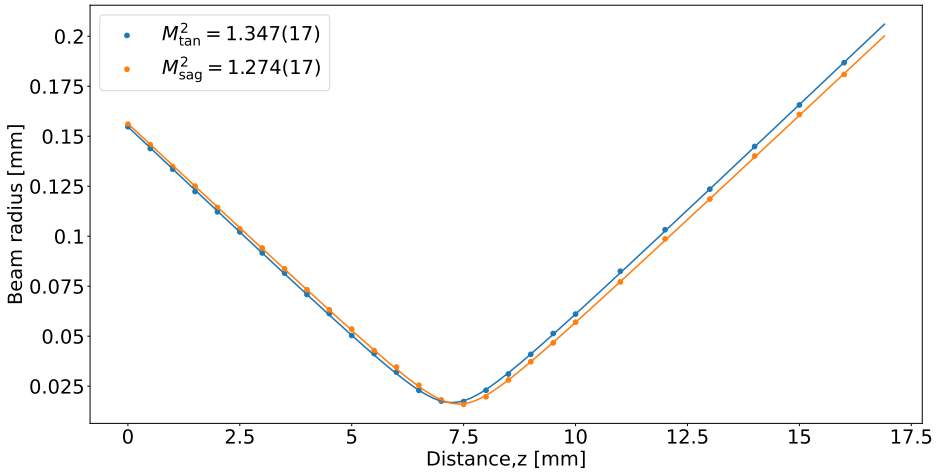

Figure 5.18: M^2 measurement of the CW-cavity beam spot in the tangential and saggitarial plane.

are pumped by a 10 kHz Nd: YAG laser for their pulsed operation. The pump laser power is distributed among the Ti: sapphire lasers using polarising beam splitters and half-wave plates. The first step laser was sent perpendicular to the direction of the atomic beam and the second step laser counter-propagating. This perpendicular geometry reduces the spectral Doppler broadening. The laser configuration used is shown in figure 5.19 [117]. The upper-left inset in the figure shows a cross-sectional 3-D view of the atomizer and the following extraction electrodes and quadrupole rods with the first-step laser expanded beam traveling perpendicular to the atomic beam axis and the second-step/ionization-step laser beam spot traveling counter-propagating to the atomic beam. The right insets show the different laser systems used for measurements. The lower-right inset shows the layout of the first-step laser having a narrow linewidth (FWHM $<$ 50 MHz) and the upper-right inset shows the layout of the second-step laser with a broader linewidth of a few GHz. The lower-left inset shows the seed laser for the first-step laser, reference cell, and wavemeter setup for accurate wavelength measurements.

The laser-produced ions in the PI LIST ion source region are then extracted via extraction electrodes to guide them to a detection system (refer to figure 5.15). The Einzel lens and the extraction electrodes allow for adjusting the beam divergence and size. The deflector plates are used to correct the beam direction and also act as a beam gate for the separation of continuously extracted surface ions from the ions of interest. The quadrupole triplet in the RISIKO system allows for compensation for astigmatism in the ion beam. The dipole magnet enables mass separation (with a mass resolving power $m/\Delta m = 600$) by adjustment of the applied magnetic files such that the selected mass is focused on the separator slit aperture. The ions are then detected with a Faraday cup or by a channeltron electron multiplier (CEM). For more details of the setup see [89]. The detected signals are then converted to TTL pulse by a discriminator and acquired with an Arduino microcontroller unit.

Americium has its first ionization potential at 5.993 eV with an energy state $5f^7\ 7s\ {}^9S^0_4$ [122, 123]. The first step laser excites the Am atom from its ground

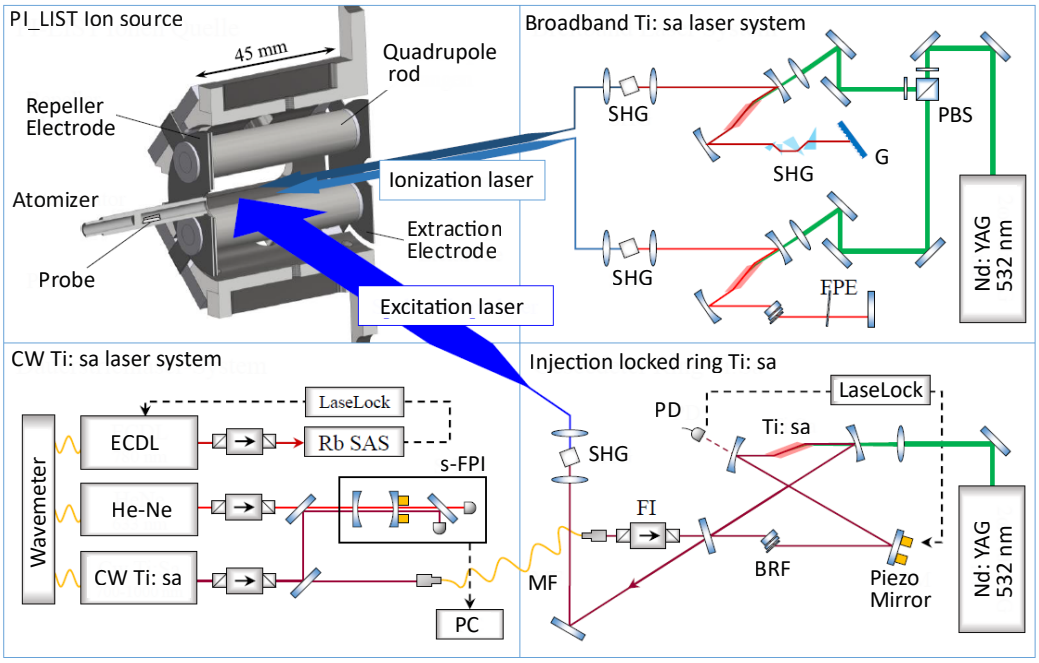

Figure 5.19: Layout of the laser system at RISIKO taken from [117]. Labels: PI LIST - perpendicularly illuminated laser ion source and trap, PBS - polarising beam splitter cubes, G - grating, SHG - second harmonic generation, FPE - Fabry Perot etalon, PD - photodiode, BRF- birefringent filter, FI- Faraday isolator, MF - multimode fiber, Rb SAS - rubidium saturation absorption spectroscopy, s-FPI - scanning Fabry Perot interferometer.

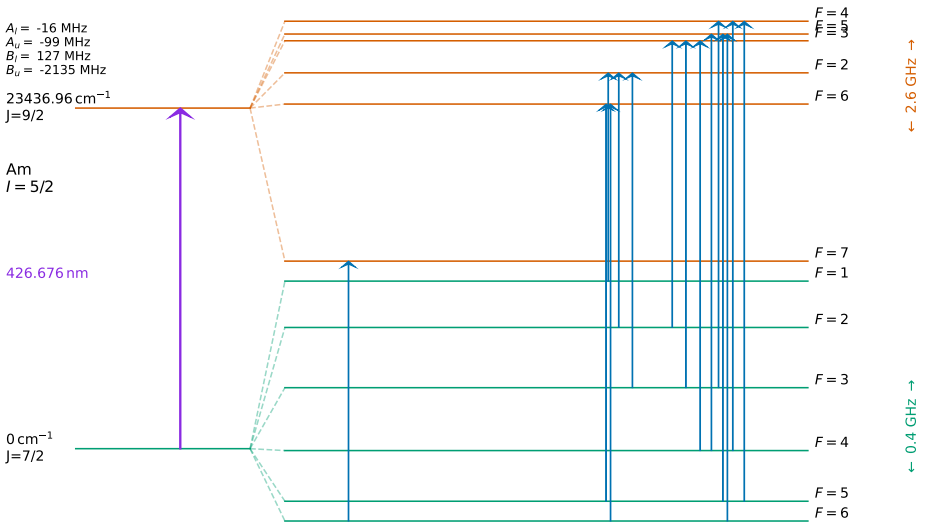

Figure 5.20: Hyperfine splitting of the 426.676 nm transition for the ground state and the first excited state is shown. The RIS scheme was plotted using the SATLAS model with hyperfine constants, A and B for the ground state fixed to values as shown in the figure. The corresponding excited level, A and B constants are also shown. The angular momentum of both states and the energies are mentioned in cm^{-1}. The purple arrow shows the atomic transition wavelength.

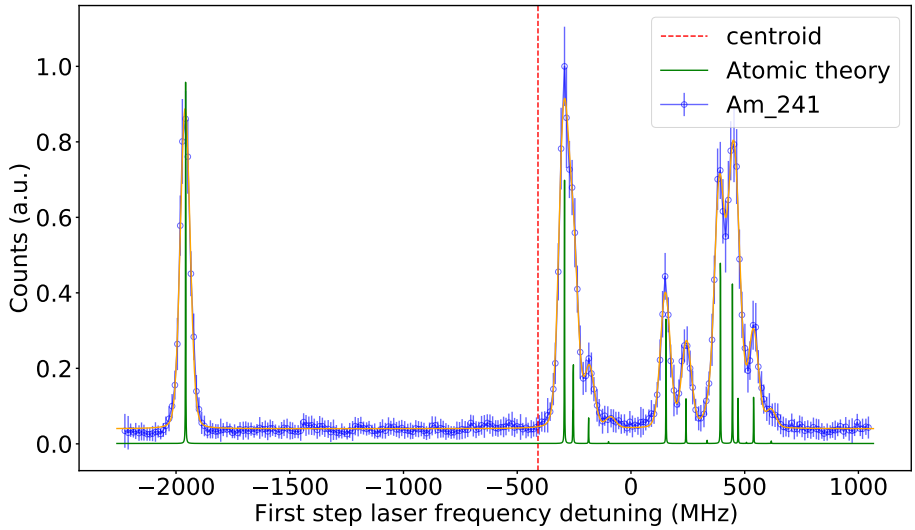

Figure 5.21: Hyperfine structure of ^{241}Am for the 426.676 nm transition is shown. The measured data is shown in blue with their statistical uncertainties. The measured data are fitted with a Voigt profile (yellow) keeping the Racah intensities free as well as the A and B parameters free. The reduced χ^2 for the fit is 0.132. Here the offset f_0 = 702,622,984.229 MHz. The deduced centroid is marked with the red vertical dashed line at -408.8 MHz. The green lines show the expected hyperfine peaks obtained from fixing I, J, and hyperfine constants A, B, and C to atomic theory with spectral FWHM fixed to 0.25 MHz

state $5f^7\ 7s^2\ {}^8S^0_{7/2}$ to a first excited state at 23436.98 cm^{-1} whose electronic configuration is unknown. The angular momentum for the ground state is J = 7/2 and the first excited level is J = 9/2. The nuclear spin is I = 5/2 [120]. The first step laser frequency was scanned over the resonance center to obtain the hyperfine spectra of ^{241}Am and ^{243}Am. The hyperfine splitting of the 426.676 nm transition with levels defined by the F quantum number is shown in figure 5.20. F can have values between $|I - J| \leq F \leq |I + J|$ (refer to section 1.2.2). The purple arrow shows the fine structure transition and the blue arrows show the possible transitions between the hyperfine levels of the ground and the excited state for ^{241}Am. The figure at the right end also shows the calculated degree of extent of the hyperfine level splitting of the ground state (green) and the excited level (orange), which are 0.4 GHz and 2.6 GHz. This indicates the hyperfine structure of ^{241}Am to extend over roughly 3 GHz.

The measured hyperfine structure of the ^{241}Am and ^{243}Am are shown in figure 5.21 and figure 5.22 respectively. The measured data points are shown in blue and their respective χ^2 fits using a Voigt profile are shown in orange. The scan data was binned with a step size of 0.2 MHz and the mean value was plotted. The error bars in the plot are the standard deviation from the mean value. The SATLAS package was used to fit the measured data. For the ^{241}Am and ^{243}Am scans, shown in figure 5.21 and figure 5.22, the fits were performed with the hyperfine A and B constants for both levels and the Racah intensities set free. From the fit, the isotope shift between the two odd isotopes was measured to be 4534(2) MHz. The hyperfine constants for the ground

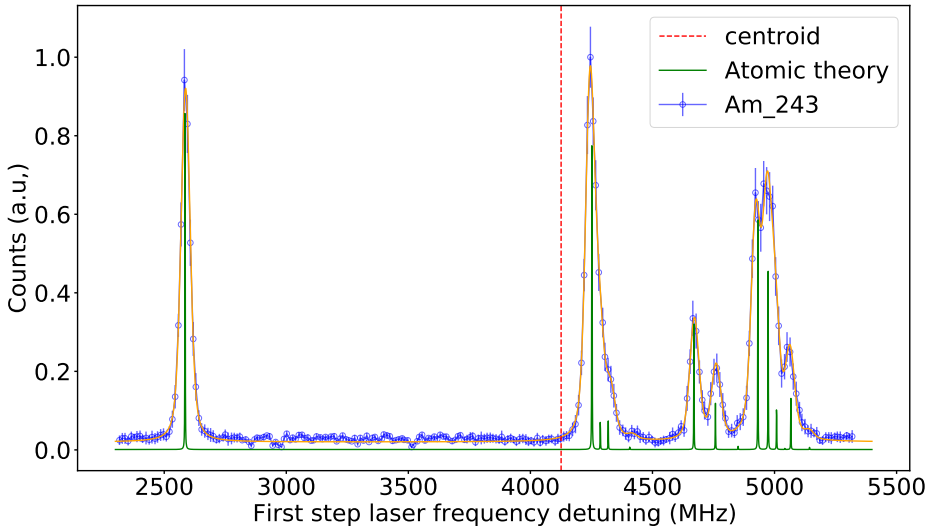

Figure 5.22: Hyperfine structure of ^{243}Am for the 426.676 nm transition is shown with the measured data in blue and their Voigt fit in yellow. The green lines show the expected hyperfine peaks obtained from fixing I, J, and hyperfine constants A, B, and C to atomic theory with spectral FWHM fixed to 0.25 MHz. The offset f_0 = 702,622,984.229 MHz. For the fit, the A and B fit parameters were kept free as well as Racah intensities were not fixed. The fit gave a reduced $\chi^2 = 1.27$. The deduced centroid is marked with the red vertical dashed line at 4125.7 MHz.

state and the excited level for 426.676 transitions have been already reported in literature [120, 124, 121, 117]. The deduced hyperfine constants A and B as well as the FWHM from fits are reported and compared with literature values in table 5.1. The results from the fit with ground state hyperfine constants and Racah intensities fixed are also presented in table 5.1. The uncertainties given in the table are statistical uncertainties from a single scan and do not include the uncertainties from the scattering of the data or systematic uncertainties and hence are underestimated. The fit results for ground-level A_l and B_l constants are in good agreement with the literature values. A considerably different result for hyperfine constants A_u and B_u in the excited level was obtained. To compare the goodness of the results, different fit parameters conditions were implemented as presented in table 5.1 and the results were compared. All of the fits performed gave comparable values. Several scans were taken for the transitions giving similar results as reported in [117]. The hyperfine constants A_u and B_u for the excited level are quoted in [125] to be from the reference [126]. However, these values could not be found in the mentioned reference. This indicates that literature values might have been wrong considering that the stated value might have been for some other transition out of 3000 americium lines measured with a 30 ft- spectrograph using optical spectroscopy in [126]. The experimental spectral linewidth (FWHM) could also be deduced from the fit. All of the fit results gave near 50 MHz FWHM which is sufficient to deduce the hyperfine A and B constants from the spectra obtained even though all the transitions do not give well-resolved peaks. The ground state level has a low splitting

Table 5.1: Hyperfine constants A and B for the ground state and excited state at 23436.98 cm^{-1} deduced from the hyperfine structure measurement is compared with the literature data from [120, 126]. ^{241}Am* and ^{243}Am* give the fit values with Racah intensities fixed.

Am isotopes	A_l (MHz)	A_u (MHz)	B_l (MHz)	B_u (MHz)	FWHM (MHz)
^{241}Am	-16.6(5)	-100.7(4)	136(6)	-2118(7)	49(2)
^{243}Am	-16.6(7)	99.5(6)	121(11)	-2139(10)	46(2)
^{241}Am*	-18(1)	-101(1)	116(9)	-2146(11)	50(2)
^{243}Am*	-17(8)	-100.4(7)	96(12)	-2168(13)	47(2)
^{241}Am*	-17.144(fixed)	-101.23(6)	123.82(fixed)	-2137(2)	50(2)
^{243}Am*	-17.144(fixed)	-100(1)	123.82(fixed)	-2139(4)	48(2)
^{241}Am[120, 126]	-17.144(8)	-66(15)	123.82(10)	-2970(30)	-
^{243}Am[120]	-17.1437(28)	-	123.8477(323)	-	-

compared to the excited level splitting. The transition to the excited hyperfine levels is hence resolved. The unresolved peaks can be identified in figure 5.21 and 5.22 by comparing the measured spectra (blue) with the plot (green) using atomic theory.

From this proof of principle measurements with Am, it can be concluded that high-resolution spectroscopy on actinides can be performed successfully using the cost-effective diode-pumped CW system as a seed laser. The hyperfine splitting of both the isotopes could be resolved using the laser system. The CW system operates with stability and the locking to the injection cavity is manageable for continuous measurements for offline studies. Thus the CW diode-pumped Ti: sapphire seeded injection locked Ti: sapphire laser system is proven to be performing well for high-resolution laser spectroscopy of elements including the heavier masses. It is a promising tool to be used in S^3-LEB for high-resolution resonance ionization laser spectroscopy. However, the CW cavity has shown problems with locking and flipping directions while scanning. This might cause challenges during limited beam times for online measurements and hence for online measurements, the cavity still has to be updated to achieve better stability and locking conditions.

CHAPTER 6

Conclusions and perspectives

As a part of this thesis work, the first off-line laser ionization and spectroscopy tests were carried out with the S^3-LEB. These results show the potential of the setup to perform high-resolution laser spectroscopy studies. Even though the spectral resolution is not as good as expected from the used nozzle, these results show an order of magnitude better resolution than those in conventional gas cell experiments, as seen for Er, which at this stage of development, gives nice prospects for laser spectroscopy of heavy elements. The collisional effects in the gas cell ionization could be quantified for the transition used. The isotope shift and the hyperfine constants were measured and they are in good agreement with the literature values. The enhanced spectral resolution in the gas jet laser spectroscopy studies in comparison to that obtained in the gas cell has been proved experimentally with this work. In-gas jet ionization technique gives a resolution of less than 300 MHz for erbium in the gas jet laser spectroscopy studies in comparison to that obtained in the gas cell. The determined Mach number of the jet was 4.5 which was below expectation. The reasons were identified which were inhomogeneity of the jet, misalignment of the laser and power broadening. More systematic studies are being performed with the resonance ionization flow mapping method to improve the spectral resolution. Adapting to the solutions achieved from the flow mapping method, the Mach number could be improved to 6 - 7. With these off-line measurements, the setup is validated for future on-line experimental studies.

The in-gas cell and gas-jet ionization were studied in detail and the transmission across the whole setup until the mass spectrometer was studied to obtain a preliminary relative transmission efficiency of 80% from the S-RFQ to the end of PILGRIM assuming an efficiency close to 100% for the S-RFQ and mini-RFQ. A measurement of the extraction efficiency of the gas cell will be performed in the future with Rn source. The optimization of the RFQs performed as a part of this thesis work is comparable with the expected efficiency. PILGRIM optimization is currently ongoing to obtain the best mass resolution. Upgradation of PILGRIM to have better voltage stability will be implemented in the near future which should improve the mass resolving power to the order of 10^5.

With these tests, the offline commissioning tests of the setup at LPC Caen

have reached their final stages. The S^3-LEB setup is thus ready to be installed at the focal plane of S^3 to start online commissioning and the measurement from this thesis work will act as a reference for benchmarking the measurements. The online commissioning will start with isotopes of erbium. For the online commissioning, entrance windows will be installed with the gas cell. Every window will be tested in the window test bench before its installation with the gas cell. For the day-1 cases, as in Er, and Sn, the windows for the gas cell have been already tested and shown to work well with this thesis work. For trans-uranium elements, further tests and developments have to be carried out to obtain the best window-gas cell combination.

The Ti: sapphire-based laser systems have been prepared and characterized for both gas cell and gas jet laser ionization and spectroscopy. With the currently commissioned laser systems, online commissioning of day-1 cases can be started. For high-resolution laser spectroscopy, the tuning capability of narrow-band laser is an important aspect. The continuous wave single mode tunable Ti: sapphire laser cavity is a cheaper and alternative approach for broad range tuning capability. The implementation of the cavity, its challenges, and its characterization have been discussed in this work. As a future perspective, this cavity will be seeded to the newly built injection-locked cavity and proof of principle measurement will be performed in an atomic beam unit. The cavity is compared with an older version installed at Mainz on which offline high-resolution laser spectroscopy measurement on americium has been performed which gives strong motivation for using the new laser system for high-resolution measurements in S^3-LEB. The americium measurements have proven that the CW laser system can act as a potential tool for high-resolution laser spectroscopy. As a proof of principle measurements, the isotope shift and hyperfine A and B constants are deduced. It shows that the tuning capability, stability, and line width of such cost-effective laser systems are sufficient for performing high-resolution laser spectroscopy even with densely populated levels of actinides and that the atomic and nuclear properties can be extracted.

Offline resonance ionization laser scheme tests have been performed for uranium which is also one of the online experiments at S^3-LEB. The heavy elements show strong collision effects in the gas cell and the tests have been performed to see the ionization efficiency of different schemes. The observations from the gas cell ionization tests indicate strong collisional effects hindering the resonant ionization of uranium isotopes. It shows the need for a stable source and systematic scheme development tests to study heavier elements. The tests with uranium show the different aspects to be considered at S^3-LEB when performing in gas cell ionization with actinides. The hot cavity tests also present suitable laser schemes that could be used for the in-gas jet spectroscopy measurements.

References

[1] *Accelerators, URL=https://www.ganil-spiral2.eu/scientists/ganil-spiral-2-facilities/accelerators/.*

[2] P. Campbell, I. Moore, and M. Pearson. "Laser spectroscopy for nuclear structure physics". In: *Progress in Particle and Nuclear Physics* 86 (2016), pp. 127–180.

[3] X. Yang, S. Wang, S. Wilkins, and R. G. Ruiz. "Laser spectroscopy for the study of exotic nuclei". In: *Progress in Particle and Nuclear Physics* 129 (2023), p. 104005.

[4] P. Van Duppen, P. Dendooven, M. Huyse, L. Vermeeren, Z. Qamhieh, R. Silverans, and E. Vandeweert. "A laser ion source for on-line mass separation". In: *Hyperfine Interactions* 74 (1992), pp. 193–204.

[5] D. Fink, S. Richter, B. Bastin, K. Blaum, R. Catherall, T. E. Cocolios, D. Fedorov, V. Fedosseev, K. Flanagan, L. Ghys, et al. "First application of the Laser Ion Source and Trap (LIST) for on-line experiments at ISOLDE". In: *Nuclear Instruments and Methods in Physics Research Section B: Beam Interactions with Materials and Atoms* 317 (2013), pp. 417–421.

[6] Y. Kudryavtsev, B. Bruyneel, M. Huyse, J. Gentens, P. Van den Bergh, P. Van Duppen, and L. Vermeeren. "A gas cell for thermalizing, storing and transporting radioactive ions and atoms. Part I: Off-line studies with a laser ion source". In: *Nuclear Instruments and Methods in Physics Research Section B: Beam Interactions with Materials and Atoms* 179.3 (2001), pp. 412–435.

[7] R. Ferrer, M. Verlinde, E. Verstraelen, A. Claessens, M. Huyse, S. Kraemer, Y. Kudryavtsev, J. Romans, P. Van den Bergh, P. Van Duppen, et al. "Hypersonic nozzle for laser-spectroscopy studies at 17 K characterized by resonance-ionization-spectroscopy-based flow mapping". In: *Physical Review Research* 3.4 (2021), p. 043041.

[8] P. Chauveau, P. Delahaye, G. De France, S. El Abir, J. Lory, Y. Merrer, M. Rosenbusch, L. Schweikhard, and R. Wolf. "PILGRIM, a multi-reflection time-of-flight mass spectrometer for SPIRAL2-S^3 at GANIL". In: *Nuclear Instruments and Methods in Physics Research Section B: Beam Interactions with Materials and Atoms* 376 (2016), pp. 211–215.

[9] Vandebrouck, M. *Spectroscopy Electron Alpha in Silicon bOx couNter – SEASON , url = https://anr.fr/Project-ANR-20-CE31-0005*.

[10] K. S. Krane. *Introductory nuclear physics*. John Wiley & Sons, 1991.

[11] R. Neugart and G. Neyens. "The Euroschool Lectures on Physics with Exotic Beams, Vol. II". In: *Lecture Notes in Physics* 700 (2006), p. 135.

[12] J. Suhonen. *From nucleons to nucleus: concepts of microscopic nuclear theory*. Springer Science & Business Media, 2007.

[13] G. W. Drake. *Springer handbook of atomic, molecular, and optical physics*. Springer Nature, 2023.

[14] A. K. Singh, D. Angom, and V. Natarajan. "Observation of the nuclear magnetic octupole moment of 173 Yb from precise measurements of the hyperfine structure in the 3 P 2 state". In: *Physical Review A* 87.1 (2013), p. 012512.

[15] W. Nörtershäuser and I. Moore. "Nuclear Charge Radii". In: *Handbook of Nuclear Physics*. Springer, 2022, pp. 1–70.

[16] J. Romans. "High-resolution laser spectroscopy developments of heavy elements using the gas jet systems". PhD thesis. Institute for Nuclear and Radiation Physics, KU Leuven, 2023.

[17] W. Demtröder. *Atoms, molecules and photons*. Vol. 3. 7. Springer, 2010.

[18] W. Demtröder. *Laser spectroscopy 1: basic principles*. Springer, 2014.

[19] R. De Groote, M. Verlinde, V. Sonnenschein, K. Flanagan, I. Moore, and G. Neyens. "Efficient, high-resolution resonance laser ionization spectroscopy using weak transitions to long-lived excited states". In: *Physical Review A* 95.3 (2017), p. 032502.

[20] Y. Kudryavtsev, R. Ferrer, M. Huyse, P. Van den Bergh, and P. Van Duppen. "The in-gas-jet laser ion source: Resonance ionization spectroscopy of radioactive atoms in supersonic gas jets". In: *Nuclear Instruments and Methods in Physics Research Section B:Beam Interactions with Materials and Atoms* 297 (2013), pp. 7–22.

[21] R. Ferrer, A. Barzakh, B. Bastin, R. Beerwerth, M. Block, P. Creemers, H. Grawe, R. de Groote, P. Delahaye, X. Fléchard, et al. "Towards high-resolution laser ionization spectroscopy of the heaviest elements in supersonic gas jet expansion". In: *Nature Communications* 8.1 (2017), pp. 1–9.

[22] K. F. Renk. *Basics of laser physics*. Springer, 2012.

[23] P. Hammerling, A. B. Budgor, and A. Pinto. *Tunable Solid State Lasers: Proceedings of the First International Conference La Jolla, Calif., June 13–15, 1984*. Vol. 47. Springer, 2013.

[24] B. E. Saleh and M. C. Teich. *Fundamentals of photonics*. john Wiley & sons, 2019.

[25] S. Kobtsev and N. Sventsitskaya. "Application of birefringent filters in continuous-wave tunable lasers: a review". In: *Opt. Spektrosk* 73 (1992), pp. 196–212.

[26] S. Rothe. "An all-solid state laser system for the laser ion source RILIS and in-source laser spectroscopy of astatine at ISOLDE, CERN". PhD thesis. Mainz U., Inst. Kernphys., 2012.

[27] O. Svelto, D. C. Hanna, et al. *Principles of lasers*. Vol. 1. Springer, 2010.

[28] T. Kessler. *Development and application of laser technologies at radioactive ion beam facilities*. 8. University of Jyväskylä, 2008.

[29] J. Billowes, P. Campbell, E. Cochrane, J. Cooke, P. Dendooven, D. Evans, I. Grant, J. Griffith, A. Honkanen, M. Huhta, et al. "First collinear laser spectroscopy measurements of radioisotopes from an IGISOL ion source". In: *Nuclear Instruments and Methods in Physics Research Section B: Beam Interactions with Materials and Atoms* 126.1-4 (1997), pp. 416–418.

[30] B. Cheal and D. Forest. "Collinear laser spectroscopy techniques at JYFL". In: *Three decades of research using IGISOL technique at the University of Jyväskylä: A Portrait of the Ion Guide Isotope Separator On-Line Facility in Jyväskylä* (2014), pp. 83–91.

[31] T. E. Cocolios, H. Al Suradi, J. Billowes, I. Budinčević, R. De Groote, S. De Schepper, V. Fedosseev, K. Flanagan, S. Franchoo, R. G. Ruiz, et al. "The collinear resonance ionization spectroscopy (CRIS) experimental setup at CERN-ISOLDE". In: *Nuclear Instruments and Methods in Physics Research Section B: Beam Interactions with Materials and Atoms* 317 (2013), pp. 565–569.

[32] S. Kujanpää, A. Raggio, R. de Groote, M. Athanasakis-Kaklamanakis, M. Block, A. Candiello, W. Gins, Á. Koszorús, I. Moore, M. Reponen, et al. "RAPTOR: a new collinear laser ionization spectroscopy and laser-radiofrequency double-resonance experiment at the IGISOL facility". In: *Nuclear Instruments and Methods in Physics Research Section B: Beam Interactions with Materials and Atoms* 541 (2023), pp. 388–391.

[33] R. Ambartzumian and V. Letokhov. "Selective two-step (STS) photoionization of atoms and photodissociation of molecules by laser radiation". In: *Applied optics* 11.2 (1972), pp. 354–358.

[34] V. Letokhov. *Laser photoionization spectroscopy*. Elsevier, 2012.

[35] V. Fedosseev, K. Chrysalidis, T. D. Goodacre, B. Marsh, S. Rothe, C. Seiffert, and K. Wendt. "Ion beam production and study of radioactive isotopes with the laser ion source at ISOLDE". In: *Journal of Physics G: Nuclear and Particle Physics* 44.8 (2017), p. 084006.

[36] V. N. Fedosseev, Y. Kudryavtsev, and V. I. Mishin. "Resonance laser ionization of atoms for nuclear physics". In: *Physica Scripta* 85.5 (2012), p. 058104.

[37] M. Reponen, T. Kessler, I. Moore, S. Rothe, and J. Äystö. "A hot cavity laser ion source at IGISOL". In: *The European Physical Journal A* 42 (2009), pp. 509–515.

[38] V. Mishin, A. Malinovsky, and D. Mishin. "Resonant Ionization Laser Ion Source (RILIS) With Improved Selectivity Achieved By Ion Pulse Compression Using In-Source Time-of-flight Technique". In: *AIP Conference Proceedings* 1104.1 (2009), pp. 207–212.

[39] R. Heinke, T. Kron, S. Raeder, T. Reich, P. Schönberg, M. Trümper, C. Weichhold, and K. Wendt. "High-resolution in-source laser spectroscopy in perpendicular geometry: Development and application of the PI-LIST". In: *Hyperfine Interactions* 238 (2017), pp. 1–9.

[40] R. Ferrer, B. Bastin, D. Boilley, P. Creemers, P. Delahaye, E. Liénard, X. Fléchard, S. Franchoo, L. Ghys, M. Huyse, et al. "In gas laser ionization and spectroscopy experiments at the Superconducting Separator Spectrometer (S^3): Conceptual studies and preliminary design". In: *Nuclear Instruments and Methods in Physics Research B:Beam Interactions with Materials and Atoms* 317 (2013), pp. 570–581.

[41] P. Papadakis, I. Moore, T. Eronen, J. Liimatainen, T. Kalvas, J. Partanen, I. Pohjalainen, M. Reponen, S. Rinta-Antila, J. Sarén, et al. "Status and development of the MARA low-energy branch". In: *AIP Conference Proceedings* 2011.1 (2018), p. 070013.

[42] J. Warbinek, B. Anđelić, M. Block, P. Chhetri, A. Claessens, R. Ferrer, F. Giacoppo, O. Kaleja, T. Kieck, E. Kim, et al. "Advancing Radiation-Detected Resonance Ionization towards Heavier Elements and More Exotic Nuclides". In: *Atoms* 10.2 (2022), p. 41.

[43] D. Münzberg, M. Block, A. Claessens, R. Ferrer, M. Laatiaoui, J. Lantis, S. Nothhelfer, S. Raeder, and P. Van Duppen. "Resolution characterizations of JetRIS in Mainz using 164Dy". In: *Atoms* 10.2 (2022), p. 57.

[44] I. Moore, T. Kessler, T. Sonoda, Y. Kudryavstev, K. Peräjärvi, A. Popov, K. Wendt, and J. Äystö. "A study of on-line gas cell processes at IGISOL". In: *Nuclear Instruments and Methods in Physics Research Section B: Beam Interactions with Materials and Atoms* 268.6 (2010), pp. 657–670.

[45] L. Vermeeren, N. Bijnens, M. Huyse, Y. A. Kudryavtsev, P. Van Duppen, J. Wauters, Z. Qamhieh, P. Thoen, E. Vandeweert, and R. Silverans. "An on-line laser ion source based on resonance photoionization in a gas cell". In: *Physical review letters* 73.14 (1994), p. 1935.

[46] E. Mogilevskiy, R. Ferrer, L. Gaffney, C. Granados, M. Huyse, Y. Kudryavtsev, S. Raeder, and P. Van Duppen. *Design of Small-Scaled De Laval Nozzle for IGLIS Experiment* , *url* = https://www.comsol.com/paper/design-of-small-scaled-de-laval-nozzle-for-iglis-experiment-15349.

[47] P. H. Dawson. *Quadrupole mass spectrometry and its applications*. Elsevier, 2013.

[48] R. E. March and J. F. Todd. *Quadrupole ion trap mass spectrometry*. John Wiley & Sons, 2005.

[49] D. Douglas. “Linear quadrupoles in mass spectrometry”. In: *Mass spectrometry reviews* 28.6 (2009), pp. 937–960.

[50] K. Blaum, C. Geppert, P. Müller, W. Nörtershäuser, E. Otten, A. Schmitt, N. Trautmann, K. Wendt, and B. Bushaw. “Properties and performance of a quadrupole mass filter used for resonance ionization mass spectrometry”. In: *International Journal of Mass Spectrometry* 181.1-3 (1998), pp. 67–87.

[51] J. Szerypo, G. Ban, C. Le Brun, P. Delahaye, E. Lienard, F. Mauger, O. Naviliat, B. Tamain, and D. Hennecart. *Design and performance of an RFQ cooler and buncher*. Tech. rep. Caen Univ., 1999.

[52] F. Herfurth, J. Dilling, A. Kellerbauer, G. Bollen, S. Henry, H.-J. Kluge, E. Lamour, D. Lunney, R. Moore, C. Scheidenberger, et al. “A linear radiofrequency ion trap for accumulation, bunching, and emittance improvement of radioactive ion beams”. In: *Nuclear Instruments and Methods in Physics Research Section A: Accelerators, Spectrometers, Detectors and Associated Equipment* 469.2 (2001), pp. 254–275.

[53] A. Nieminen, J. Huikari, A. Jokinen, J. Äystö, P. Campbell, E. Cochrane, E. Collaboration, et al. “Beam cooler for low-energy radioactive ions”. In: *Nuclear Instruments and Methods in Physics Research Section A: Accelerators, Spectrometers, Detectors and Associated Equipment* 469.2 (2001), pp. 244–253.

[54] R. Wolf, F. Wienholtz, D. Atanasov, D. Beck, K. Blaum, C. Borgmann, F. Herfurth, M. Kowalska, S. Kreim, Y. A. Litvinov, D. Lunney, V. Manea, D. Neidherr, M. Rosenbusch, L. Schweikhard, J. Stanja, and K. Zuber. “ISOLTRAP’s multi-reflection time-of-flight mass separator/spectrometer”. In: *International Journal of Mass Spectrometry* 349 (2013), pp. 123–133.

[55] A. Casares, A. Kholomeev, and H. Wollnik. “Multipass time-of-flight mass spectrometers with high resolving powers”. In: *International Journal of Mass Spectrometry* 206.3 (2001), pp. 267–273.

[56] A. Orduz, M. Di Giacomo, R. Ferdinand, B. Jacquot, O. Kamalou, J. Lagniel, G. Normand, A. Savalle, and D. Uriot. “Commissioning of a high power linac at GANIL: Beam power ramp-up”. In: *Physical Review Accelerators and Beams* 25.6 (2022), p. 060101.

[57] *New GANIL injector, URL = https://anr.fr/ProjetIA-21-ESRE-0018*.

[58] D. Ackermann, B. Blank, L. Caceres, M. Caamaño, G. De France, B. Gall, S. Grévy, C. Grygiel, E. Lamour, X. Ledoux, et al. *NEWGAIN White Book-Science Requirements-Work Package Physics*. Tech. rep. (2021).

[59] *NFS-Neutron for Science, URL=https://www.ganil-spiral2.eu/scientists/ganil-spiral-2-facilities/experimental-areas/nfs/*.

[60] F. Dechery, A. Drouart, H. Savajols, J. Nolen, M. Authier, A. Amthor, D. Boutin, O. Delferriére, B. Gall, et al. “Toward the drip lines and the superheavy island of stability with the Super Separator Spectrometer S^3”. In: *The European Physical Journal A* 51 (2015), pp. 1–16.

[61] A. Drouart, A. Amthor, D. Boutin, F. Déchery, J. Nolen, and H. Savajols. "Fusion-evaporation studies with the Super Separator Spectrometer (S3) at Spiral2". In: *EPJ Web of Conferences* 17 (2011), p. 14004.

[62] A. Drouart, J. Nolen, H. Savajols, S. collaboration, et al. "The Super Separator Spectrometer (S3) for the SPIRAL2 facility". In: *Journal of Physics: Conference Series*. Vol. 1643. 1. IOP Publishing. 2020, p. 012032.

[63] N. Karkour, B. Sulignano, J. Piot, H. Savagols, A. Drouart, M. Authier, V. Alaphilippe, A. Boujrad, P. Brionnet, T. Chaminade, et al. "SIRIUS project (spectroscopy & identification of rare isotopes using S3)". In: *IEEE Nuclear Science Symposium, Medical Imaging Conference and Room-Temperature Semiconductor Detector Workshop (NSS/MIC/RTSD)* (2016), pp. 1–6.

[64] A. Zadvornaya, P. Creemers, K. Dockx, R. Ferrer, L. Gaffney, W. Gins, C. Granados, M. Huyse, Y. Kudryavtsev, M. Laatiaoui, et al. "Characterization of supersonic gas jets for high-resolution laser ionization spectroscopy of heavy elements". In: *Physical Review X* 8.4 (2018), p. 041008.

[65] Y. Kudryavtsev, P. Creemers, R. Ferrer, C. Granados, L. Gaffney, M. Huyse, E. Mogilevskiy, S. Raeder, S. Sels, P. Van Den Bergh, et al. "A new in-gas-laser ionization and spectroscopy laboratory for off-line studies at KU Leuven". In: *Nuclear Instruments and Methods in Physics Research Section B: Beam Interactions with Materials and Atoms* 376 (2016), pp. 345–352.

[66] S. M. C. Sels. "Laser spectroscopy of neutron-deficient mercury isotopes and commissioning of a gas-jet based RFQ ion guide". PhD thesis. CERN, 2018.

[67] J. Romans, A. Ajayakumar, M. Authier, F. Boumard, L. Caceres, J.-F. Cam, A. Claessens, S. Damoy, P. Delahaye, P. Desrues, et al. "First Offline Results from the S^3 Low-Energy Branch". In: *Atoms* 10.1 (2022), p. 21.

[68] W. M. Brubaker. "An improved quadrupole mass analyzer". In: *Adv. Mass Spectrom* 4 (1968), pp. 293–299.

[69] D. Etasse. *Introduction to the FASTER acquisition system*. Tech. rep. http://faster.in2p3.fr/index.php/about-faster.

[70] B. M. Retailleau. "PILGRIM: un spectromètre de masse par temps de vol pour S^3, et brisure de symétrie d'isopin dans le 38K". PhD thesis. Normandie Université, 2021.

[71] S. Raeder, R. Ferrer, C. Granados, M. Huyse, T. Kron, Y. Kudryavtsev, N. Lecesne, J. Piot, J. Romans, H. Savajols, et al. "Performance of Dye and Ti: sapphire laser systems for laser ionization and spectroscopy studies at S3". In: *Nuclear Instruments and Methods in Physics Research Section B: Beam Interactions with Materials and Atoms* 463 (2020), pp. 86–95.

[72] R. Ferrer, V. Sonnenschein, B. Bastin, S. Franchoo, M. Huyse, Y. Kudryavtsev, T. Kron, N. Lecesne, I. Moore, B. Osmond, et al. "Performance of a high repetition pulse rate laser system for in-gas-jet laser ionization studies with the Leuven laser ion source @ LISOL". In: *Nuclear Instruments and Methods in Physics Research Section B: Beam Interactions with Materials and Atoms* 291 (2012), pp. 29–37.

[73] K. Wendt, K. Blaum, C. Geppert, R. Horn, G. Passler, N. Trautmann, and B. Bushaw. "Laser resonance ionization for efficient and selective ionization of rare species". In: *Nuclear Instruments and Methods in Physics Research Section B: Beam Interactions with Materials and Atoms* 204 (2003), pp. 325–330.

[74] V. Sonnenschein. "Laser developments and high resolution resonance ionization spectroscopy of actinide elements". In: *Research report/Department of Physics, University of Jyväskylä* 1/2015 (2014).

[75] V. Sonnenschein, I. Moore, S. Raeder, M. Reponen, H. Tomita, and K. Wendt. "Characterization of a pulsed injection-locked Ti: sapphire laser and its application to high resolution resonance ionization spectroscopy of copper". In: *Laser Physics* 27.8 (2017), p. 085701.

[76] S. Rothe, V. Fedosseev, T. Kron, B. Marsh, R. Rossel, and K. Wendt. "Narrow linewidth operation of the RILIS titanium: Sapphire laser at ISOLDE/CERN". In: *Nuclear Instruments and Methods in Physics Research Section B: Beam Interactions with Materials and Atoms* 317 (2013), pp. 561–564.

[77] M. Reponen, V. Sonnenschein, T. Sonoda, H. Tomita, M. Oohashi, D. Matsui, and M. Wada. "Towards in-jet resonance ionization spectroscopy: An injection-locked Titanium: Sapphire laser system for the PALIS-facility". In: *Nuclear Instruments and Methods in Physics Research Section A: Accelerators, Spectrometers, Detectors and Associated Equipment* 908 (2018), pp. 236–243.

[78] M. Reponen, I. Moore, T. Kessler, I. Pohjalainen, S. Rothe, and V. Sonnenschein. "Laser developments and resonance ionization spectroscopy at IGISOL". In: *Three decades of research using IGISOL technique at the University of Jyväskylä: A Portrait of the Ion Guide Isotope Separator On-Line Facility in Jyväskylä* (2014), pp. 295–309.

[79] H. Lotem. "Littrow-mounted diffraction grating cavity". In: *Applied optics* 33.6 (1994), pp. 930–934.

[80] J. Romans, A. Ajayakumar, M. Authier, F. Boumard, L. Caceres, J.-F. Cam, A. Claessens, S. Damoy, P. Delahaye, P. Desrues, et al. "High-resolution laser system for the S^3-Low Energy Branch". In: *Nuclear Instruments and Methods in Physics Research Section B: Beam Interactions with Materials and Atoms* 536 (2023), pp. 72–81.

[81] V. Sonnenschein, M. Ohashi, H. Tomita, and T. Iguchi. "A direct diode pumped continuous-wave Ti: sapphire laser as seed of a pulsed amplifier for high-resolution resonance ionization spectroscopy". In: *Nuclear Instruments and Methods in Physics Research Section B: Beam Interactions with Materials and Atoms* 463 (2020), pp. 512–514.

[82] P. F. Moulton, J. G. Cederberg, K. T. Stevens, G. Foundos, M. Koselja, and J. Preclikova. "Characterization of absorption bands in Ti: sapphire crystals". In: *Optical Materials Express* 9.5 (2019), pp. 2216–2251.

[83] V. Sonnenschein, H. Tomita, K. Kotaro, H. Koya, D. Studer, R. Terabayashi, F. Weber, K. Wendt, N. Nishizawa, and T. Iguchi. "A direct diode pumped Ti: sapphire laser with single-frequency operation for high resolution spectroscopy". In: *Hyperfine Interactions* 241 (2020), pp. 1–9.

[84] DataRay. *M^2 Measurement , url =* https://dataray.com/blogs/dataray-blog/m2-measurement.

[85] P. Berman. "Optical faraday rotation". In: *American Journal of Physics* 78.3 (2010), pp. 270–276.

[86] D. Ford and J. Shaw. "Rapid method of aligning Fabry-Perot etalons". In: *Applied Optics* 8.12 (1969), pp. 2555–2556.

[87] M. Tanzer, B. Lang, and A. Bergmann. "Fabrication of a Low-Cost, Fiber-Coupled, and Air-Spaced Fabry-Pérot Etalon". In: *JoVE (Journal of Visualized Experiments)* 192 (2023), e65174.

[88] A. Ortiz Cortes. "Palladium: a Study of Nuclear Deformation of a Refractory Element. Laser Spectroscopy at the IGISOL (Jyväskylä, Finland) and S3-LEB (GANIL, France)". In: *Ph.D. thesis, University of Jyvaskyla* (2023).

[89] D. Studer. "Resonanzionisationsspektroskopie hochliegender Zustände in Dysprosium und Erbium zur Entwicklung effizienter Anregungsschemata und Bestimmung des ersten Ionisationspotentials". Diploma thesis. Johannes Gutenberg-Universität Mainz, 2015.

[90] Y. Balasmeh. "The PILGRIM mass spectrometer: toward high accuracy measurements of exotic nuclei at S^3". Master thesis, Normandie Université, 2022.

[91] I. Pohjalainen. "Gas-phase chemistry, recoil source characterization and in-gas-cell resonance laser ionization of actinides at IGISOL". In: *Research report/Department of Physics, University of Jyväskylä* 5 (2018).

[92] I. Pohjalainen, I. Moore, S. Geldhof, V. Rosecker, J. Sterba, and T. Schumm. "Gas cell studies of thorium using filament dispensers at IGISOL". In: *Nuclear Instruments and Methods in Physics Research Section B: Beam Interactions with Materials and Atoms* 484 (2020), pp. 59–70.

[93] A. Raggio, I. Pohjalainen, and I. D. Moore. "Observation of Collisional De-Excitation Phenomena in Plutonium". In: *Atoms* 10.2 (2022), p. 40.

[94] W. Gins, R. P. de Groote, M. L. Bissell, C. G. Buitrago, R. Ferrer, K. M. Lynch, G. Neyens, and S. Sels. "Analysis of counting data: Development of the SATLAS Python package". In: *Computer Physics Communications* 222 (2018), pp. 286–294.

[95] A. Kramida, Y. Ralchenko, J. Reader, et al. "NIST atomic spectra database". In: *National Institute of Standards and Technology* (2018).

[96] N. Allard and J. Kielkopf. "The effect of neutral nonresonant collisions on atomic spectral lines". In: *Reviews of Modern Physics* 54.4 (1982), p. 1103.

[97] H. Okamura and S. Matsuki. "Isotope shift in erbium I by laser-atomic-beam spectroscopy". In: *Physical Review C* 35.4 (1987), p. 1574.

[98] W. J. Childs, L. S. Goodman, and V. Pfeufer. "Hyperfine structure of the $4f^{12}\ 6s^2\ ^3$H and ^{3}F terms of ^{167}Er I by atomic-beam, laser-rf double resonance". In: *Physical Review A* 28 (1983), pp. 3402–3408.

[99] S. Ahmad, C. Ekstrom, W. Klempt, R. Neugart, and K. Wendt. "Nuclear spins and moments of radioactive odd-A isotopes of erbium studied by collinear fast-beam laser spectroscopy". In: *Proceedings of the "Symposium on Quantum Electronics"* (1985).

[100] W.-G. Jin, H. Ono, and T. Minowa. "Isotope Shifts in High Lying Levels of Dy I and Er I by High-Resolution UV Laser Spectroscopy." In: *International Journal of Spectroscopy* (2011).

[101] J. S. Ross. "Isotope shifts in the spectra of Dy i and Er i". In: *Journal of the Optical Society of America* 62.4 (1972), pp. 548–554.

[102] O. Tarasov and D. Bazin. "LISE++ : design your own spectrometer". In: *Nuclear Physics A* 746 (2004). Proceedings of the Sixth International Conference on Radioactive Nuclear Beams (RNB6), pp. 411–414. ISSN: 0375-9474. URL: https://www.sciencedirect.com/science/article/pii/S0375947404010048.

[103] J. Ziegler, J. Biersack, and M. Ziegler. "SRIM (The Stopping and Range of Ions in Solids)-2013". In: *MD: USA* (2013).

[104] J. Ziegler, J. Biersack, and U. Littmark. *The Stopping and Range of Ions in Solids, Pergamon Press, New York*. Springer US, 1985.

[105] G. Schiwietz and P. Grande. "Improved charge-state formulas". In: *Nuclear Instruments and Methods in Physics Research Section B: Beam Interactions with Materials and Atoms* 175 (2001), pp. 125–131.

[106] D. Wittwer, F. S. Abdullin, N. Aksenov, Y. V. Albin, G. Bozhikov, S. Dmitriev, R. Dressler, R. Eichler, H. Gäggeler, R. Henderson, et al. "Gas phase chemical studies of superheavy elements using the Dubna gas-filled recoil separator–stopping range determination". In: *Nuclear Instruments and Methods in Physics Research Section B: Beam Interactions with Materials and Atoms* 268.1 (2010), pp. 28–35.

[107] P. V. GmbH. *Leak detection compendium, url = https://leak-detection.pfeiffer-vacuum.com/*.

[108] R. K. Sheline. "Definition of the actinide region of static quadrupole-octupole deformation". In: *Physics Letters B* 197.4 (1987), pp. 500–504.

[109] J. Billowes and M. Garcıa-Borge. *Octupole deformed nuclei in the actinide region*. Tech. rep. 1992.

[110] E. Verstraelen, P. Van Duppen, and R. Ferrer Garcia. "Laser spectroscopy of actinides: Octupole deformation and gas-jet characterization". In: (2021).

[111] B. Isselhardt, M. Savina, K. Knight, M. Pellin, I. Hutcheon, and S. Prussin. "Improving precision in resonance ionization mass spectrometry: influence of laser bandwidth in uranium isotope ratio measurements". In: *Analytical chemistry* 83.7 (2011), pp. 2469–2475.

[112] S. Raeder, S. Fies, T. Gottwald, C. Mattolat, S. Rothe, and K. Wendt. "In-source resonance ionization spectroscopy of high lying energy levels in atomic uranium". In: *Hyperfine Interactions* 196 (2010), pp. 71–79.

[113] P. L. Smith, C. Heise, J. R. Esmond, et al. *Atomic spectral line database from CD-ROM 23 of RL Kurucz*. accessed 20 September. 1995. URL: http://cfa-www.harvard.edu/amdata/ampdata/kurucz23/sekur.html.

[114] S. Raeder. "Spurenanalyse von Aktiniden in der Umwelt mittels Resonanzionisations massenspektrometrie". PhD thesis. Doktorarbeit, Institut für Physik, Universität Mainz, 2010.

[115] N. Kneip, C. E. Düllmann, V. Gadelshin, R. Heinke, C. Mokry, S. Raeder, J. Runke, D. Studer, N. Trautmann, F. Weber, et al. "Highly selective two-step laser ionization schemes for the analysis of actinide mixtures". In: *Hyperfine Interactions* 241 (2020), pp. 1–7.

[116] M. R. Savina, R. Trappitsch, A. Kucher, and B. H. Isselhardt. "New resonance ionization mass spectrometry scheme for improved uranium analysis". In: *Analytical chemistry* 90.17 (2018), pp. 10551–10558.

[117] M. Stemmler. "Aufbau eines Dioden-gepumpten, schmalbandigen Titan: Saphir-Lasers Anwendung zur hochaufl¨osenden Spektroskopie an Americium". Masterthesis, Institut für Physik, Universität Mainz, 2021.

[118] H. Backe, M. Hies, H. Kunz, W. Lauth, O. Curtze, P. Schwamb, M. Sewtz, W. Theobald, R. Zahn, K. Eberhardt, et al. "Isotope shift measurements for superdeformed fission isomeric states". In: *Physical review letters* 80.5 (1998), p. 920.

[119] H. Backe, W. Lauth, M. Block, and M. Laatiaoui. "Prospects for laser spectroscopy, ion chemistry and mobility measurements of superheavy elements in buffer-gas traps". In: *Nuclear Physics A* 944 (2015), pp. 492–517.

[120] R. Marrus, W. A. Nierenberg, and J. Winocur. "Hyperfine structure of americium-241". In: *Physical Review* 120.4 (1960), p. 1429.

[121] L. Armstrong Jr and R. Marrus. "Nuclear Moments of Americium-241 and 16-h Americium-242 and Analysis of the Hyperfine Fields". In: *Physical Review* 144.3 (1966), p. 994.

[122] G. Passler, M. Nunnemann, G. Huber, R. Deissenberger, N. Erdmann, S. Köhler, J. Kratz, N. Trautmann, A. Waldek, and J. Peterson. "Determination of the first ionization potential of nine actinide elements by resonance ionization mass spectroscopy". In: *AIP Conference Proceedings*. Vol. 454. 1. American Institute of Physics. 1998, pp. 183–188.

[123] R. Deissenberger, S. Köhler, F. Ames, K. Eberhardt, N. Erdmann, H. Funk, G. Herrmann, H.-J. Kluge, M. Nunnemann, G. Passler, et al. "First determination of the ionization potential of americium and curium". In: *Angewandte Chemie International Edition in English* 34.7 (1995), pp. 814–815.

[124] B. Le Garrec and A. Petit. "The hyperfine structure of 2 eV level in americium-241". In: *Journal of the Less Common Metals* 122 (1986), pp. 55–58.

[125] J. Blaise and J.-F. Wyart. *Selected constants energy levels and atomic spectra of actinides*. URL: http://www.lac.universite-paris-saclay.fr/Data/Database.

[126] M. Fred and F. S. Tomkins. "Preliminary term analysis of Am I and Am II spectra". In: *Journal of the Optical Society of America* 47.12 (1957), pp. 1076–1087.

Appendix

A In-gas cell ionization

The Voigt fits performed for the in-gas cell ionization measurements for each gas cell pressure are shown in figure A.1. The error bars for the Lorentzian FWHM and centroid are scaled with their reduced χ^2 values using the SATLAS program.

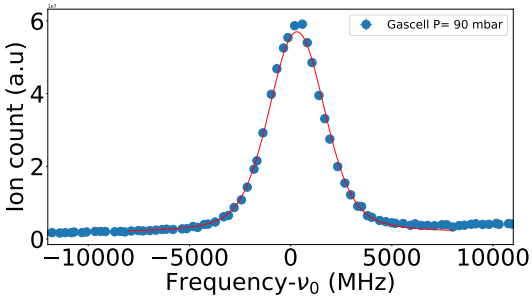

(a) P=90 mbar

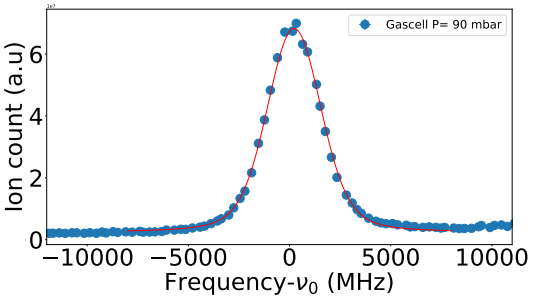

(b) P=90 mbar

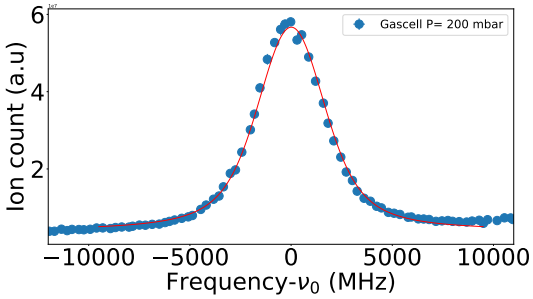

(c) P=200 mbar

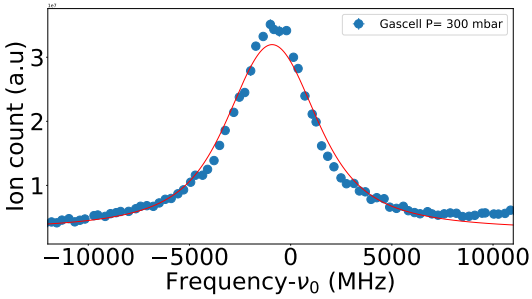

(d) P=300 mbar

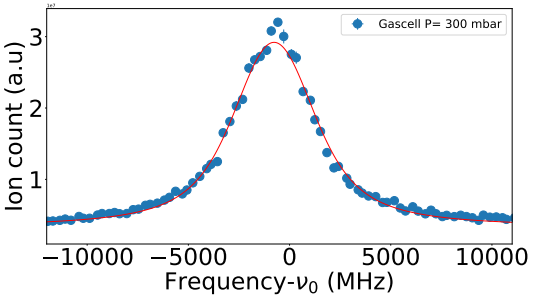

(e) P=300 mbar

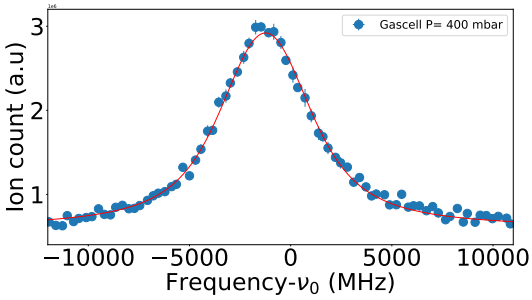

(f) P=400 mbar

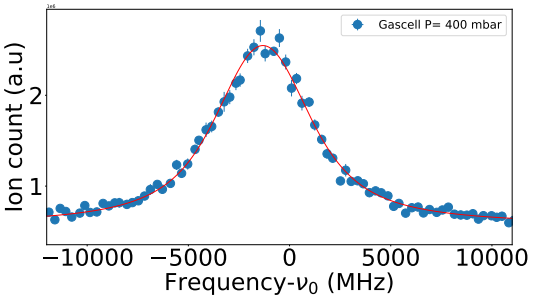

(g) P=400 mbar

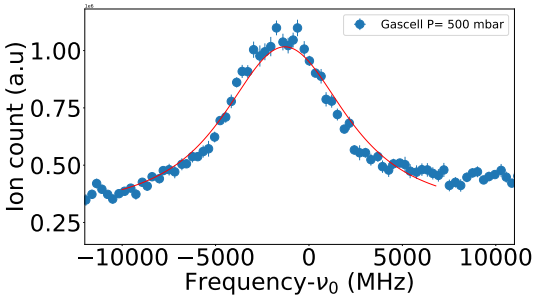

(h) P=500 mbar

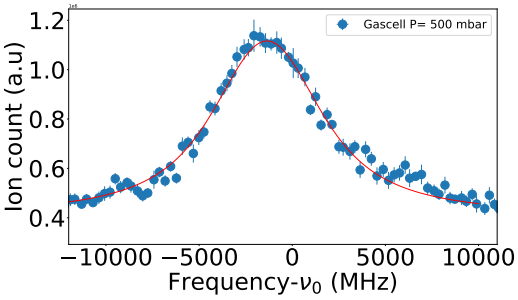

(i) P=500 mbar

Appendix A.1: Voigt fitting of resonance excitation spectra data.

B Uranium tests at JYU

Saturation scans

For different laser powers, the count rate was measured. The plot in steps for the different laser powers for each laser step are shown in figure B.2, B.3, and B.4. Data was collected in the following order. First the count rate with all lasers in, then the first step blocked, and then all lasers blocked. At the end of each measurement, the count rate for the full laser power was remeasured to obtain the correction factor for decreasing the count rate. The slope of the yellow line gives the correction for the decaying counts. The red line shows the background counts from non-resonant laser ionization. The uncertainty of the count rate for each laser power is the standard deviation from the mean of binned data for each laser power. The binning range for each laser power is shown by the blue lines. The data was binned with a step size of 0.05 to obtain the mean in each laser power range. The shaded portions show the range chosen for each laser power and their corresponding backgrounds.
First step laser powers in mW=[120,100,80,60,50,40,30,20]
Second step laser powers in mW=[430,400,354,305,250,200,150,100,50]
Third step laser powers in mW =[2000,1750,1000,1500,1250,750,500,250]

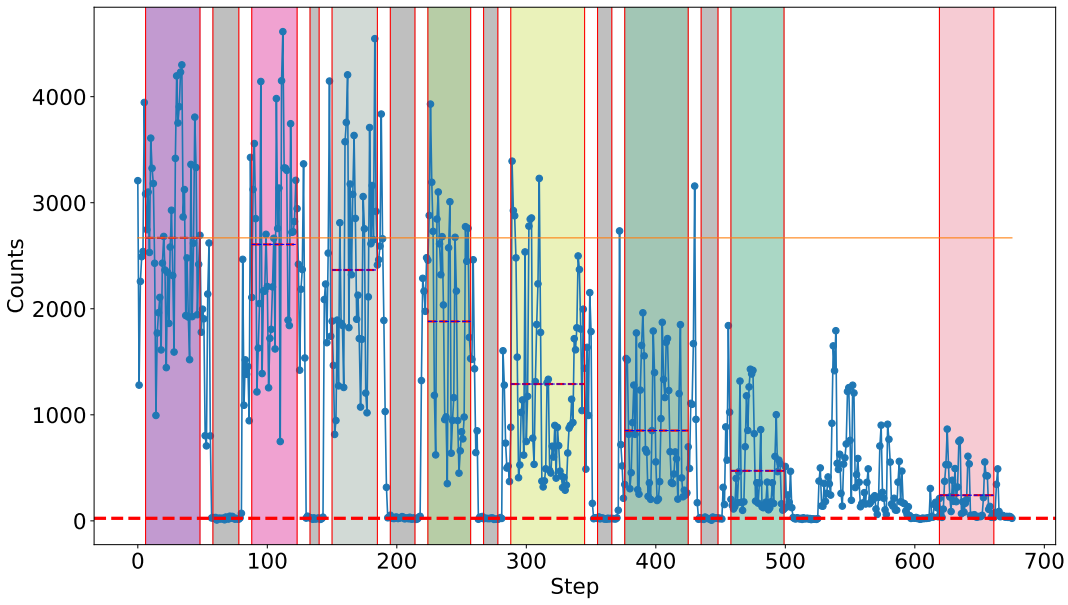

Appendix B.2: Scheme 1: Raw data for first laser step saturation studies.

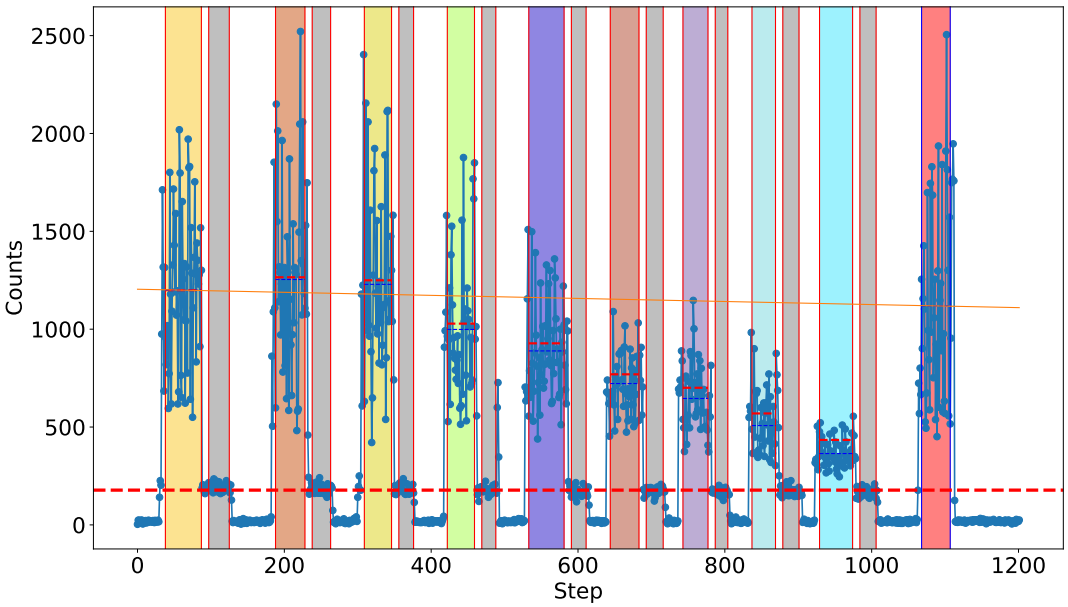

Appendix B.3: Scheme 1: Raw data for second laser step saturation studies.

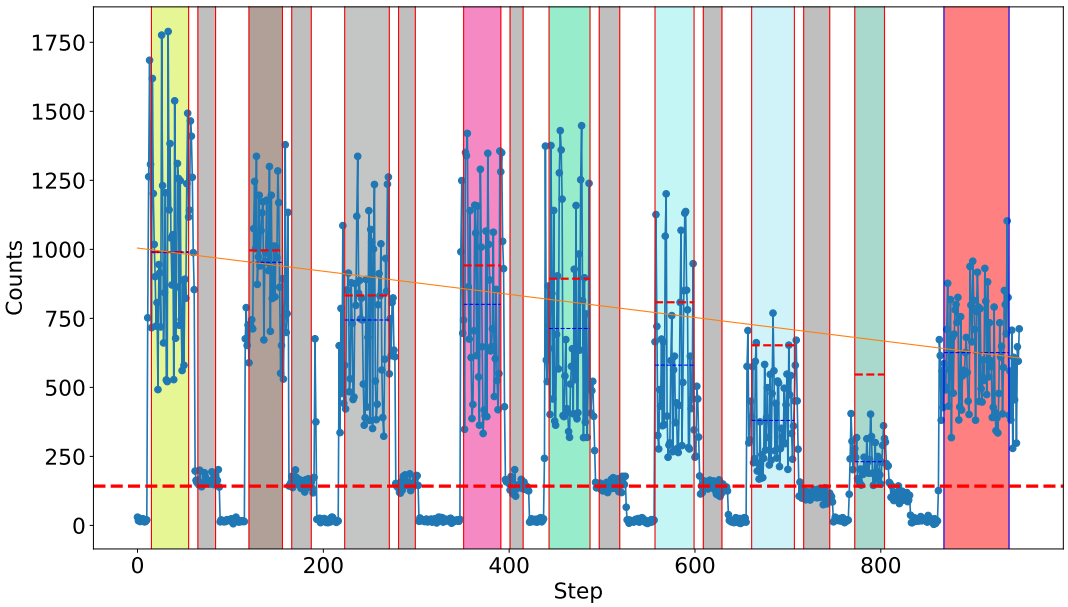

Appendix B.4: Scheme 1: Raw data for second laser step saturation studies.

Laser scans

More than one laser scan was performed for the uranium laser ionization in the gas cell. Figure B.5 are the plots from the different scans.

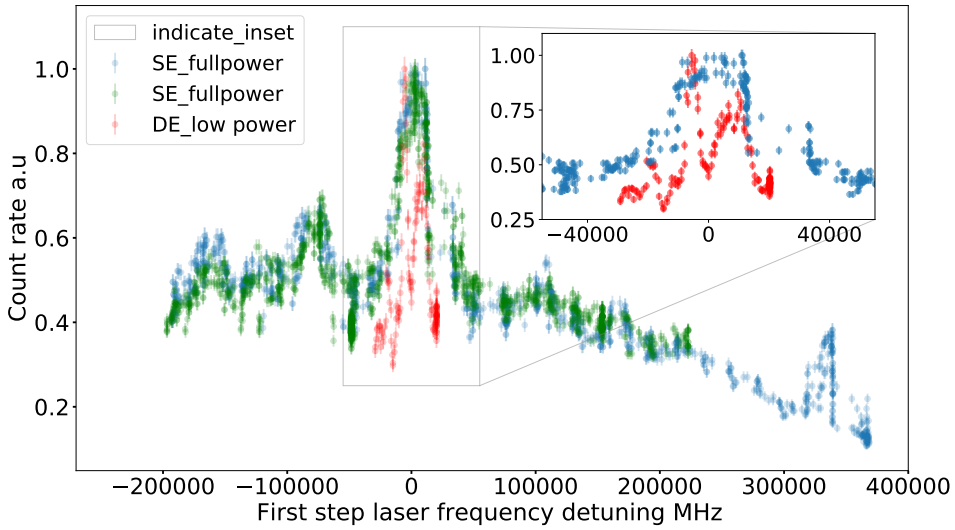

Appendix B.5: Long-range mass scan performed for the laser-produced ions in the gas cell. Labels: SE-single etalon and DE-dual etalon. Single etalon scans were performed at full power. Dual etalon scans were produced at lower laser powers

Mass scans

Several mass scans were taken for uranium tests in the gas cell. Below are plots in different conditions. Figure B.6 shows adducts of uranium with oxygen molecules. Figure B.8 shows mass scans showing the contribution of each laser step to the resonance ionization of uranium.

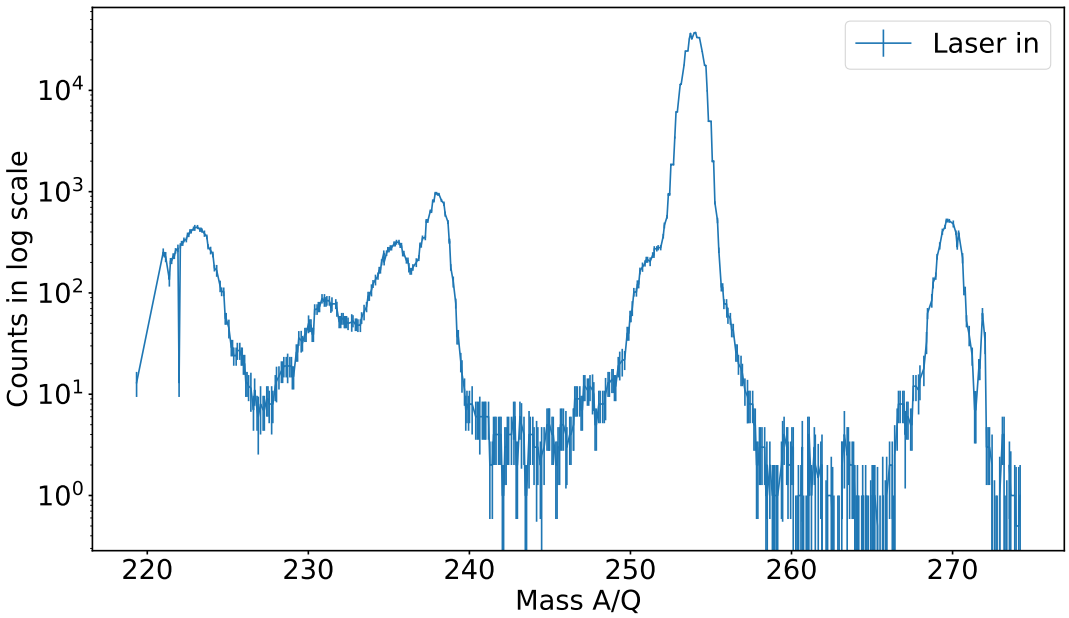

Appendix B.6: Long-range mass scan performed for the laser-produced ions in the gas cell showing the presence of U0 and UO_2 in the mass region 254 and 270.

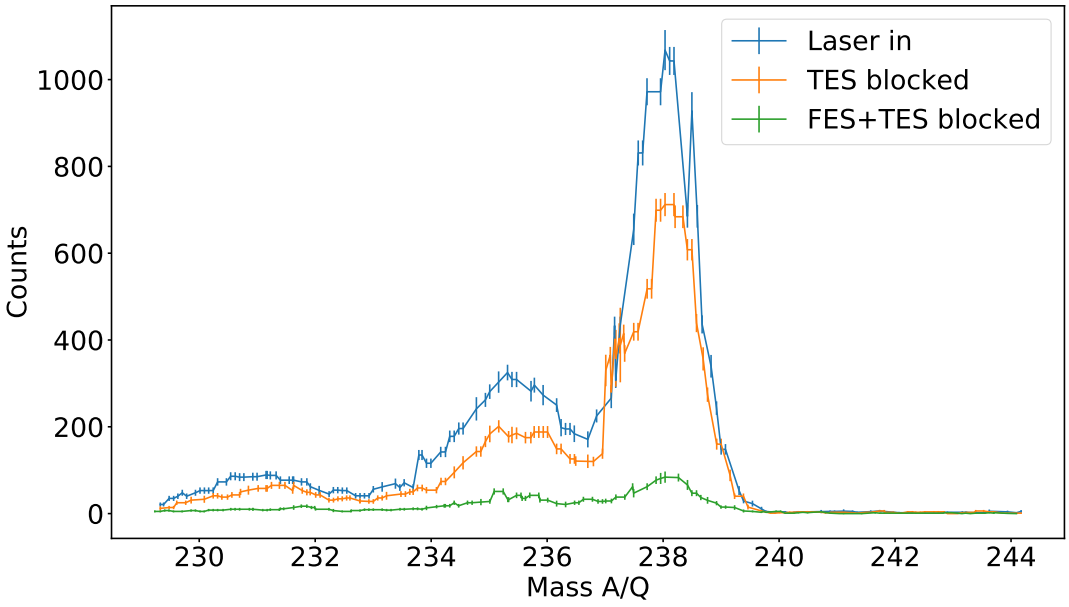

Appendix B.7: Mass scan performed for the laser-produced ions in the gas cell. Labels: FES - First excitation laser step and TES - third laser step

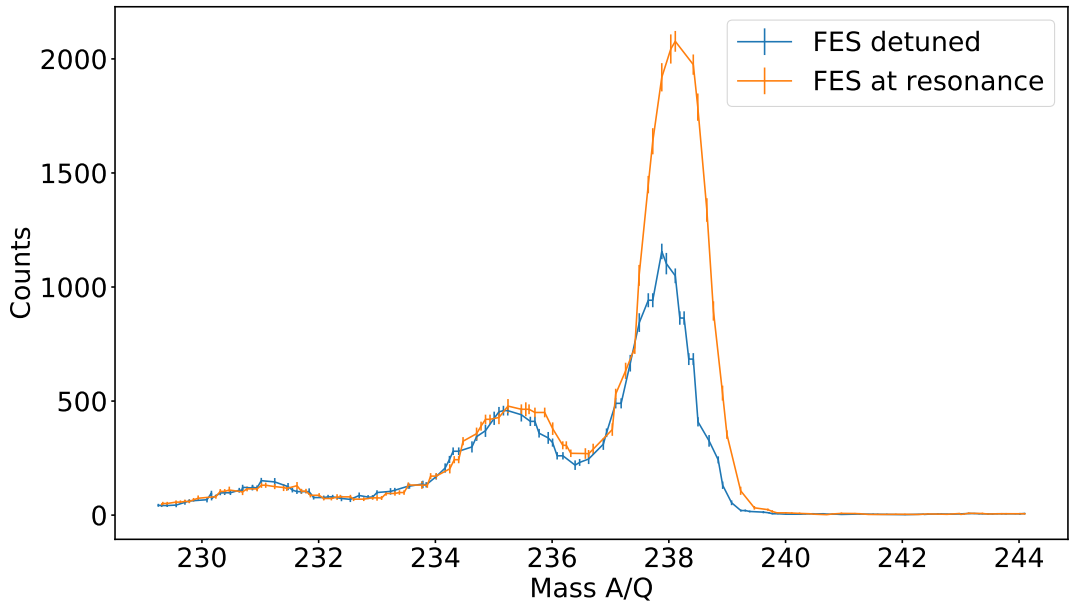

Appendix B.8: Mass scan performed for the laser-produced ions in the gas cell. Labels: FES-First excitation step